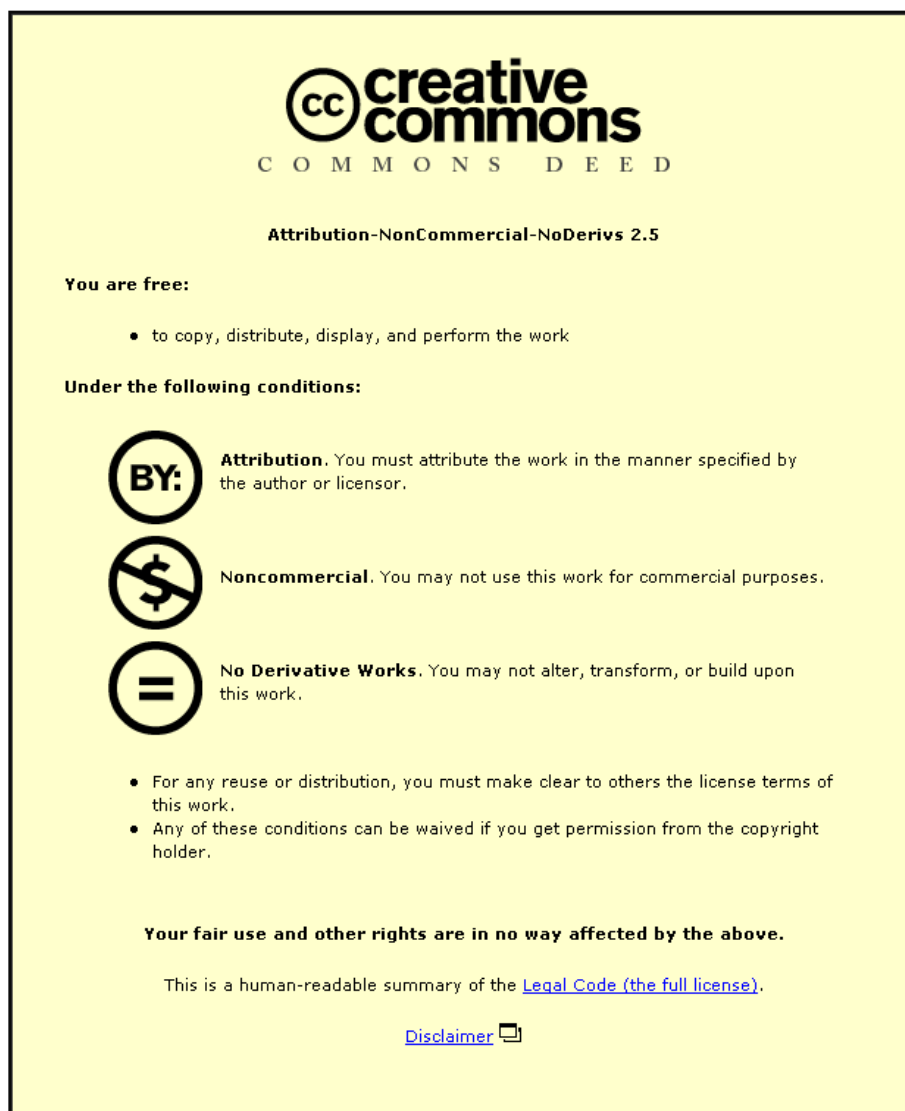


This item was submitted to Loughborough University as a PhD thesis by the author and is made available in the Institutional Repository (<https://dspace.lboro.ac.uk/>) under the following Creative Commons Licence conditions.



For the full text of this licence, please go to:
<http://creativecommons.org/licenses/by-nc-nd/2.5/>

Automatic Surface Defect Quantification in 3D

By

Mitulkumar J Tailor

A doctoral thesis submitted in partial fulfilment of the requirements
for the award of Doctor of Philosophy of Loughborough University

September 2013

© by Mitulkumar Tailor 2013

ABSTRACT

Three-dimensional (3D) non-contact optical methods for surface inspection are of significant interest to many industrial sectors. Many aspects of manufacturing processes have become fully automated resulting in high production volumes. However, this is not necessarily the case for surface defect inspection. Existing human visual analysis of surface defects is qualitative and subject to varying interpretation. Automated 3D non-contact analysis should provide a robust and systematic quantitative approach. However, different 3D optical measurement technologies use different physical principles, interact with surfaces and defects in diverse ways, leading to variation in measurement data. Instrument's native software processing of the data may be non-traceable in nature, leading to significant uncertainty about data quantisation.

Sub-millimetric level surface defect artefacts have been created using Rockwell and Vickers hardness testing equipment on various substrates. Four different non-contact surface measurement instruments (Alicona InfiniteFocus G4, Zygo NewView 5000, GFM MikroCAD Lite and Heliotis H3) have been utilized to measure different defect artefacts. The four different 3D optical instruments are evaluated by calibrated step-height created using slipgauges and reference defect artefacts. The experimental results are compared to select the most suitable instrument capable of measuring surface defects in robust manner.

This research has identified a need for an automatic tool to quantify surface defect and thus a mathematical solution has been implemented for automatic defect detection and quantification (depth, area and volume) in 3D. A simulated defect softgauge with a known geometry has been developed in order to verify the implemented algorithm and provide mathematical traceability. The implemented algorithm has been identified as a traceable, highly repeatable, and high speed solution to quantify surface defect in 3D. Various industrial components with suspicious features and solder joints on PCB are measured and quantified in order to demonstrate applicability.

Keywords: Surface defect, 3D measurement, quantification, softgauges

ACKNOWLEDGEMENT

My deepest gratitude goes first and foremost to Dr Jon Petzing, my first supervisor, for his encouragement and guidance throughout this research work. His feedback during our numerous discussion sessions helped me to develop more confidence in myself and also gain broader knowledge of the subject area.

I am also grateful to my co-supervisors Professor Mike Jackson and Professor Rob Parkin for their help and supervision. I cannot forget that critical time when both of them showed immense faith in me and supported me to carry on with this research work. I am also indebted to Professor Mike Jackson for his helpful comments during various stages of this research.

I would also like to thank Mr Jagpal Singh, Mr Richard Greenhough, Mr Andy Sandaver and Mr Robert Smith for their advice and assistance. I am grateful for the camaraderie shown by all the colleagues at the EPSRC Centre for Innovative Manufacturing in Intelligent Automation, especially Luke and Phil. Special thanks are also due to friends for their care and concern, especially Hemal who always kept me motivating to do this work.

I give glory to my father, Mr Jayantibhai Tailor and my mother, Mrs Nayantikaben Tailor, for their grace and protection over my life throughout the period of this research work. The phrase “Thank you” is just not enough for their blessings, constant prayers, unconditional love and never ending support. I would also like to thank the lady of my life, Rudra, to whom I got engaged in the last year of my research work. It would have been much more difficult to write this thesis without her understanding, co-operation, love and care.

Finally, I want to dedicate this thesis to my brother Mr Nimesh Tailor, sister-in-law Mrs Vaishali Tailor and my nephew Vedaant. My brother has been like a father figure to me throughout this journey and my sister-in-law has taken care of all basic requirements so that I can focus on my work. Vedaant has always given me a reason to smile even in tense situations. Without their support and encouragement, I do not think I would have come this far. No words can justify their stature and contributions.

PUBLICATIONS

The following publications have been generated from this work:

- M. Taylor, P.Phaithoonbuathong, J.Petzing, M. Jackson, R. Parkin, “Real-time surface defect detection and the traceable measurement of defect depth in 3D” 10th International Conference on Laser Metrology, Machine Tool, CMM & Robotic Performance – Proceedings of Lamdamap 2013, 171-180, UK. March 2013. ISBN 978-0-9566790-1-7. Oral presentation.
- M. Taylor, J.Petzing, P.Phairatt, M. Jackson, R. Parkin, “Real-time surface defect detection and the traceable measurement of defect in 3D”, 11th International Symposium on Measurement and Quality Control 2013, Poland, September 2013. Oral Presentation.
- M. Taylor, J.Petzing, P.Phairatt, M. Jackson, R. Parkin, “Developing confidence in automatic on-line quantification of surface defects”, 2nd Annual EPSRC Manufacturing the Future Conference 2013, UK. September 2013. Poster Presentation.
- P. Ogun, M. Chamberlain, P. Phairatt, M. Taylor, M. Jackson, “An active 3D vision system for automated detection and measurement of surface defect” Under review, to be submitted to the Journal of Engineering Manufacturing, 2013.

CONTENT

ABSTRACT	i
ACKNOWLEDGEMENT	ii
PUBLICATIONS	iii
CONTENT	iv
List of Figures	viii
List of Tables	xii
1 INTRODUCTION	1
1.1 Research background	1
1.2 Research objectives and novelty	2
1.3 Overview of thesis.....	3
2 LITERATURE REVIEW	5
2.1 Introduction	5
2.2 Measurement	5
2.3 Research overview	7
2.3.1 Surface defect	7
2.3.2 Surface defect measurement	11
2.3.2.1 Evaluation of 3D measuring system.....	21
2.3.3 Filtration.....	23
2.3.4 Defect detection	26
2.3.5 Quantification	28
2.3.5.1 Automatic defect quantification	29
2.3.6 Validation.....	30
2.4 Summary	31
3 STANDARD DEFECT ARTEFACT GENERATION	33
3.1 Introduction	33

3.2	Justification for generation of a standard defect artefact	33
3.3	Generation of defect artefact	34
3.3.1	Substrate preparation	35
3.3.2	Defect artefact.....	40
3.3.2.1	Rockwell indentation.....	41
3.3.2.2	Vickers indentation.....	44
3.3.3	Repeatability of the instruments	46
3.4	Traceability	50
3.5	Summary	51
4	INTER-COMPARISON OF 3D MEASURING INSTRUMENTS.....	52
4.1	Introduction	52
4.2	Surface texture measurement techniques	52
4.2.1	Focus variation.....	54
4.2.1.1	Alicona InfiniteFocus G4	55
4.2.2	Coherence scanning interferometer	56
4.2.2.1	Zygo NewView 5000	58
4.2.3	Digital fringe projection.....	59
4.2.3.1	GFM MikroCAD Lite.....	60
4.2.4	Parallel optical coherence tomography.....	61
4.2.4.1	Heliotis H3.....	63
4.3	Depth measurement.....	64
4.3.1	Step height	65
4.3.2	Artefact defect height.....	69
4.4	Instruments Performance	70
4.4.1	Alicona InfiniteFocus G4.....	70
4.4.2	Zygo NewView 5000.....	74
4.4.3	GFM MikroCAD Lite.....	78

4.4.4	Heliotis H3	82
4.5	Summary	86
5	DEVELOPMENT OF NOVEL ALGORITHM	95
5.1	Introduction	95
5.2	Need for a novel algorithm	95
5.3	Implementation of algorithm.....	101
5.3.1	Data re-arrangement	101
5.3.2	Filtration Techniques	103
5.3.2.1	Noise removal – Gaussian filter	104
5.3.2.2	Surface fitting – Robust Gaussian regression filter	106
5.3.2.3	Residual surface extraction.....	111
5.3.3	Thresholding	112
5.3.4	Defect isolation	116
5.3.5	Defect quantification.....	118
5.3.5.1	Depth measurement	118
5.3.5.2	Area measurement	120
5.3.5.3	Volume measurement	121
5.4	Summary	121
6	VALIDATION OF NOVEL ALGORITHM.....	124
6.1	Introduction	124
6.2	Defect softgauges	124
6.2.1	Mathematical model of defect softgauge	127
6.2.2	Measurement using the novel algorithm.....	132
6.2.3	Repeatability	136
6.3	Artefact measurement	141
6.3.1	Artefacts in different Plate substrates	142
6.3.2	Artefacts of different size	145

6.3.3	Artefacts in different shapes of substrate.....	150
6.3.4	Artefacts of different shape.....	154
6.4	Summary	156
7	MEASUREMENT OF INDUSTRIAL COMPONENTS.....	158
7.1	Introduction.....	158
7.2	Automotive components	158
7.2.1	Bearing shell	159
7.2.2	Piston	171
7.3	Solder joints on a Printed Circuit Board (PCB).....	176
7.4	Summary	184
8	CONCLUSION & FUTURE WORK	185
8.1	Introduction.....	185
8.2	Conclusion.....	185
8.3	Future work	191
	REFERENCES.....	193

List of Figures

Figure 2-1 Surface texture measurement methods	12
Figure 2-2 Three types of standard optical methods	14
Figure 2-3 Surface comprised of waviness, roughness and form	23
Figure 2-4 (a) Surface profile with Gaussian filter line (b) roughness profile	24
Figure 2-5 (a) Measured surface profile with Gaussian regression filter (b) roughness profile [89]	25
Figure 2-6 Procedure for comparing software	30
Figure 3-1 Flat plate – A	35
Figure 3-2 Talysurf Intra	36
Figure 3-3 Flat Plate B generated using bead blasting	37
Figure 3-4 Flat Plate C generated using grinding paper scratching	38
Figure 3-5 Flat Plate D generated using manual polishing	39
Figure 3-6 Single curvature metal plate	40
Figure 3-7 Double curvature metal plate	40
Figure 3-8 Avery Rockwell test equipment	41
Figure 3-9 Test cycle for a Rockwell hardness test	42
Figure 3-10 Defect artefacts using the diamond indenter	43
Figure 3-11 Defect artefacts using the steel ball indenter	44
Figure 3-12 Vickers hardness test equipment	44
Figure 3-13 Defect artefacts using Vikers hardness test equipment	45
Figure 3-14 Steps for manual depth measurement of the indentation	47
Figure 3-15 Manual depth measurement of a conical indentation	48
Figure 3-16 Manual depth measurement of the pyramidal indentation	49
Figure 3-17 Traceability Chain	50
Figure 4-1 Optical arrangement of a FV based measurement equipment	54
Figure 4-2 Alicona InfiniteFocus G4	55
Figure 4-3 Optical arrangement of CSI	57
Figure 4-4 Zygo NewView 5000	58
Figure 4-5 Schematic of DFP system	60
Figure 4-6 GFM MikroCAD Lite	61
Figure 4-7 Schematic of pOCT	62
Figure 4-8 Heliotis H3	64

Figure 4-9 Slip-gauge arrangement to create a step-height of 100 μm	65
Figure 4-10 Nikon Metrology (Metris) Ultra CMM.....	66
Figure 4-11 Step-height measured using the Alicona IFM G4.....	67
Figure 4-12 Step-height measurement	67
Figure 4-13 Step height measurement using four different instruments	68
Figure 4-14 Manual depth measurement	69
Figure 4-15 Defect number 2 on Plates A to D measured using the Alicona.....	73
Figure 4-16 Defect depth measurement on different substrates using the Alicona	74
Figure 4-17 Defect number 2 on Plates A to D measured using the Zygo	77
Figure 4-18 Defect depth measurement on different substrates using the Zygo	78
Figure 4-19 Defect number 2 on Plates A to D measured using GFM.....	81
Figure 4-20 Defect depth measurement on different substrates using the GFM	82
Figure 4-21 Defect number 2 on Plates A to D measured using the Heliotis.....	85
Figure 4-22 Defect depth measurement on different substrates using Heliotis.....	86
Figure 4-23 Inter-comparison of optical instruments on different defects on Plate D (Rq = 0.06 μm)	89
Figure 4-24 Inter-comparison of optical instruments on different defects on Plate A (Rq = 0.16 μm)	90
Figure 4-25 Inter-comparison of optical instruments on different defects on Plate C (Rq = 0.78 μm)	91
Figure 4-26 Inter-comparison of optical instruments on different defects on Plate B (Rq = 1.27 μm)	92
Figure 5-1 Five cross-sections of defect	95
Figure 5-2 Determining the boundary of the defect	97
Figure 5-3 3D data arrangement (a) 16 x 3 matrix (b) 4 x 4 matrix (c) size of a pixel	102
Figure 5-4 Gaussian 5 x 5 kernel matrix.....	104
Figure 5-5 Conical defect in Plate A (a) raw data (b) smooth surface	105
Figure 5-6 Defect in Plate A (a) Filtered surface (b) Mean surface (c) Two profiles ..	109
Figure 5-7 Defect in double curvature plate (a) Filtered surface (b) Mean surface (c) Two profiles	110
Figure 5-8 Residual surface	111
Figure 5-9 Binary image of the defect in Plate A using the Otsu's method.....	113
Figure 5-10 Binary image of the defect in Plate B using Otsu's method	114

Figure 5-11 Binary image of conical defect in Plate A using the new thresholding approach.....	115
Figure 5-12 Binary image of the smallest defect in Plate B using the new thresholding approach.....	116
Figure 5-13 Conical defect region in binary image	117
Figure 5-14 Isolated conical defect.....	118
Figure 5-15 Reference plane generation	119
Figure 5-16 Highlighted defect area on the top of the surface	120
Figure 5-17 Flow chart of the novel algorithm for defect quantification	122
Figure 6-1 Reference data for a profile given in ISO 5436-2	125
Figure 6-2 Reference data – a sinusoidal profile	126
Figure 6-3 Procedure for comparing software	126
Figure 6-4 Defect softgauge	128
Figure 6-5 Defect softgauge with a resolution of 1 in the matrix form	131
Figure 6-6 Isolated defect softgauge.....	132
Figure 6-7 Depth evaluation at different resolutions	134
Figure 6-8 Area evaluation at different resolutions	134
Figure 6-9 Volume evaluation at different resolutions	135
Figure 6-10 Time evaluation at different resolutions	136
Figure 6-11 A conical defect (a) Raw data (b) Isolated defect.....	138
Figure 6-12 Comparison of measured quantities of artefacts in different roughness substrates.....	142
Figure 6-13 Depth measurement of artefacts in different roughness substrates.....	144
Figure 6-14 Area measurement of artefacts in different roughness substrates.....	144
Figure 6-15 Volume measurement of artefacts in different roughness substrates.....	145
Figure 6-16 Comparison of measured quantities of artefact of different size	147
Figure 6-17 Depth measurement of artefacts of different sizes.....	148
Figure 6-18 Area measurement of artefacts of different sizes.....	148
Figure 6-19 Volume measurement of artefacts of different sizes.....	149
Figure 6-20 Comparison of measured quantities of artefact in different shapes of substrate	150
Figure 6-21 Depth measurement of artefacts in different shapes of substrate.....	152
Figure 6-22 Area measurement of artefacts in different shapes of substrate.....	152
Figure 6-23 Volume measurement of artefacts in different shapes of substrate	153

Figure 6-24 Measurement of the spherical shaped defect	155
Figure 6-25 Measurement of the pyramidal shaped defect.....	156
Figure 7-1 Defect on the convex side of the plain bearing (Defect ID – 1)	160
Figure 7-2 Raw data of the defect on the convex side (Defect ID -1).....	160
Figure 7-3 (a) Cropped raw data (b) Isolated defect in residual surface	161
Figure 7-4 Defect on the concave side of the plain bearing (Defect ID – 2).....	163
Figure 7-5 Raw data of Defect ID – 2	163
Figure 7-6 Inverted raw data.....	164
Figure 7-7 Isolated defect in the residual surface (Top view)	165
Figure 7-8 Positive Defect ID – 2.....	165
Figure 7-9 The defect on the concave side of the plain bearing (Defect ID – 3).....	167
Figure 7-10 Raw data of Defect ID – 3	168
Figure 7-11 Cropped raw data of Defect ID – 3	169
Figure 7-12 Inverted cropped data.....	169
Figure 7-13 Isolated defect in the residual surface (Top veiw)	170
Figure 7-14 Positive Defect ID – 3	171
Figure 7-15 Surface defect (Defect ID – 4) embedded in the piston crown.....	172
Figure 7-16 (a) Raw data (b) Residual surface	173
Figure 7-17 (a) Isolated negative part of the defect (b) Isolated positive part of the defect.....	175
Figure 7-18 PCB (a) Circular solder joint (b) Square solder joint.....	177
Figure 7-19 Raw data of circular solder joint	178
Figure 7-20 (a) Inverted raw data (b) Isolated circular solder joint.....	179
Figure 7-21 Isolated solder joint on the PCB surface.....	180
Figure 7-22 Square solder joint raw data.....	181
Figure 7-23 (a) Inverted raw data (b) Isolated solder joint.....	182
Figure 7-24 Isolated solder joint in the surface	183

List of Tables

Table 2-1 Summary of contact and non-contact measurement methods	14
Table 2-2 Measurement systems' capability to detect and quantify surface defect	22
Table 2-3 Technical specification of four technologies.....	23
Table 2-4 Surface profile roughness parameters	28
Table 2-5 Surface areal roughness parameters	29
Table 3-1 Roughness parameters of Plate A.....	36
Table 3-2 Roughness parameters of Plate B	37
Table 3-3 Roughness parameters of Plate C	38
Table 3-4 Roughness parameters of Plate D.....	39
Table 3-5 Loads used to generate different sizes of Rockwell indentations.....	43
Table 3-6 Loads used to generate different sizes of Vickers indentations	45
Table 3-7 Repeatability of the hardness testing instruments	49
Table 4-1 Step height measurement.....	67
Table 4-2 Manual depth measurement by Alicona on Plates A to D	72
Table 4-3 Defect depth measurement by Zygo on Plates A to D	76
Table 4-4 Defect depth measurement by GFM on Plate A to D.....	80
Table 4-5 Defect depth measurement by Heliotis on Plates A to D.....	84
Table 4-6 Depth measurement for defects on substrate having $Rq = 0.06 \mu\text{m}$ (Plate D).....	89
Table 4-7 Depth measurement for defects on substrate having $Rq = 0.16 \mu\text{m}$ (Plate A).....	90
Table 4-8 Depth measurement for defects on substrate having $Rq = 0.78 \mu\text{m}$ (Plate C).....	91
Table 4-9 Depth measurement for defects on substrate having $Rq = 1.27 \mu\text{m}$ (Plate B).....	92
Table 4-10 Inter-comparison of performance characteristics	93
Table 5-1 Manual depth measurement (Test method 1).....	96
Table 5-2 Manual measurement using MountainMap software (Test method 2).....	98
Table 5-3 Depth measurements by expert users using Test method 1.....	99
Table 5-4 Manual measurement by expert users using Test method 2.....	100
Table 6-1 Theoretical measurement of the defect softgauge	129
Table 6-2 Measurement of softgauges with different resolution	133
Table 6-3 Measurement error at different resolution.....	133
Table 6-4 Repeatability measurement	137
Table 6-5 Repeatable quantification of the conical defect	139
Table 6-6 Comparison of the manual and automatic depth measurement.....	140

Table 6-7 Comparison of the manual and automatic quantification of the defect.....	140
Table 6-8 Measurement of artefacts in different roughness substrates	143
Table 6-9 Measurement of different size artefact on Plate A ($Rq = 0.16 \mu\text{m}$)	146
Table 6-10 Measurement of artefacts in different shape of substrate.....	151
Table 6-11 Measurement of the spherical shaped artefact	154
Table 6-12 Measurement of the pyramidal shaped defect	155
Table 7-1 Quantification of Defect ID – 1	162
Table 7-2 Quantification of Defect ID – 2.....	166
Table 7-3 Quantification of Defect ID – 3.....	170
Table 7-4 Quantification of both positive and negetive side of the Defect ID – 4.....	176
Table 7-5 Quantification of the circular solder joint	180
Table 7-6 Quantification of the square solder joint	183
Table 8-1 Objectives completion and resultant novelty	189

1 INTRODUCTION

1.1 Research background

In recent years, there has been an increased need for quality control in the manufacturing sector. Many manufacturing processes have become fully automated resulting in high production volumes. However, this is not the case for surface inspection of a critical component in quality control. The aerospace and automotive industries may reject any materials with defects as a function of manufacturing processes because a minor defect in a manufactured part might result in a failure at a later stage [1]. Therefore it is a continuous challenge for inspection engineers to cope with the pace of high speed automated CNC machines and to ensure inspection quality in comparable time frames. In addition, the high cost involved in manual inspection by inspection engineers has prompted the need and development of automated inspection and defect quantification systems capable of performing various inspection tasks. In the context of the semiconductor industry, the accuracy rates of manual classification are typically 60 % - 80 %, though rates as low as 30 % - 50 % have been reported [2]. Automated inspected system equipped with machine vision system may offer consistency, accuracy and round the clock repeatability, in contrast to the subjectivity, fatigue, slowness and costs associated with human inspectors [2,3].

Generally, a human inspector checks the part visually and decides if it has to be rejected or accepted for further processing. To meet the customer requirements, and also to establish a standard in this manual process, the inspector must follow the inspection guideline. This guideline is a document which typically presents a sketch of the part divided into areas with different inspection requirements. The time invested to inspect the part and the visual path that the human inspector must follow during the inspection is also defined in this guideline. The result of this manual inspection depends on human factors such as subjectivity and visual tiring that lead to dissatisfactory quality control. For this reason, a fully automated inspection system may be highly desirable [4] .

Machine vision based mechatronic systems have been developed to tackle the automated inspection and defect characterization challenges. The key objective of

machine vision algorithms is to provide an automatic detection and quantification of objects based on their visual similarity. Xue-Wi *et al* [5] and Rosati *et al* [6] developed automatic visual inspection systems for detecting the defect on highly reflective metal surfaces. Sun *et al* implemented an x-ray based real time imaging system that detected weld defects in steel pipes [7]. Lin developed a computer-aided visual inspection system for surface defects in ceramic chips for capacitors [8]. Xiaoli *et al* proposed a 2D wavelet transform method for automatic defect detection in castings measured using x-ray, whilst wavelet based defect detection in solar cell was proposed by Li and Tsai [9].

It is noted that all of these systems have been implemented in the 2D domain thus the measurement of depth and volume of the detected defect is not feasible. In order to determine the volumetric information of the defect, a surface defect needs to be measured using 3D imaging techniques. It is important to evaluate the depth and volume of the defect as these parameters are often key factors in quality assurance in order to determine pass/failure of the manufactured part.

Defect detection and its quantification on freeform surface inspection in 3D is a highly process specific problem which is very challenging for current technologies. Moreover size of the defect may also be crucial. Automation of the manual visual inspection operations for surface defects on industrial components in 3D presents great challenges such as components having different dimensions, complex and freeform surfaces with different surface conditions, critical different sized surface defects and location of such defects [10-12].

1.2 Research objectives and novelty

Measurement and quantification of a surface defect in 3D is a relatively new and developing field. This research work concentrates on measuring small surface defects (as small as 20 μm in depth) followed with automatic quantification in 3D.

The objective and perceived novelty of this work presented here is identified as follows:

- (1) To investigate 3D optical surface measurement techniques that are capable of measuring fine surface defects. Selection of potential measuring techniques will

be made from the investigation of the limitations of each measuring technique. This section of work will recognize and use existing intellectual knowledge.

- (2) To develop standard and traceable defect artefacts to evaluate the functional performance of the selected 3D measuring techniques. Potential methods of generating defect artefacts include Rockwell and Vickers hardness test equipment. This section of work is expected to have novelty with respect to surface defects.
- (3) To conduct experiments using developed defect artefacts as a benchmark to derive the measuring technique that will be used to measure surface imperfection on the industrial components. This section of work will recognize existing intellectual knowledge, but, is expected to have novelty with respect to surface defect measurement.
- (4) To investigate data analysis and signal/image processing techniques to quantify surface defects and identify their limitation followed with implementation of mathematical algorithm to quantify defects automatically with high repeatability and high reproducibility. This section of work is expected to have novelty.
- (5) To develop a traceable simulated defect in software to evaluate and verify the correctness of implemented algorithm. This section of work is expected to have high novelty.
- (6) With the combination of evaluated 3D measuring technique and implemented algorithm, to measure and quantify different industrial components that contain surface imperfection.

1.3 Overview of thesis

This thesis consists of eight chapters organised as follows:

Chapter 1: The first chapter presents a brief introduction of the topic to be investigated, identifying the motivations which have led to this research. The aims of the research

and its objectives are outlined with a clear identification of the proposed novel content of the research.

Chapter 2: This chapter provides the context for the research and details aspects of existing literature. Focus is placed on the importance of the surface defect measurement in different industries followed with automated surface measurement techniques in 3D and data analysis techniques for the quantification of surface defects. The review also focuses on the validation aspects of the analysis techniques.

Chapter 3: In this chapter, standard and traceable defect artefacts are developed using the Rockwell hardness test and the Vickers hardness test.

Chapter 4: This chapter focuses on the inter-comparison of four different 3D measuring instruments. Functional capabilities of these instruments are evaluated using standard defect artefacts. Based on the results from a series of experimentation, a 3D instrument is selected for the surface imperfection measurement on the industrial components.

Chapter 5: In this chapter, limitations of current methods of data analysis are explained. To overcome these limitations, a mathematical algorithm is developed that is capable of detecting surface defects automatically followed with quantification in 3D.

Chapter 6: In this chapter, a novel simulated defect is generated to validate the implemented novel algorithm. The main purpose of this work is to evaluate the functional characteristics of the algorithm. Various standard defect artefacts are measured and quantified using the novel algorithm to check the ability of the algorithm to deal with complex surfaces.

Chapter 7: In this chapter, surface imperfection on industrial components are measured and quantified. Different components such as piston crowns and plain bearings from automotive industry and solder joints on the printed circuit board are measured and quantified automatically using the novel algorithm in 3D.

Chapter 8: The last chapter summarises and concludes the research work and also identifies possible areas of future work.

2 LITERATURE REVIEW

2.1 Introduction

This thesis considers the role of surface defects affecting the overall performance capability of the industrial components. Chapter 2 identifies the need for an automatic, high speed and highly repeatable surface defect measurement and quantification system. The chapter provides an overview of small surface defects affecting performance in the aerospace and automotive industries. The chapter then gives brief information about surface texture measurement techniques that are useful for defect measurement. The chapter introduces data process techniques and identifies the issue of validation, before finishing with a brief summary.

2.2 Measurement

“When you can measure what you are speaking about, and express it in numbers, you know something about it but when you cannot measure it, when you cannot express it in numbers, your knowledge is of a meagre and unsatisfactory kind.” – Lord Kelvin

This statement about measurement was made by the Victorian scientist Lord Kelvin [13], and neatly summarises the importance of measurement. It follows that measurement leads to knowledge, knowledge leads to understanding and understanding leads to improvement. Measurement is the way of quantifying details about a workpiece, for example its dimensions [14].

For the measurement science, it has its own set of definitions. Some of the most important technical terms are used frequently in this thesis. The definitions which identified here are not put together in alphabetical order as the definitions are mutually supporting each other as they are described [15].

Quantity: The property of a phenomenon, body, or substance, where the property has a magnitude that can be expressed as a number and a reference.

Quantity value: Value of a quantity.

Metrology: The science of measurement.

Measurand: The quantity intended to be measured.

True quantity value: Quantity value consistent with the definition of a quantity.

Accuracy: The closeness of agreement between a measured quantity value and a true quantity value of a measurand.

Precision: The closeness of agreement measured between quantity values obtained by replicate measurements on the same or similar objects under specific condition.

Measurement error: The measured quantity value minus the true value.

Repeatability: The closeness of agreement measured between quantity values obtained under specific conditions that include the same measurement procedure, same operators, same measuring system, same operating conditions and same location, and replicate measurement on the same or similar objects over a short period of time.

Reproducibility: The closeness of agreement measured between quantity values obtained under specific conditions that include different location, operators, measuring systems and replicate measurement on the same or similar objects.

Measurement uncertainty: Non-negative parameter characterizing the dispersion of the quantity values being attributed to a measurand, based on the information used.

Calibration: Operation that, under specified conditions, in a first step, establishes a relation between the quantity values with measurement uncertainties provided by measurement standards and corresponding indications with associated measurement uncertainties and, in a second step, uses this information to establish a relation for obtaining a measurement result from an indication.

Traceability: The property of a measurement result whereby the result can be related to a reference through a documented unbroken chain of calibrations, each contributing to the measurement uncertainty.

Resolution: The smallest change in a quantity being measured that causes a perceptible change in the corresponding indication.

Field of view: The diameter of the circle of illumination on the object [16].

Depth of field: The thickness of the optical section along the principle axis of the objective lens within which the object is in focus [16].

2.3 Research overview

Apart from the UK EPSRC Centre for Innovative Manufacturing in Intelligent Automation (EPSRC - IACIM) at Loughborough University, another community conducting research in the area of surface defect measurement in 3D has also been identified. It is the Surface Metrology Research Group of the Centre for Precision Technologies at the University of Huddersfield in the UK. Similarly to the EPSRC – IACIM, one of the missions of this group is to conduct research aimed at surface defect measurement and quantification in 3D.

The field of surface defect detection is so vast that it is impossible to cover all the aspects of visual inspection. The main aim of the literature review is to review the state-of-the-art measurement techniques for the purpose of visual inspection and validated data manipulation technique to detect and to quantify of the surface defects automatically in 3D. The purpose of this chapter is to review some of these research activities that are relevant to the current project. Outlines of the areas that are covered in this review are given below:

- Surface defects
- Surface texture measurement techniques
- Surface filtration
- Surface defect detection
- Surface defect quantification
- Software validation

2.3.1 Surface defect

In the aerospace industry, an aerofoil section has a vital role to play in a turbine engine. The temperature, and hence pressure and velocity, of the gases exiting the combustion chamber can have a direct influence on the overall performance of the engine. The components that these gases encounter are compressor blades, high-pressure turbine blades and nozzle guide vanes. It is crucial that these components are able to operate

efficiently within these hostile environments, where operating temperatures frequently exceed the melting point of the blade parent material. Given this, rotating aerofoil blades are liable to thermal fatigue cracks and corrosion at various areas on the components. After a pre-specified operational time designated at the design stage, these blades are removed for inspection and repair, or replacement, depending on their condition [17].

Harvey and Jones reported that the inspection for surface breaking cracks has been carried out using Fluorescent Penetrant Inspection (FPI). When conducting FPI, the components must be completely clean with no surface contamination present, otherwise indications may appear that are not due to cracks alone, resulting in false detect calls. Due to the operating conditions experienced by these blades, it is not a trivial operation to prepare the surface to the finish required for inspection, and this process can be both time-consuming and expensive. This expense is increased considerably when blades are scrapped immediately after inspection stage. Therefore, the introduction of non-destructive technique prior to cleaning that can identify obvious scrap independent of surface contaminant is an attractive cost-saving solution to this challenge [17].

Ejaz *et al* investigated a crashed aircraft in an accident. Initial investigations identified that the accident was due to the failure of a compressor rotor. The engine had a nine-stage axial flow compressor in which the nine disks were joined together through riveting. After the accident a number of blades and broken pieces of the outer ring of the 9th stage compressor disc were found scattered on the runway and near the crashed aircraft. On removal of the engine from the aircraft, the mid casing was found ruptured. Initial investigation concluded that the failure of the 9th stage disc of the compressor rotor caused the aircraft crash. Failure analysis of the 9th stage disk showed that the disk failed due to fatigue which started from one of the six holes present on the disk. The origins of fatigue cracks were machining marks, which were present on the surface of the disk and the lengths of these cracks were in the range of 2 mm to 36 mm [18].

Xi *et al* investigated the abrupt failure of the engine of an aircraft that was about to take off and found that the accident resulted from the fracture failures of the rotor blade and disk in the first stage compressor [19]. In both cases if these defects had been detected at an earlier stage during manufacture process, the accident may have been avoided.

Not only critical components such as aerofoils but the inspection of the outer skin of aircraft is also important. The outer skin of aircraft, exposed to wear and tear and accidental damage during service life, undergoes regular in-service inspections in the search for surface defects such as impact damage in composite panels or corrosion in metallic parts, which may compromise the structural integrity of the aircraft. The large inspection areas and severe time constraints involved prevent the intensive use of conventional methods such as ultrasound or eddy currents techniques during routine maintenance. Instead, trained operators perform a visual inspection of the entire structure, and an in-depth assessment is restricted to regions where there is visual evidence of damage. As a result, the structure must be designed to cope with any defects that could pass unnoticed i.e. defects with a size below the visibility threshold, commonly accepted at 300 μm [20]. This imposes severe design constraints, and there is a need for a method that can significantly improve on the sensitivity and reliability of visual inspections while retaining low cost, simplicity and speed.

It is noted that a very little amount of information has been found on the surface imperfection on the critical aerospace engine components. This is probably due to the confidentiality of the manufacturing processes and related intellectual property of the aerospace industries leading to non-disclosure of defect occurrence and detection techniques.

Similarly, in the automotive industry, quality control of car body parts is of critical importance. This is because the competition between the manufacturers is always getting sharper. The ability to predict surface defects in outer panels is of vital importance especially for brands in the premium car segment. Today, measures to prevent these defects cannot be taken until a test part has been manufactured, which involves the expenditure of much time and money. If these defects could be predicted at an early stage in the development process, the time and cost reduction would be significant [21] increasing customer satisfaction, sales and market shares.

The first impression of a car is made by the observation of the exterior appearance. A flawless exterior with smooth surfaces and edges suggest technical superiority. Customers intentionally look for objects in the environment with a linear texture, e.g. fluorescent light tubes and observe the course of reflection lines on the surface of the

body. Sárosi *et al* identified that dents and bumps of ten micrometres depth and several millimetres lateral dimension can be visually perceived on a varnished car-body [22].

In the early production stages, these small defects are hidden from the human observer because of the rough and dull surface quality of raw parts. They become clearly visible and disturbing only after the later production steps, in which parts get painted and varnished, meaning they become specularly reflecting. With each production step, the price of the part increases, due to additional work, time and material. The later the defect gets detected, the more correction will cost [22].

Armesto *et al* [11] have observed that skilled operators inspect car bodies for defects detection in the initial stages of the process and they usually do not detect 80 % of minor defects. The size of the defect increases incrementally with each additional paint application until they do not meet the quality control standards, resulting in the rejection of the vehicle.

These non-detected defects constitute corrosion sources that reduce the life of the products. However, even if the defects are detected before a car leaves the factory; the cost of repairing them at the end of the manufacturing process is very high. Firstly because they have to be repaired by hand and sometimes offline in external centres; and second because in the paint application the primer layers that protect the metal surface from corrosion are often damaged so that the product life is greatly reduced. For these reasons, it is very important to detect defects as soon as possible in order to reduce costs in terms of energy consumption, paint expenditure and of course, time. Wan from Audi AG suggests that small surface defects, with size of 10 μm to 100 μm in depth are clearly visible after painting due to reflections and hence it is very important to detect such micro defects at early stages [10].

Automotive defects are not only limited to body panels. Beretta *et al* [23] worked to estimate the fatigue strength of engine connecting rods containing various defects due to manufacturing processes. They have found that the size of the defects, typical lateral dimension of the defects ranging from 300 μm - 2000 μm , is one of the critical aspects that affect the fatigue strength estimation.

Sikder *et al* [24] suggests that there is a clear need to develop a suitable method to quantify surface defects, typically with depth size of 10 μm to 100 μm and lateral size

of 10 μm to 1000 μm and relate back to product performance. This is because surface defects not only deteriorate surface aesthetics but also accelerate the surface degradation process leading to product failure faster than predicted. Quantification and fundamental understanding is not only a key to product differentiation but also to position new grades of quality.

Apart from defects on the aerospace and automotive components, corrosion is also a critical surface feature. It is important to measure and quantify corrosion as it may influence the functional performance of the components. Corrosion is the gradual destruction of materials, usually metals, by chemical reaction with its environment. In the most common use of the word, this means electrochemical oxidation of metals in reaction with an oxidant such as oxygen. Corrosion degrades the useful properties of materials and structures including strength and appearance. Many structural alloys corrode merely from exposure to moisture in air, but the process can be strongly affected by exposure to certain substances.

Corrosion can be concentrated locally to form a pit or crack or it can extend across a wide area. One of the most destructive forms is pitting corrosion [25]. The pitting corrosion is characterized by the presence of a number of small pits on the exposed metal surface. Wu *et al* [26] measured pitting corrosion using a laser triangulation technique on metallic pipes and Fang *et al* measured pitting corrosion of mild steel using the focus variation technique [27]. Both researchers evaluated depth of the pitting corrosion by taking a cross-sectional profile manually, however, it was unclear about the method to select the reference points of the profiles to quantify the depth.

2.3.2 Surface defect measurement

In order to quantify a surface defect, it is important to measure the surface defect. Surface defects are measured using surface texture measuring instruments. Surface texture measurements are undertaken by two groups of methods; contact measurement and non-contact measurement. Each group is then divided into subgroups which can be seen in Figure 2-1. It is noted that this section surveys surface texture measuring techniques that may be capable of measuring surface defects embedded on metallic surfaces for inspection applications. The most practical imaging techniques are discussed with particular emphasis to their applicability and bottlenecks. The choice of

the technique is strongly connected to the characteristics of the flaws, the nature of the surface and the required spatial resolutions.

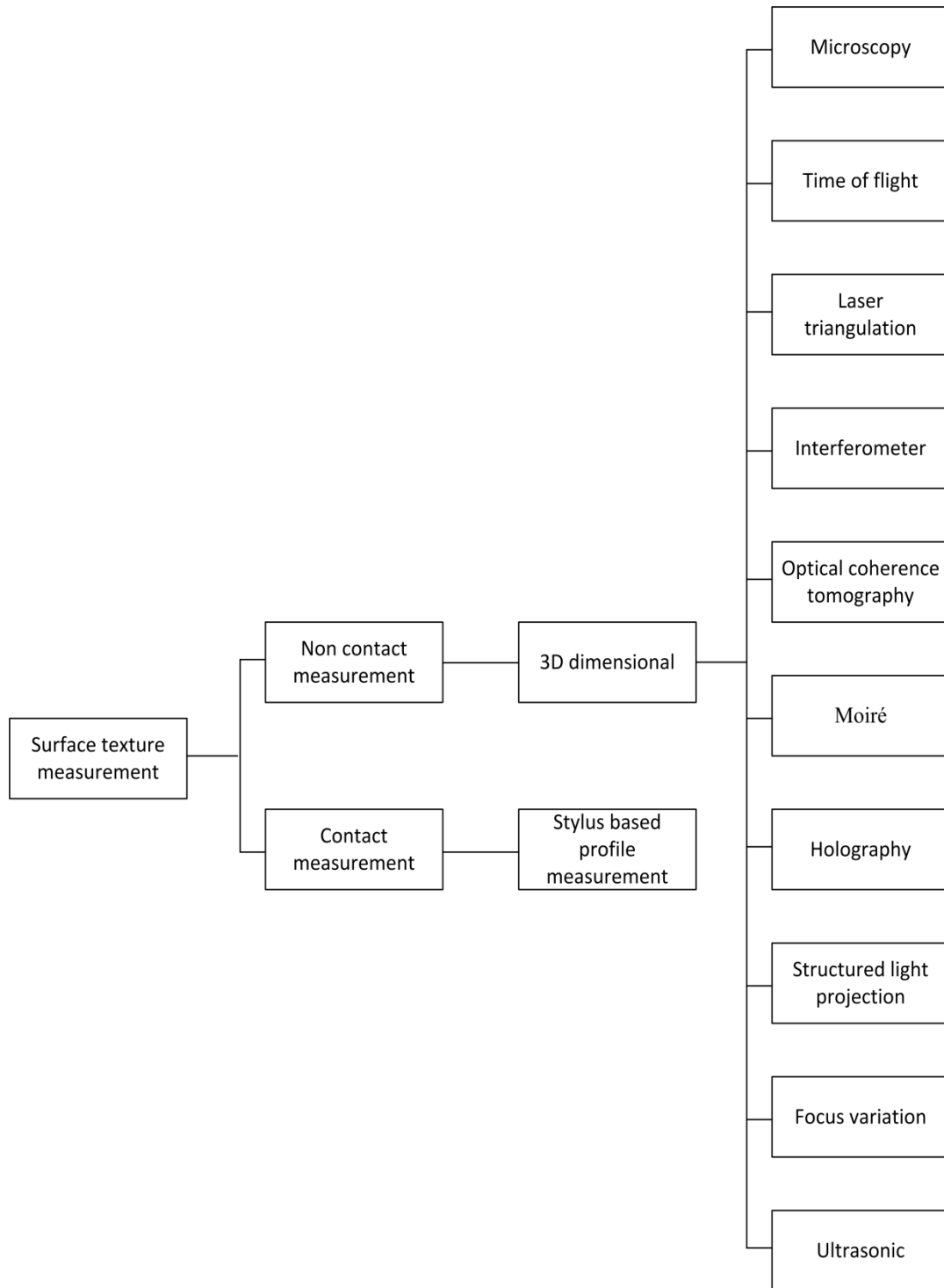


Figure 2-1 Surface texture measurement methods

The research work detailed in this thesis is aiming to measuring small defects (10 μm to 500 μm in depth, 50 μm to 500 μm in length) embedded on components that have

complex geometries, freeform surfaces and different surface roughness. In order to measure such defects, a simplified selection criterion for measuring technique for measuring a finest surface defect are identified as below

- Vertical resolution: $\leq 2 \mu\text{m}$
- Lateral resolution: $\leq 15 \mu\text{m}$
- Minimum stand-off distance: $\geq 20 \text{ mm}$
- Field of view: $\geq 1 \text{ mm} \times 1 \text{ mm}$
- Depth of field : $\geq 500 \mu\text{m}$

Since the first coordinate measuring machine (CMM) was developed by the Ferranti Company of UK in the 1960s, the measuring efficiency of dimensional metrology has been greatly improved in the industry [28]. Conventionally, most CMMs are equipped with the touch-trigger probes for a contact type of measurement on geometrical elements, such as line, plane, circle, cylinder, sphere, cone, etc. The measuring process is indeed very fast and repeatable with respect to the above elements, since it requires only a limited number of probing points. However, as the demands for 3D freeform surface topographic measurements have increased in recent years, CMMs are not useful to represent the surface texture because the sparse probing points are not adequate to represent the measured surface texture [14].

Another common contact type of equipment is stylus-based surface texture instrumentation which measures two dimensional profiles of the surface. Although stylus-based surface texture equipment has been a reliable and traceable method, the main drawback is the physical size of the stylus that prevents it from penetrating sharp surface valleys, and convolution effects occur where sharp steps on a specimen surface tend to be smoothed. Another problem is that the stylus can damage or scratch the surface (depending on material hardness) and therefore the stylus technique may potentially be a destructive test [29]. Moreover, the surface topography is reproduced as a two-dimensional profile, it is not truly representative of the surface.

Non-contact measurement is of significant interest because it avoids deformation of the products and mechanical errors in the contact measurement. The basic principle of non-contact range measurement systems is to project an optical source onto an object and

process the reflected signal to determine its vertical range [16]. Optical methods are more suitable for generating areal surface texture parameters due to fast scan speeds and small resolution [29,30]. With an optical measurement system many of the above mentioned problems associated with contact measurement methods can be avoided and there are additional advantages. Figure 2-2 shows three types of standard optical measurement methods: point, line and area. There are various optical measurement technologies that measure the surface texture. Table 2-1 summarizes the overall comparison between contact measurement and non-contact measurement methods.

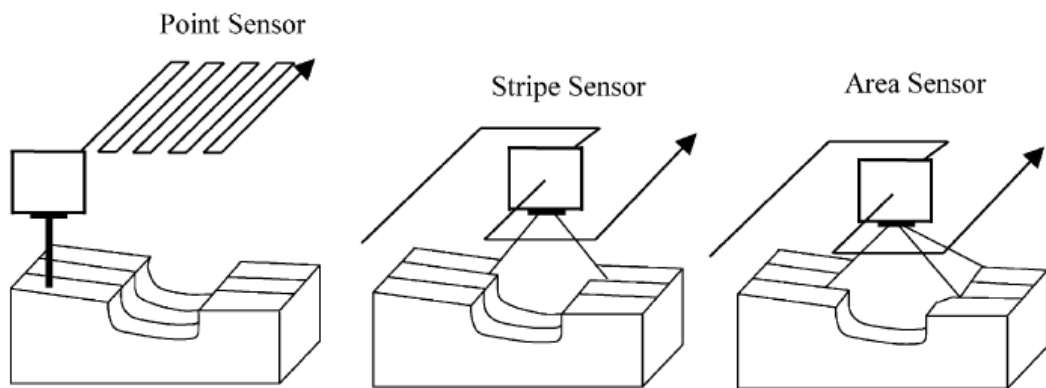


Figure 2-2 Three types of standard optical methods [31].

Table 2-1 Summary of contact and non-contact measurement methods [19, 20]

Contact measurement	Non-contact measurement
Destructive test	Non-destructive test
Measures geometry	Measures optical path
Tip dimension and angle independent	Spot resolution and angle dependent
Stylus can break	Probe cannot be broken
Relatively slow in measurement	Can be very fast
Roughness calibration accepted at all scales	Difficult to calibrate by standards
Existing ISO standards for 2D (e.g. ISO 4287/4288)	ISO standard in development (ISO 25178)

Microscopy

Microscopy is usually used for surface texture measurement in limited range of micro and nano scales. Scanning electron microscopy (SEM) is one of the most common measurement tools [32]. However, nearly all non-conductive specimens examined using SEM need to be coated with a thin film of conducting material and moreover SEM tests are time consuming and not suitable for a production environment. Atomic force microscopy (AFM) test is also very slow typically with a limited range of field of view (in the order of tens of micrometres) for surface texture measurement [27,33]. Hence SEM and AFM test methods are out of scope for this study due to the specific set criteria for selecting the measurement technique.

Time of Flight

The time of flight (TOF) method is based on the direct measurement of the time of travel of a laser or other light source pulse [34]. During measurement, an object pulse is reflected back to the receiving sensor and a reference pulse is passed through an optical fibre and received by the sensor. The time difference between the two pulses is converted into distance. For large structures, a TOF scanner is by far the preferred choice for measurement at longer range as it provides stand-off distances above 5 metres up to a few hundreds of metres depending upon the manufacturer [35]. A typical resolution for the time of flight method is around a millimetre [36] and thus a TOF system is not a suitable instrument to measure small surface defects.

Laser Triangulation

Laser triangulation employs the well-known triangulation principle in optics. The laser scanner is a line scanner that measures a part by one laser stripe at a time. The laser scanner consists of a laser beam projector and CCD cameras that detect the reflected laser beam. The detected laser beam is stored as intensity information for each pixel, and by going through image processing and triangulation of this information, a coordinate value is assigned for each measured point in a three-dimensional space [37]. Many commercial laser scanners are available having stand-off distances in range of 100 mm to 800 mm with resolutions of approximately 50 μm and above depending upon the manufacturer [35], and thus laser scanning is not deemed to be suitable equipment to measure surface imperfection in the context of this work.

Interferometry

The interference of two or more waves can be utilized to investigate various properties of an object. In shape and depth measurement, interferometry normally involves measuring the phase difference between two waves.

Shapes having a smooth surface, where height variations between adjacent measurement points are less than one quarter of the wavelength used, can be accurately measured using an interferometer that employs light of a single wavelength, such as a laser interferometer. There exist, however, objects possessing surface height gradients that are larger than this, for example rough objects or objects with surface steps. For these, conventional monochromatic interferometers have difficulty in determining the height distribution because the interference pattern becomes discontinuous and – in the case of rough surfaces - the reflected light is ‘speckled’ and the interference fringes may no longer be visible [38].

Another type of interferometry configuration, called low coherence interferometry (LCI), has been developed to avoid the problem of laser interferometry mentioned above. In LCI a broadband, polychromatic, and hence low (temporal) coherence light source is used in place of the conventional single wavelength light source such as a laser [39]. One of the most widely-used forms of LCI for surface measurement is the Scanning White Light Interferometer (SWLI) where a white light source is in use [40,41] to replace a laser as the probing light. SWLI is also known as coherence scanning interferometer (CSI) [42].

The technique is based on the scanning of a series of white light interference fringes over the depth of the roughness to be measured and using signal processing along the z-axis at each pixel to determine the peak of the fringe envelope and thus the corresponding height of the surface at each point in the image. To extract the surface position and therefore the surface roughness or shape, it is necessary to develop an efficient and precise peak detection process of the fringe envelope.

Hillman *et al* have found that estimates of surface roughness derived from CSI measurements differ significantly from the stylus profilometry [43]. Rhee [44] and Leach [45] have also found similar problems with CSI measurements differing from other measurement techniques. Gao *et al* have completed research to study the surface

measurement errors using commercial CSI instruments and concluded that most of the problems cited in the literature have been observed when a surface gradient is large compared to the NA of the optics [46]. CSI systems are usually more expensive, more sensitive to vibrations and need more frames for accurate measurement [47].

As an interferometry technique, the vertical resolution of CSI is limited by the precision to which the phase of the reflected signal can be identified and is typically around one thousandth of the mean wavelength (i.e. sub-nanometre). CSI promises lateral resolution upto 0.5 μm for objectives of large numerical aperture (NA) [46]. CSI is appropriate for the roughness measurements because of their higher vertical resolution.

Optical coherence tomography

Within the last 15 years, LCI-based methods have also been developed to provide measurement from under an object's surface, aimed particularly at scattering media. This class of LCI methods is called Optical Coherence Tomography (OCT) [48]. In OCT a broadband light source is used compared to traditional LCI. A super luminescent diode with a near infrared centre wavelength have become a light source of choice in such applications because of the combination of high spatial coherence and low temporal coherence.

OCT is an emerging technology for 3D imaging at micrometre scale resolution. OCT forms clear 3D images through highly scattering materials such as biological tissues. Most common OCT systems are based on a fibre-optic interferometer with a fast axial scanning unit as an optical delay line for the reference mirror, a slow translation unit for the lateral scanning of the sample and a photo-detector. These delay lines are very complex and delicate mechanical systems, and their performance limits the acquisition speed of the sequential OCT system. OCT systems are widely used in biomedicine, tissue engineering and biomaterials [49].

In a parallel OCT (pOCT) system, a free space interferometer replaces the fibre-optic interferometer and a charge couple device (CCD) replaces the photodetector. This allows the simultaneous detection of a multitude of measurement spots and completely obviates the need for lateral scanning. The speed of the axial scanning unit is reduced by a factor equivalent to the number of parallel pixels, which can amount to many thousand and hence, a reduction by a few orders of magnitude [50]. However, CCD

cameras suffer from two drawbacks when used in pOCT systems: (1) the high optical DC intensity reflected by the reference mirror reduces the dynamic range available for AC interferometric signal detection, (2) the CCD frame rate is much lower than the interferometric signal frequency [51].

To overcome this problem, Beer *et al* have developed a CMOS based custom pOCT sensor with data processing at pixel level allowing demodulation of the optical signal in each individual pixel [52]. Lambelet [53] has measured expanded cartridges, defective metal rod and metallic electrodes that collect the electrons from the silicon in solar cell using pOCT system. The vertical resolution of 1 μm and lateral resolution of 2 μm – 10 μm can be achieved in the pOCT system. The pOCT has successfully found its place in medical applications but has not yet fully entered industrial applications [53].

Moiré projection

The Moiré technique is a projection technique. The key to the moiré technique is two gratings, one is a master grating from which contour fringes can be generated and resolved by a CCD camera. Initially, an image of the grating is projected on a surface and an image of the surface with projected grating is formed on a reference grating in a camera [54]. Increased resolution is realized since the gratings themselves do not need to be resolved by the camera. However, if the reference grating is computer generated, the master grating must be resolved by the camera. The penalties for high resolution are the implementation of complex systems [55]. This system is very useful for form measurement and out of plane displacement in controlled environments [36,56,57] but it is not useful for small surface defect quantification.

Holography

Holography is a technique that measures displacement of objects that have rough surfaces. Holography enables the light field scattered from an object to be recorded and replayed. If this recorded field is superimposed on the ‘live field’ scattered from the object, the two fields will be identical. If, however, a small deformation is applied to the object, the relative phases of the two light fields will alter and it is possible to observe interference and this technique is known as live holographic interferometry [58]. The time delay between exposure and reconstruction is too long for on-line inspection purpose. Electronic Speckle Pattern Interferometry (ESPI) represents an interesting

alternative to conventional hologram interferometry. The ESPI system is based on direct video recording of holograms with subsequent electronic filtering and video display and act at the speed of the video system (25 Hz) [59]. The ESPI system is also known as TV holography [58]. This technique has wide potential applications in stress and strain measurement [60], vibration analysis [61] as it measures displacement.

Structured light

The structured light method is also categorized as active triangulation, includes both projected coded light and sinusoidal fringe techniques. The structured light projection system is comprised of a projector and a camera. The projector projects a predefined fringe pattern onto the object surface whereas the camera captures the distorted image on the surface for further processing. Depth information of the object is encoded into a deformed fringe pattern recorded by an image acquisition sensor [62,63]. Although related to projection moiré techniques, shape is directly decoded from the deformed fringes recorded from the surface of a diffuse object instead of using a reference grating to create moiré fringes. The structured light method is also known as fringe projection techniques.

With the recent development of digital micro-mirror devices (DMD) phase shifting can be realized without moving parts [64,65]. Due to fast data acquisition, high resolution (sub-micrometre) and good stand-off distance (above 100 mm) fringe projection techniques for generating 3D surface information has become one of the most active research areas in optical metrology [64].

As an example, Wan [10] from Audi AG has developed a system based on fringe projection technique that detects small surface defects on bodies on white car so that propagation of these defects into the painting process can be prevented. Huang *et al* and Jang *et al* have used structured light system to quantitative evaluation of corrosion [66,67] and Spagnolo has measured surface roughness using digital fringe projection strategy [68]. This technique is quite useful in a field of dermatology as skin topography can also be obtained using fringe projection in 3D [69,70].

Depth from focus:

Depth from focus was developed for microscopic objects. The high magnification of a microscope results in images that capture brightness variations caused by the micro-structure of the surface. Most surfaces that appear smooth and non-textured to the naked eye produce highly textured images under a microscope. Microscopic depth from focus was demonstrated to be an effective approach [71]. The depth from focus method is also known as shape from focus or focus variation technique. An inherent weakness of focus-based methods is that they require the imaged scene to have rough surfaces. It is not a viable technique for smooth surfaces [72].

In the measuring principle of the focus variation technique, the sample of interest is placed on the translation stage of the microscope. The sample is magnified using the objective lens of the microscope and imaged by a standard CCD camera. The sample is illuminated using bright-field illumination of the microscope where light rays emitted by a source are projected onto the sample through the same objective lens used to image the sample resulting in uniform illumination over the entire field of view. The stage of the microscope is motorized and computer controlled. The optics are displaced in the z direction in increments of Δz and a set of images is taken. As the stage moves, each surface patch on the sample increases in image focus and then again decrease in focus [71,72]. From these image sets, maximum focus is obtained for each image point and hence a depth map is derived using various algorithms [73,74].

The focus variation technique can provide up to 10 nm of vertical resolution and upto 400 nm of lateral resolution depending upon the selection of the objective lens. Due to the high resolution, it is useful for surface roughness measurement [75]. It should be noted that these are challenging specifications to achieve. Recently, focus variation has been used for corrosion analysis. Turnbull *et al* measured the corrosion cracking on stainless steel using focus variation and results were compared with SEM test and it is shown that results are approximately identical [76]. Mahat *et al* studied microbiologically influenced corrosion of mild steel using focus variation system [77]. This technique is gaining popularity for measuring sub-micrometre features on surfaces and it could be a viable tool to measure surface defects.

Ultrasonic

Ultrasonic methods are widely used especially time of flight diffraction (TOFD) in the detection of both internal and surface defects in structural materials and the determination of the thickness of sheets and plates [78]. In a TOFD system, a pair of ultrasonic probes sits onto surface. One of the probes, the transmitter, emits an ultrasonic pulse that is picked up by the other side, the receiver. In flawless materials, the signals picked up by the receiver probe are from two waves: one that travels along the surface and one that reflects off the far wall. When a crack is present, there is a diffraction of the ultrasonic wave from the tip of the crack. Using the measured time of flight of the pulse, the depth of a crack tip can be calculated by simple trigonometry [79].

McKerrow *et al* [80] have reported that due to the very nature of ultrasonic waves, the surface texture, roughness and orientation of an object limit how it can be inspected ultrasonically. Surface roughness can be thought of as small surface patches that make up the surface. When the dimensions of these patches are greater than acoustic wavelength, each patch acts as a small specular reflector (mirror-like) and if the patch dimensions are much smaller than the wavelength, the entire surface acts as a specular reflector (mirror). As acoustic wavelengths are very much larger than those of light, rough surfaces still produce specular reflection of ultrasonic waves. To inspect small surface features, such as roughness and defects, requires use of an interrogating wavelength of comparable or small size. Therefore a wave of very high frequency is required. However, high frequency ultrasonic waves severely attenuate in air. Hence the main area of application is internal inspection of materials [81]. Moreover, crack angle is a critical issue as TOFD precisely detects the defect which is perpendicular to the inspecting surface. The problem is the angle of the crack cannot be assumed to be vertical [82].

2.3.2.1 Evaluation of 3D measuring system

This literature review is carried out considering the 3D optical measurement of small surface defects embedded in different scales of surface roughness and in planar or free-

form surfaces. There exists, the relative capabilities of different sensors and sensing methods are evaluated based on lateral resolution, vertical resolution, acquisition time and stand-off distance.

Table 2-2 shows the simplified functional ability of each 3D measuring system to measure small scale surface defects on a planar or free-form surface. It is clear from the analysis that CSI, pOCT, structured light and depth from focus techniques are capable of measuring and quantifying surface defects. Photometry systems are able to detect the surface defects but are not able to quantify defects as the system does not measure absolute height. Based upon the literature review Table 2-3 shows the capabilities of the CSI system, pOCT system, structured light system and depth from focus system with respect to given criteria.

Table 2-2 Measurement systems' capability to detect and quantify surface defect

Technique	Major application	Small surface defect measurement	Defect quantification
Microscopy	Topography measurement	Yes	Yes
Time of Flight	Range finding, Shape measurement	No	No
Laser Scanner	Shape measurement	No	No
CSI	Topography measurement	Yes	Yes
pOCT	Topography/Tomography measurement	Yes	Yes
Moiré	Displacement measurement	May be	May be
TV Holography (ESPI)	Displacement measurement	May be	May be
Structured light	Topography & form measurement	Yes	Yes
Depth from focus	Topography measurement	Yes	Yes
Ultrasonic	Sub-surface measurement	No	No

Table 2-3 Technical specification of four technologies

Technical Specification	CSI	pOCT	Structured light	Depth from focus
Resolution	High	High	Medium	High
Stand-off distance	Low	Medium	High	Low
Acquisition time	Low	High	High	Medium
Field of View	Low	Medium	High	Medium
Depth of Field	High	High	Medium	High
Defect acquisition	Yes	Yes	May be	Yes

No claims are made regarding the completeness of this survey, and the inclusion of commercial sensors should not be interpreted in any way as an endorsement of a vendor's product. Moreover, if the figure of merits ranks one sensor better than another, this doesn't mean that it is better than the other for any given application.

2.3.3 Filtration

Surface topography is comprised of different surface components, i.e roughness, waviness, form and surface defects. The high frequency or short wavelength components are referred to as roughness, the medium frequencies as waviness and low frequency components as form that can be seen in Figure 2-3[83]. It is noted that form is in millimetric scale and roughness is typically in the micrometre scale.

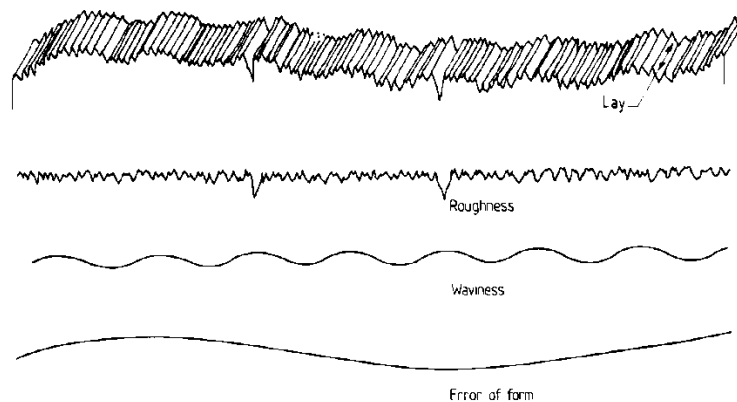
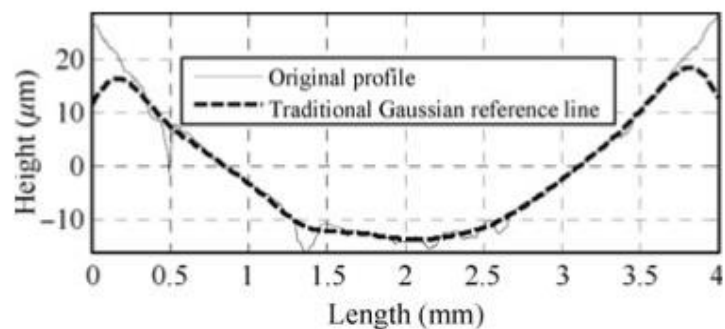


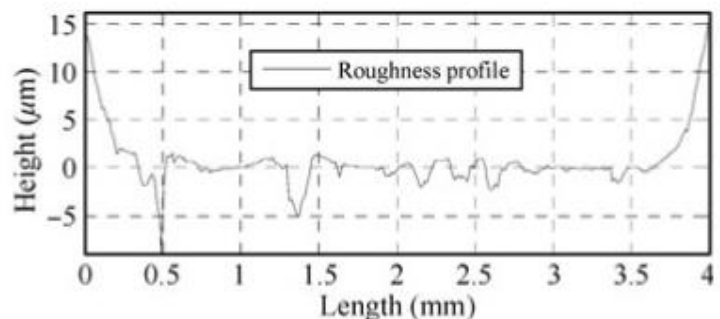
Figure 2-3 Surface comprised of waviness, roughness and form [83]

Historically, it has been accepted that different aspects of the manufacturing process generate different wavelength components and these affect the function of a part differently [84]. However, there are no case studies that conclusively prove this relationship [83]. By separating surface profile into various bands, it is possible to map the frequency spectrum of each band to the manufacturing process that generated it. Thus, filtering of surface profiles serves as a useful tool for process control and diagnostics.

Filtration has always been important in surface metrology as it is the means by which surface features of interest are extracted from the measured data for further analysis [85, 86]. To obtain the roughness parameter it is very important to remove the waviness and form component from the measured surface. Surface metrology as a discipline is currently undergoing a huge paradigm shift: from profile to areal characterization and from simple geometries to complex free-form geometries. Filtration, is one of the most important parts of surface metrology, is also undergoing this shift [87, 88].

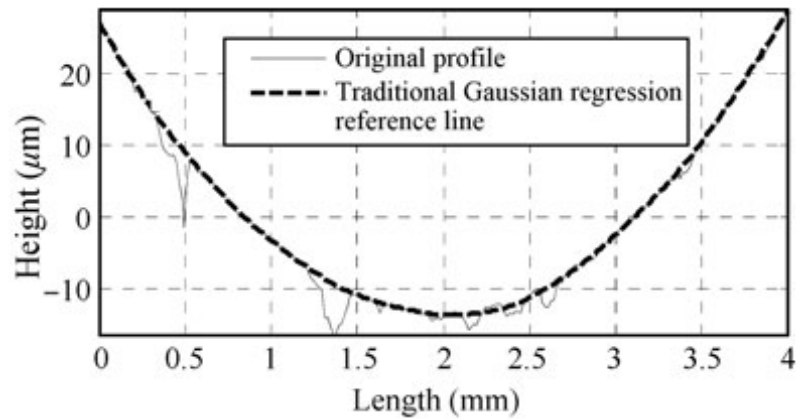


(a)

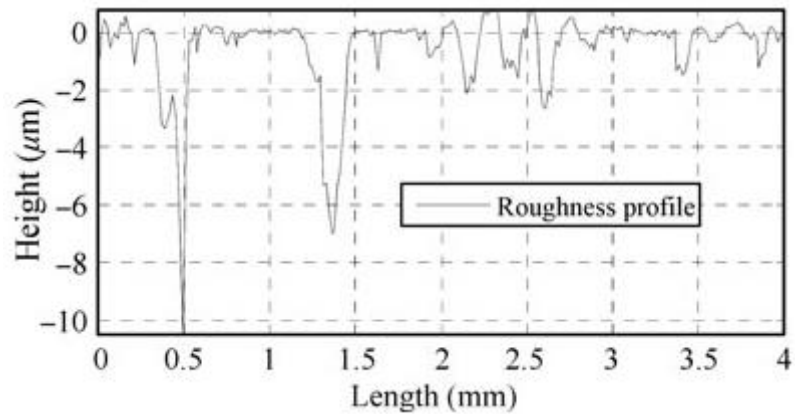


(b)

Figure 2-4 (a) Surface profile with Gaussian filter line (b) roughness profile [89]



(a)



(b)

Figure 2-5 (a) Measured surface profile with Gaussian regression filter (b) roughness profile [89]

Conventionally, the separation of form component was accomplished by using polynomial fitting based on the least square principle [90]. It is assumed the original surface as a given polynomial. For free-form surfaces, this technique is complex and difficult and fitting is not unique [91]. Eventually the Gaussian filter for profile was recommended to generate the mean line and it has been defined as the standard filtering technique for profile analysis [87,92]. The areal Gaussian filter which is straightforwardly expanded from its profile counterparts has the same merits as the profile Gaussian filter [93].

However the significant features on a surface, such as a small defect is usually smoothed and the boundary of the surface is distorted during the filtration process using a Gaussian filter [93] as seen in Figure 2-4. It is these topographical features that play

important roles in functional performance thus it is important to keep these features to evaluate the surface functionality.

To address the boundary effect and form removal issues with the ordinary Gaussian filtering for profile, a Gaussian regression filtering technique has been proposed by Bodschwinn and Brinkman for profile analysis [94,95], which can simultaneously process profiles with form components and with no boundary removal. Furthermore, Seewig introduced a reweighted iteration procedure for the regression Gaussian profile filter that is robust against outliers [95] as seen in Figure 2-5.

The robust Gaussian regression filter for profile analysis is a new ISO GPS technical specification ISO 16610-31 [96]. A model of a Gaussian regression filter for areal surface analysis is under an ISO draft specification [97], based on the early work carried by Seewig and Bodschwinn [94,95]. Zeng has proposed FFT based a second order areal robust Gaussian regression filter to generate the surfaces which is faster than the areal Gaussian filter. Zeng, in his research work, has successfully removed form from an aspheric lens and cylindrical surface for further surface characterization [93].

Apart from robust Gaussian regression, profile spline filter [98] and morphological profile filters [99] are applicable to compute surface data and these filters are under ISO draft specification ISO 16610-72 and ISO 1660-81 respectively [100]. However, the areal robust Gaussian regression filtration technique is well explored compared to others for obtaining residual surface for surface characterization. Thus robust Gaussian regression can be a potential tool to extract the surface defect.

2.3.4 Defect detection

In order to automate the process of quantifying the defect in 3D, it is very important to extract the defect from the residual surface. The residual surface is extracted by subtracting generated form surface from the measured surface. For 2D imaging, automatic defect detection is very well explored. In image processing, thresholding is an important technique for image segmentation and machine vision application. The basic idea of automatic thresholding is to automatically select an optimal grey-level threshold value for separating objects of an interest in an image from the background based on their grey-level distribution. This thresholding technique has been widely used

in the industry for automated visual inspection of defects [101]. An in-depth survey and evaluation of various thresholding methods are given by Sahoo *et al* [102], Lee *et al* [103], Glasbey [104] and Sezgin and Sankur [105].

Automated thresholding techniques can be roughly categorized into global thresholding and local thresholding. Global thresholding selects a single threshold value from the histogram of the entire image. Local thresholding uses localized grey-level information to choose multiple thresholding values; each is optimized for a small region in the image. Global thresholding is simpler and easier to implement but its result relies on good illumination. Local thresholding methods can deal with non-uniform illumination but they are complicated and slow.

Automatic visual inspection techniques for images generally compute a set of features in the spatial domain or in the frequency domain and then search for the significant local deviations in the feature values. In digital images, typical noise processes tend to dramatically alter local spatial variation of intensity while having relatively uniform representation in the spectral domain [106]. Spectral-domain features are generally less sensitive to noise than spatial-domain features. In spectral-domain approaches, the textural features are generally derived from Fourier transform, Gabor transform or wavelet transform [107]. Chan used the Fourier analysis for fabric defect detection [108]. The Gabor filtering techniques have been applied to inspect wooden surfaces [109] and steel surfaces [47]. The wavelet-based feature extraction methods have been applied to the inspection of cold rolled strips [110] and woven fabrics [111]. For more information, in depth survey for defect detection methods is given by Xie [112].

Automatic defect detection in 2D is very well explored and it may be adopted to 3D surface data however there is a very little evidence available for determining the surface defect automatically in 3D. Kong *et al* [113] adopted the Otsu's method [114] for extracting the boundaries of a microlens surface profile in 3D that was measured using CSI from the binary image. However, the method of determining the depth of the feature was not well defined.

2.3.5 Quantification

Once the defect boundary is extracted, it is very important to quantify the geometry (such as depth, area and volume) to understand surface functionality. Quantification of defects is a key element in quality assurance in order to determine the pass or failure of certain manufactured parts within the relevant industrial sector.

Although significant work has been completed in detecting surface defects using a variety of instruments solutions, robust, traceable and automatic methods for quantification of defect is less well explored. Currently, standards based on the ISO Geometrical Product Specification (GPS) are available to quantify surface features in terms of roughness parameters from contact and non-contact surface profilometry [90]. Example roughness parameters for surface texture profile based on ISO 4287 are shown in Table 2-4.

Whilst, a profile measurement may give some functional information about a surface, to really determine functional information, areal measurement is necessary. Areal measurement gives a more realistic representation of the whole surface. Hence ISO 25178-2 has been developed to quantify surface features in terms of roughness parameters for areal surface texture [115].

Table 2-4 Surface profile roughness parameters [90]

Parameter	Description
<i>R_t</i>	Sum of the largest profile peak height and the largest profile valley depth
<i>R_p</i>	Maximum profile peak height
<i>R_v</i>	Maximum profile valley depth
<i>R_z</i>	Maximum height of profile
<i>R_a</i>	Arithmetical mean height
<i>R_q</i>	Root mean square height of the roughness profile
<i>R_{sk}</i>	Skewness of the roughness profile
<i>R_{ku}</i>	Kurtosis of the roughness profile

Table 2-5 Surface areal roughness parameters [115]

Parameter	Description
S_p	Maximum peak height of the scale limited surface
S_v	Maximum pit depth of the scale limited surface
S_z	Maximum height of the scale-limited surface
S_a	Arithmetical mean height of the scale limited surface
S_q	Root mean square height of the scale limited surface
S_{sk}	Skewness of the scale limited surface
S_{ku}	Kurtosis of the scale limited surface

Parameter for surface texture areal based on ISO 25178-2 are shown in Table 2-5. These standards provide tools to allow the measurement of negative or positive height components with respect to mean line datum or plane fitted through the surface data. But these standards focus on surface topography but do not uniquely isolate larger scale defects and correctly quantify the defect in terms of depth, area and volume.

2.3.5.1 Automatic defect quantification

Existing human visual analysis of surface defects is qualitative and subject to varying interpretation. Manual measurement methods introduce measurement errors and may have issues of repeatability and reproducibility. Automatic defect quantification is an approach that can improve results. It has been found that the field of automatic surface defect quantification is not well explained. Recknagel *et al* has developed a wavelet based algorithm to quantify the surface defect depth automatically on a smooth surface [116]. They have demonstrated that the matrix based algorithm is scale and instrument independent as they have implemented this algorithm on point cloud data obtained from a confocal microscope, fringe projection and white light interferometer. The results showed that the smallest defect (8.5 μm in depth) was quantified with a 7% of measurement error, however the method statement of depth measurement is not given. Thus there is a need for an automatic defect quantification in 3D.

2.3.6 Validation

As in many areas of metrology, instruments that measure surface texture generally interface to a computer that collects, filters and analyses the measured data. As part of this analysis, parameters are calculated that allow surfaces to be described quantitatively in order to gain information concerning a manufacturing process or to draw some inference on the functionality of a surface. There is a wealth of calibration artefacts that are used to calibrate surface measuring instruments and define the traceability in the metre but such artefacts do not allow specific validation or verification of the numerical correctness of the software that is used to filter and analyse the data [117].

Blunt *et al* developed Type F1 (reference data sets) and type F2 (reference software) software measurement standards to provide mathematically well-defined and unambiguous specification of surface profile parameters. Blunt *et al* referred to these software measurement standards as *Softgauges*. *Softgauges* are inspired from ISO 5436-2 specified two Type F software measurement standards for verification purposes: Type F1 (reference data sets) and type F2 (reference software) [117,118]. To test the numerical correctness of software, a common data set is input into both the software under test and the reference software. The test results delivered by the software under test and those obtained from the reference software are compared (see Figure 2-6).

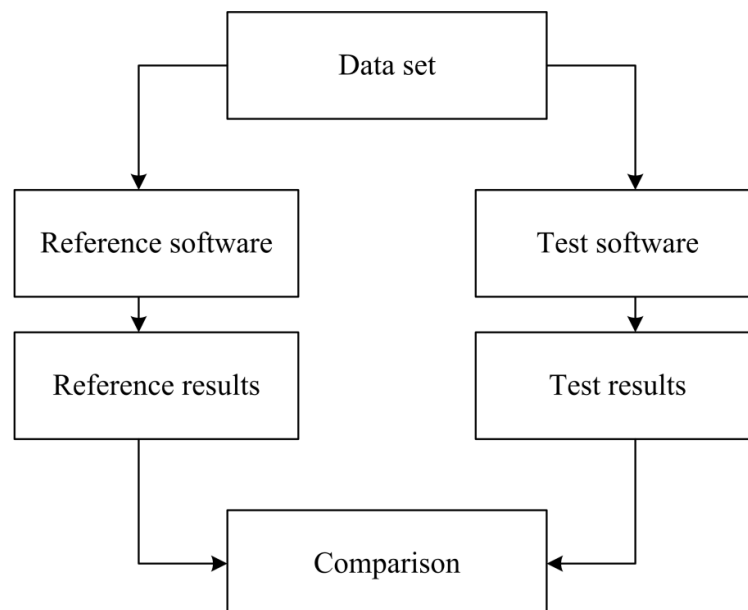


Figure 2-6 Procedure for comparing software

Similarly, Harris *et al* have developed software measurement standards for areal surface texture parameters [119,120]. However, there is no evidence for reference data illustrating simulated surface defects that can be used for evaluating the numerical correctness of the software measuring surface defects.

2.4 Summary

In this chapter, the background of this research has been introduced. Brief importance of the measurement has been explained along with the important definitions that are used throughout in this thesis. Before introducing the surface texture measurement techniques, the importance of surface defects on industrial components is explored. It has been found that even the finest defects on the surface of a component can affect the functional performance and thus it is essential to detect and quantify surface defects for quality inspection.

Contact and non-contact surface texture measurement techniques are illustrated that can be useful for measuring the surface defects. Non-contact and three-dimensional (3D) surface texture measurement techniques have been found to be a powerful concept compared to two-dimensional (2D) contact profilometry for measuring surface defects. Various 3D surface measurement techniques are evaluated and it has been found that CSI, pOCT, structured light and depth from focus techniques are viable methods to measure surface defects.

Data analysis techniques have been discussed in detail that includes filtration processes, isolation processes and quantification processes. It is found that the filtration process is an essential for separating the surface topography components before isolating the surface defect. Defect isolation has been very well explored in 2D however this is not the case for surface defects in 3D. However, evidence suggests that thresholding methods can be useful to isolate surface features in 3D.

Currently, the GPS standards for surface texture measurements (profile and areal) are used to attempt to quantify defects. However these standards focus on surface topography measurement and do not isolate and correctly quantify the defect in terms of depth, area and volume. In the majority of research literature, the method statement for measuring the depth quantity is not clear. Thus there is a clear need for development of

algorithms that quantify defects automatically in 3D. Moreover, the importance of validation for the software has been highlighted. Research literature shows that the Softgauges have been developed for validating software that evaluates both profile and areal surface texture parameters. However there is a lack of a bespoke defect softgauge to achieve the same level of traceability and assurity for defect analysis software.

The lack of a significant body of knowledge concerning automatic surface defect measurement and quantification in 3D, is both a hindrance (i.e. a lack of published research direction) but also an opportunity for this current research to demonstrate unique and novel findings.

3 STANDARD DEFECT ARTEFACT GENERATION

3.1 Introduction

Measurement of surface defects is the key issue of this research. In this chapter, justification for the development of standard defect artefacts is given before exploring mechanical methods to generate different roughness scales and shape of substrates. Chapter 3 proposes the Rockwell and the Vickers hardness test equipment for generation of a novel and traceable defect artefact.

3.2 Justification for generation of a standard defect artefact

Quantitative surface metrology topography measurement has been carried out in industry for over a century. However, despite the vast amount of research into surface metrology and its importance in almost all areas of manufacturing industry, there has only been limited standardisation of the methods employed to measure surface metrology. The measurement of 2D profiles using a stylus instrument is well explored and supported by a standard infrastructure [121] however this is not necessarily the case for optical 3D measuring instruments.

With the growing need for standardisation of areal surface texture measurement, the ISO technical committee (ISO/TC 213) has formed a working group (WG - 16) to address standardization of areal surface texture measurement methods. The WG - 16 is currently developing a number of standards encompassing definitions of terms and parameters, calibration methods and characteristics of instruments. Several standards have been published and a number are at various stages in the review and approval process. However the standardization for characterizing specific instruments has still not been achieved [122].

Over recent years in UK, National Physics Laboratory (NPL) have been developing artefacts to allow a user to calibrate and to determine the metrological characteristics of 3D surface texture measuring instruments. The artefacts include an optical flat, a series of step heights, a series of crossed square wave gratings with different patches, star

patterns and a pseudo-random surface. Such artefacts give confidence in surface texture measurement taken with the instrument, and provide measurement uncertainties for a specific instrument. The artefacts are developed for; stylus instruments, coherence scanning interferometers and scanning confocal microscopes [122].

Moreover, there is a wealth of reference standard calibration tools available by commercial vendors such as Rubert [123], VLSI [124] to evaluate the performance of the surface texture measuring instruments in 2D and 3D. However such artefacts are not useful for the evaluation of the functional behaviour of 3D measuring instrument whilst measuring surface defects. This is because a surface defect may not have the same features as the inherent surface texture moreover such defects typically pose irregular shapes. Different optical instruments use disparate physical principles, interact with surfaces and defects in diverse ways. Hence an instrument capable of measuring surface texture may not necessarily be able to measure surface defects.

Consequently, if standard defect artefacts were developed they could be used to evaluate the performance of different instruments especially for defect analysis. However such defect artefacts have not yet been commercially developed. Furthermore, a lack of defect artefacts has hampered the development of traceable defect artefacts. Section 3.3 illustrates the methodology that has been used to generate defect artefacts which are subsequently used for inter-comparison of four different instruments as explained in Chapter 4.

3.3 Generation of defect artefact

Generation of different shapes of defect artefacts has been proposed using Rockwell hardness testing equipment and Vickers hardness testing equipment. Such defects are generated on different scales of rough substrate. Furthermore, a set of defect artefacts are produced on a single curvature plate and a double curvature plate. Typical defect artefacts embedded on various roughnesses will aid to determine the capabilities of each measuring instrument. Instrument's limitation can also be identified using defect artefacts.

Conical shaped, hemispherical shaped and pyramidal shaped defect artefacts have been generated on stainless steel metal plate samples. Four different sizes of defect artefacts

of each shape type have been developed. Typical set of defect artefacts have been produced on four flat plates having different roughness values, a single curvature plate and a double curvature plate. The generation of these defects samples are detailed as follows:

3.3.1 Substrate preparation

Stainless steel metal (SAE grade 305) is selected to develop a standard defect artefact. Four different flat plates of size 90 mm x 25 mm x 1 mm each were prepared. Mechanical abrasion methods such as grinding paper scratching and bead blasting were investigated to assess the capability of rough surface generation on the stainless steel plates.



Figure 3-1 Flat plate – A

Figure 3-1 shows typical flat Plate A. Plate A was kept in its natural form and its inherent roughness was measured using Talysurf Intra (Figure 3-2) contact stylus instrument. The Talysurf Intra is traceably calibrated using UKAS standard gauge ball with radius of 12.5 mm (Serial no. GT35968) with specific Pt value less than equivalent to 0.25 μm . The measurement performance in Pt value of the instrument was 0.078 μm . The specifications of the instrument are:

- Lateral resolution: 0.5 μm
- Vertical resolution: 16 nm
- Tip radius: 2 μm
- Lateral range: 50 mm
- Vertical range: 1 mm

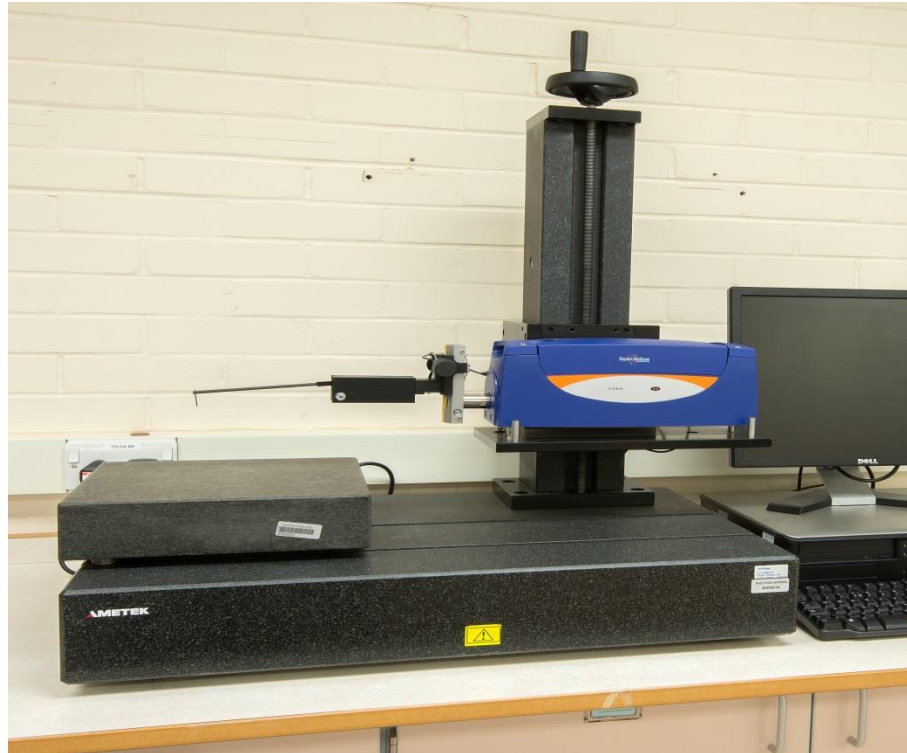


Figure 3-2 Talysurf Intra

Using the Talysurf Intra, 4.0 mm long 2D profiles on Plate A were measured five times repetitively and different roughness parameters calculated at a cut-off wavelength of 0.8 mm. Roughness parameters were calculated according to ISO 4287 [90]. Table 3-1 illustrates various roughness parameters related to the Plate A.

Table 3-1 Roughness parameters of Plate A

No of Exp	Roughness Parameter (μm)				
	R_p	R_v	R_z	R_a	R_q
1	0.49	0.72	1.22	0.13	0.19
2	0.47	0.67	1.14	0.12	0.12
3	0.33	0.62	0.95	0.10	0.15
4	0.41	0.67	1.08	0.12	0.17
5	0.36	0.59	0.96	0.11	0.16
Avg	0.41	0.65	1.07	0.12	0.16
StdDev	0.07	0.05	0.12	0.01	0.03

A second plate sample was textured using a bead blasting method. Bead blasting is the process of removing surface materials by applying fine glass beads at a high pressure. In this study, GUYSON Formula F1400 equipment was used and Honite 14 (nominal

size range of glass bead; 75 μm – 150 μm) was selected to generate the rough surface on one of the flat metal plates.



Figure 3-3 Flat Plate B generated using bead blasting

Figure 3-3 shows Plate B generated using bead blasting and Table 3-2 illustrates the roughness parameters associated with Plate B derived using the Talysurf Intra. It is clearly observed from Table 3-2 and Table 3-1 that Plate B is rougher than Plate A as the average Rq values for Plate A and Plate B is 0.16 μm and 1.27 μm respectively.

It is noted that bead blasting process introduces residual stress. This may not be good in a standard artefact that should have long term stability because the residual stress could cause a change of shape eventually. In this research work, the element of residual stress has not been considered as it is out of the scope of this research work due to time limitation.

Table 3-2 Roughness parameters of Plate B

No of Exp	Roughness Parameter (μm)				
	Rp	Rv	Rz	Ra	Rq
1	3.44	2.94	6.39	1.08	1.35
2	3.14	2.71	5.85	1.06	1.29
3	2.65	2.59	5.24	0.94	1.16
4	3.27	2.61	5.88	1.08	1.34
5	3.37	2.63	5.64	1.05	1.23
Avg	3.17	2.70	5.80	1.04	1.27
StdDev	0.31	0.14	0.42	0.06	0.08

Plate C (Figure 3-4) was prepared using P320, P600 and P800 grinding papers with an average particle diameter of 46.2 μm , 25.8 μm and 21.8 μm respectively. Abrasive scratch lines can be seen on the Plate C. Roughness parameters were again evaluated

using the Talysurf Intra. Table 3-3 shows the roughness parameters of the Plate C. An average Rq value of Plate C is $0.78 \mu\text{m}$ thus Plate C is rougher than Plate A but smoother than Plate B.



Figure 3-4 Flat Plate C generated using grinding paper scratching

Table 3-3 Roughness parameters of Plate C

No of Exp	Roughness Parameter (μm)				
	Rp	Rv	Rz	Ra	Rq
1	1.82	2.44	4.25	0.6	0.79
2	1.90	2.45	4.35	0.61	0.78
3	2.04	2.40	4.44	0.62	0.78
4	1.77	2.39	4.16	0.61	0.78
5	1.95	2.45	4.4	0.61	0.79
Avg	1.90	2.43	4.32	0.61	0.78
StdDev	0.11	0.03	0.11	0.01	0.01

Figure 3-5 illustrates Plate D. Plate D was initially prepared in the same manner as Plate C and then even manual polishing was applied to generate different roughness. Manual polishing is achieved by applying $6.0 \mu\text{m}$ diamond paste followed with $2.0 \mu\text{m}$ diamond polishing. Plate D appeared to have a mirror like finish and a very specularly reflective surface. Using the Talysurf Intra, the roughness of Plate D was measured in a similar fashion to the other three plates.



Figure 3-5 Flat Plate D generated using manual polishing

It is noted that due to the mirror finish, Plate D does not photograph well. Table 3-4 highlights the roughness parameters and it can be seen that Plate D has the smoothest surface among the four plates. The Rq value for Plate D was $0.06 \mu\text{m}$ which was almost 21 times less than the roughest, Plate B.

It is observed that Talysurf Intra measures the majority of the roughness parameters with the standard deviation in a range of $0.01 \mu\text{m} - 0.4 \mu\text{m}$ in each plate thus the measuring instrument is performing in a repeatable manner.

Table 3-4 Roughness parameters of Plate D

No of Exp	Roughness Parameter (μm)				
	Rp	Rv	Rz	Ra	Rq
1	0.14	0.30	0.44	0.04	0.07
2	0.09	0.29	0.38	0.05	0.06
3	0.09	0.30	0.39	0.04	0.06
4	0.08	0.27	0.36	0.03	0.07
5	0.09	0.29	0.38	0.04	0.06
Avg	0.10	0.29	0.39	0.04	0.06
StdDev	0.02	0.01	0.03	0.01	0.01

Different shapes of the substrates such as single curvature and double curvature were generated. Both single curvature and double curvature plates were created manually by bending a flat metal plate on a metal rod. Components such as an aerofoil can be explained in the simplest form as the single curvature and double curvature shape. Thus typical substrates were manufactured to evaluate the functional capabilities of 3D instruments measuring defects embedded on complex shapes.



Figure 3-6 Single curvature metal plate

Figure 3-6 represents a single curvature metal plate (70 mm x 25 mm x 1 mm) with a radius of approximately 52 mm. Figure 3-7 illustrates a double curvature metal plate (65 mm x 25 mm x 1mm). On the convex side and the concave side of the plate, the radius is approximately 32 mm and 38 mm respectively. Both plates were kept in their natural form.



Figure 3-7 Double curvature metal plate

3.3.2 Defect artefact

Once the substrates had been prepared, novel defect artefacts were generated using Rockwell hardness test equipment and Vickers hardness test equipment. The Rockwell hardness test and the Vickers hardness test are empirical indentation hardness tests. In both tests, the material under test is penetrated with a specific type of indenter that creates a small indentation on the surface of the material. This indentation is useful to evaluate hardness of the material [125]. Irrespective of the material hardness, these indentations have unique shape and geometry that can be used as a standard defect artefact to develop a robust method to quantify surface defects in 3D. In this context,

the geometric parameters of a standard defect (depth for instance) can be directly traced to the SI definition of the metre.

3.3.2.1 Rockwell indentation

The Rockwell hardness test is a measure of the deformation that occurs when the material under test is penetrated with a specific type of indenter. Typical Rockwell hardness test equipment is shown in Figure 3-8.

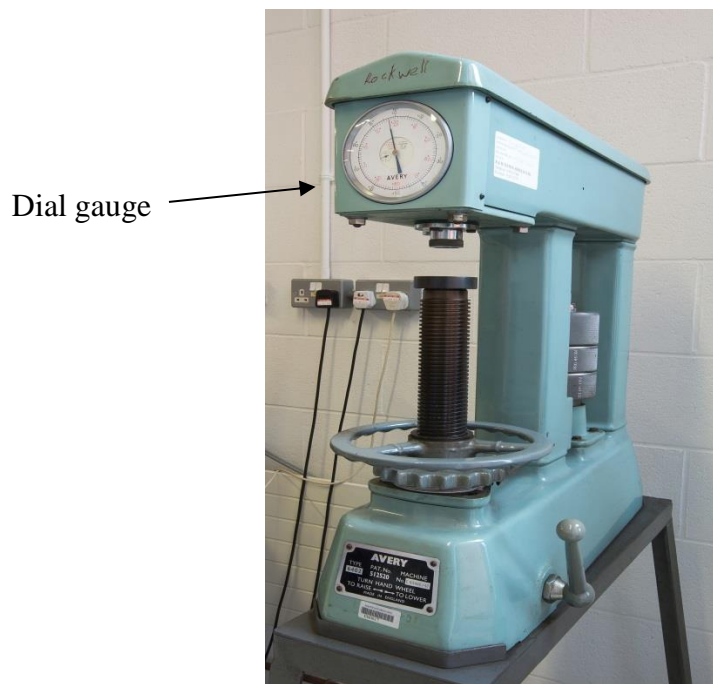


Figure 3-8 Avery Rockwell test equipment

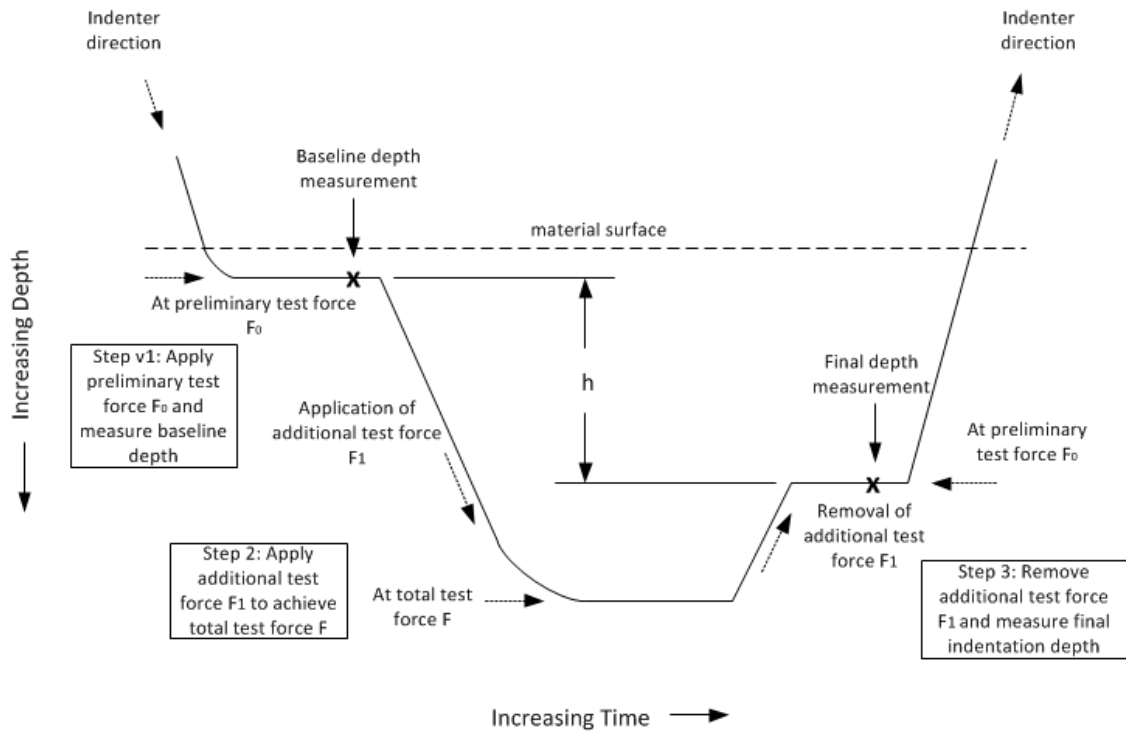


Figure 3-9 Test cycle for a Rockwell hardness test [126]

In this test, two levels of force are applied to the indenter at specific rates and with specific dwell times, as illustrated Figure 3-9. The test is separated into three stages of force application and removal as mentioned in the British Standard BS EN ISO 6508 -1 [126].

- The indenter is carried into contact with the test specimen and the preliminary force F_0 is applied. After holding the preliminary force for a specific time (less than 3 s), the baseline depth of indentation is measured.
- The force on the indenter is increased gradually to the additional test force F_1 to achieve the total test force F . The total test force is also held for a specified time (between 2 s – 8 s).
- The additional test force F_1 is removed and the force level must return to the preliminary test force F_0 . After holding the preliminary test force for a specific time, the final depth of indentation is measured. The Rockwell hardness value is derived from the difference h in the final and baseline indentation depths while under the preliminary test force. The preliminary test force is removed and the indenter is removed from the test specimen.

In this test procedure, the depth is measured using the dial gauge from the test equipment. The depth information is then used to calculate the hardness number. However, the main intention of this test is to consider the deformation as a defect artefact rather than evaluating the hardness of the test specimen.

To generate the defect artefacts a diamond indenter and a 1.58 mm radius of steel ball indenter were used to create a conical shape indentation and a hemispherical shape indentation on the surface of the test specimen respectively. Four different sizes of indentations were created as stated in test procedure using the diamond indenter by applying four different loads (Table 3-5) and the defects are illustrated in Figure 3-10 . By repeating the same procedure, four different hemispherical shape defects were created by changing the diamond indenter to the steel ball indenter as seen in Figure 3-11. This process was used to produce defect artefacts on each of the substrates prepared in Section 3.3.1.

Table 3-5 Loads used to generate different sizes of Rockwell indentations

Defect Number	1	2	3	4
Load (kg)	150	100	60	0

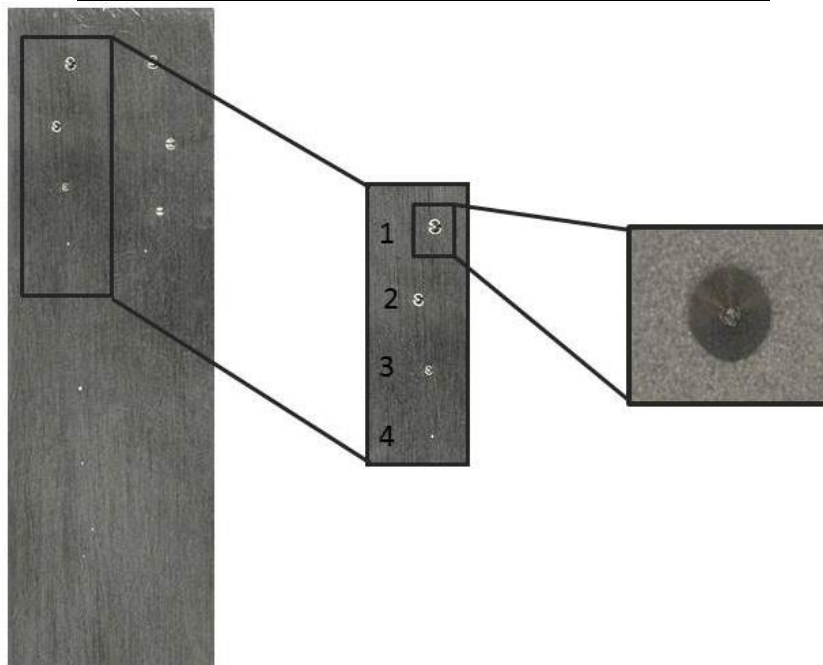


Figure 3-10 Defect artefacts using the diamond indenter

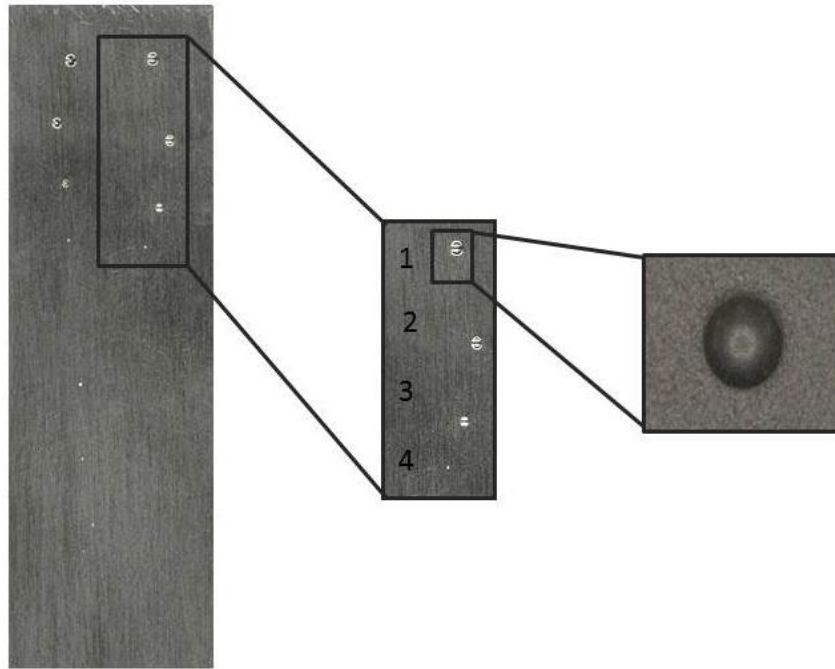


Figure 3-11 Defect artefacts using the steel ball indenter

3.3.2.2 Vickers indentation

The Vickers test is another method to measure the hardness of materials. This method is easier to use than other methods because the requirement of calculations is independent of the size of the indenter and indenter can be used for all materials irrespective of hardness. Typical Vickers hardness test equipment can be seen in Figure 3-12.



Figure 3-12 Vickers hardness test equipment

A typical Vickers indenter is made of a diamond and is in the form of a square-based pyramid with an angle of 136° between facets. The facets are highly polished, free from surface imperfections and the point sharp. As mentioned in the standard document ISO 6507-1 [127], the Vickers diamond indenter is forced into the surface of the test specimen. The force is held for a specific time (between 2 s to 8 s) and then the test force is removed. In order to evaluate a hardness number, the diagonal length of the indentation left in the surface is measured using a microscope and graticule.

It is noted that in this test procedure the depth of the indentation is not measured to calculate the hardness of the test specimen. However, for this research work, the main intention of this test was to consider an indentation as a defect artefact.

Four different sizes of indentations were created by applying four different loads (Table 3-6) and are illustrated in Figure 3-13.

Table 3-6 Loads used to generate different sizes of Vickers indentations

Defect Number	1	2	3	4
Load (kg)	10	5	2.5	1

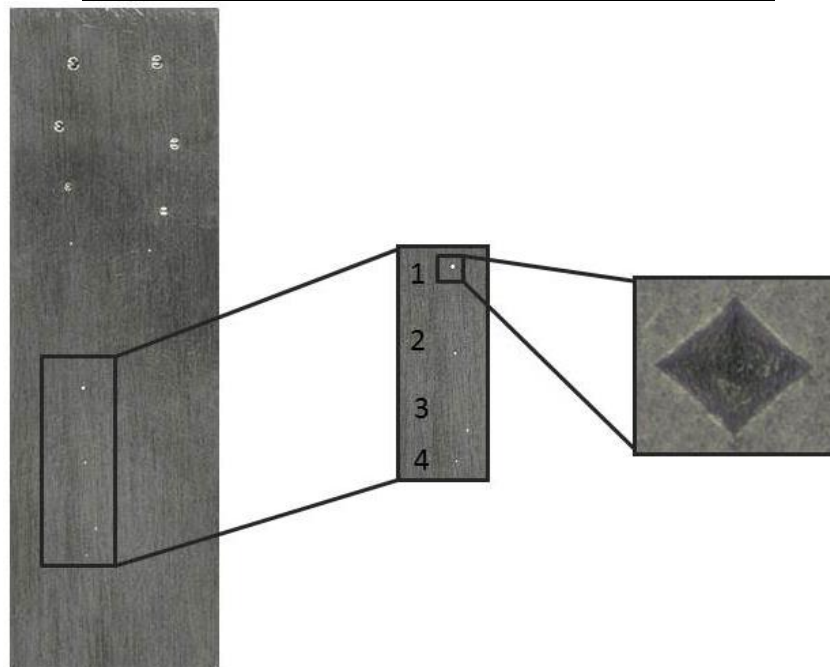


Figure 3-13 Defect artefacts using Vickers hardness test equipment

Similar pyramidal defects are created in each substrate prepared in Section 3.3.1.

3.3.3 Repeatability of the instruments

In order to consider indentations created using hardness test equipment as standard defect artefacts, it is important that indentations which are created every time pose constant geometric quantities (for instance depth) for a given applied load. Both the Rockwell and Vickers hardness test equipment were not maintained in a valid calibrated state hence repeatability tests were carried out to gain confidence in the generation of indentations and the consistency of the instruments.

Ten indentations were generated repetitively in a flat Plate A using the Rockwell hardness test keeping a constant load of 60 kg. Similarly, another ten indentations were produced in the same plate using the Vickers hardness test by keeping a fix load of 10 kg.

Once the indentations were generated then they were measured using the Alicona InfiniteFocus 3D instrument. This instrument works on the physical principle of the focus variation technique which is briefly explained in Section 2.3.2. The instrument is traceably calibrated with reference to a Physikalisch-Technische Bundesanstalt (PTB) certified calibration artefact which is a carbide step height of 1.0 mm (Serial no. 002116201208). The vertical measurement error specification of the instrument is 1.0 μm . The PTB is the national institute for natural and engineering sciences and the highest technical authority for metrology and physical safety engineering in Germany. Further detail about the instrument is given in Section 4.2.1.1 of Chapter 4.

For the measurement of the indentations, a 10 x objective lens was selected with 1 x optical zoom, producing 3D datasets with a field of view (FOV) of approximately 1.4 mm x 1.0 mm. Once the 3D datasets were acquired using the Alicona system, they were processed using DigitalSurf MountainMap (v5) software [128]. This software is a common software solution widely used in research and industries for analysis of 3D surface data acquired from various instruments. Data processing using the MountainMap software to manually evaluate the depth of indentations is illustrated in Figure 3-14.

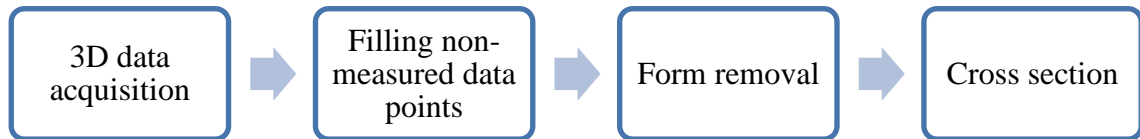


Figure 3-14 Steps for manual depth measurement of the indentation

Due to the optical limitation of the measuring instrument, the datasets often contained non-measured data points (holes or voids) that required filling before any further analysis. This was achieved using the MountainMap software's built-in linear interpolation toolbox. Typically, the 3D datasets also contained geometric form that needed to be removed for better assessment of the surface. Leaving large scale form in place often masked the indentation detail. The MountainMap software has built-in filter banks that can be used to remove such form from the surface. The robust Gaussian regression filter for profile explained in ISO 16610-31 was selected to remove the form with cut-off wavelength of 0.008 mm [96].

Once the surface form was removed, it was possible to generate a cross sectional profile at the deepest point of the indentation. The profile height parameter P_t was used to measure the depth characteristics of the indentation, where P_t is defined as [90],

“Total height of the profile P_t is a sum of the height of the largest profile peak height P_p and the largest profile valley depth P_v within the evaluation length”

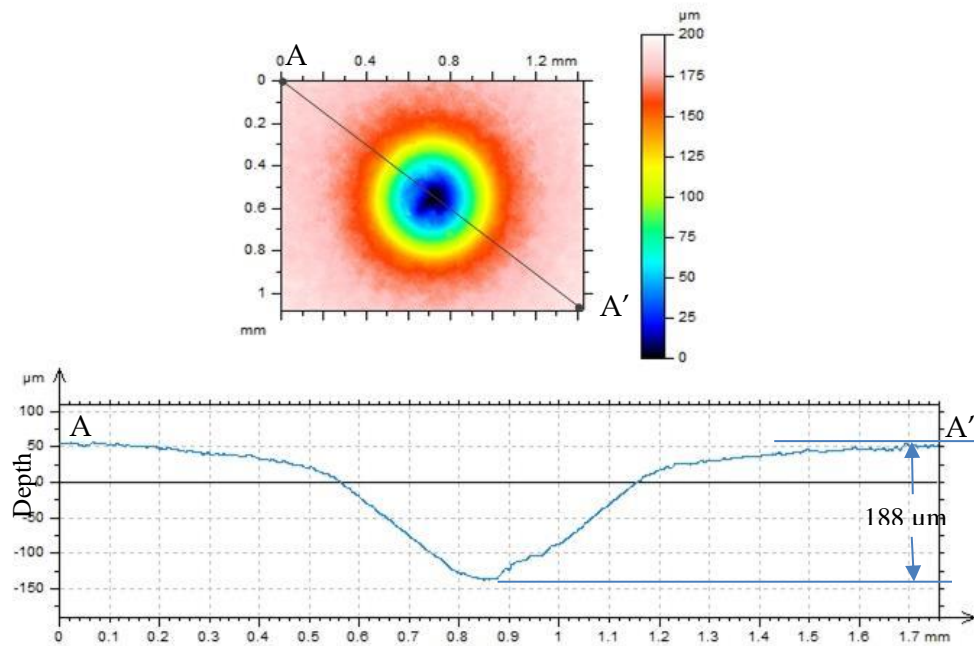


Figure 3-15 Manual depth measurement of a conical indentation

This process is illustrated in Figure 3-15, showing the top view of one of the conical indentations generated using the Rockwell hardness test equipment, with a line profile AA' created through the minimum point of the indentation depth. The subsequent Pt value of 188.0 μm is illustrated on the line profile although clearly the analysis is subjective in terms of the user defining of the orientation and position of the line profile.

Similarly, Figure 3-16 illustrates the top view of one of the pyramidal shape indentations generated using Vickers hardness test equipment, with a line profile BB' created through the deepest point of the indentation. The depth of the indentation was found to be 44.5 μm .

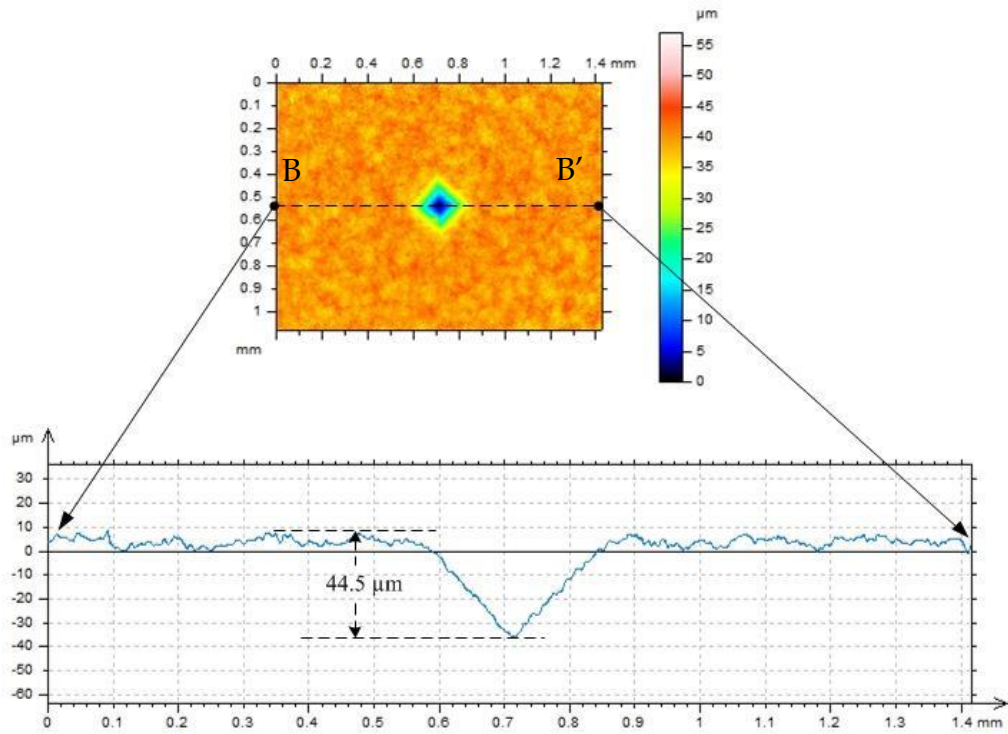


Figure 3-16 Manual depth measurement of the pyramidal indentation

Table 3-7 Repeatability of the hardness testing instruments

Indentation No	Depth of indentation (μm)	
	Rockwell	Vickers
1	188.0	44.5
2	187.0	44.9
3	186.1	46.7
4	189.3	46.6
5	185.8	46.5
6	187.4	43.9
7	190.2	47.8
8	185.3	47.5
9	188.7	47.8
10	184.9	44.3
Avg	187.3	46.1
StdDev	1.8	1.5

Using the process illustrated in Figure 3-14, the depth of each of the defects generated using the Rockwell and Vickers hardness test equipment was evaluated and the

corresponding results are shown in Table 3-7. The calculated average depth of the Rockwell indentations and the Vickers indentations was 187.3 μm and 46.1 μm respectively. The standard deviation associated with the Rockwell and Vickers instrument was 1.8 μm and 1.5 μm respectively. The standard deviation can be considered as a repeatability statement of each instrument [15].

3.4 Traceability

Generally, Rockwell and Vickers hardness testing equipment are calibrated using a standard certified test block which is traceable to SI definition of the kilogram. However, this research work only focuses on the indentation generated using these equipments regardless of hardness of the test samples. In order to gain confidence in the measurement process, the repeatability test was carried out and each of these indentations was measured using the 3D instrument. A typical instrument is calibrated to a standard step height that is traceable to SI definition of the metre as held by NPL, PTB and NIST (National Institute of Standards and Technology).

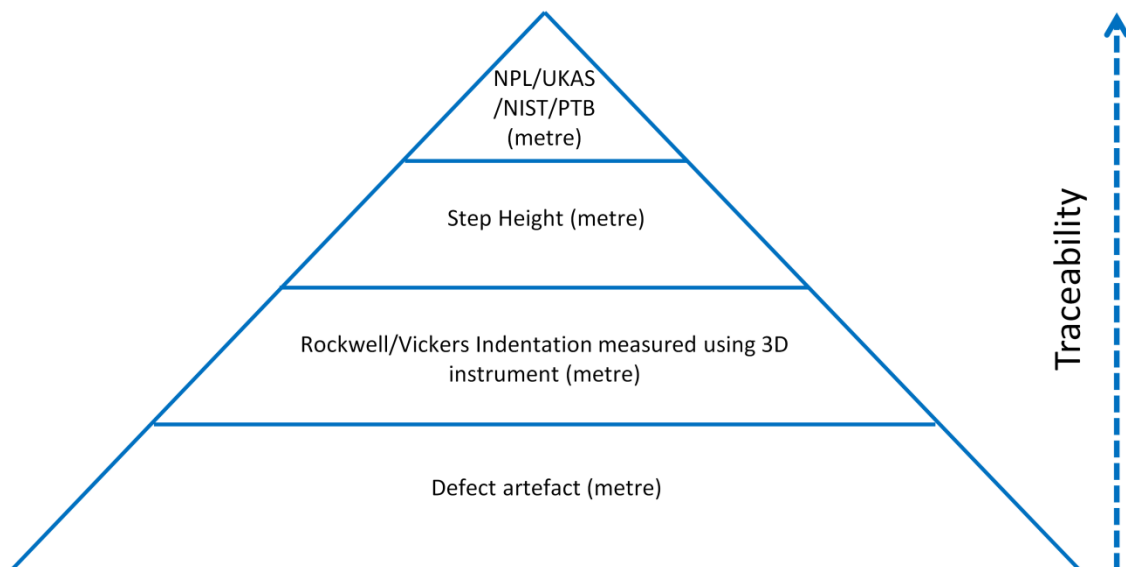


Figure 3-17 Traceability Chain

Figure 3-17 illustrates the traceability chain associated with defect artefact. It can be seen that the geometric parameters (depth for instance) of a defect artefacts can be directly traced to the SI definition of the metre. It is noted that the calculation of the

uncertainty budget associated with each step is complex and requires some further work beyond the scope of this thesis in this aspect.

3.5 Summary

The Rockwell hardness test equipment and the Vickers hardness test equipment have been used to generate controlled various size defect artefacts on different substrates. Mechanical methods have been experimentally investigated for the surface modification of metal to generate random surfaces. It is noted that these surface treatment methods provide different surface roughness characteristics. Roughness parameters have been evaluated using a traceably calibrated stylus based instrument (Talysurf Intra). The depths of the indentations were measured using ISO 4287 which is useful to evaluate surface profile texture parameters. Repeatability testing of both instruments has been carried out. The developed defect artefacts are traceable to the SI definition of metre. Generation of traceable defect artefacts is a novel step in the context of this research because no evidence has been found in literature or commercial sources of available defect gauges of its nature. Developed defect artefacts are used for evaluating the measuring instruments in Chapter 4 and for manual and automatic quantification methods for surface defect assessment in Chapter 5.

4 INTER-COMPARISON OF 3D MEASURING INSTRUMENTS

4.1 Introduction

Surface defect measurement and quantification are important elements and functionality indicators in the context of this study. This chapter introduces the Alicona InfiniteFocus (focus variation based instrument), the Zygo NewView 5000 (coherence scanning interferometer based instrument), the GFM MikroCAD (digital fringe projection based instrument) and the Heliotis H3 (parallel optical coherence tomography based instrument) as potential defect measuring instruments. Step height measurement and depth measurement of defect artefacts detailed in Chapter 3 are carried out for inter-comparison of these instruments, before consideration is given to the Heliotis H3 unit for the rest of the study.

4.2 Surface texture measurement techniques

The development of surface topography measurement owes much to the recent technological improvements of the instruments used which allows collection of texture data over areas instead of only along profile lines. There has been momentous development of digital data processing techniques along with the dramatic increase of computing power and speed. Moreover, new and reliable measurement techniques have been introduced offering interesting prospects. These advantages meet the growing needs of industry to potentially achieve better control of production and of the functional properties of surfaces.

Areal surface topography measurements are undertaken by either contact or non-contact measurement instruments. The most common contact type of equipment is stylus-based surface texture instrumentation. The basic principle of non-contact range measurement systems is to project an optical source onto an object and process the reflected signal to determine its vertical range [16]. Table 2-1 has already summarized the comparison between optical and stylus methods.

Although stylus-based surface texture equipment has been a reliable and traceable method, the main drawback is the physical size of the stylus that prevents it from penetrating sharp surface valleys and the stylus can potentially damage or scratch the surface and therefore the stylus technique may potentially be a partially destructive test. Non-contact measurement is of significant interest because it avoids deformation of the products and mechanical errors in the contact measurement. In Chapter 2, Table 2-2 summarized the capability of various non-contact measurement techniques to measure and to quantify small scale surface defects.

Four different measurement techniques were identified that could potentially measure surface defects. In this study, advanced measurements of surface defects have been carried out using; an Alicona InfiniteFocus focus variation (FV) technique [129], a Zygo NewView 5000 coherence scanning interferometer (CSI) [130], a GFM-MikroCAD Lite digital fringe projection (DFP) [131] and a Heliotis H3, parallel optical coherence tomography (pOCT) [132].

In order to derive the most suitable instrument that can measure small-scale surface defects with high speed, high accuracy and high repeatability, two sets of experimentations have been carried out. In the first set of experimentation, a standard step-height measurement was completed using each of the instruments and results were compared with a true value of the step height, obtained using contact measurement. This experimentation would help to evaluate the accuracy of the instrument in measuring the step-height. In the second set of experimentation, various sizes of defect artefacts embedded in different flat substrates were measured using each of the instruments. Inter-comparison of the measurement results was completed to identify the repeatability and the robustness of the measuring instruments.

In the following sub-sections, a brief working principle of each instrument is explained along with the specification of the particular instrument.

4.2.1 Focus variation

FV combines the small depth of focus of an optical system with vertical scanning to provide topographical and colour information from the variation of focus.

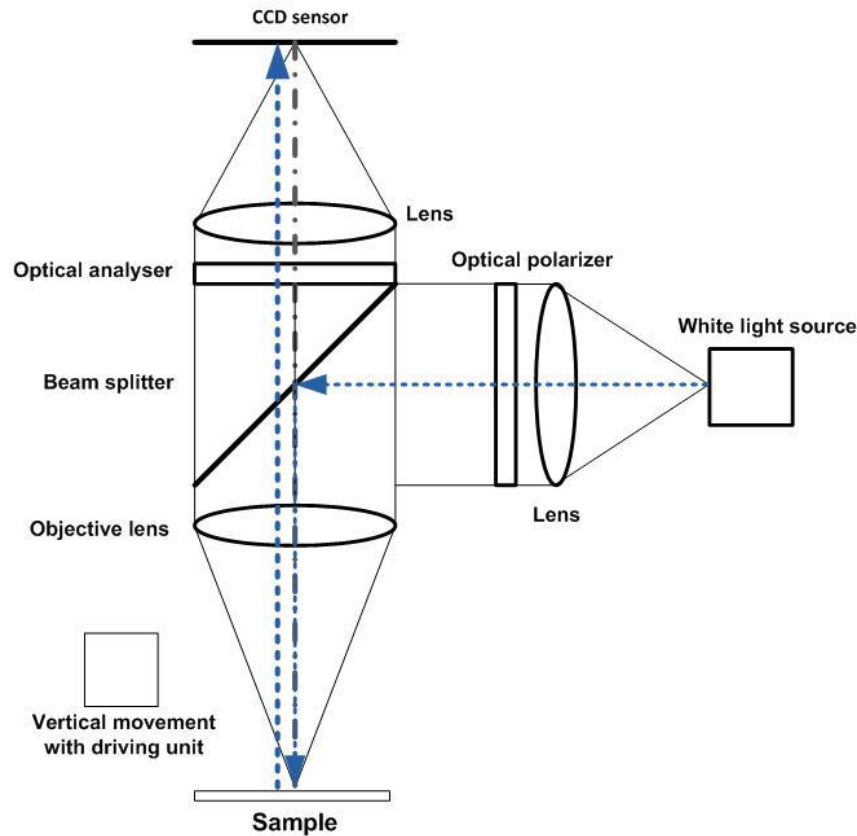


Figure 4-1 Optical arrangement of a FV based measurement equipment [16]

A schematic diagram of a typical focus variation instrument is shown in Figure 4-1. The operating principle of focus-variation moves the small depth of focus of an optical system, combined with light with continuous vertical scanning, producing a topographic 3D data model of the surface. As the distance between the object and objective lens is varied, the variation of sharpness is used for measuring 3D depth information, and a dense 3D point cloud is obtained. Depth measurement by focus variation is acquired by searching the best focus position of an optical element pointing to a sample. This focus position is associated to a certain distance from the sample depth value. By carrying out this process for entire lateral positions, a depth map of the sample can be generated [133].

The illumination source, typically a white light LED, is transmitted through the objective lens to the sample. Due to variation in the topography and the reflectivity of the sample, the light is reflected in different directions. The reflected light is partly collected by the objective and projected to the CCD sensor. By moving the objective lens in the vertical direction in relation to the sample, the degree of focus varies from low to high, and back to low again. This change of focus is related to a change of intensity on the CCD sensor. By analysing this intensity on the CCD sensor, the position where the sample was in focus can be measured. By repeating this for every lateral position on the CCD sensor, the topography of the sample in the field of view can be measured [133,134].

4.2.1.1 Alicona InfiniteFocus G4

Alicona GmbH, a company based in Austria, has been developing the focus variation technology over the last decade. Figure 4-2 shows their current optical 3D measurement device the InfiniteFocus G4.



Figure 4-2 Alicona InfiniteFocus G4

The system is based on the FV principle which vertically scans a surface and continuously acquires data. Since the system has a very limited depth of field, only small regions of a surface are in focus at the same time. By analysing the variation of

focus for each surface point during the scanning process the height of each point is obtained. In addition to the height information the device also provides true colour information for each measurement point, which is registered to the height data. Another important aspect in the context of surface texture measurement is that the system is able to measure very steep surface flanks of 80° [133].

The InfiniteFocus system can be equipped with objectives of different magnification ranging from 2.5 x to 100 x. At the largest magnification a vertical resolution up to 10 nm can be reached thus providing very high lateral and vertical resolution with the drawback of small field of view. In order to cover larger surface areas, the system provides field or image stitching capability. In the process of data stitching, the system measures several single 3D datasets with a slight overlap (10 % to 25 %) that are consecutively stitched together based on colour and on topographical information to form a large measurement map [133,134].

For the experimentation, the 10 x objective was selected from the interchangeable objectives to measure the defects. The Alicona provides the functionality to vary the lateral resolution (10 x objective) in range of $1.75\ \mu\text{m}$ to $11.74\ \mu\text{m}$ and upto 100 nm vertical resolution. Technical specifications with this selection of objective are:

- Stand-off distance: 17.5 mm
- Field of View (FOV): 1.4 mm x 1.0 mm
- Vertical resolution: $1\ \mu\text{m}$
- Lateral resolution: $2\ \mu\text{m}$

4.2.2 Coherence scanning interferometer

Generally, the CSI technique utilizes the superposition property of light waves. The amplitudes of two light waves with the same frequency will maximise or cancel depending on whether these two waves are in phase or out of phase by 180° which results in a set of dark and light bands known as interference fringes that indicate the surface structure of the part being tested. The schematic of a CSI system is shown in Figure 4-3. Quantitative measurement of specimen surface height is carried out by detecting the phase of a number of interference patterns produced by the two reflecting wavefronts from the reference surface, and the specimen surface and implementing

appropriate algorithms. This characterizes how well a wave can interfere with itself at a different time by measuring interference patterns each associated with a different axial position of the reference or specimen surface [42,135].

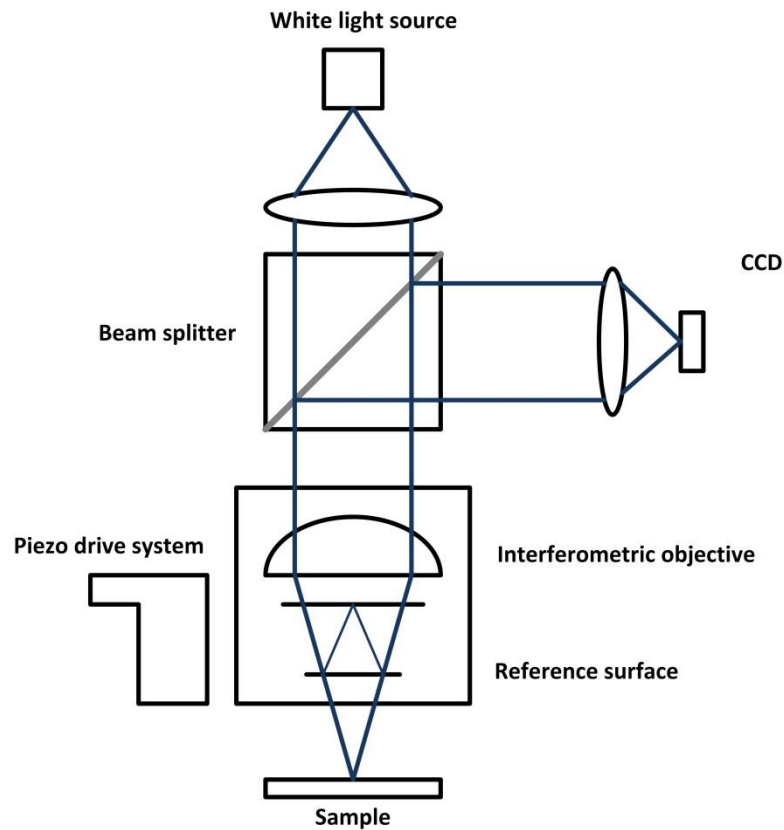


Figure 4-3 Optical arrangement of CSI [136]

The CCD detector measures the intensity of the light as the interferometric objective is actuated in the vertical direction and detects the maximum interference. Each pixel of the image sensor measures the intensity of the light and the fringe envelope obtained can be used to calculate the position of the surface. When the objective lens is moved downwards, there is a change of intensity due to interference that will be observed for each pixel when the distance from the test surface to the beam splitter is the same as the distance from the reference plane to the beam splitter and the highest points on the surface will cause interference first. A series of interferograms are generated as the objective is scanned perpendicular to the illuminated surface, while recording the detector data. The interferograms stored in the computer are individually processed and

generate a complete three dimensional image constructed from the height data and corresponding image plane coordinates [42,135]

4.2.2.1 Zygo NewView 5000

The Zygo NewView 5000 (Figure 4-4) is a commercial coherence scanning interferometer from Zygo Corporation from USA and can be divided into two basic subsystems: the microscope and the computer. The microscope measures the sample surface topography and generates the raw data needed for analysis and includes: the microscope itself, objectives, stage, video monitor, electronics, and a vibration isolation system. Automated systems also include a motorized stage and related electronics. The computer controls the measurement process, performs calculations, and displays measurement results on a colour monitor. The instrument includes interferometric Mirau and Michelson optics for imaging an object surface and a reference surface with both images brought together onto a CCD, resulting in an interference intensity pattern that is read electronically into the computer.



Figure 4-4 Zygo NewView 5000

Illumination from a white light halogen source is passed through an interferometric objective and is split into a reference beam and a test beam. The reference beam reflects from an internal reference surface in the objective and the test beam reflects from the

object surface. These two illumination components are combined to create interference. Both beams are directed onto a solid-state camera and the intensities are converted into images for three dimensional measurements by the Zygo Corporation MetroPro software. The test part is scanned by vertically moving the objective with a piezoelectric transducer (PZT). As the objective scans, the video system captures intensities at each camera pixel.

The instrument is traceably calibrated with reference to a NIST certified calibration step height standard artefact SHS 1.8QC (Serial NO. 7657-09-11) from VLSI. The uncertainty statement of this step height is $1.798 \pm 0.011 \mu\text{m}$. The measurement error of this instrument is stated as being 0.1 nm. NIST is the national institute for natural and engineering sciences and the highest technical authority for metrology and physical safety engineering in United State of America.

For the experimentation, consistency has been maintained throughout the measurement process by selecting a 10 x Mirau objective with 0.5 x optical zoom and the 640 x 480 pixel camera mode to capture the image field. Technical specifications with this selection of objective are as below:

- Stand-off distance: 7.5 mm
- Field of View (FOV): 1.4 mm x 1.06 mm
- Vertical resolution: 0.1 nm
- Lateral resolution: $0.95 \mu\text{m}$

4.2.3 Digital fringe projection

The majority of fringe projection systems are based on the principle of structured light triangulation in similar manner as stereo vision systems but replacing one of the two cameras in the latter system with a projector-like device as shown in Figure 4-5 [137].

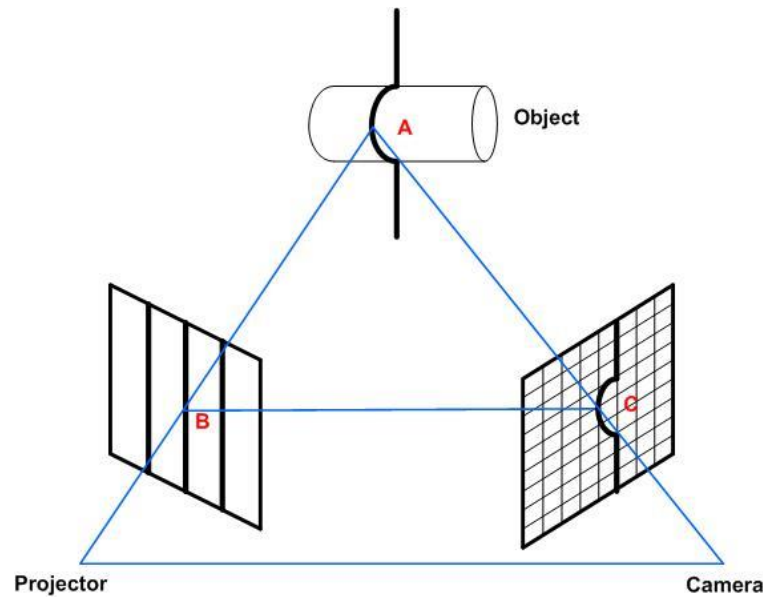


Figure 4-5 Schematic of DFP system [137]

The fringe projector, camera and the object form a triangle base. If the correspondence between the camera pixel (C) and the projector pixel (B) is identified, the depth information at point A can be recovered through the triangulation (ΔABC). Specifically, the projector projects a fringe pattern of known characteristics onto the object and due to the geometrical profile of the object the fringe is deformed as seen from a perspective different from the projection axis. Usually, the fringe pattern on a reference plane is recorded by the system. By comparing between the distorted fringe pattern over the object and the reference fringe pattern, the 3D profile of the object can be retrieved with respect to the reference plane. The object geometry is actually encoded in the phase difference between the deformed and reference fringes images [138,139].

4.2.3.1 GFM MikroCAD Lite

The GFM MikroCAD Lite (as shown in Figure 4-6) is a commercial instrument from GFMesstechnik GmbH from Germany and uses the method of phase-measuring fringe projection technology. The GFM MikroCAD Lite uses advanced digital light projection (DLP) technology (based on micro-mirror based projection developed by Texas Instrumentation) which projects the fringe pattern onto the measuring object [65]. The distorted fringes are captured using a high-speed camera and phase shift of fringes is

measured at each pixel level. Height is calculated from the phase by the ODSCAD 6.0 software [140].



Figure 4-6 GFM MikroCAD Lite [131]

The instrument is traceably calibrated with reference to a PTB certified calibration step height standard artefact of 1.00 mm. The measurement error of the instrument is stated as being 0.1 μm .

The MikroCAD Lite has a single camera that provides a fixed field of view. In this study of measuring defects, the MikroCAD Lite equipment has been used and the technical specifications for this instrument are:

- Stand-off distance: 100 mm
- Field of View (FOV): 13 mm x 8 mm
- Vertical resolution: 1 μm
- Lateral resolution: 17.3 μm

4.2.4 Parallel optical coherence tomography

Optical coherence tomography (OCT) is an optical 3D technology rapidly growing in importance, both in biomedical as well as in other scientific and technical applications. The parallel optical coherence tomography (pOCT) approach using a custom designed

optical sensor represents a significant advance on the way to miniaturized, high-speed, and cost-effective 3D-imaging systems [141,142].

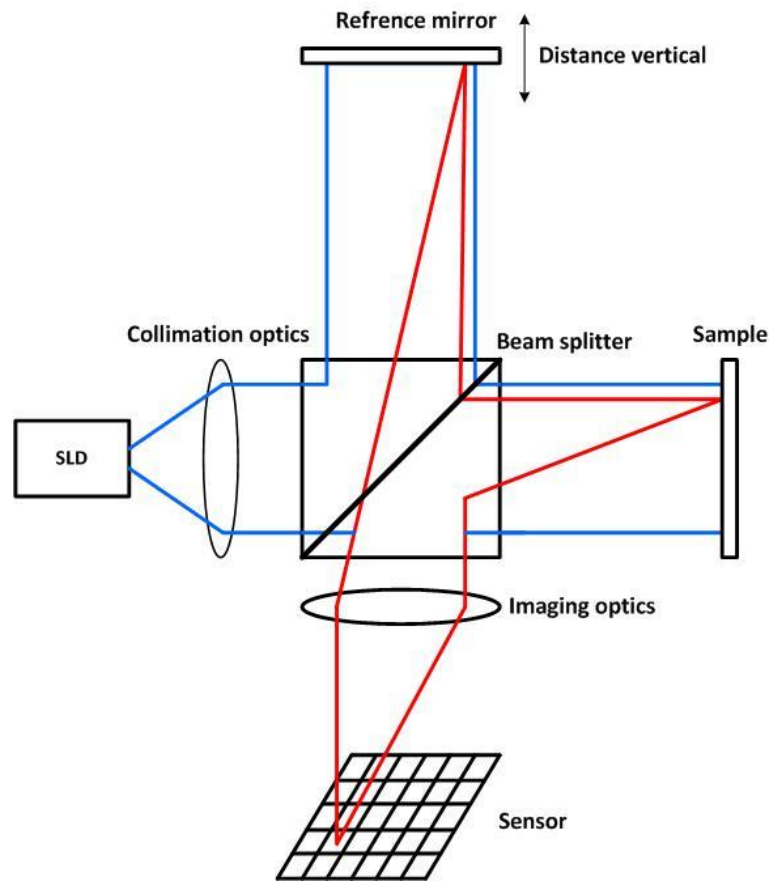


Figure 4-7 Schematic of pOCT [141,142]

Figure 4-7 is an extension of a low-coherence interferometer system that contains a Michelson type interferometer [143]. The light beam from the illumination source is split into two paths by the beam splitter. In the sample path, the light is partially reflected by the inspected sample; in the reference path, the reference mirror reflects the beam. The two beams are recombined in the beam splitter and this produces the interference signal. Interferometric modulation of the output intensity is detected by the photodetector. The photodetector converts the received optical signal into an electrical signal. The detector output is demodulated to produce the envelope of the interferometric signal which is then digitized and stored on the computer [141,144].

The light source is very important as there is some general requirement for OCT imaging; emission in the near infrared, short temporal coherence length and high irradiance [145]. The most commonly used sources are edge-emitting light emitting

diodes and super luminescent diodes (SLD). Conventional OCT uses CCD cameras but it does not have any signal processing function and these post processes delay the image acquisition time and hence smart array CMOS detectors are used. The detector array consists of photodiode pixels and each pixel contains a photo diode, band-pass filter, an amplifier, a rectifier and a low pass filter. Output of this smart array finds the envelop of the interference signal that is modulated by a fringe frequency. The electronically generated envelopes are then fed to the demodulator that converts the electrical signals into digital signal to be processed in the computer [146].

4.2.4.1 Heliotis H3

The Heliotis H3 is commercial pOCT instrument for 3D measurement from the company Heliotis AG based in Switzerland. The optical instrument is shown in Figure 4-8. A light beam from the SLD is passed through an interferometric objective and is split into a reference beam and a sample beam. The reference beam reflects from reference mirror and a sample beam reflects from the sample. These two optical components are combined and produce interference signal. Interference signal is captured by the sensor that uses CMOS based smart pixel architecture that converts optical signal into corresponding electrical signal following with parallel signal processing to generate the 3D data. The test part is scanned by vertically moving the objective with a linear translation stage. As the objective scans, the sensor captures the interference signal at each pixel [147].

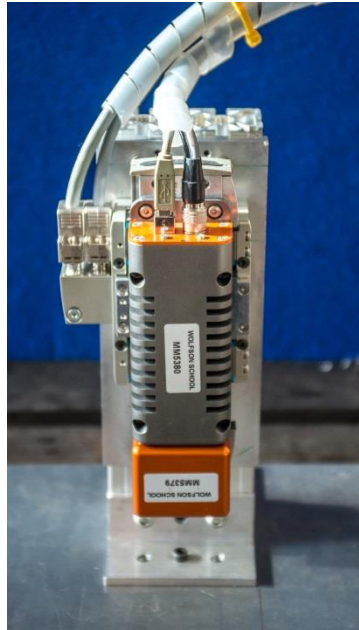


Figure 4-8 Heliotis H3

Currently, the instrument is not calibrated to any reference standard. The vendor is currently developing the process of calibrating the instrument. The Heliotis H3 has a single camera that provides a fixed field of view but has interchangeable optics. In this study of measuring defects, the technical specifications for this instrument are:

- Stand-off distance: 22 mm
- Field of View (FOV): 2.4 mm x 2.4 mm
- Vertical resolution: 1 μm
- Lateral resolution: 8 μm

4.3 Depth measurement

Two types of experiments were carried out in order to compare the performance characteristics of the above mentioned optical transducers:

- (1) Step height measurement
- (2) Artefact defect depth measurement

It is important to know the measurement error, repeatability, and detectability in order to select the most suitable equipment to detect the sub-millimetre level defect artefacts generated on metal plates. It was anticipated that results from such measurements

would aid the selection of the 3D instrument which could most reliably measure surface defects in the context of this research.

4.3.1 Step height

In an attempt to demonstrate the basic functionality of the measurement systems, a measurement of a step height was carried out. A step height of 100 μm was created using two standard slip-gauges of 1.1 mm and 1.0 mm. The slip-gauges (manufactured by Micronaid) were calibrated using UKAS accredited route with an uncertainty budget of 0.08 μm . The measured calibrated step-height difference was 99.52 μm . The two slip-gauges were placed on optically flat glass as illustrated in Figure 4-9. A coordinate measuring machine (CMM) was used to measure the physical geometrical characteristics of the step height.



Figure 4-9 Slip-gauge arrangement to create a step-height of 100 μm

A Nikon Metrology (Metris) Ultra CMM was selected which has a Renishaw PH10MQ probe-head and a Renishaw SP25M probe with a ruby sphere of 1 mm radius. The instrument was traceably calibrated with reference to UKAS certified calibration artefacts using procedures described in ISO 10360-2 [148]. The measurement error of this instrument was stated as being $(0.7 + L/600)$ μm (where L is the length (in mm) of the component being measured). In this study, the experimental result from the CMM

equipment (See Figure 4-10) was considered as a true value of the step height for comparing each optical instrument's measurement.

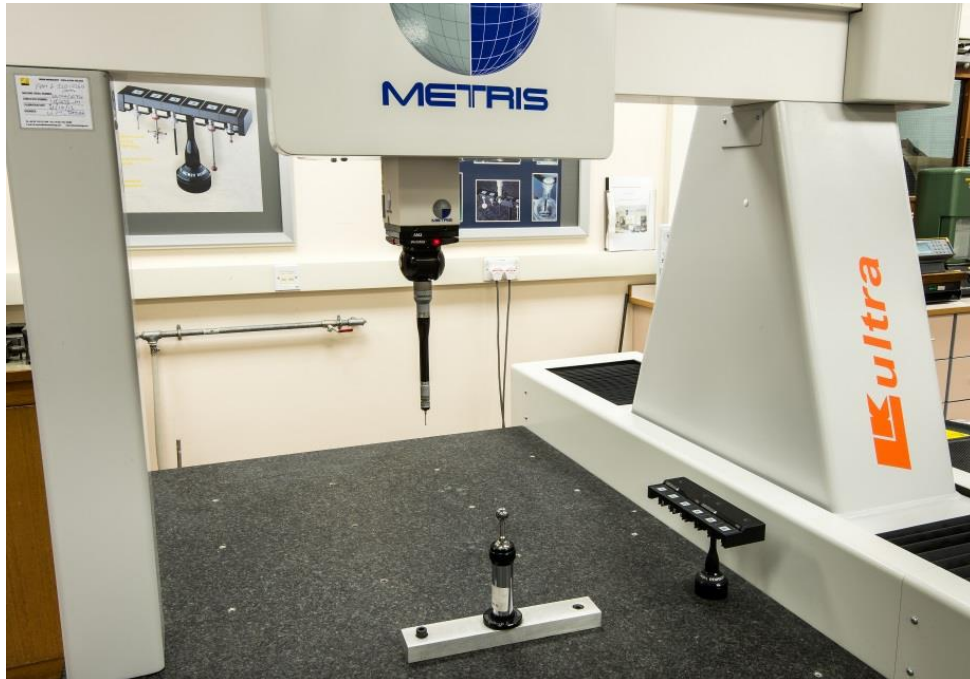


Figure 4-10 Nikon Metrology (Metris) Ultra CMM

Using the CMM equipment, four different points were obtained on the surface of each slip-gauge. Once two sets of four points on each slip-gauge were obtained, a least square plane was fitted in both sets. An absolute height was calculated between the two planes. The measurement was repeated five times and the average step height was measured as $98.9 \mu\text{m}$ with a standard deviation of $0.15 \mu\text{m}$.

As described in the set specifications for each optical instrument in Sections 4.2, step height was measured using all four instruments and the results are shown in Table 4-1. Once the 3D dataset was acquired from each optical instrument, it was then processed using the DigitalSurf MountainMap (v5) software instead of using instrument's native software [149] for better more consistent inter-comparison of the 3D instruments. The 3D data may contain tilt that needs to be removed before height measurement. Tilt can be removed using the software's built-in least square technique. Figure 4-11 shows a typical 3D dataset of the slip-gauges measured using the Alicona system with a cross-section AA'.

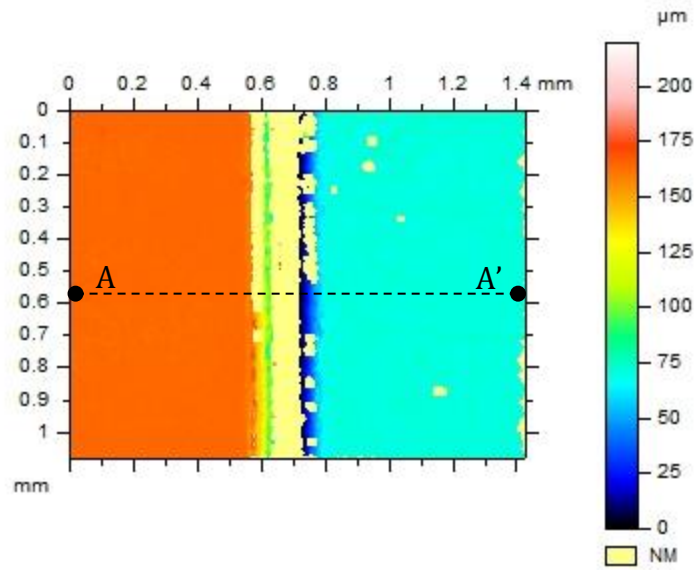


Figure 4-11 Step-height measured using the Alicona IFM G4

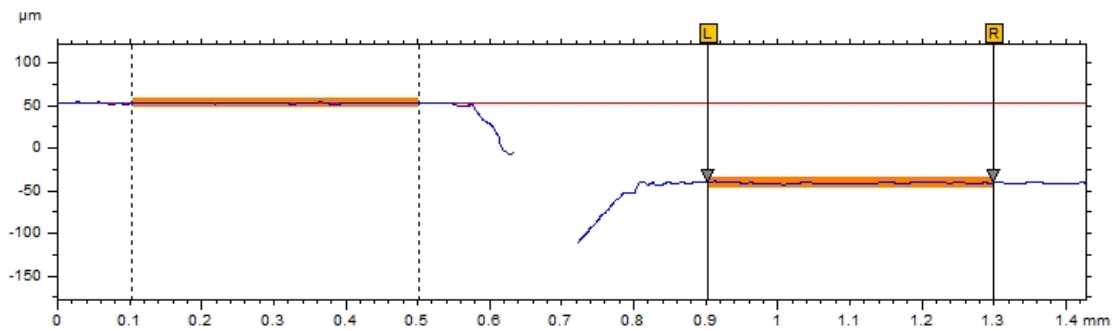


Figure 4-12 Step-height measurement

Table 4-1 Step height measurement

No of Experiments	Step Height (μm)			
	Alicona	GFM	Heliotis	Zygo
1	97.9	96.9	98.3	101
2	99.9	96.9	96.9	101
3	99.6	93.7	97.2	101
4	98.4	93.4	97.1	101
5	94.4	98.9	101.1	102
6	98.9	91.2	98.3	101
7	98.6	96.1	99.4	102
8	97.8	109	99.8	101
9	98.5	98.7	96.9	102
10	99.0	95.9	97.4	101
Mean	98.3	97.1	98.2	101.3
Std Dev	1.5	4.8	1.4	0.5

After selecting the cross-sectional profile, an average line was calculated for each of the surface profiles of the slip-gauges of a length of 0.4 mm and the absolute height was calculated between two average lines. This process is illustrated in Figure 4-12

The step height was measured 10 times on each instrument at the same time under the same conditions without changing any parameter to evaluate the repeatability and measurement error of the each instrument. The results are shown in Table 4-1. The measured average step height of the slip gauges using the Alicona, GFM, Heliotis and Zygo was 98.3 μm , 97.1 μm , 98.2 μm and 101.3 μm respectively and the standard deviation was 1.5 μm , 4.8 μm , 1.4 μm and 0.5 μm respectively.

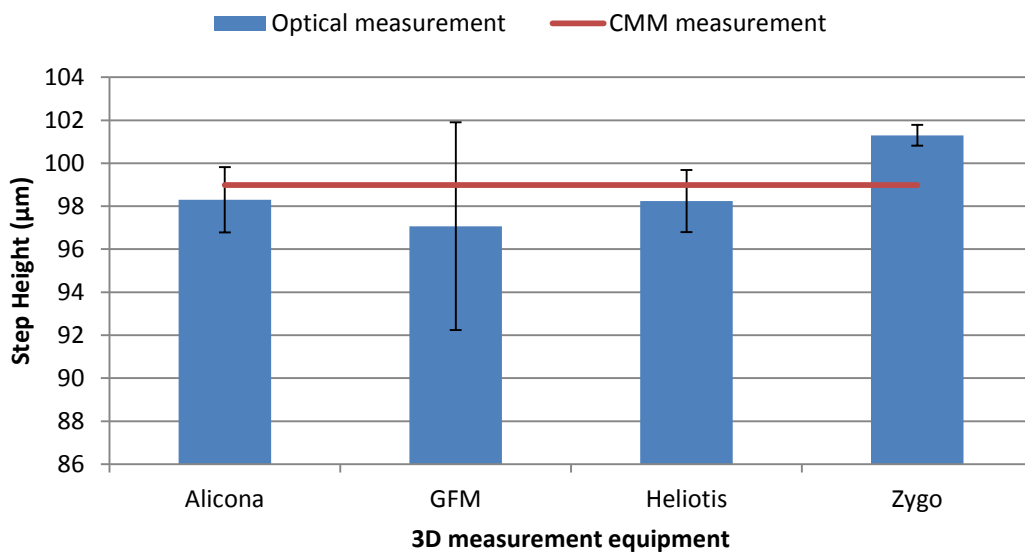


Figure 4-13 Step height measurement using four different instruments

Figure 4-13 indicates the true value of the step height measured by the CMM (98.9 μm) and the four optical instruments. The graph shows that the Zygo had the highest repeatability while the repeatability of Alicona and Heliotis were almost equal but lower than Zygo. The measurement error for the Alicona was the least among the instruments (0.6 μm) resulting in it being the most accurate instrument in measuring step height. The Heliotis's measurement error was slightly higher than the Alicona (0.7 μm). The Zygo had the highest measurement error (2.4 μm). The GFM MikroCAD was the least repeatable among all of the instruments with a measurement error of 1.8 μm which was less than the Zygo. Hence, both the Alicona and the Heliotis performed better than the remaining instruments in measuring the step height.

4.3.2 Artefact defect height

In this study, defects with conical geometry on each substrate with all sizes were used to evaluate the performance characteristics. As described in the specification for each optical instrument in Section 4.2, the depth of the each artefact was measured using all four instruments. Once the 3D dataset was acquired from each optical instrument, it was then processed using the DigitalSurf MountainMap (v5) software instead of using each instrument's native software. Instrument native software processing of 3D data was often subject to issues of repeatability and may be non-traceable in nature, leading to significant uncertainty about data quantisation and representation. Moreover, for better inter-comparison of these instruments, using the third party software for data analysis is an appropriate approach.

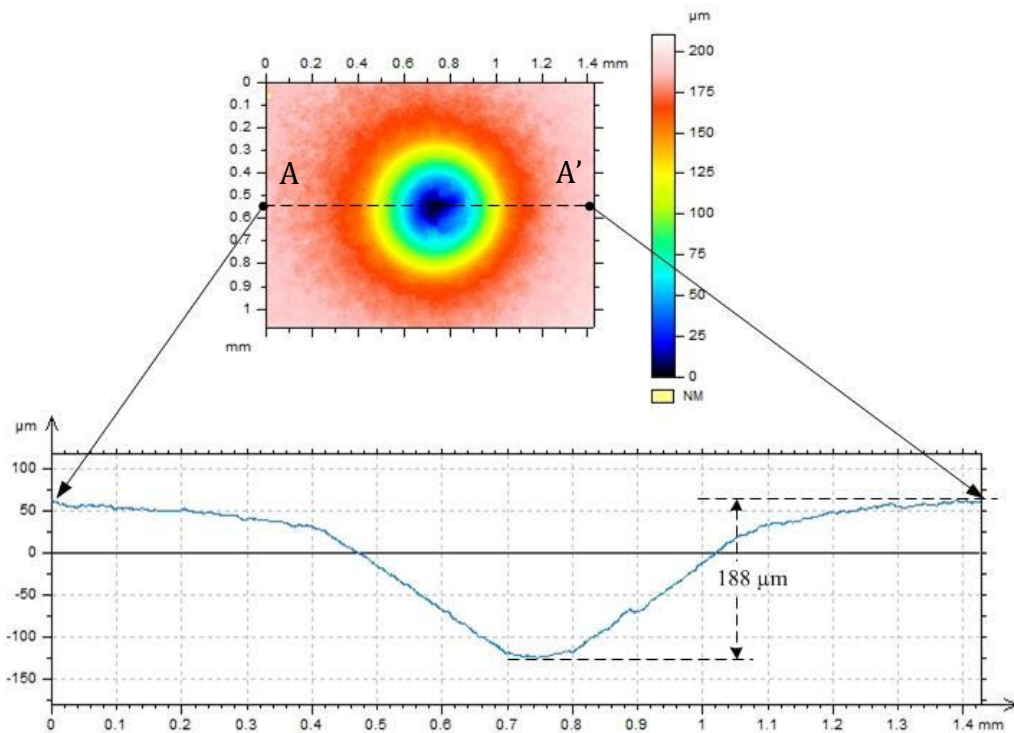


Figure 4-14 Manual depth measurement

The data process for measuring the depth of the defect artefact is explained in Section 3.3.3. Typically, the 3D datasets contained geometric form that needed to be removed for better assessment of the surface. Once the form was removed, it was possible to generate a cross sectional profile at the user's perceived deepest point of each defect,

allowing the manual measurement the depth of the defect. The profile height parameter Pt was used to measure the depth characteristics of each defect.

This process is illustrated in Figure 4-14, showing the top view of a conical defect on the flat Plate A with surface roughness of $Rq = 0.16 \mu\text{m}$ with a line profile AA' created through the maximum point of the defect depth. The subsequent Pt value of $188 \mu\text{m}$ is illustrated on the line profile.

4.4 Instruments Performance

In this section, all individual optical transducers are evaluated by measuring defect depths on four different substrates.

4.4.1 Alicona InfiniteFocus G4

Table 4-2 shows the depth measurement of four different Rockwell defects embedded on four different flat substrates ranging from $0.06 \mu\text{m}$ to $1.27 \mu\text{m}$ using the Alicona InfiniteFocus. Each defect was measured five times without changing any of the instrument's parameters to evaluate the measuring functionality of the instrument.

Figure 4-15 highlights defect number 2 in all substrates measured using the Alicona. From the Alicona measurement, it is observed that

- The substrate with a roughness of $Rq = 0.06 \mu\text{m}$ is very specularly reflective (Plate D), the system struggled to generate the 3D data from the defect which is well illustrated in Figure 4-15 (a). Significant amount of non-measured data points are observed. A large amount of linear interpolation is required to fill this extent of non-measuring data points. Such filled 3D data cannot be considered authentic to represent the actual surface defect as it may change the shape of the defect. The highest standard deviation of $14.5 \mu\text{m}$ is observed in measuring one of the conical defects.
- The substrate with a roughness of $Rq = 0.16 \mu\text{m}$ was not too specularly reflective (Plate A), the system generated the 3D data with repeatability between ($0.4 \mu\text{m}$ to $3.8 \mu\text{m}$) as seen from Figure 4-15 (b) and Table 4-2 (b).

- The substrate with a roughness of $Rq = 0.78 \mu\text{m}$ was rough and specularly reflective (Plate C) and the system generated 3D data with a lower amount of non-measured data points (Figure 4-15 (c)) but that were filled using MountainMap software's built-in interpolation toolbox. The system measured defects with a repeatability in the range of $0.9 \mu\text{m}$ to $2.8 \mu\text{m}$ (Table 4-2 (c)).
- The substrate with the highest roughness of $Rq = 1.27 \mu\text{m}$ (Plate B) was measured with a repeatability approximately of $1.4 \mu\text{m}$.
- The data acquisition time for each defect was approximately 30 s to 40 s.
- The data stitching of 2×2 image fields was required to measure the biggest defect on all substrates. This is because of the small field of view.

Table 4-2 Manual depth measurement by Alicona on Plates A to D

No.of Test	Depth measurement (μm)			
	1	2	3	4
1	320	251	177	58.2
2	309	283	184	56.5
3	300	255	177	58.0
4	305	278	184	56.5
5	303	258	189	57.2
Avg	307.4	265.0	182.2	57.3
Std Dev	7.8	14.5	5.2	0.8

(a) $Rq = 0.06 \mu\text{m}$

No.of Test	Depth measurement (μm)			
	1	2	3	4
1	311	268	186	47.1
2	312	267	191	46.1
3	310	264	193	47.0
4	312	267	185	46.3
5	311	264	193	46.9
Avg	311.2	266.0	189.6	46.7
Std Dev	0.8	1.9	3.8	0.4

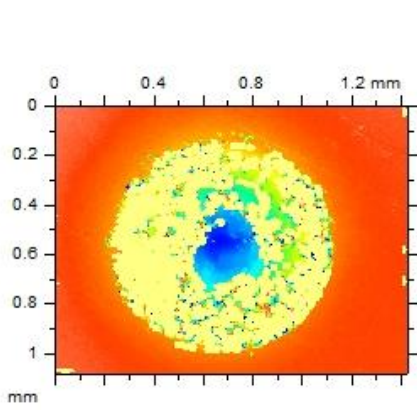
(b) $Rq = 0.16 \mu\text{m}$

No.of Test	Depth measurement (μm)			
	1	2	3	4
1	306	257	173	46.8
2	307	256	171	45.6
3	307	258	174	46.6
4	310	251	173	48.2
5	306	257	177	46.4
Avg	307.2	255.8	173.6	46.7
Std Dev	1.6	2.8	2.2	0.9

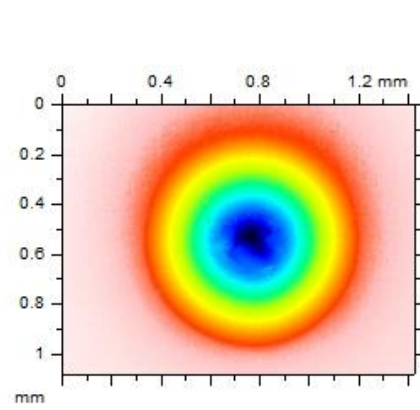
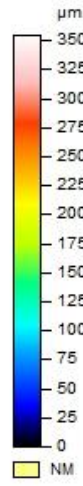
(c) $Rq = 0.78 \mu\text{m}$

No.of Test	Depth measurement (μm)			
	1	2	3	4
1	305	260	189	44.5
2	307	261	192	44.3
3	305	259	191	46.6
4	303	263	189	47.2
5	305	260	189	44.3
Avg	305.0	260.6	190.0	45.4
Std Dev	1.4	1.5	1.4	1.4

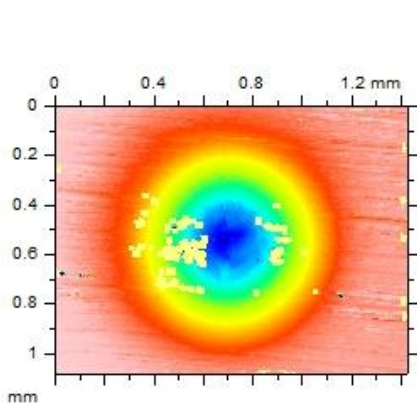
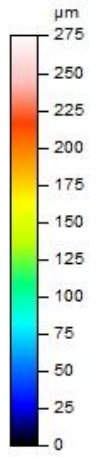
(c) $Rq = 1.27 \mu\text{m}$



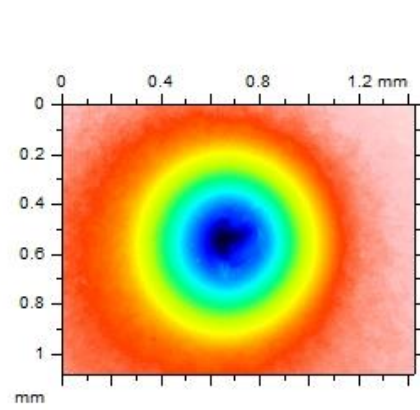
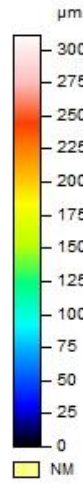
(a) $Rq = 0.06 \mu\text{m}$



(b) $Rq = 0.16 \mu\text{m}$



(c) $Rq = 0.78 \mu\text{m}$



(d) $Rq = 1.27 \mu\text{m}$

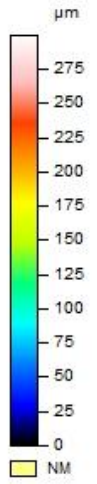


Figure 4-15 Defect number 2 on Plates A to D measured using the Alicona

Figure 4-16 illustrates the comparison of the depth measurement of all defects in the four substrates having surface roughness Rq values ranging from $0.06\ \mu\text{m}$ to $1.27\ \mu\text{m}$. It is observed that the system performance deteriorated with smooth and specularly reflective surfaces. The repeatability of the measuring instrument on the roughest substrate is the highest compared among the rest of the substrate which is highlighted by the one sigma standard deviation bars in Figure 4-16.

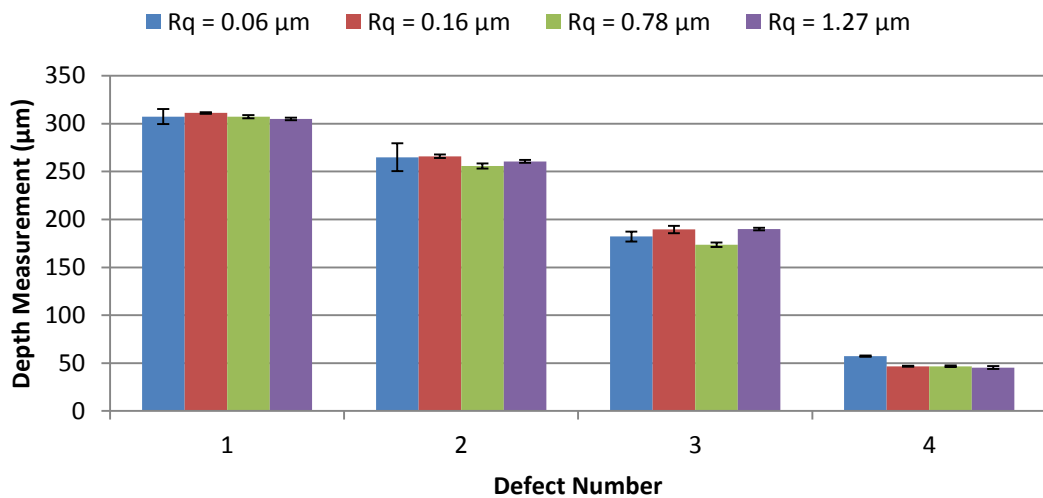


Figure 4-16 Defect depth measurement on different substrates using the Alicona

4.4.2 Zygo NewView 5000

Table 4-3 shows the depth measurement of four different defects embedded on the four different substrates using the Zygo NewView 5000. Each defect was measured five times repetitively without changing any of the instrument's parameters to evaluate measuring functionality of the instrument.

Figure 4-17 highlights defect number 2 in all substrates measured using the Zygo. From the Zygo measurement, it is observed that

- Measured defects were seen with no side walls especially with the specularly reflective substrate that presents Rq values of $0.06\ \mu\text{m}$, $0.16\ \mu\text{m}$ and $0.78\ \mu\text{m}$. (Figure 4-17 (a), (b) & (c)). This happens because of the multiple reflections

occurring during measurement due to the angle of the surface defect. This phenomenon is explained in Chapter 7 of NPL Good Practise Guide [42].

- Table 4-3 (a) and (c) and Figure 4-17 (a) and (c) suggests that the instrument struggles to measure defects embedded in very specularly reflective surfaces (Plate D and Plate C). Compared to the other two substrates, the amount of non-measured data points is very high. After filling the non-measured data points for such defect artefacts, the standard deviation are observed to be very low (less than 1.5 μm). Although the standard deviation is low, the filled data does not represent typical or ideal surface defects.
- Table 4-3 (b) and Figure 4-17 (b) suggests that the Zygo has measured defects embedded in the normal surface and roughest surface. The instrument measures such defects with missing data points to the instrument, however the missing data points in such substrates are less than specularly reflective substrates (plate C and D). The repeatability of measuring the typical defect was noted to be in the range of 2 μm to 6 μm .
- Significantly very high interpolation was required to fill the missing data points in most of the defects. Hence the detectability of this instrument for measuring the surface defects is poor. The system was able to image the bottom of the defect along with the top surface of the plates but this is not sufficient to represent a 3D structure of the defect. This is a classic problem with CSI instrument. Once the wall angle of the defect goes beyond the numerical aperture of the lens, the instrument will not correctly measure the defect [42].
- Data acquisition time for each measurement ranged between 40 s to 150 s depending upon the vertical scanning range.
- The data stitching of 2 x 2 image fields was required to measure the biggest defect on all substrate. This is because of the small field of view.

Table 4-3 Defect depth measurement by Zygo on Plates A to D

No.of Test	Depth measurement (μm)			
	1	2	3	4
1	292	234	173	43.1
2	292	234	174	42.3
3	292	234	173	43.6
4	291	233	174	43.1
5	292	234	175	43.5
Avg	291.8	233.8	173.8	43.1
Std Dev	0.4	0.4	0.8	0.4

(a) $Rq = 0.06 \mu\text{m}$

No.of Test	Depth measurement (μm)			
	1	2	3	4
1	315	255	185	43.9
2	307	249	188	43.8
3	316	259	179	44.8
4	317	254	179	43.6
5	313	254	176	43.3
Avg	313.6	254.2	181.4	43.9
Std Dev	4.0	3.6	4.9	0.6

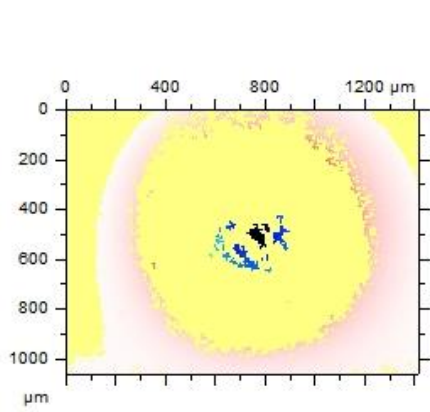
(b) $Rq = 0.16 \mu\text{m}$

No.of Exp	Depth measurement (μm)			
	1	2	3	4
1	312	244	169	45.1
2	313	243	169	44.5
3	316	243	169	43.2
4	311	242	171	44.1
5	313	240	169	44.7
Avg	313.0	242.4	169.4	44.3
Std Dev	1.9	1.5	0.9	0.7

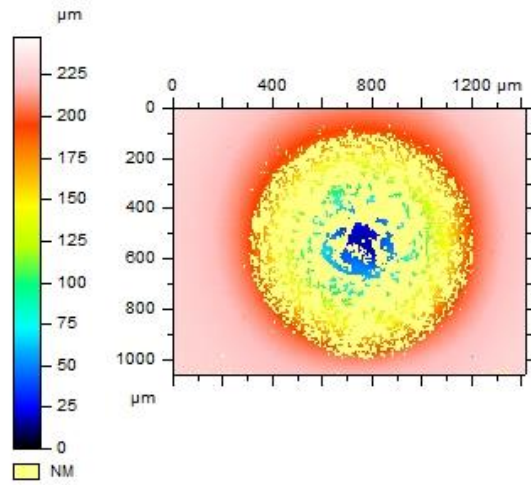
(c) $Rq = 0.78 \mu\text{m}$

No.of Test	Depth measurement (μm)			
	1	2	3	4
1	319	259	180	42.3
2	312	256	183	42.5
3	312	263	186	40.7
4	309	259	185	41.4
5	302	256	184	41.8
Avg	310.8	258.6	183.6	41.7
Std Dev	6.1	2.9	2.3	0.7

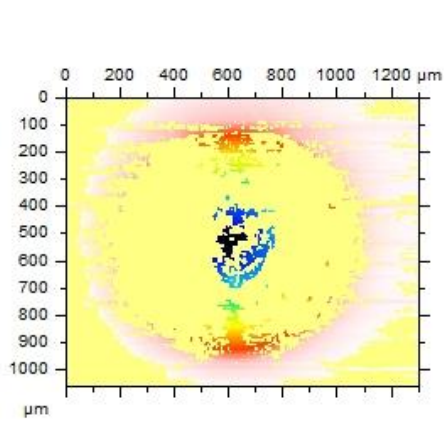
(d) $Rq = 1.27 \mu\text{m}$



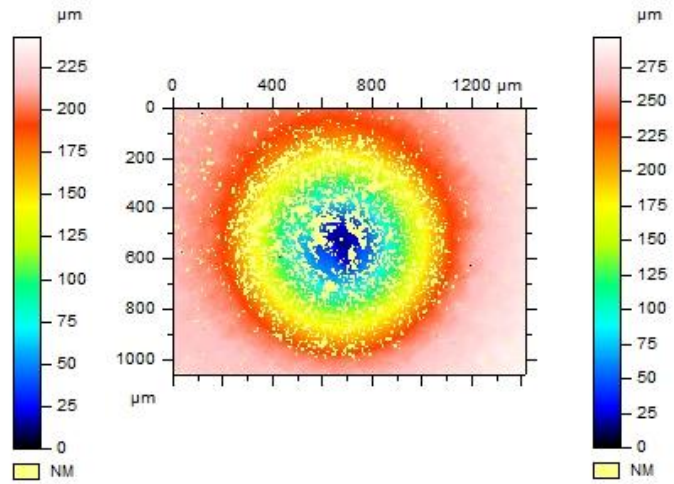
(a) $Rq = 0.06 \mu\text{m}$



(b) $Rq = 0.16 \mu\text{m}$



(c) $Rq = 0.78 \mu\text{m}$



(d) $Rq = 1.27 \mu\text{m}$

Figure 4-17 Defect number 2 on Plates A to D measured using the Zygo

Figure 4-18 shows the comparison of the depth measurement of all defects in the Plates A to D. It is observed that the system performance deteriorates with smooth and specularly reflective surfaces but the system is repeatable in all substrates as the standard deviation is low. It is noted that for the specularly reflective surface with a Rq value of $0.06\ \mu\text{m}$ (Plate D) the Zygo underestimated the height values in all defects with very high repeatability and this is because of poor detectability. For the smallest defect, the Zygo detected the defect precisely in all four substrates with high repeatability of approximately $0.7\ \mu\text{m}$.

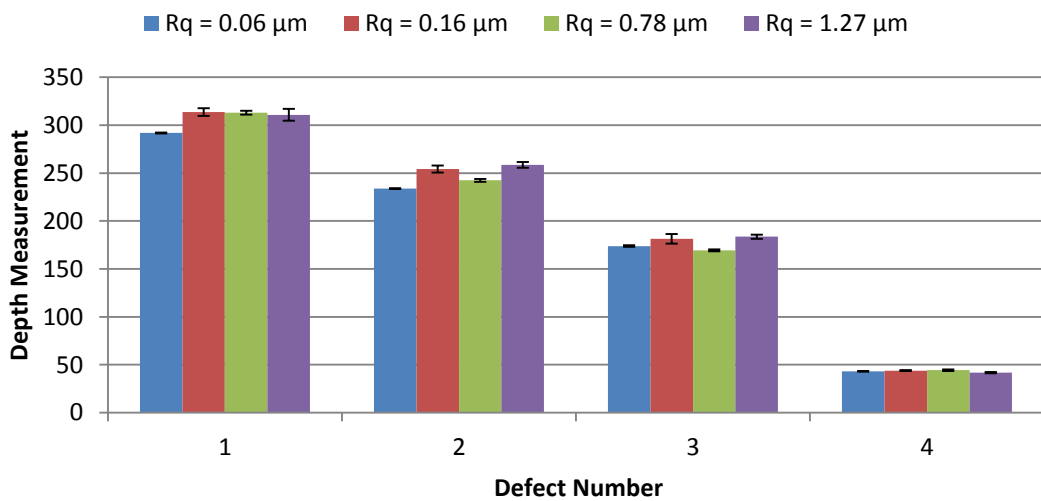


Figure 4-18 Defect depth measurement on different substrates using the Zygo

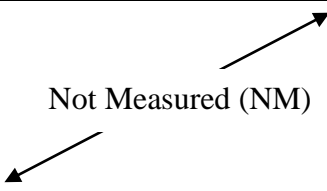
4.4.3 GFM MikroCAD Lite

Table 4-4 highlights the depth measurement of four different defects embedded on all four different substrates with a roughness Rq value ranging from $0.06\ \mu\text{m}$ to $1.27\ \mu\text{m}$ using the GFM equipment. Each defect was measured five times repetitively without changing any of the instrument's parameters to evaluate the functional performance of the instrument.



From the GFM measurement, it is observed that;

- The GFM equipment has a large field of view and hence it captures a large surface area. Figure 4-19 illustrates the measured surface defects using the GFM instrument on each Plate.
- The GFM can detect defects on very specularly reflective surface of $Rq = 0.06 \mu\text{m}$ (Plate D) but the quality of the data is not good. Due to high specularity of the surface, the instrument is not able to obtain height parameters and thus resulting into spurious spikes. This instrument is not effective for quantifying the defects however it may crudely detect surface defects (see Figure 4-19 (a)).
- The biggest defect embedded in Plate C with $Rq = 0.78 \mu\text{m}$ was not captured using the instrument as the substrate was specularly reflective. The instrument produced measurement noise thus 3D data is not available for the defect.
- The instrument was not able to detect the smallest defect of roughly $40 \mu\text{m}$ in all substrates.
- Overall measured repeatability across the set of defects is very poor (See Table 4-4). The measured standard deviation is in the approximate range of $6 \mu\text{m}$ to $15 \mu\text{m}$.
- The data acquisition time of the instrument for each measurement was approximately 1 s to 2 s.
- Data stitching was not required because of the big field of view.





Table 4-4 Defect depth measurement by GFM on Plate A to D

No.of Test	Depth measurement (μm)			
	1	2	3	4
1	Not Measured (NM) 			
2				
3				
4				
5				
Avg				
Std Dev				



(a) $Rq = 0.06 \mu\text{m}$

No.of Test	Depth measurement (μm)			
	1	2	3	4
1	336	299	213	 NM 
2	344	292	224	
3	339	284	213	
4	335	296	209	
5	341	295	217	
Avg	339.0	293.2	215.2	
Std Dev	3.7	5.7	5.7	

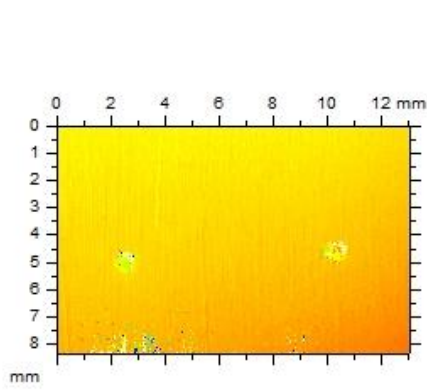
(b) $Rq = 0.16 \mu\text{m}$

No.of Test	Depth measurement (μm)			
	1	2	3	4
1	 NM 	277	165	 NM 
2		269	182	
3		277	185	
4		256	186	
5		263	188	
Avg		268.4	181.2	
Std Dev		9.1	9.3	

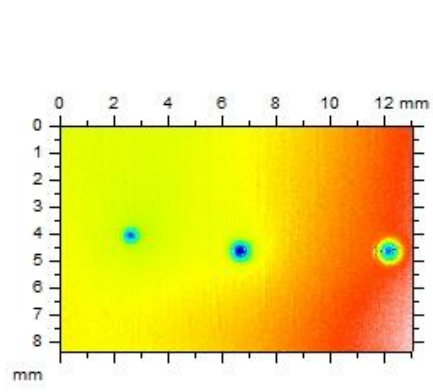
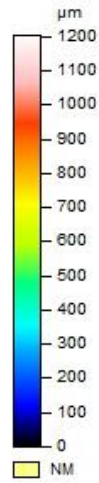
(c) $Rq = 0.78 \mu\text{m}$

No.of Test	Depth measurement (μm)			
	1	2	3	4
1	336	277	187	 NM 
2	330	272	193	
3	338	281	208	
4	343	281	219	
5	331	305	221	
Avg	335.6	283.2	205.6	
Std Dev	5.3	12.7	15.2	

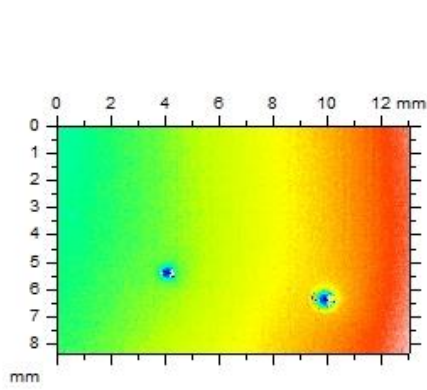
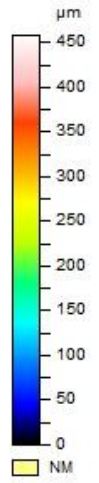
(d) $Rq = 1.27 \mu\text{m}$



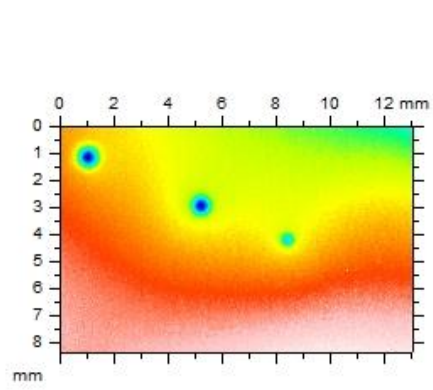
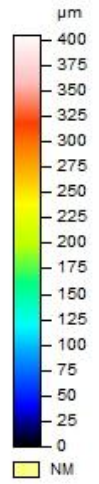
(a) $Rq = 0.06 \mu\text{m}$



(b) $Rq = 0.16 \mu\text{m}$



(c) $Rq = 0.78 \mu\text{m}$



(d) $Rq = 1.27 \mu\text{m}$

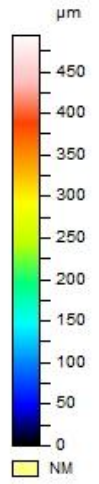


Figure 4-19 Defect number 2 on Plates A to D measured using GFM

Figure 4-20 demonstrates the comparison of the depth measurement of all defects in the four substrates of increasing surface roughness Rq values ranging from $0.06\ \mu\text{m}$ to $1.27\ \mu\text{m}$ respectively. It is observed that the system performance deteriorates with smooth and specularly reflective surfaces. However, the instrument has measured defects on the normal surface that has a roughness of $0.16\ \mu\text{m}$ with a standard deviation of less than $6\ \mu\text{m}$.

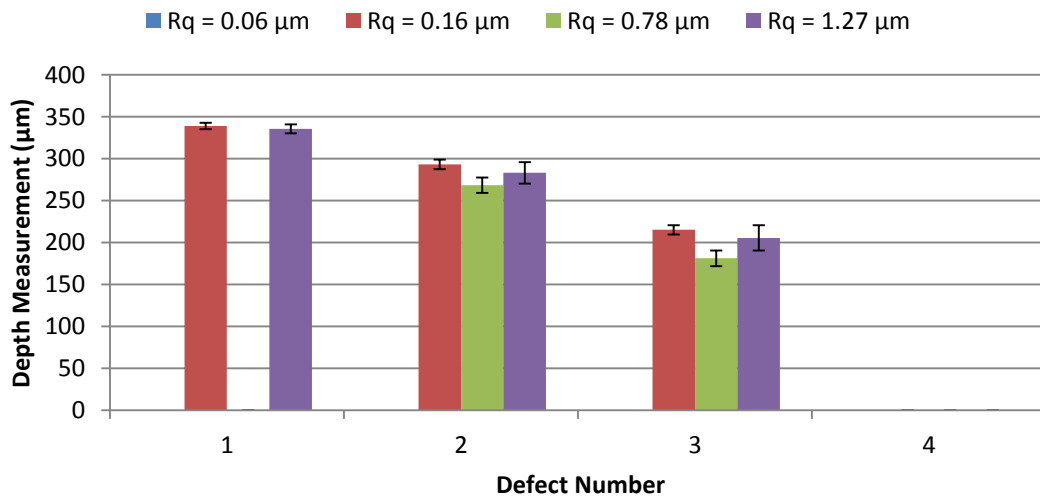


Figure 4-20 Defect depth measurement on different substrates using the GFM

4.4.4 Heliotis H3

Table 4-5 shows the depth measurement of the four different defects embedded on the four different substrates having Rq values ranging from $0.06\ \mu\text{m}$ to $1.27\ \mu\text{m}$ (Plate A to D) using the Heliotis unit. Each defect was measured five times without changing any of the instrument's parameter to evaluate the functional capabilities of the instrument.

From the Heliotis measurement, it can be observed that

- The instrument has obtained 3D data of the surface defects embedded in each of the substrates. Figure 4-21 shows defect number 2 in all substrates measured using the Heliotis.

- The measurement noise occurred in the form of spurious spikes in the majority of the surface however it can be removed using the 2D Gaussian filter.
- The defect on the normal substrate with a roughness value Rq of $0.06\ \mu\text{m}$ (Plate D) was obtained with noise that can be seen in Figure 4-21 (a). Similar observation was made in the defect embedded in the substrate with Rq value of $0.78\ \mu\text{m}$ (Plate C). However, the same defect in the rest of the substrates was obtained with small amount of noise spikes.
- Table 4-5 illustrates that the depth measurement was achieved for all defects with high repeatability in range of $1\ \mu\text{m}$ to $3\ \mu\text{m}$.
- The data acquisition time for each measurement was 1 s to 2 s.
- Data stitching was not required because of big field of view.

Figure 4-22 highlights the comparison of depth measurement of all defects in the four substrates (Plates A to D) having surface roughness Rq values ranging from $0.06\ \mu\text{m}$ to $1.27\ \mu\text{m}$. It is observed that the system overestimates the depth values of defects embedded in the roughest substrate (Plate B). This is due to the subjectivity of profile selection by the user when completing the manual height measurement. Overall, the standard deviation is low in measuring each defect in each substrate. Thus the instrument is highly repeatable (less than $3\ \mu\text{m}$) for each substrate.

Table 4-5 Defect depth measurement by Heliotis on Plates A to D

No of Test	Depth measurement (μm)			
	1	2	3	4
1	324	266	194	50.8
2	321	272	189	49.3
3	320	271	189	55.6
4	321	269	184	52.8
5	324	270	184	50.1
Avg	322.0	269.6	188	51.7
Std Dev	1.9	2.3	4.2	2.5

(a) $Rq = 0.06 \mu\text{m}$

No.of Test	Depth measurement (μm)			
	1	2	3	4
1	320	265	189	45.6
2	318	267	184	44.3
3	318	271	189	45.2
4	319	271	186	46.3
5	319	271	187	44.8
Avg	318.8	269.0	187.0	45.2
Std Dev	0.8	2.8	2.1	0.7

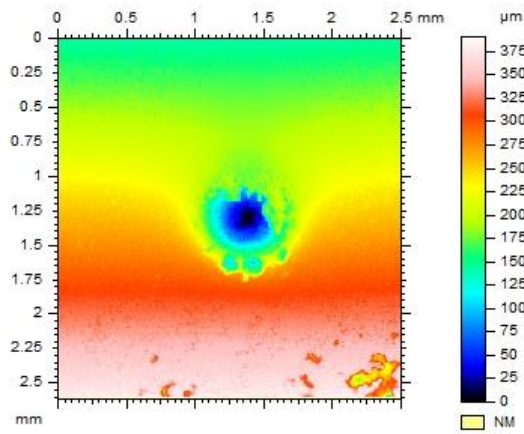
(b) $Rq = 0.16 \mu\text{m}$

No.of Test	Depth measurement (μm)			
	1	2	3	4
1	314	259	177	44.9
2	314	258	179	46.2
3	313	254	178	47.5
4	312	257	176	46.9
5	311	257	176	45.0
Avg	312.8	257.0	177.2	46.1
Std Dev	1.3	1.9	1.3	1.1

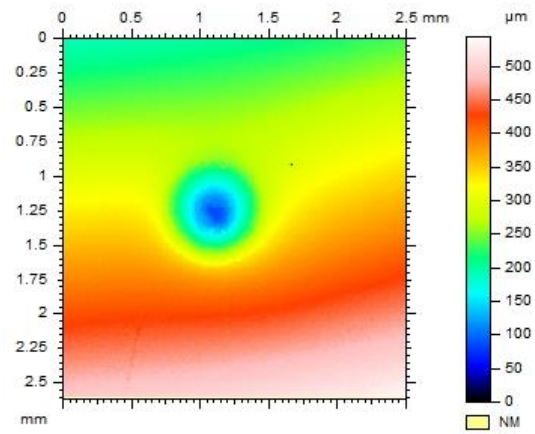
(c) $Rq = 0.78 \mu\text{m}$

No.of Test	Depth measurement (μm)			
	1	2	3	4
1	314	259	177	44.9
2	314	258	179	46.2
3	313	254	178	47.5
4	312	257	176	46.9
5	311	257	176	45.0
Avg	312.8	257.0	177.2	46.6
Std Dev	1.3	1.9	1.3	1.1

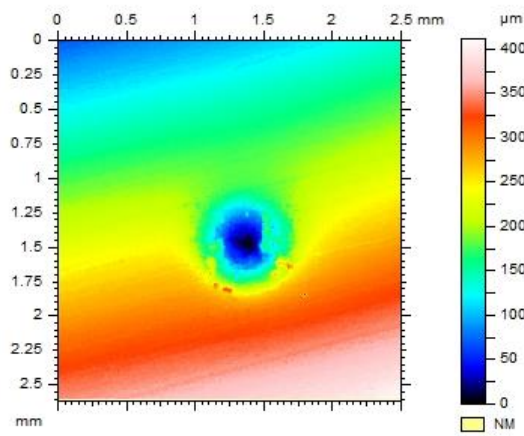
(d) $Rq = 1.27 \mu\text{m}$



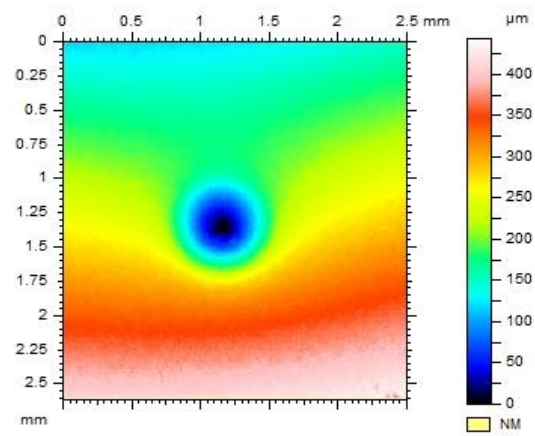
(a) $Rq = 0.06 \mu\text{m}$



(b) $Rq = 0.16 \mu\text{m}$



(c) $Rq = 0.78 \mu\text{m}$



(d) $Rq = 1.27 \mu\text{m}$

Figure 4-21 Defect number 2 on Plates A to D measured using the Heliotis

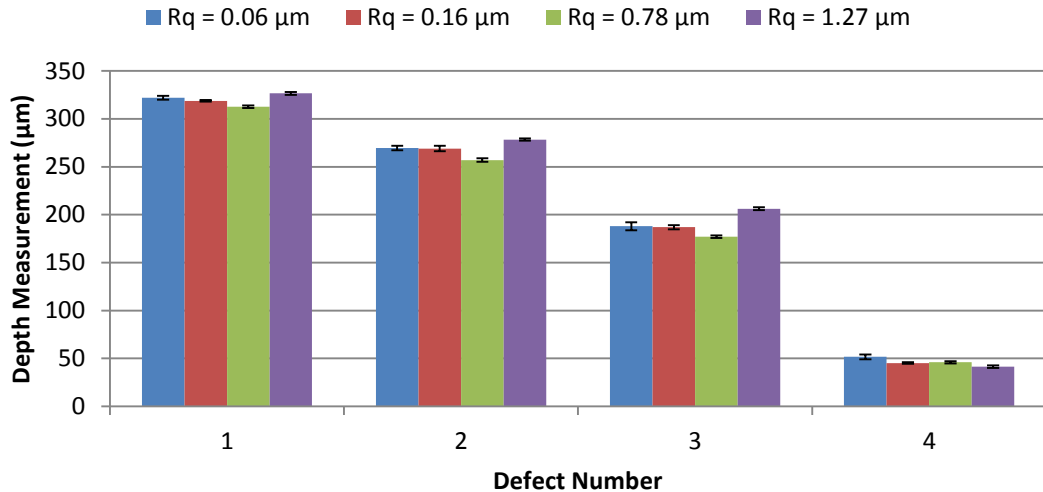


Figure 4-22 Defect depth measurement on different substrates using Heliotis

4.5 Summary

In Section 4.4 each individual instrument was evaluated on four different substrates (Plates A to D) giving the performance characteristics of the instruments. In this section all four optical instruments have been evaluated on a single substrate one by one, to provide an inter-comparison among the four instruments. In order to achieve this, data from Table 4-2, Table 4-3, Table 4-4 and Table 4-5 are rearranged into Table 4-6, Table 4-7, Table 4-8 and Table 4-9 (shown on the following pages).

Table 4-6 and Figure 4-23 illustrates the inter-comparison of the four different instruments measuring the depth of the defects embedded in specularly reflective and smooth flat Plate D (Rq of $0.06\ \mu\text{m}$). The Zygo is repeatable (approximately $0.4\ \mu\text{m}$) across the range of defects however it is also noted that the non-measured data points are very high and thus interpolation is high. The resulting generation of the 3D data of the defect cannot represent the true surface defect. The repeatability of the Zygo is highest among all the instruments but as seen in Figure 4-17 detectability is very low compared to all other instruments.

The repeatability of the Heliotis is approximately $2\ \mu\text{m}$ to $4\ \mu\text{m}$ which is much less than the Alicona. The Alicona system struggles to generate the defect data on the specularly reflective surfaces thus resulting in high standard deviation which can be seen as the one sigma error bars in Figure 4-23. The GFM system is unable to measure any defect

on specularly reflective and smooth surface. In most cases, the Heliotis overestimates and the Zygo underestimates the depth of the defects. However, the measurement of the true value of the depth of the defect is not possible due the lack of defect measurement standard. For a typical substrate, the Heliotis is the obvious choice of instrument for defect measurement due to high repeatability and detectability.

Table 4-7 and Figure 4-24 demonstrates the inter-comparison of the four different instruments measuring the depth of the defects embedded in Plate A ($Rq = 0.16 \mu\text{m}$). Both the Heliotis and the Alicona measured approximately the same depth values in each defect with similar ranges of repeatability ($0.5 \mu\text{m}$ to $3.0 \mu\text{m}$). The GFM measured the depth of the defects higher compared to the other three instruments. This may be due to the measurement noise of the instrument. The repeatability of the Zygo was approximately $4 \mu\text{m}$ which is lower compared to the Alicona and the Heliotis and higher than the GFM.

In Plate A, the Zygo underestimated the depth of the defects compared to other instruments. For the defect measurement embedded in particular this substrate, the Alicona and the Heliotis is capable of measuring small surface defects. If high-speed data acquisition is required then the Heliotis overtakes the Alicona instrument as the measurement time for the Heliotis and the Alicona is 2 s and 18 s respectively. If the requirement for measuring volume is large then the Alicona is a better choice over the Heliotis, because the Alicona provides stitching capability.

Table 4-8 and Figure 4-25 depicts the inter-comparison of the four different instruments measuring the depth of the defect embedded in a flat Plate C ($Rq = 0.78 \mu\text{m}$). In this substrate, both the Heliotis and the Alicona measured approximately the same values for depth measurement in each defect, with the repeatability range of $1.0 \mu\text{m} - 3.0 \mu\text{m}$. However, non-measured data points are observed in the 3D data obtained using the Alicona. The repeatability of the Zygo was higher compared to both the Alicona and the Heliotis but as stated earlier the non-measured data points were significantly high and thus high interpolation was required to fill the voids. Moreover, the measurement time for the Zygo instrument ($40 \text{ s} - 150 \text{ s}$) was higher than all three instruments. The repeatability of the GFM instrument for measuring two defects was approximately $9.0 \mu\text{m}$ and it could not measure the biggest and the smallest defect. This suggests that the Heliotis is overall the most capable instrument among the all instruments.

Table 4-9 and Figure 4-26 shows the inter-comparison of the four different instruments measuring surface defects embedded in a flat Plate B ($Rq = 0.16 \mu\text{m}$). The Alicona system had the highest repeatability across the range of the defects ($1.4 \mu\text{m}$). The repeatability of the Heliotis instrument was in the range of $1.1 \mu\text{m}$ to $1.9 \mu\text{m}$, slightly lower than the Alicona. The GFM system overestimated the depth of the defects with poor standard deviation compare to all other instruments.

Table 4-6 Depth measurement for defects on substrate having $Rq = 0.06 \mu\text{m}$ (Plate D)

No. of Test	Depth measurement of different defects (μm)															
	1				2				3				4			
	Alicona	GFM	Heliotis	Zygo	Alicona	GFM	Heliotis	Zygo	Alicona	GFM	Heliotis	Zygo	Alicona	GFM	Heliotis	Zygo
1	320	↑	324	292	251	↑	266	234	177	↑	194	173	58.2	↑	50.8	43.1
2	309	↑	321	292	283	↑	272	234	184	↑	189	174	56.5	↑	49.3	42.3
3	300	NM	320	292	255	NM	271	234	177	NM	189	173	58.0	NM	55.6	43.6
4	305	↓	321	291	278	↓	269	233	184	↓	184	174	56.5	↓	52.8	43.1
5	303	↓	324	292	258	↓	270	234	189	↓	184	175	57.2	↓	50.1	43.5
Avg	307.4		322.0	291.8	265.0		269.6	233.8	182.2		188	173.8	57.3		51.7	43.1
Std Dev	7.8		1.9	0.4	14.5		2.3	0.4	5.2		4.2	0.8	0.8		2.5	0.4

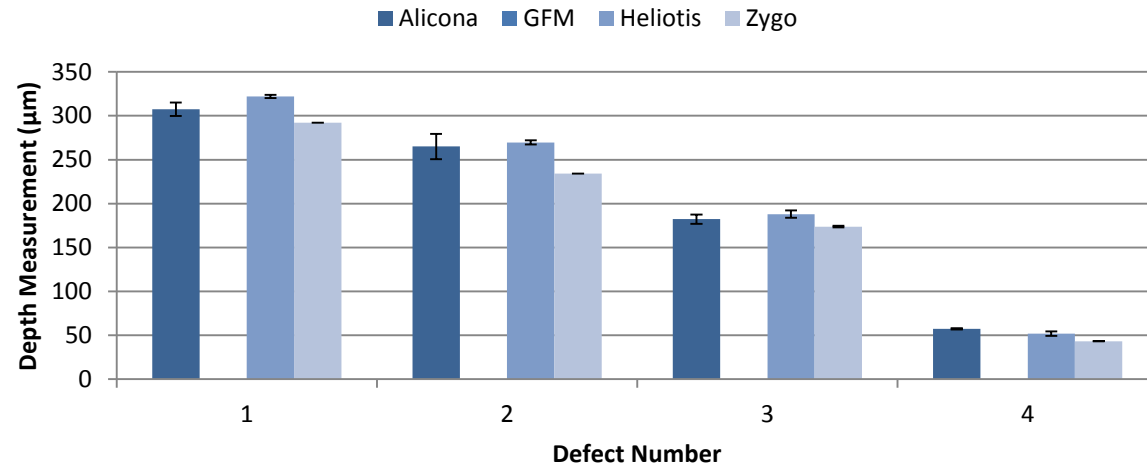


Figure 4-23 Inter-comparison of optical instruments on different defects on Plate D ($Rq = 0.06 \mu\text{m}$)

Table 4-7 Depth measurement for defects on substrate having $Rq = 0.16 \mu\text{m}$ (Plate A)

No. of Test	Depth measurement of different defects (μm)															
	1				2				3				4			
	Alicona	GFM	Heliotis	Zygo	Alicona	GFM	Heliotis	Zygo	Alicona	GFM	Heliotis	Zygo	Alicona	GFM	Heliotis	Zygo
1	311	336	320	315	268	299	265	255	186	213	189	185	47.1	↑	45.6	43.9
2	312	344	318	307	267	292	267	249	191	224	184	188	46.1	↑	44.3	43.8
3	310	339	318	316	264	284	271	259	193	213	189	179	47.0	NM	45.2	44.8
4	312	335	319	317	267	296	271	254	185	209	186	179	46.3	↓	46.3	43.6
5	311	341	319	313	264	295	271	254	193	217	187	176	46.9	↓	44.8	43.3
Avg	311.2	339.0	318.8	313.6	266.0	293.2	269.0	254.2	189.6	215.2	187.0	181.4	46.7		45.2	43.9
Std Dev	0.8	3.7	0.8	4.0	1.9	5.7	2.8	3.6	3.8	5.7	2.1	4.9	0.4		0.7	0.6

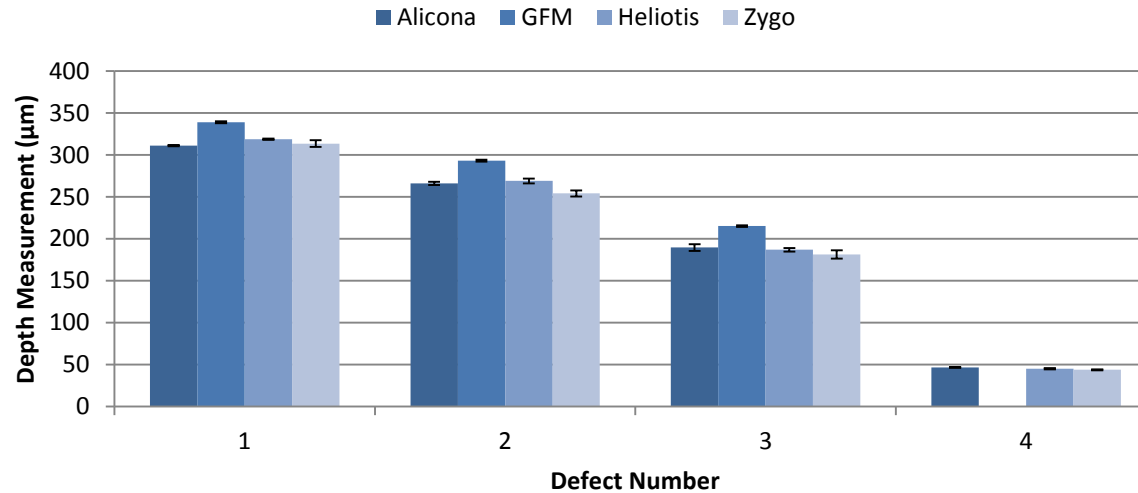


Figure 4-24 Inter-comparison of optical instruments on different defects on Plate A ($Rq = 0.16 \mu\text{m}$)

Table 4-8 Depth measurement for defects on substrate having $Rq = 0.78 \mu\text{m}$ (Plate C)

No. Of Test	Depth measurement of different defect (μm)															
	1				2				3				4			
	Alicona	GFM	Heliotis	Zygo	Alicona	GFM	Heliotis	Zygo	Alicona	GFM	Heliotis	Zygo	Alicona	GFM	Heliotis	Zygo
1	306	↑	314	312	257	277	259	244	173	165	177	169	46.8	↑	44.9	45.1
2	307	↑	314	313	256	269	258	243	171	182	179	169	45.6	↑	46.2	44.5
3	307	NM	313	316	258	277	254	243	174	185	178	169	46.6	NM	47.5	43.2
4	310	↓	312	311	251	256	257	242	173	186	176	171	48.2	↓	46.9	44.1
5	306	↓	311	313	257	263	257	240	177	188	176	169	46.4	↓	45	44.7
Avg	307.2		312.8	313.0	255.8	268.4	257.0	242.4	173.6	181.2	177.2	169.4	46.7		46.1	44.3
Std Dev	1.6		1.3	1.9	2.8	9.1	1.9	1.5	2.2	9.3	1.3	0.9	0.9		1.1	0.7

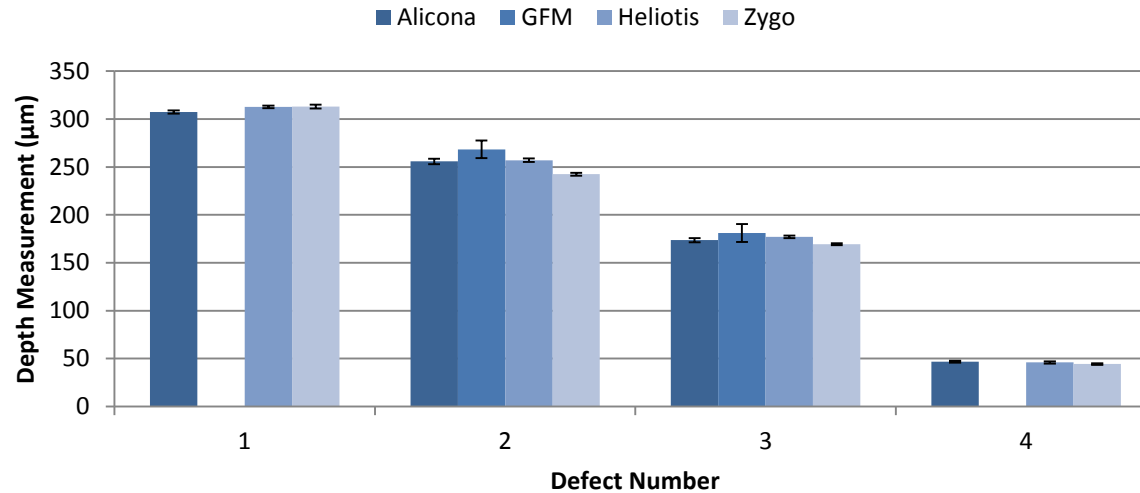


Figure 4-25 Inter-comparison of optical instruments on different defects on Plate C ($Rq = 0.78 \mu\text{m}$)

Table 4-9 Depth measurement for defects on substrate having $Rq = 1.27 \mu\text{m}$ (Plate B)

No. Of Test	Depth measurement of different defect (μm)															
	1				2				3				4			
	Alicona	GFM	Heliotis	Zygo	Alicona	GFM	Heliotis	Zygo	Alicona	GFM	Heliotis	Zygo	Alicona	GFM	Heliotis	Zygo
1	305	336	314	319	260	277	259	259	189	187	177	180	44.5	↑ NM ↓	44.9	42.3
2	307	330	314	312	261	272	258	256	192	193	179	183	44.3		46.2	42.5
3	305	338	313	312	259	281	254	263	191	208	178	186	46.6		47.5	40.7
4	303	343	312	309	263	281	257	259	189	219	176	185	47.2		46.9	41.4
5	305	331	311	302	260	305	257	256	189	221	176	184	44.3		45.0	41.8
Avg	305.0	335.6	312.8	310.8	260.6	283.2	257.0	258.6	190.0	205.6	177.2	183.6	45.4		46.1	41.7
Std Dev	1.4	5.3	1.3	6.1	1.5	12.7	1.9	2.9	1.4	15.2	1.3	2.3	1.4		1.1	0.7

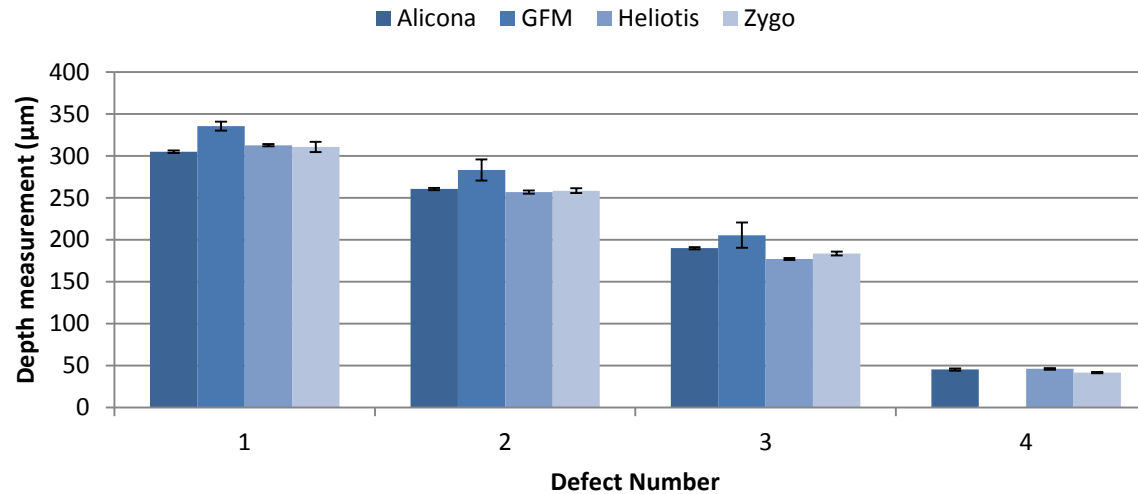


Figure 4-26 Inter-comparison of optical instruments on different defects on Plate B ($Rq = 1.27 \mu\text{m}$)

Table 4-10 summarizes the overall performance characteristics of the four optical instruments derived from the series of experiments detailed in Chapter 4, across the range of defects. In this table, the performance characteristics are ranked from 1 (good) to 4 (poor). In the last row of the Table 4-10, total ranking of each instruments have been derived by summing up ranking for performance characteristics. It can be seen that the Heliotis is a high speed, high accuracy, highly repeatable and robust solution for measuring surface defects.

Table 4-10 Inter-comparison of performance characteristics

Performance Characteristics	Alicona	Zygo	Heliotis	GFM
Technology	FV	CSI	pOCT	DFP
Accuracy	1	4	2	3
Repeatability	2	4	1	3
Detectability	2	4	1	3
Data acquisition	2	3	1	1
Working distance	3	4	2	1
Compactness of system	3	3	1	2
Optics interchangeability	Possible	Possible	Possible	Not possible
Total ranking	13	25	8	13

However, it is noted that the selection of a profile to the lowest point of the defect is a key step in the evaluation the depth of the defect. The selection of a profile is clearly subjective in terms of the operator defining the orientation and the position of the line profile. Defining the the lowest point is also very problematic. In smooth substrates, there is a clear definition of the boundaries of the indented defect. As the surface roughness increases, then defining the boundary conditions becomes more problematic,

with spurious surface peaks and valleys disrupting the boundary conditions. Thus high variation is observed in measuring the depth of the defect. It is fully anticipated that if the single time measured defect is quantified repetitively, the measured repeatability would be very low. It is also noted that each manual measurement typically takes 2 minutes to 3 minutes to complete the quantification process. High ambiguity in the selection process of a line profile and lack of a surface defect measurement standard has triggered the need for an automatic defect detection and quantification algorithm that is high speed, highly repeatable and traceable.

5 DEVELOPMENT OF NOVEL ALGORITHM

5.1 Introduction

Defect quantification is a key element of this research work. Chapter 5 highlights the need of a novel algorithm for defect quantification. Development of a novel algorithm to isolate a defect automatically from the surface is explained in detail. A new approach to measure geometrical parameters automatically such as depth, area and volume of the defect is described which will be used in rest of the study.

5.2 Need for a novel algorithm

In this section two different test methods have been explained to evaluate defect quantification. In test method 1, the determination of the depth of the defect has already been explained in section 4.3.2. Evaluation of the depth of a defect embedded in Plate A was achieved through a line profile created through the deepest point of the defect (Figure 4-14) along cross-section AA'.

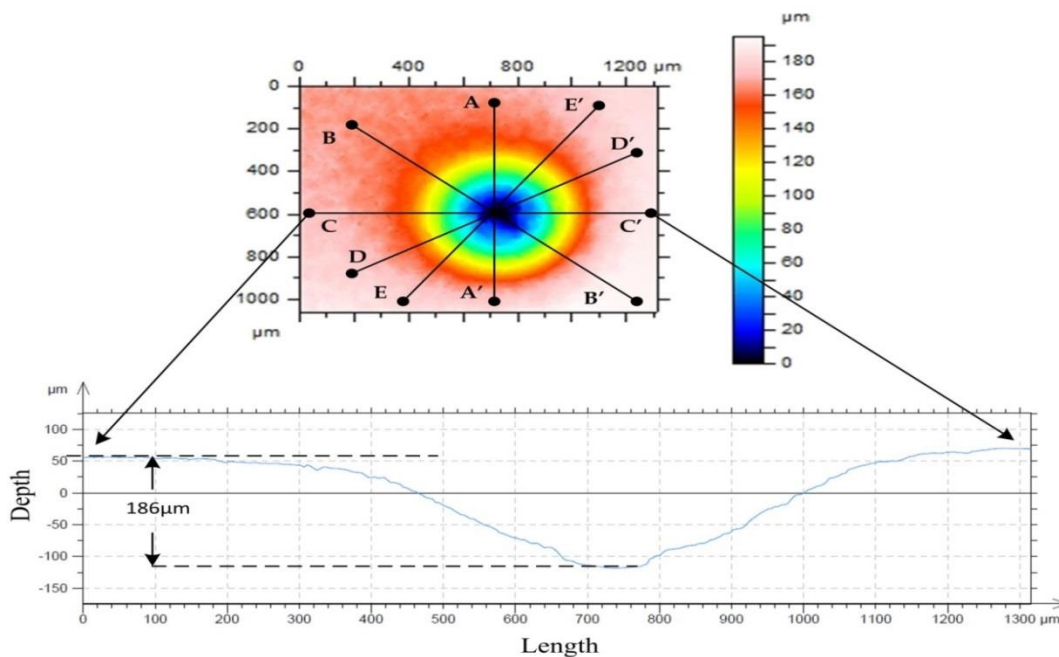


Figure 5-1 Five cross-sections of defect

The subsequent R_t value of 186 μm was illustrated on the line profile although clearly the analysis is subjective in terms of the operator defining the orientation and the position of the line profile. To explain this problem, five different cross sections AA', BB', CC' DD' and EE' have been taken manually, shown in Figure 5-1, at different positions on a single time measured defect embedded on a smooth substrate. Each cross-section was taken at the perceived deepest point of the defect. The visualization of the deepest point was user estimated from the colour variation in the 3D image. However, it is very difficult to determine the true deepest point every single time the cross-section is taken. Individual measured depth of the defect from each cross-section is shown in Table 5-1. It is clearly seen that human analysis introduces variability in the measurement because the standard deviation of the manual depth measurement is 5.6 μm for the average depth of 185.2 μm .

Table 5-1 Manual depth measurement (Test method 1)

Cross-section	Depth (μm)
AA'	186.0
BB'	178.0
CC'	190.0
DD'	181.0
EE'	191.0
Avg	185.2
Std Dev	5.6

Moreover, the DigitalSurf MountainMap software has a toolbox named “Volume of Peak/Valley” which is useful to compute the maximum depth of the valley, top surface area and volume of the valley manually. In this manual test method 2, the user has to determine the boundary of the defect. Once the boundary is obtained, a reference plane is fitted into a selected region for the software to compute the maximum depth, area and volume of the defect. However visually driven manual delimiting of a defect is again subjective and qualitative that leads to repeatability/reproducibility issues and errors in measurement. It is noted that the throat of the defect is not a clearly defined sharp change of slope but a gradual change of slope thus placement of the boundary is difficult. To explain this in detail, a single time measured conical defect using the Zygo NewView 5000 was quantified five times using the MountainMap software.

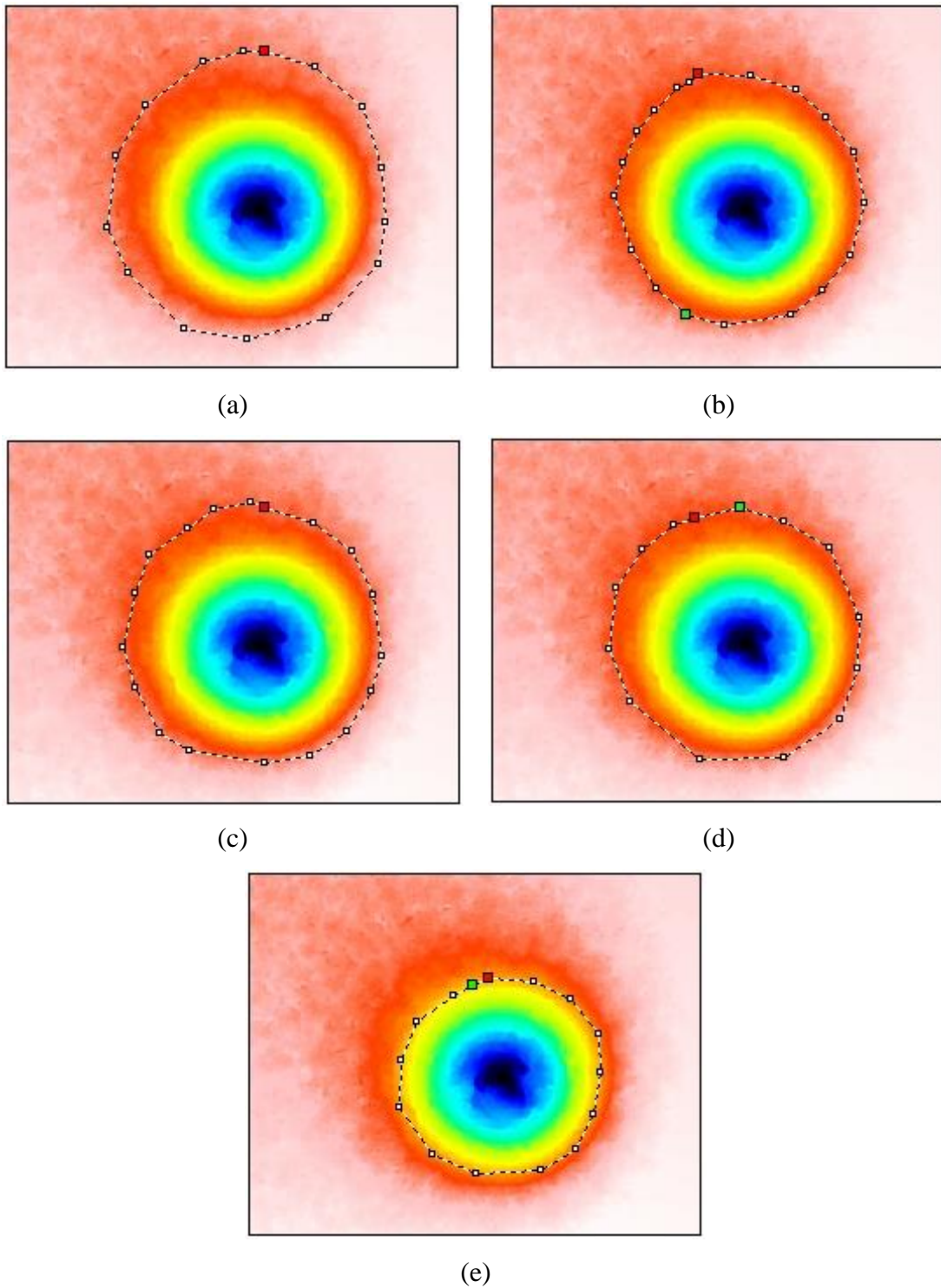


Figure 5-2 Determining the boundary of the defect

The boundary of the surface defect was determined but due to the lack of a standard for isolating the defect, variation was observed in the determination of the boundary of the defect which can be seen in Figure 5-2. Variation in tracing the boundary, a fundamental step for the software to calculate geometrical quantities, leads to variation

in the maximum depth, area and volume measurement which can be seen in Table 5-2. Significant effects of selecting regions (Figure 5-2 (a) to Figure 5-2 (e)) on measurement parameters are well illustrated in Table 5-2.

It can be seen that human analysis introduces variability in measuring geometrical quantities. The standard deviation for depth, area and volume is 13.4 μm , 0.08 mm^2 and 4,194,107 μm^3 respectively. The standard deviation for volume is very high but it is noted that this is due to the units being in micrometre. However, if the unit is converted into millimetre then the standard deviation is 0.0041 mm^3 . This is due to unit conversion and large variation in quantity, the standard deviation is not effective in representing the repeatability. In such a case, a relative standard deviation (RSD) is used to represent the repeatability. RSD is expressed in percentage terms and is obtained by multiplying the standard deviation by 100 and dividing this product by the average value which represents the repeatability [150]. Here the measured RSD values for depth, area and volume measurement are 8.6 %, 22.0 % and 19.8 % respectively. In the rest of the thesis, RSD will be used to represent the repeatability of measurements.

Table 5-2 Manual measurement using MountainMap software (Test method 2)

No. of measurement	Depth measurement (μm)	Area measurement (mm^2)	Volume measurement (μm^3)
a	166	0.52	25,383,759
b	159	0.40	21,362,812
c	162	0.43	23,000,530
d	158	0.41	21,889,223
e	132	0.27	14,191,377
Mean	155.4	0.4	21,165,540
Std Dev	13.4	0.08	4,194,107
%RSD	8.6	20.0	19.8

Furthermore, the manual method for measuring defects (explained in section 4.3.2), measures the average defect depth of 185.2 μm (Table 5-1) with a standard deviation of 5.6 μm and RSD of 3.0 %. Using MountainMap's inbuilt tool measures the same conical defect with a depth of 155.4 μm with the standard deviation of 13.4 μm , and RSD of 8.6 % (Table 5-2). Thus, major differences are observed for the measurement of the same defect using two different manual methods. Hence, in both measurement

methods, the repeatability is poor and the result of depth is inconsistent. Moreover, if both methods are repeated again by the same operator, the probability of achieving the same numbers as shown in Table 5-1 and Table 5-2 is low due to the position of the selected cross section and delimiting the defect boundary may differ.

Due to the lack of measurement standard, if the same defect is measured by different operators, results may vary. To illustrate this, two skilled operators were selected to measure the depth, area and volume of the same defect using both of the above methods. Both users have more than 20 years of experience in the field of metrology.

By very careful inspection, each user took the cross-section at the deepest point, however, both struggled to define the deepest point. Each user took five cross-sections and Table 5-3 illustrates the manual depth measurement derived from those cross-sections. It can be seen that User 1 derived the depth of 184.8 μm with a standard deviation of 10.7 μm , User 2 measured the depth of 189.8 μm with a standard deviation of 7.7 μm . In Table 5-1 the depth of the same defect was measured of 185.2 μm with a standard deviation of 5.6 μm . Thus the reproducibility is very low.

Table 5-3 Depth measurements by expert users using Test method 1

No.of Exp.	Depth (μm)	
	User 1	User 2
1	170	194
2	190	188
3	179	177
4	187	195
5	198	195
Mean	184.8	189.8
Std Dev	10.7	7.7
% RSD	5.8	4.1

Table 5-4 represents the depth, area and volume measurement derived using MountainMap software (Test method 2) achieved by both expert users. In this method, both users evaluated the boundary of the defect by looking for the change in colour because the colour-map represents the height in 3D data. The standard deviation for depth measurement for User 1 was almost double that of User 2 (6.19 μm). User 2 measured a RSD value for volume measurement of 6 % which was almost half of what

User 1 measured. User 1 derived a RSD of 5 % for area measurement, half of the value for User 2. In Table 5-2, the measured average depth was 155.4 μm using Test method 2. Using the same Test method 2, User 1 and User 2 measured average depths of 172.6 μm and 169.4 μm respectively (Table 5-4).

Table 5-4 Manual measurement by expert users using Test method 2

No.of Exp.	User 1			User 2		
	Depth μm	Area mm^2	Volume μm^3	Depth μm	Area mm^2	Volume μm^3
1	168	0.53	25,261,942	164	0.44	22,709,235
2	168	0.55	25,727,821	170	0.55	25,641,474
3	171	0.59	27,054,188	170	0.54	25,645,364
4	173	0.59	27,196,991	172	0.57	26,796,127
5	183	0.60	33,814,177	171	0.53	25,361,550
Mean	172.6	0.6	27,811,023.8	169.4	0.5	25,230,750
Std Dev	6.19	0.03	3,457,789.65	3.13	0.05	1,513,782.57
% RSD	3.6	5.0	12.4	1.8	10.0	6.0

From Table 5-1, Table 5-2, Table 5-3 and Table 5-4, it is clearly observed that due to the lack of a defect measurement standard, repeatability and reproducibility of manual measurement is significantly low. The quantification of the defect using manual methods is inconsistent leading to high ambiguity. Moreover, it should not be underestimated how long this process can take especially when a surface defect is masked by significant surface roughness. Usually, for all users, it takes approximately 3 minutes to 4 minutes to characterise a single defect embedded in the surface by manual measurement methods.

Hence there is a clear need for an automatic system that detects, isolates and quantifies the surface defect automatically in 3D. To this end, a novel algorithm which is a complete mathematical solution based upon a quantitative approach is developed. The work reported in the rest of this chapter explains the development of the novel algorithm to quantify the surface defect automatically in 3D.

5.3 Implementation of algorithm

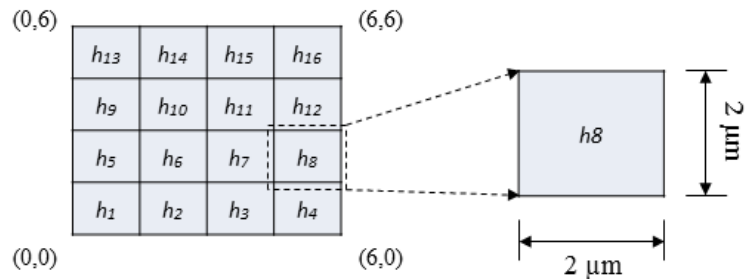
The following section explains the devised methodology to quantify the surface defect in 3D. The novel algorithm for quantification of the defect is developed using MATLAB R2012b [151]. MATLAB is a programming environment for algorithm development, data analysis, visualisation and numerical computation. The author has used MATLAB's in-built Image Processing Toolbox that provides a comprehensive set of reference-standard algorithms to develop the novel algorithm.

5.3.1 Data re-arrangement

Data manipulation is relatively straight forward if the data is in matrix form. 3D measuring instruments typically provide discrete point cloud data of the scanned objects in three column vectors that representing the x , y and z position of each point in the space. The first and second column vector represents the position of a point in x and y position respectively, while the third column vector provides height information of the point at a particular x and y position. After inspecting 3D data, it is realised that the x and y position is increasing at approximately constant interval that can be useful to determine the actual lateral resolution of a 3D measurement system and pixel size. Thus, the measured data which is in the form of column vectors can be converted into matrix form that represents the height level at each pixel level. The validation of this matrix conversion can be made by checking the size of the matrix that should be equivalent to measuring instrument's camera pixel array size.

x (μm)	Y (μm)	Z (μm)
0	0	h_1
2	0	h_2
4	0	h_3
6	0	h_4
0	2	h_5
2	2	h_6
4	2	h_7
6	2	h_8
0	4	h_9
2	4	h_{10}
4	4	h_{11}
6	4	h_{12}
0	6	h_{13}
2	6	h_{14}
4	6	h_{15}
6	6	h_{16}

(a)



(b)

(c)

Figure 5-3 3D data arrangement (a) 16 x 3 matrix (b) 4 x 4 matrix (c) size of a pixel

To explain this data re-arrangement in detail, let it be assumed that an arbitrary matrix size of 16 x 3 is the output of a 3D measuring instrument that has a lateral resolution of 2 μm and camera pixel array of 4 x 4 (See Figure 5-3(a)). In this matrix, the first and second column vector represents a point in the x and the y direction respectively and the third column vector illustrates the height value h at a particular x - y position. With careful inspection, it can be observed that initially x is increasing from 0 μm to 6 μm with a step size of a resolution (2 μm) while the value of y remains 0. Thus four discrete points are obtained in x direction with height values of h_1 to h_4 as seen in Figure 5-3(b).

Once these four points are obtained then the y value increases from 0 μm to 2 μm and the x value is reset to 0 μm thus h_5 is placed. Again the value of x is increasing from 0 μm to 6 μm with a step size of the resolution while the value of y remains at 2 μm . This cycle will repeat until it reaches the last point.

If the data is arranged in this pattern then the data can be re-arranged in a height distributed matrix that can be seen in Figure 5-3(b). It can be seen that h_1 to h_4 are placed in the x direction as the y value for each point is 0 μm , while at h_5 the y value increases from 0 μm to 2 μm and the x value becomes 0 μm . Similarly the y value increases from 2 μm to 4 μm and from 4 μm to 6 μm for h_9 and h_{13} respectively while

the x value is reset to the original x position. Thus a height distributed matrix can be achieved. The data that was originally in the form of 16×3 size matrix is converted into a 4×4 matrix. The size of the re-arranged matrix is equal to the size of the camera array of the 3D measuring instrument which is 4×4 . The dimensional size of each matrix cell is $2 \mu\text{m} \times 2 \mu\text{m}$. Once the data is in height distributed matrix form, it is convenient to do further data analysis. To simplify the computational process, in the entire study, the point cloud data acquired from 3D instrument has been arranged in height distributed matrix form.

5.3.2 Filtration Techniques

Instrument noise is always present in acquired data from any 3D measurement instrument. It is typically a small random error superimposed on the measured data. Internal noise can be due to electronic noise such as amplifier or optical noise such as stray light. Ambient light or a power cable near the instrument can also cause noise. It is important to remove such noise before assessment of surface topography.

Filtration is one of the core elements of analysis tools in geometrical metrology. It is the means by which the information of interest is extracted from the measured data for further analysis [87,88]. Filtration techniques are employed in surface metrology to separate the roughness components from the waviness components and form components, so that suitable characterization parameters can be applied [85,86]. They also serve in dimensional metrology for data smoothing to remove noise. In such a manner, noise is removed by filters before fitting routines are applied to generate the geometry of measurand [89].

Filtering characteristics and parameters required for surface texture profile analysis have been developed over many years with specifications already defined within a number of ISO documents (ISO 4287, ISO 11562, ISO 16610) [90,92,152].

The S-filter which is defined in ISO 25178-3 [153] is implemented using the areal Gaussian filter that produces a smooth surface free from unwanted small-scale components of the measured surface. The smooth surface contains form and waviness. To remove these components the F-operator which is also defined in ISO 25178-3 [153] is implemented using an areal robust Gaussian regression (RGR) filter which is

currently under an ISO draft specification [97]. Both filters are explained in detail in the following section.

5.3.2.1 Noise removal – Gaussian filter

The S-filter is implemented using an areal Gaussian filter which is a low pass filter that removes high frequency components such as unwanted measurement noise, spikes or functionally irrelevant small features. There are other low pass filters available such as the Butterworth filter and the Chebyshev filter, however, in the field of metrology the Gaussian filter is widely used. Here, the Gaussian smoothing operator is a two dimensional (2D) convolution operator. The 2D Gaussian filter is simply the product of two individual one dimensional (1D) Gaussian filters (one for each direction) and is expressed as,

$$S(x, y) = \frac{1}{2\pi\sigma^2} e^{-\left(\frac{x^2+y^2}{2\sigma^2}\right)} \quad (1)$$

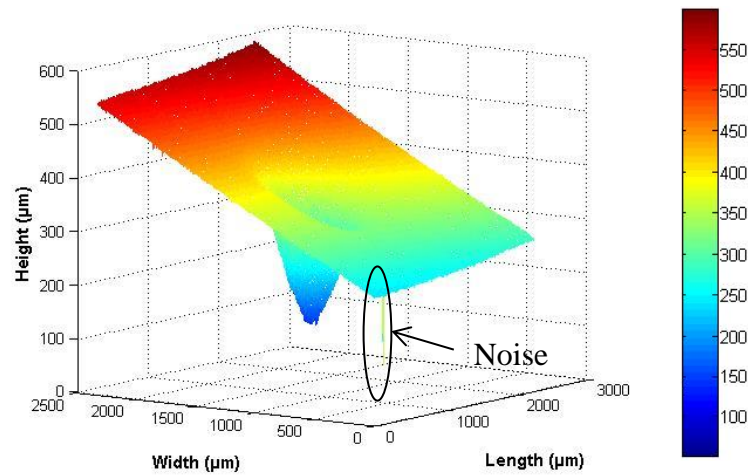
Where, $S(x, y)$ is a two dimensional Gaussian function, σ is a variance of Gaussian filter, x is a distance from the origin in the horizontal axis, y is a distance from the origin to vertical axis.

$S(5,5) =$

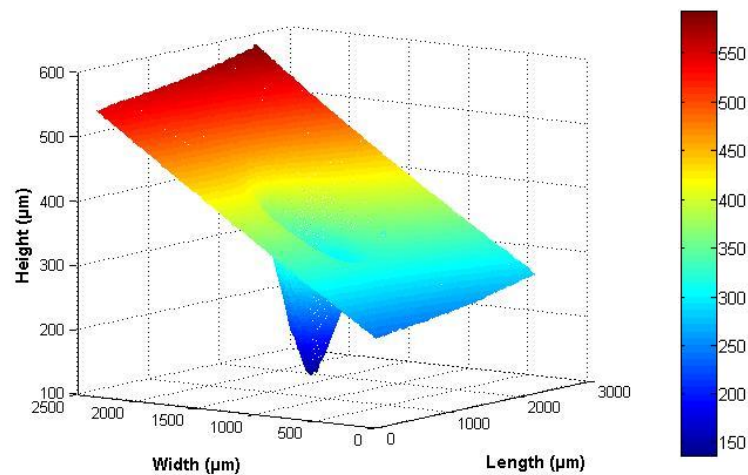
0.003	0.013	0.021	0.013	0.003
0.013	0.059	0.098	0.059	0.013
0.021	0.098	0.162	0.098	0.021
0.013	0.059	0.098	0.059	0.013
0.003	0.013	0.021	0.013	0.003

Figure 5-4 Gaussian 5 x 5 kernel matrix

The Gaussian filter works by using the 2D distribution as a point-spread function. This is achieved by convolving the 2D Gaussian distribution function with the measured data. Each pixel's new value is set to a weighted average of that pixel's neighbourhood. The original pixel's value receives the heaviest weight and neighbouring pixels receive smaller weights as their distance to the original pixel increase and these results into a surface free from high frequency components. In this work, the size of the convolution matrix was kept to 5 x 5 and variance was chosen as 1.0 for this study and matrix values can be seen in Figure 5-4. The selection of the kernel size and variance was based on trial and error method in the context of recognising kernel coefficient values with respect to the Gaussian distribution. MATLAB inbuilt function was used to develop this filter.



(a)



(b)

Figure 5-5 Conical defect in Plate A (a) raw data (b) smooth surface

Figure 5-5 (a) shows the raw data of a conical defect embedded in Plate A ($Rq = 0.16 \mu\text{m}$) with unwanted noise, measured using the Heliotis H3 unit. The raw data is processed using the Gaussian filter and unwanted spikes are removed and the filtered surface is generated as seen in Figure 5-5 (b). It is noted that, in the context of this study, quantification of the noise in terms of frequency is not achieved and it is recommended for the future work so that bespoke low pass filters can be implemented to remove the unwanted noise more precisely. A MATLAB inbuilt function “conv” was used to develop this filter

As shown in Figure 5-5 (b), the defect is embedded into the surface of the plate but consists of form and tilt. To determine the boundary of the defect effectively, it is important to remove the form and the tilt components from the surface.

5.3.2.2 Surface fitting – Robust Gaussian regression filter

Functionally and geometrically complicated surfaces appear as the output of modern product manufacturing technologies. In response to these new developments, filtration techniques are required to be robust to deal with complex geometry and reliable across whole range of measurement data. These motivations bring out a set of robust filtration techniques, most of which are presented in ISO 16610 [152], including a Robust Gaussian Regression (RGR) filter, robust spline filters and morphological filters.

Early research work has been completed on a RGR for areal surface analysis [94]. Various surfaces such as cylinder surfaces, spherical surfaces and typical structured surfaces with complex geometry have been successfully studied for areal surface analysis using RGR filter [154] and thus the idea of using this filter is adopted in this work.

The main purpose of a RGR filter is to generate the mean surface that follows the geometrical form component of the surface. Once the mean surface is generated, assessment of surface topography becomes much easier. As explained in Section 2.3.3, measured 3D datasets consist of two major components: the roughness of the surface and geometrical form of the surface. Typically high frequency components in a measured surface represent the roughness of the surface while low frequency components represent the geometrical form component. Using a Fourier transform,

measured 3D data is converted into the frequency domain. Spectral analysis of the 3D data gives two main frequency components available in the measured 3D data sets. Among the two main frequencies, the higher frequency is related to roughness of the surface while the lower frequency component represents the frequency of geometrical form of the surface. The lowest frequency is selected as the cut-off frequency in order to generate the mean surface that follows the geometrical form of the surface.

This work has used a RGR filter as a tool and its brief summary is explained as follows,

Let $z(\xi, \eta)$ and $w(x, y)$ be the measured surface that contains form and the filtered mean surface defined over the measurement interval $0 \leq x \leq lx, 0 \leq y \leq ly$ respectively. The general model of the areal Gaussian regression filter can be described by the following minimization problem [94],

$$\int_0^{ly} \int_0^{lx} \rho(r)(z(\xi, \eta) - w(x, y)) \cdot s(\xi - x, \eta - y) d\xi d\eta \Rightarrow \text{Min } w(x, y) \quad (2)$$

where

$\rho(r)$ is error metric function of the estimated residual

$(z(\xi, \eta) - w(x, y))$ is error between the measured surface $z(\xi, \eta)$ and the filter mean curve $w(x, y)$

$s(\xi - x, \eta - y)$ is a local variant weighting function of the Gaussian filter.

$s(x, y)$ is the Gaussian weighting function over the interval of $0 \leq x \leq lx, 0 \leq y \leq ly$ and it is defined by equation (3) below with x, y being the spatial co-ordinates in two orthogonal directions respectively,

$$s(x, y) = \left(\frac{1}{\alpha^2 \lambda_{cx} \lambda_{cy}} \right) \exp \left[-\pi \left(\frac{x}{\alpha \lambda_{cx}} \right)^2 - \pi \left(\frac{y}{\alpha \lambda_{cy}} \right)^2 \right] \quad (3)$$

where

$\lambda_{cx}, \lambda_{cy}$ being the cut-off wavelengths in x and y directions respectively,

$\alpha = \sqrt{\log 2/\pi} = 0.4697 \dots$, which make the 50% amplitude transmission characteristics at the cut-off wavelength.

By the zeroing of the partial derivatives in the direction of $z(\xi, \eta)$ the mean surface $w(x, y)$ can be obtained by solving the following linear equation iteratively over the interval $0 \leq x \leq lx, 0 \leq y \leq ly$:

$$A^{(k-1)}(x, y)w^{(k)}(x, y) = F^{(k-1)}(x, y), \quad k = 1, 2, \dots, 0 \leq x \leq lx, 0 \leq y \leq l \quad (4)$$

where,

$$A^{(k-1)}(x, y) = \int_0^{ly} \int_0^{lx} \delta^{(k-1)}(\xi, \eta) s(\xi - x, \eta - y) d\xi d\eta \quad (5)$$

$$F^{(k-1)}(x, y) = \int_0^{ly} \int_0^{lx} \delta^{(k-1)}(\xi, \eta) z(\xi, \eta) \cdot s(\xi - x, \eta - y) d\xi d\eta \quad (6)$$

k is the iteration step.

The mean surface $w(x, y)$ can be solved linearly by,

$$w(x, y) = \frac{F(x, y)}{A(x, y)} = \frac{\int_0^{ly} \int_0^{lx} z(\xi, \eta) s(\xi - x, \eta - y) d\xi d\eta}{\int_0^{ly} \int_0^{lx} s(\xi - x, \eta - y) d\xi d\eta} \quad (7)$$

Figure 5-6 shows the filtered data of a conical defect in Plate A ($Rq = 0.16 \mu\text{m}$) and is then processed using implemented second order RGR filter. Figure 5-6 (a) is a smooth surface, Figure 5-6 (b) shows the mean surface generated using the second order RGR filter which is fitted through the smooth surface. To demonstrate the effectiveness of filtration process cross-section AA' is taken from the filtered surface and the mean surface. Figure 5-6 (c) shows the two selected horizontal cross-sectional profiles of the filtered surface and the mean surface.

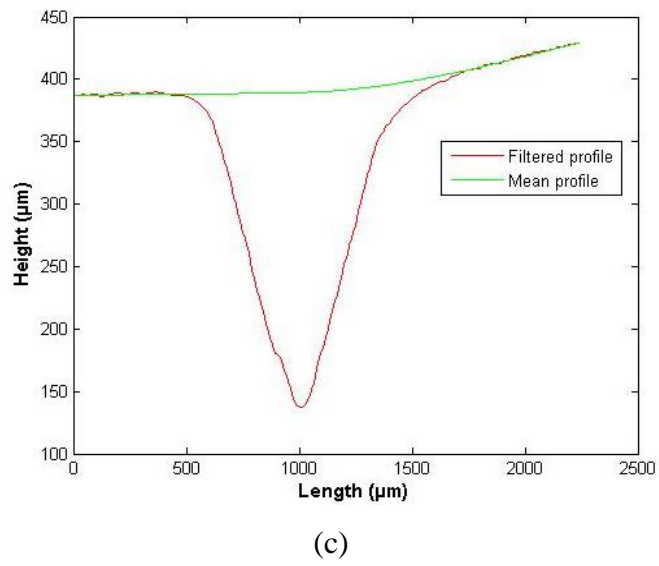
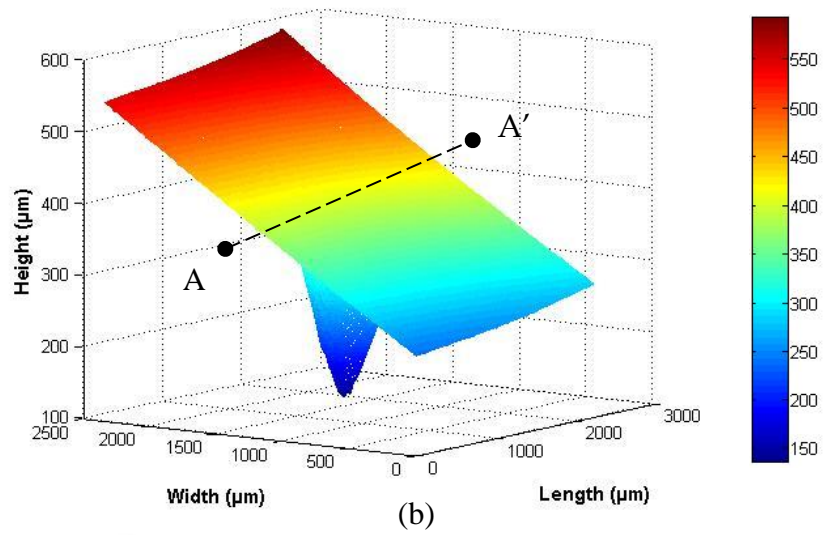
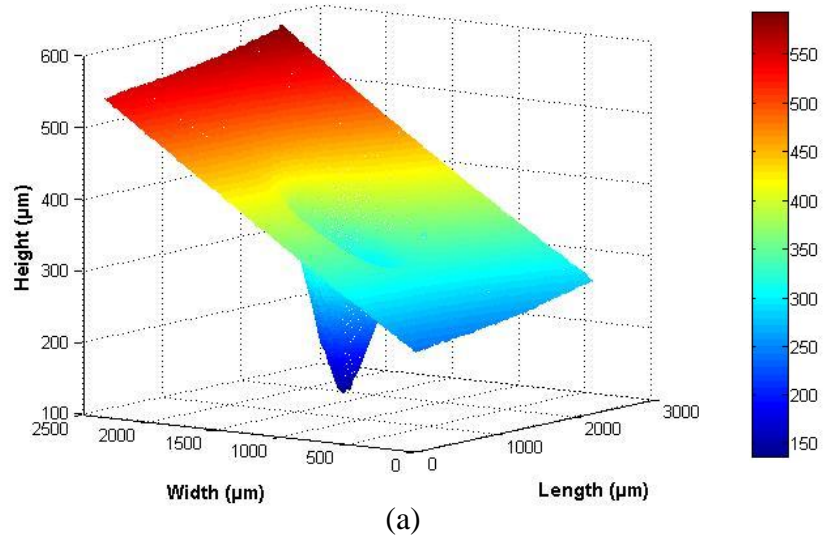


Figure 5-6 Defect in Plate A (a) Filtered surface (b) Mean surface (c) Two profiles

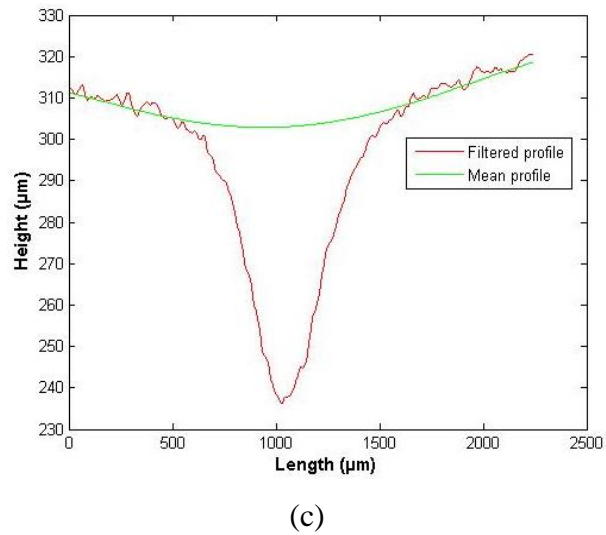
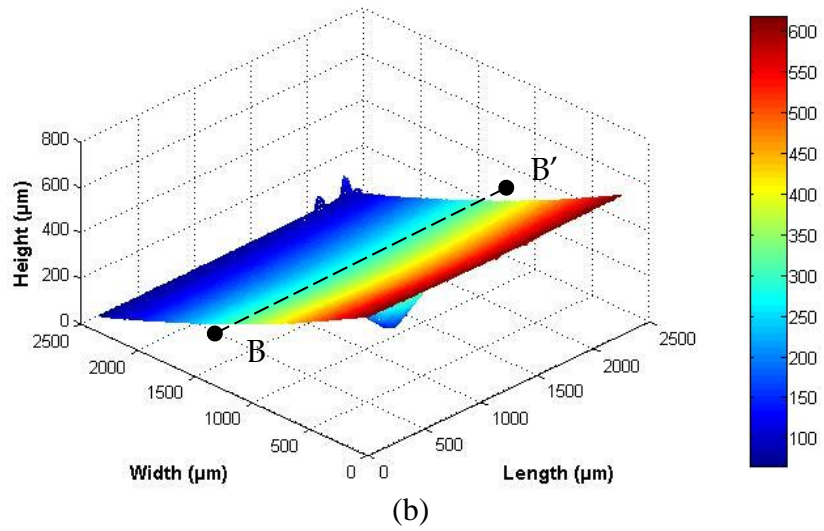
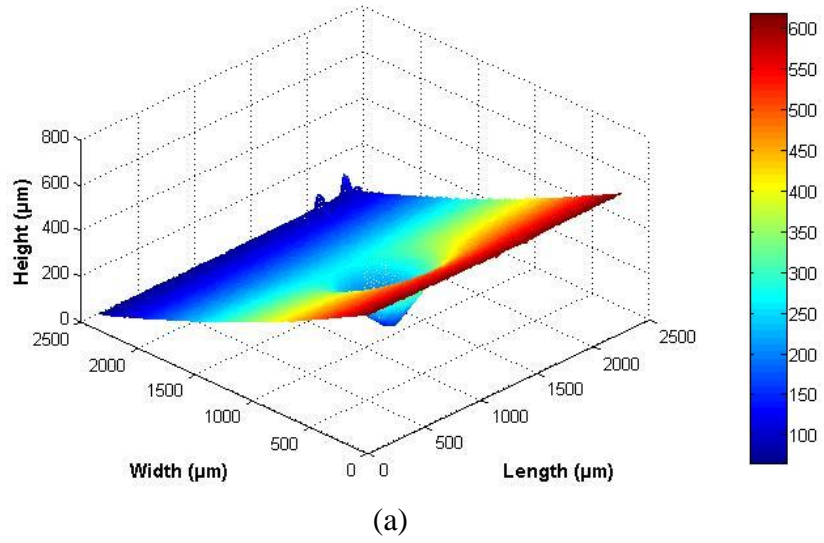


Figure 5-7 Defect in double curvature plate (a) Filtered surface (b) Mean surface (c) Two profiles

Figure 5-7 shows the filtered data of a conical defect in the double curvature plate ($Rq = 1.27 \mu\text{m}$) and then processed using the second order RGR filter. Figure 5-7 (a) is a smooth surface, Figure 5-7 (b) illustrates the mean surface generated using the second order RGR filter that is fitted through the smooth surface. To highlight the effectiveness of the filtration process, a cross-section BB' is taken from the filtered surface and the mean surface. Figure 5-7 (c) shows the two horizontal cross-sectional profiles of the filtered surface and the mean surface.

From Figure 5-6 and Figure 5-7 it is clear that, the second order robust Gaussian regression filter follows the form components and generates the mean surface effectively.

5.3.2.3 Residual surface extraction

The residual surface is very important for better surface texture and special feature assessment as the residual surface is noise free and form free. Once the mean surface is generated using RGR filtering, it is relatively straight forward to extract the residual surface. The residual surface is obtained by removing the mean surface from the filtered surface by matrix subtraction. Figure 5-8 shows the residual surface of the conical defect in the Plate A ($Rq = 0.16 \mu\text{m}$).

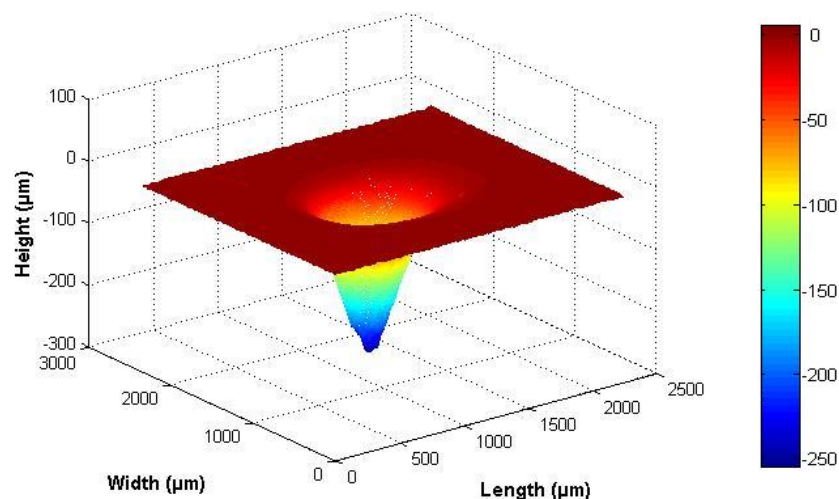


Figure 5-8 Residual surface

It can be seen in Figure 5-8 that the form and the tilt that was present in the filtered surface (Figure 5-5 (b)) is now completely removed by subtracting the mean surface (Figure 5-6 (b)) from the smooth surface.

5.3.3 Thresholding

Once the residual surface is generated it is important to trace the boundary of the surface defect and 3D data portions for later dimensional calculations. In human-visual inspection, the defect boundary is defined as the change of surface height on the 3D data. There are several techniques to determine boundary such as edge detection [155] and thresholding [156] in image processing. However the application of edge detection in 3D is less explored. Due to surface roughness, edge detection using gradient operators in 3D is more complex and hence thresholding methods have been adapted to define the defect region. In the thresholding process, the residual surface data are converted into a binary image. One of the key issues in the conversion of the residual surface data into a binary image is the determination of its threshold value.

In computer vision and image processing, Otsu's method is commonly used to automatically perform histogram based image thresholding [114]. Kong *et al* adopted Otsu's method for extracting the boundaries of a microlens surface profile in 3D from the binary image. 3D data was acquired measured using CSI [113].

Otsu's method reduces the between-class variance which is defined by equation (8),

$$\sigma_w^2(t) = w_1(t)\sigma_1^2(t) + w_2(t)\sigma_2^2(t) \quad (8)$$

where, weights w_i are the probabilities of the two classes separated by a threshold t and σ_i^2 variances of these classes. Using Otsu's method, the binary image of the residual surface (see in Figure 5-8) is obtained as seen in Figure 5-9. Otsu's method computes the threshold value here as 0.47 μm .

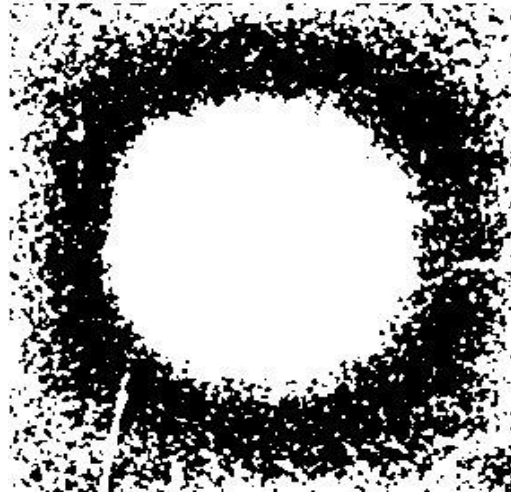


Figure 5-9 Binary image of the defect in Plate A using the Otsu's method

In the thresholded image, black pixels represent the region above the threshold value and white pixels represent the region below the threshold value. The white pixels are regions of interest for the quantification of the defect. The main reason behind performing thresholding is to derive the boundary of the defect. From Figure 5-9, it is computationally very difficult to determine the boundary of the defect due to ambiguity in the white pixels region. Ironically, the human eye/brain is very adapt at performing this operation in a subjective manner. To illustrate this issue, the binary image of the smallest conical defect embedded in the Plate B ($Rq = 1.27 \mu\text{m}$) is obtained using Otsu's method (Figure 5-10). Otsu's method computes the thresholding value of $0.46 \mu\text{m}$. It is clearly seen from Figure 5-10 that Otsu's method is unable to obtain the thresholding value that can isolate the defect region from the surface. Here, the roughness elements of the surface are the reason that Otsu's method is not effective to determine the defective region.

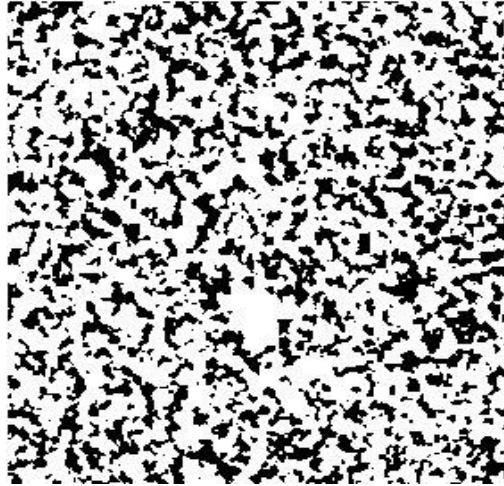


Figure 5-10 Binary image of the defect in Plate B using Otsu's method

To overcome this problem, a new approach that incorporates the roughness of the surface is adopted to achieve the thresholding. To set the thresholding value for the determination of the defect boundary, an assumption is made here that if the defect region is neglected, a sum of area of profile portion above the mean surface is approximately equal to sum of area of profile portion below the mean surface. An area of a profile portion is calculated by summing all the height values of pixels that cover the profile portion which is equal to average peak values. Once the area of a profile portion above the zero line is calculated, the threshold value T is calculated using equation (9)

$$T = \frac{H_p + H_n}{N_p + N_n} \quad (9)$$

where,

H_p is the sum of absolute positive height values

H_n is the sum of absolute negative height values except defect region

N_p is the total number of pixels that have absolute positive height values.

N_n is the total number of pixels that have absolute negative height values except defect region.

But if $H_p = H_n$ and consequently $N_p = N_n$ then equation (9) can be rewritten as below,

$$T = \frac{H_p}{N_p} \quad (10)$$

Using equation (10), a threshold value for the residual surface in Figure 5-8 was calculated as 1.68 μm and a binary image is produced as seen in Figure 5-11. The region of interest (white pixels region), is obtained with a definite boundary.

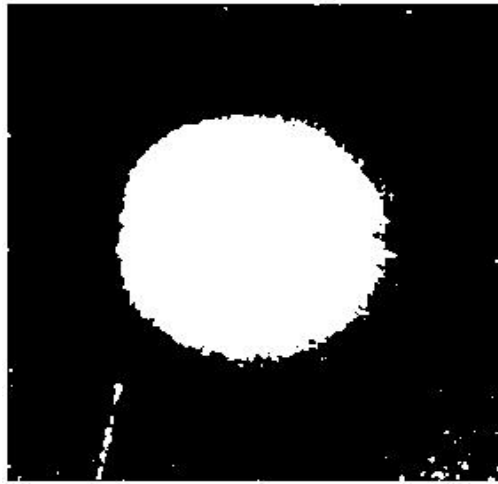


Figure 5-11 Binary image of conical defect in Plate A using the new thresholding approach

Moreover, the binary image of the smallest conical defect embedded in the Plate B ($Rq = 1.27 \mu\text{m}$) is obtained using the threshold value calculated using equation (10) that is 1.81 μm . The binary image can be seen in Figure 5-12 for the smallest defect embedded in the most rough surface. From Figure 5-11 and Figure 5-12, it is demonstrated that the new approach is able to obtain the threshold value that can aid the isolation of the defect region that is embedded in rough surfaces.

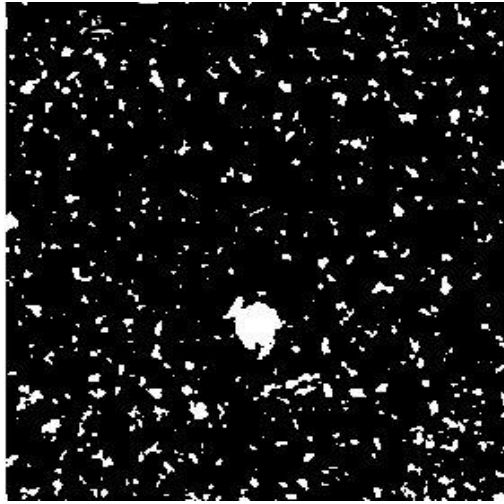


Figure 5-12 Binary image of the smallest defect in Plate B using the new thresholding approach

5.3.4 Defect isolation

Defect isolation is a very important aspect and step to quantify the defect precisely. In Figure 5-11, there are several regions (groups of white pixels) that may be a potential defect or may be surface texture. Hence it is important to isolate the region of interest (defect for instance). For this, it is essential to evaluate the number of objects which has a group of white pixels that can be seen in Figure 5-11. To evaluate these objects in detail, the 'regionprops' command of MATLAB Image Processing Toolbox was used. The 'regionprops' command determines the object by the 8-connected neighbourhood method and then measures a set of various properties for each object [157].

In this research work, it is considered that the object which has the maximum area is the region of surface defect. However, quantification can be achieved on each object but requires more computational efforts. The 'regionprops' command provides the area property of all the objects that are in white pixels by summing the actual number of white pixels in that particular object [157]. Hence the surface defect region is evaluated by finding the object with maximum area among all the objects.

Figure 5-13 shows the binary image of the only conical defect region in the Plate A by converting the rest of all the white pixel objects into black pixels (present in Figure 5-11). Once the surface defect region is obtained, it is important to trace the boundary

of the defect. To trace the boundary of the object, the 'bwboundaries' command is used which is also a feature of MATLAB Image Processing Toolbox. The 'bwboundaries' implements the Moore-Neighbor tracing algorithm modified by Jacob's stopping criteria [158].

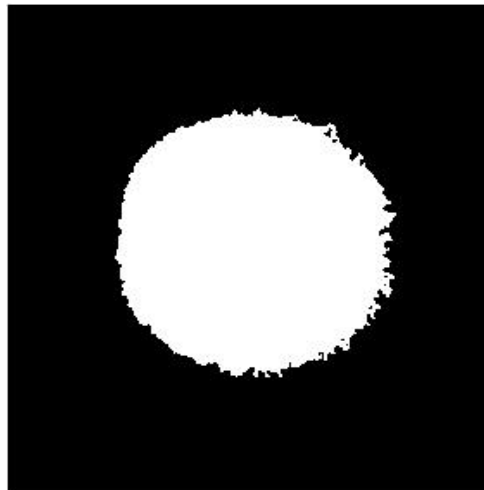


Figure 5-13 Conical defect region in binary image

Using the 'bwboundaries' command in the defect region (Figure 5-13), the boundary of the defect is traced in the x and the y directions. The command 'bwboundaries' returns the x and the y ordinates of the boundary that enclosed the defect region. If the exact position of the defect is known in the binary image, the third dimensional value at each x-y position can be determined from the residual surface and thus the defect boundary in 3D is obtained from the 2D defect. The boundary of the defect can be seen as a blue circumferential line at the throat of the defect in Figure 5-14 and thus the isolation of the conical defect in the Plate A is successfully achieved.

It is noted that using 'bwboundaries' function, some noise was observed at the edge of the defect which can be seen in Figure 5-13. It is anticipated that results could be improved if mathematical morphological operators (such as opening, closing, erosion etc) were used. However, the morphological operators are computationally complex and it may alter the original data which is undesirable at this point of time.

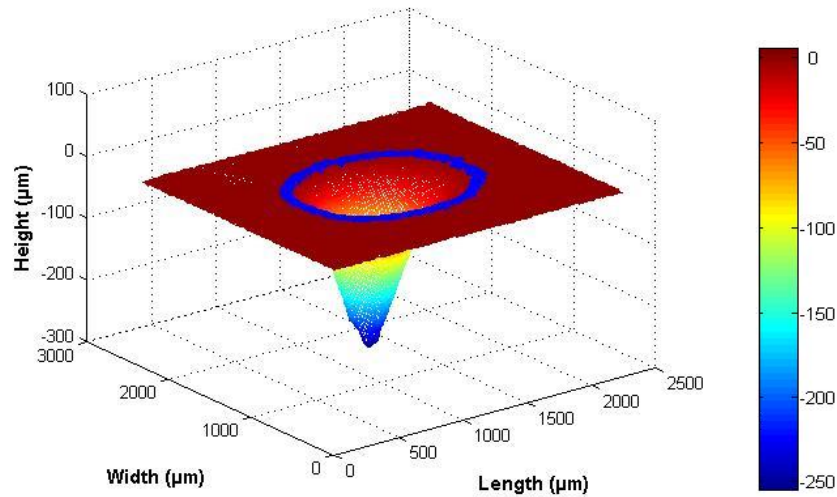


Figure 5-14 Isolated conical defect

5.3.5 Defect quantification

Defect quantification is important in the quality checking element of many manufacturing processes. In this sub-section, a new approach for automatic depth measurement, area measurement and volume measurement is explained in detail.

5.3.5.1 Depth measurement

Volumetric measurement is proposed to measure the depth element of the defect. After isolating the defect region from the defect embedded in the surface, the boundary of the defect is obtained. A least square plane is fitted through the boundary of the conical defect in the Plate A (Figure 5-14) in 3D. This is a reference plane of the defect which can be seen in Figure 5-15. Once the reference plane is generated, the perpendicular distance from any point in defect residual surface to the plane can be calculated.

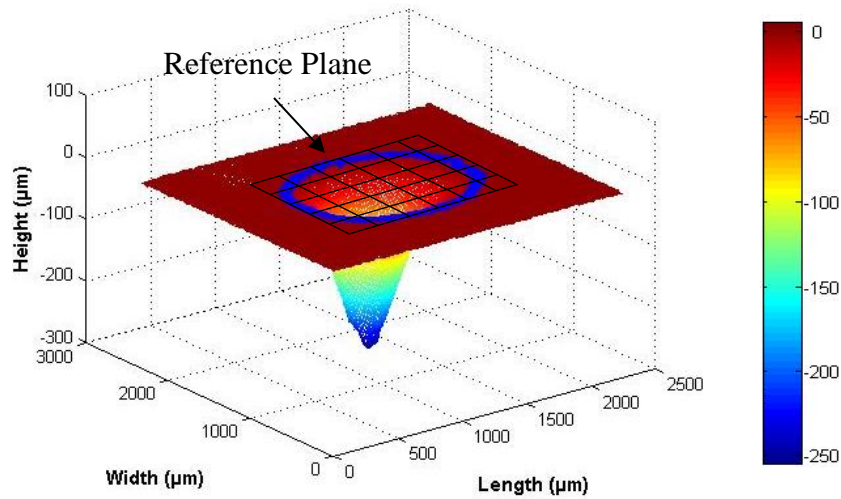


Figure 5-15 Reference plane generation

Let it be assumed that the given least square plane which is fitted through the defect boundary is,

$$ax + by + cz + d = 0 \quad (11)$$

and $X = (x, y, z)$ is any point in the residual surface of the defect as below,

The lowest point of the residual surface in the z -direction is $X_0 = (x_0, y_0, z_0)$. The perpendicular distance from the lowest point X_0 to the reference plane can be calculated as equation (12),

$$D = \frac{|ax_0 + by_0 + cz_0 + d|}{\sqrt{a^2 + b^2 + c^2}} \quad (12)$$

There is always only one perpendicular line that can be achieved from the selected point to the reference plane and consequently the perpendicular distance between that point to the reference plane is fixed and unique. Thus the perpendicular distance from the lowest point in the Z direction to the generated reference plane can be considered as the depth of the defect.

In this case, the measured value of conical defect depth using the novel algorithm is $252.63 \mu\text{m}$.

5.3.5.2 Area measurement

Area measurement of the surface defect region can be computed using the binary image of the defect. As explained in Section 5.3.4, the command 'regionprops' of the MATLAB's Image Processing Tool calculates the area of all the objects in the binary image. The defect area can be calculated by summing all the white pixels in the particular object [157].

The total number of pixels in the object that has the maximum area is the defect region. But the size of the pixel also comes into account when calculating the actual area. Hence, the actual area of the defect on the top surface is a multiplication of the pixel size and total number of pixels in the maximum area of the object.

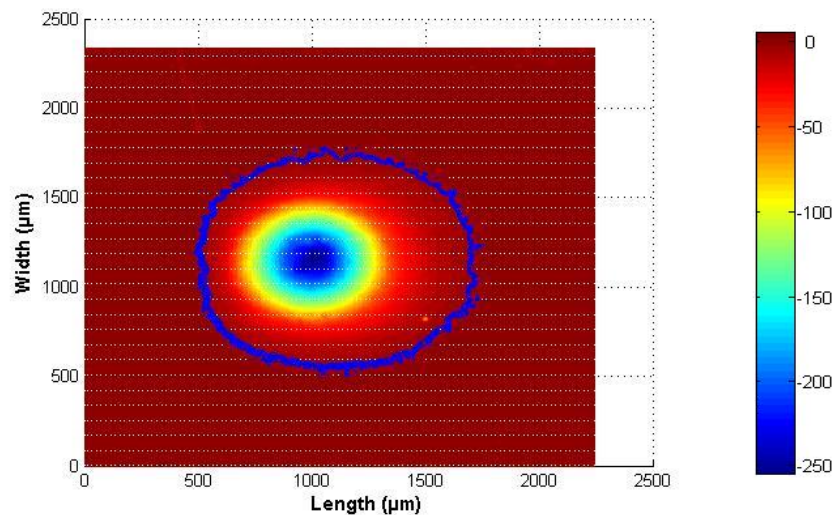


Figure 5-16 Highlighted defect area on the top of the surface

The conical defect in Plate A is optically measured using the Heliotis H3 unit with a lateral resolution of the instrument is $8 \mu\text{m}$ and hence pixel area is $64 \mu\text{m}^2$. The defect region can be seen in the top view of the residual surface (Figure 5-16).

In this case, the measured value of the defect area using the novel algorithm is $1,274,880 \mu\text{m}^2$.

5.3.5.3 Volume measurement

Volumetric measurement is proposed to measure the volume of the defect. After isolating the defect region, the boundary of the defect is obtained. The least square plane is fitted through the boundary of the conical defect in the Plate A (Figure 5-14) in 3D which is the reference plane of the defect which can be seen in Figure 5-15.

If the perpendicular distance from each pixel in the defect region to reference plane is measured, the volume of the defect can be computed easily. The perpendicular distance at each pixel level is calculated using equation (12) so the overall volume of the defect is calculated using equation (13),

$$\text{Volume} = \sum_{N=1}^N (\text{Perpendicular distance at } N \text{ pixel}). (\text{pixel size}) \quad (13)$$

where N is number of the pixel.

Thus the volume of the defect is calculated for the defect region successfully. In this case, the measured value of volume of the conical defect in the flat plate using the novel algorithm is 56,899,000 μm^3 .

5.4 Summary

In this chapter, a need for the novel algorithm for defect quantification is illustrated. It is noted that existing human driven software solutions do not perform effective evaluation for defect quantification. Thus a novel algorithm for the surface defect quantification in terms of depth measurement, area measurement and volume measurement has been proposed. The flow chart in Figure 5-17 represents the stepwise process of the novel algorithm.

The proposed algorithm is segmented into three main individual objectives,

- Filtration
- Defect isolation
- Defect quantification

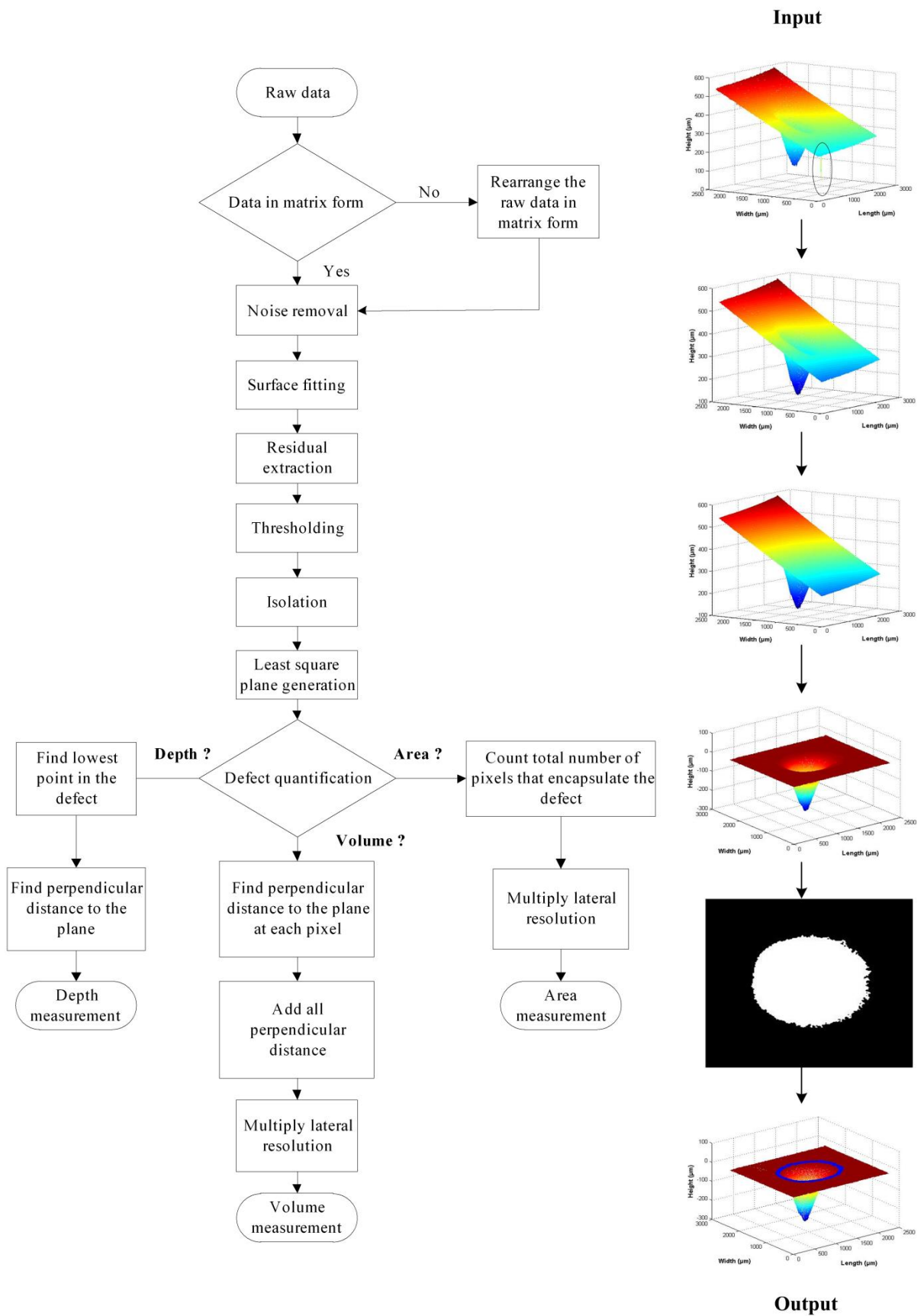


Figure 5-17 Flow chart of the novel algorithm for defect quantification

The areal Gaussian filter is implemented to remove the unwanted features in the measured surface and the areal second order robust Gaussian filter is implemented to approximate the form of measured surface to extract the residual surface. Defect isolation is a key element of the novel algorithm. The new approach to isolate the defect region with an assumption is proposed. The assumption is made that the profile portion below the zero line is approximately equal to profile portion above the zero line considering the elimination of the defect regions and thus the threshold value is set to isolate the defect. Moreover, a new approach has been proposed to compute the geometrical parameter of the extracted defect. To isolate the defect region from the surface and its automatic quantification in 3D are the novel elements of this section of work.

The algorithm is the combination of existing intellectual knowledge and novel elements. The current limitation of this algorithm is that it measures only a single defect that has maximum size of a throat of the defect in a measured surface. Validation, functional capabilities and robustness of the novel algorithm to quantify surface defect automatically is studied in Chapter 6.

6 VALIDATION OF NOVEL ALGORITHM

6.1 Introduction

Validation of any measurement method is a key element in order to build-up confidence in an implemented measurement technique. Chapter 6 explores the validation technique to evaluate the novel algorithm to quantify surface defect automatically which is explained in Chapter 5. Development of defect softgauges is explained and functional variables affecting the performance of the novel algorithm are studied in detail. Various standard real defect artefacts are measured and processed using the novel algorithm to evaluate the functional capabilities of the novel algorithm.

6.2 Defect softgauges

3D measuring instruments that measure surface texture generally interface to a computer that collects raw data followed with post processing for further analysis. As part of the data analysis, parameters are calculated that allow surfaces to be described quantitatively to gain information concerning a manufacturing process or the functionality of the surface. There is a range of material artefacts that are used to calibrate surface measuring instruments but such artefacts do not allow validation or verification of the software aspects of the instrument.

Instrument native software processing of the data is often subject to issues of repeatability, reproducibility and may be non-traceable in nature, leading to significant uncertainty about the data manipulation, quantisation, interpolation and representation. Hence there has been a growing need to validate the accuracy of the software embedded in surface measurement instruments. To this end, software measurement standards have been introduced in the form of the international standard ISO 5436-2 in the context of surface texture [118]. The standard defines Type F1 (reference data) and Type F2 (reference software) softgauges for testing the numerical correctness of the software used in surface texture measuring instruments. Software measurement standards are defined as softgauges. Figure 6-1 illustrates the reference data of a profile that is given in ISO 5436-2.

In addition to this, Blunt *et al* has reported the further development of the Type F1 (reference data) that represents profiles of various manufacturing processes, such as turning, grinding, rolling, honing. In this reference data – Type 1 includes mathematically defined profiles (such as sinusoidal (Figure 6-2), saw, pulse, step), simulated profiles associated to a process, and practical profiles of master work pieces relating to typical manufacturing process [117].

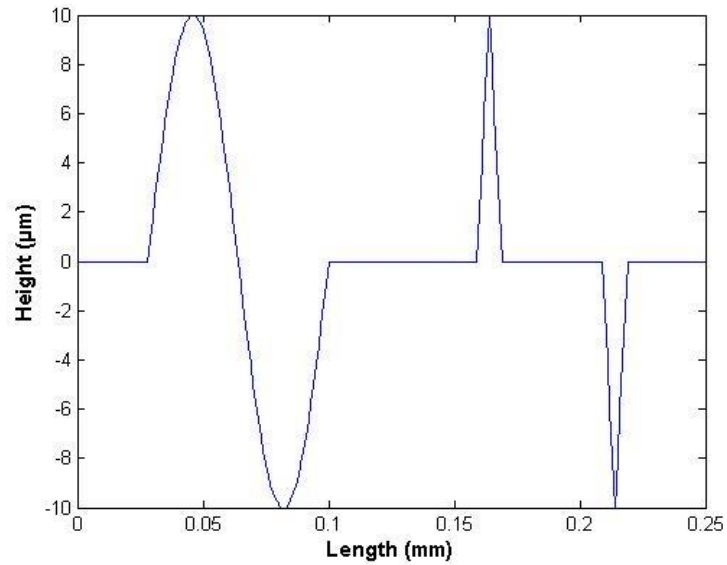


Figure 6-1 Reference data for a profile given in ISO 5436-2 [118]

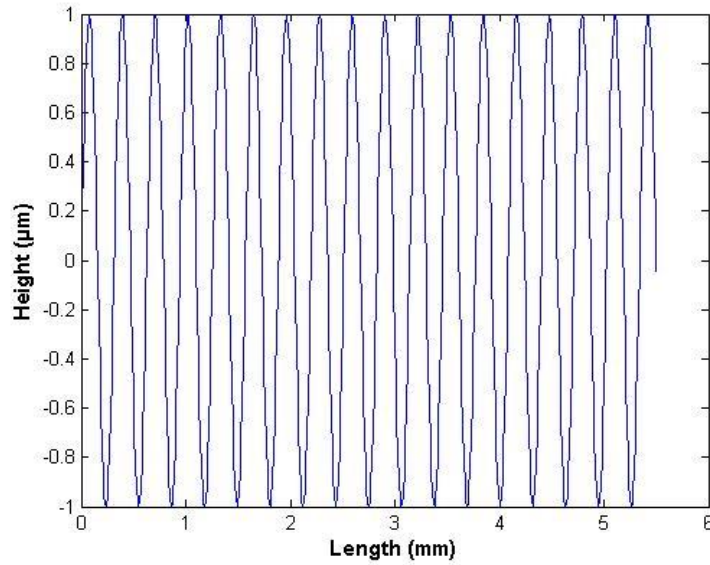


Figure 6-2 Reference data – a sinusoidal profile [117]

Type F2 (reference software) is a software system composed of filter algorithm software and parameter evaluation algorithm software. These algorithms in the reference software are based on original definitions in relevant algorithm standards. Reference software can be calibrated by reference data and used to analyse and evaluate data of practical surface profiles [159].

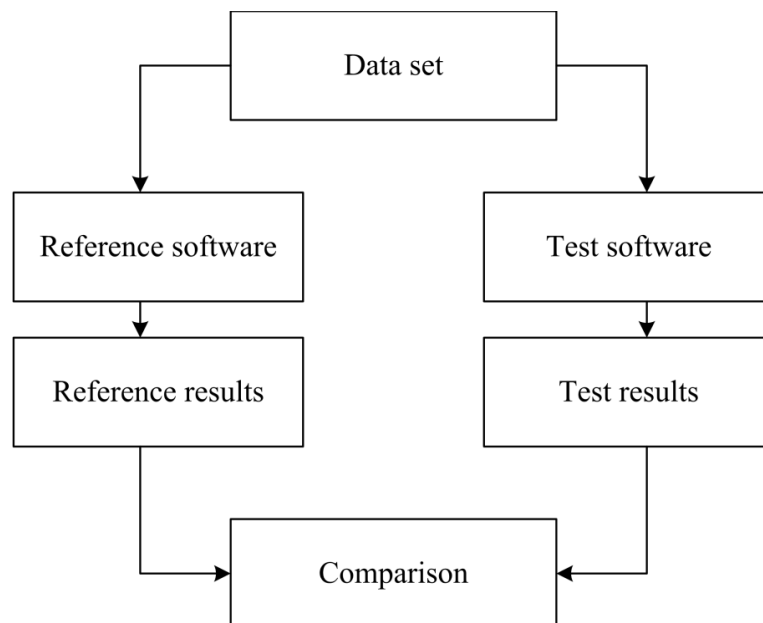


Figure 6-3 Procedure for comparing software [117]

To set the numerical correctness of software, a common data set is input into both the software under test and the reference software. The results delivered by the software under test and those obtained from the reference software are compared. The procedure for comparing software can be seen in Figure 6-3. Similarly Harris *et al* developed softgauges for evaluating the software that measures areal surface texture parameters [119,120].

Softgauges are useful to evaluate the efficiency and accuracy of the software that evaluate profile surface texture parameters and areal surface texture parameters, but they are not useful to evaluate surface defects and their quantification because there is no standard reference data that defines surface defects in 3D. Chapter 5 defined the novel algorithm to quantify surface defects automatically in 3D. However, it is important to validate the algorithm in order to verify the results and build-up confidence in the automatic defect analysis system and generated data thus a defect softgauge is designed and generated. In this section the development of a novel 3D defect softgauge with known size geometry is explained in detail.

6.2.1 Mathematical model of defect softgauge

A novel defect softgauge is developed using MATLAB R2012b in order to verify the implemented novel algorithm to quantify defect automatically in 3D. A mathematical geometric shaped defect of known size embedded in a theoretically flat plate can be used as a softgauge. A pyramidal shaped defect embedded in a flat surface is considered as a defect softgauge as one of the physically generated standard defect artefacts (in Chapter 3) has a pyramidal shape. Moreover, mathematically defined geometric quantities of the pyramidal shape, such as depth, area and volume, are well understood. Similarly the conical or hemispherical shape defect can also be considered as a softgauge but the work reported here concentrates on the pyramidal shape defect softgauge.

The defect softgauge can potentially be implemented using two different methods. Firstly, theoretically well-defined softgauge can be designed and implemented using CAD design software. Secondly, the softgauge can be developed using an iterative process. However through investigation, it was observed that CAD software does not produce datasets in the form of point cloud data that is generated using typical 3D

optical instruments. Thus an iterative process has been chosen to design and create a softgauge in the matrix form.

To develop such a softgauge, a height distributed matrix is needed that represents a known size geometrical shape defect embedded in a flat surface. This is because the input of the generated algorithm is in the form of the height distributed matrix. A matrix of pyramidal shape defect embedded in a theoretically flat surface is generated. Each pixel in the matrix exhibits the height level. The combination of all height distributed pixels generates the defect softgauge in a form of the matrix. Here it is noted that the defect softgauge is a mathematical model and hence each pixel represents just a number that does not have attributed dimension. Moreover the x axis, y axis and z axis represent length, width and height respectively.

Let us consider a pyramidal shape defect embedded in a flat surface. The length, width and depth of the defect are 100 units, 100 units and 50 units respectively. The starting position of the defect in height is 500 units and the end position of the defect in height is 450 units. Such a defect is embedded in the surface that has a length and a width of 300 units. The location of this surface is at height 500 units. Figure 6-4 represents the specific defect softgauge.

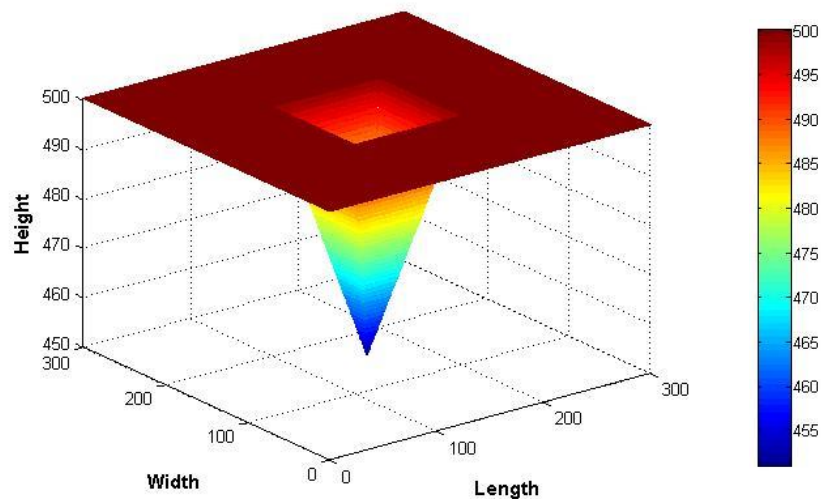


Figure 6-4 Defect softgauge

The depth of the defect softgauge is equal to the absolute height of the defect softgauge. As the softgauge has a known geometry, area and volume is calculated using equation (14) and (15). Table 6-1 represents the theoretical measurement of defect softgauge.

$$Area = Length \times Width \quad (14)$$

$$Volume = \frac{1}{3} \times Area \times Height \quad (15)$$

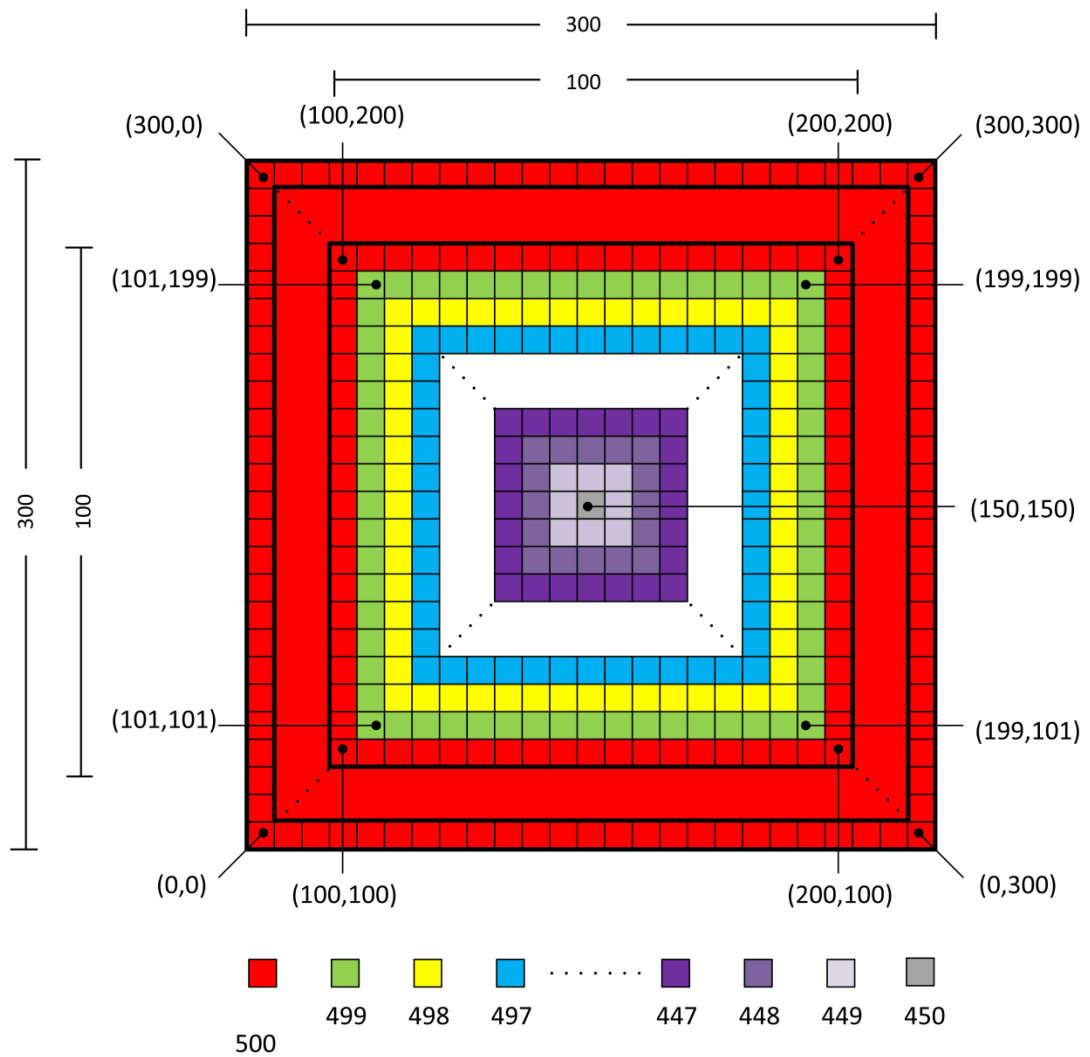
Table 6-1 Theoretical measurement of the defect softgauge

Depth	Area	Volume
50	10,000	166,666.67

For the given specification of the defect softgauge, a step by step procedure to generate the defect softgauge in the form of a matrix with different resolution is given below,

- (1) Create a matrix that represents the surface that has a length (l) of 300 units and width (w) of 300 units at a height (z) of 500 units
- (2) Create a matrix of a pyramidal shape defect embedded in the centre of the matrix of the surface. The length, width and depth (h) of the defect as being 100 units, 100 units and 50 units respectively
- (3) Define a resolution (re)
- (4) For the given resolution, the number of points in the length (p) of the defect is determined by $(100/re)$. Thus, $p = (100/re)$.
- (5) For the given resolution, the number of points in the width (q) of the defect is determined by $(100/re)$. Thus $q = p$.
- (6) Total number of points in the matrix that represents the defect size of (100 x 100) is determined by $(p \times p)$. The size of the defect matrix is $[p, p]$.
- (7) Total number of points in the matrix that represents the surface size of (300 units x 300 units) at height (z) 500 units is determined by $(3p \times 3p)$. The size of the defect matrix is $[3p, 3p]$.

- (8) The depth of the defect ' h ' is represented in the number of steps. The number of step (n_p) is determined by (h/re) . The index of the n_p is denoted as i .
- (9) The boundary of the defect is obtained in the matrix of the surface at the height. For that, four corner points of the square defect is defined by (xl, yl) , (xr, yl) , (xl, yr) and (xr, yr) . Where, $xl = yl = I + p$ and $xr = yr = 2p - i$. ($i = 0$).
- (10) Set the boundary value to z .
- (11) Decrease $z = z - re$.
- (12) Increase i by 1.
- (13) Repeat the step (9) to (12) until i reaches n_p .



6.2.2 Measurement using the novel algorithm

In order to validate the novel algorithm, the defect softgauge with the specification as described in section 6.2.1 was measured using the algorithm. Measurement results from the algorithm should match the theoretical values in order to validate the algorithm that leads to traceability to the mathematically defined size geometry. The defect softgauge was processed and the novel algorithm isolated the defect from the surface as shown in Figure 6-6 as a blue circumferential line outlining the throat of the pyramidal defect region.

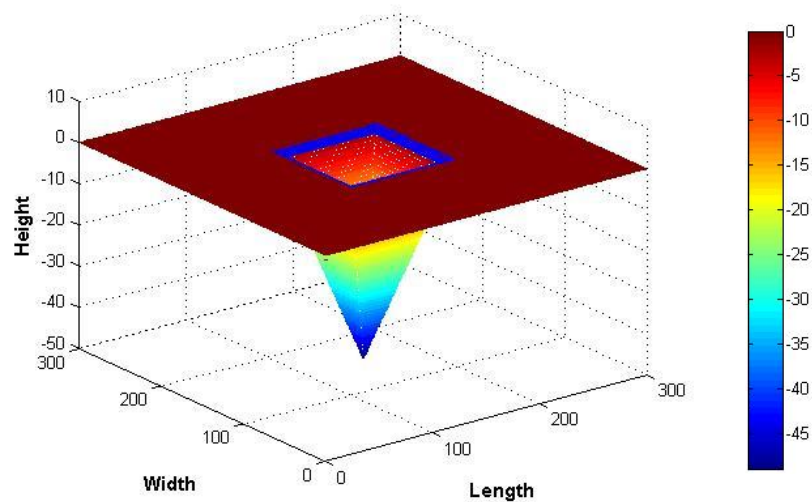


Figure 6-6 Isolated defect softgauge

With a resolution of 1 unit, the depth, area and volume of the defect were computed as 49, 9801 and 156820 respectively. The novel algorithm measured the depth of the defect with 2.0 % of measurement error, the area of the defect region with 1.99 % measurement error and the volume of the defect with 5.91 % measurement error, which is approximately three times the measurement error for both measurement of depth and area. Here measurement error is a function of resolution. By increasing the resolution (effectively decreasing the pixel size), the measurement error can be minimised.

Table 6-2 Measurement of softgauges with different resolution

Resolution	Depth	Area	Volume	Number of data points	Time (s)
5.0	45.0	9,025	120,560	3,600	2
2.0	48.0	9,604	147,290	22,500	6
1.0	49.0	9,801	156,820	90,000	20
0.5	49.5	9,900	161,710	360,000	75
0.2	49.8	9,960	164,670	2,250,000	500
0.1	49.9	9,980	165,670	9,000,000	2094

To demonstrate this phenomenon, defect softgauges were generated with different resolutions and then each of them was measured using the novel algorithm. Defect softgauges are generated to the same specification as described in section 6.2.1 but with different resolutions. An increment in resolution leads to an increased data points in the matrix of the defect softgauges.

Table 6-2 shows the measured depth, area and volume of the defect softgauges with different resolutions along with the computational time required for each measurement.

Table 6-3 Measurement error at different resolution

Resolution	Measurement Error (%)		
	Depth	Area	Volume
5.0	10.00	9.75	27.66
2.0	4.00	3.96	11.63
1.0	2.00	1.99	5.91
0.5	1.00	1.00	2.97
0.2	0.40	0.40	1.20
0.1	0.20	0.20	0.60

Table 6-3 shows the error in depth measurement, area measurement and volume measurement of the defect softgauges at different resolution. It is observed that the measurement error in depth and area measurement is approximately the same for all the resolutions. The error in volume measurement is approximately three times the error in both depth and volume measurement.

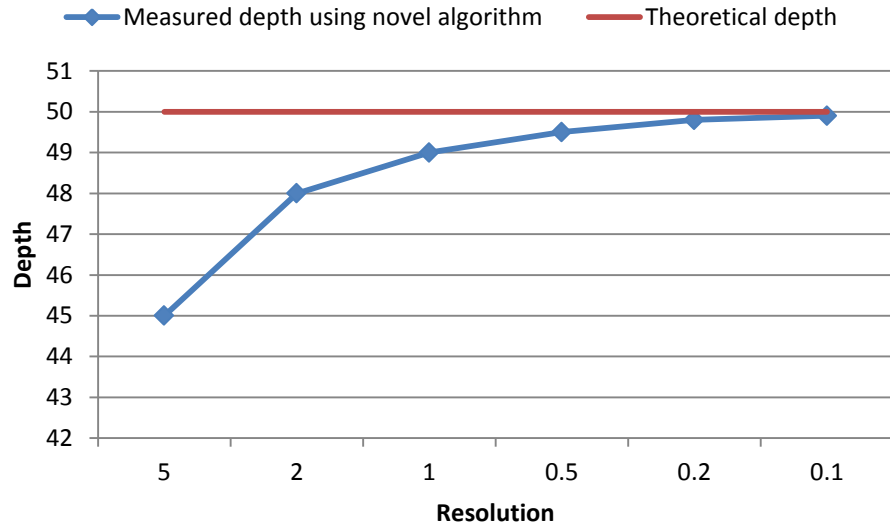


Figure 6-7 Depth evaluation at different resolutions

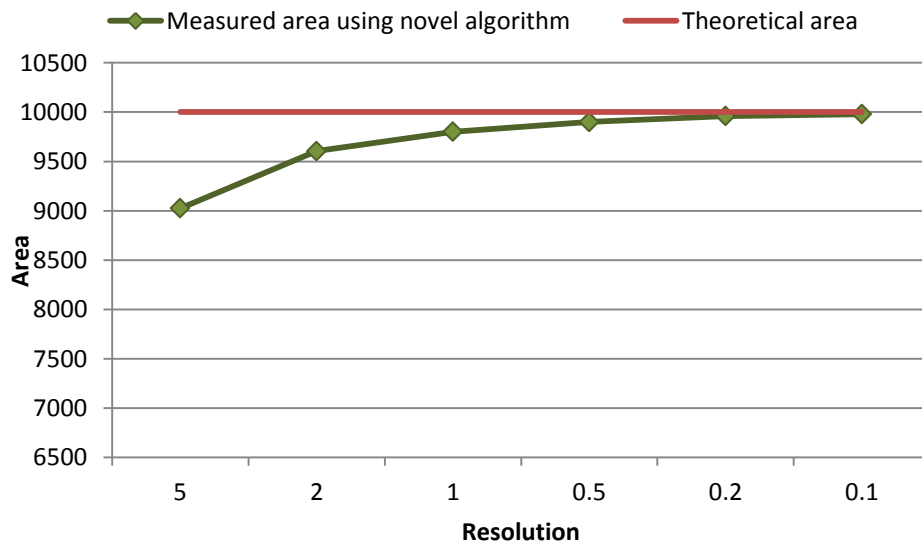


Figure 6-8 Area evaluation at different resolutions

From Table 6-2 and Table 6-3 following observations can be made:

By increasing the resolution, the measured depth of the defect softgauges approaches the theoretical depth value which is described in Figure 6-7. With a resolution of 1 unit, the algorithm computes the depth of 49 units with measurement error of 2 %, but with a resolution of 0.1 units the depth is calculated as of 49.9 which is close to the theoretical value of 50.

By improving the resolution, the measured area of the defect softgauges also approaches the theoretical area value which can be seen in Figure 6-8. With a resolution of 1 unit, the algorithm measures an area of 9801 units squared with measurement error of 1.99 % but again by increasing the resolution to 0.1 units, 9980 units squared of defect area is achieved with a 0.2 % measurement error.

By increasing the resolution, the measured volume of the defect softgauges approaches the theoretical value of the volume as seen in Figure 6-9. It is observed that the measurement error in the volume measurement is approximately three times than the measurement error in depth and area measurement. For the volume measurement, the perpendicular distance from each pixel to the least square plane is obtained and the summation of all the perpendicular distances is computed. Hence the orientation of the plane could lead to the measurement error in volume measurement. However at the 0.1 units resolution, the measurement error is 0.6 %, the error is tending towards zero.

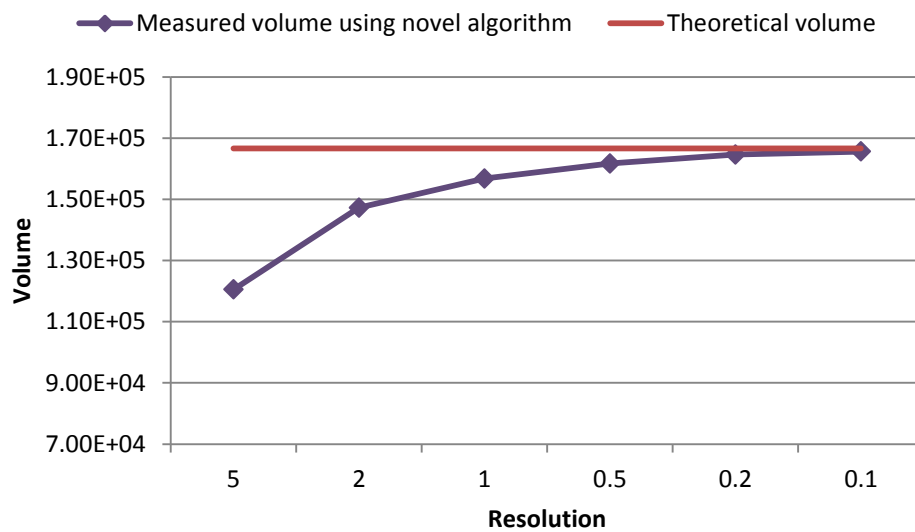


Figure 6-9 Volume evaluation at different resolutions

A significant effect on computational time is observed as a function of increasing the resolution. From Table 6-2 and Figure 6-10 it can be seen that the time is exponentially increasing.

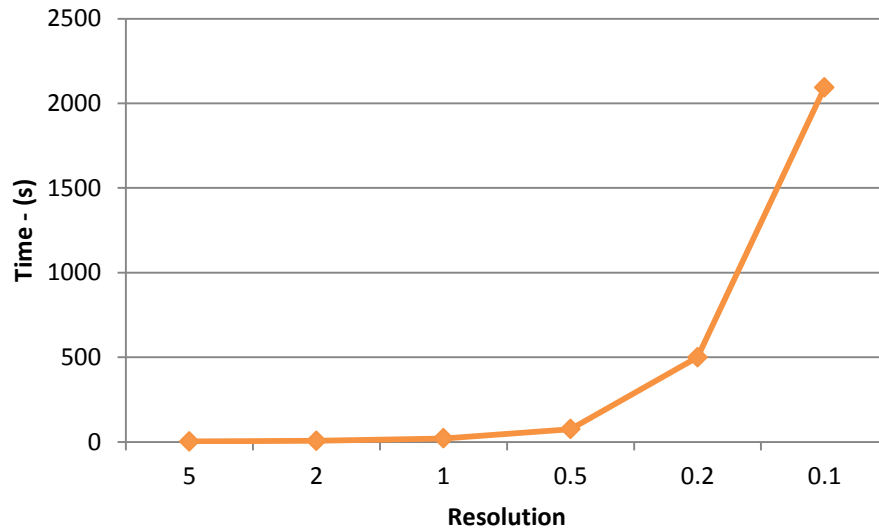


Figure 6-10 Time evaluation at different resolutions

As an example, to quantify a defect softgauge with a resolution of 0.1 units, the novel algorithm takes 2094 seconds whilst for a resolution of 5 units, it just takes 2 seconds. It is because of the number of data points available in the matrix of the defect softgauge. By increasing the resolution, the total number of data points is also increasing and that leads to significant computational time thus there is a strong correlation between number of data points and computational time. However, the computational time can be reduced at the higher data points by code optimization, development of executable code and introducing parallel computing. It should also be recognised that this research is primarily concerned with prototyping the novel ideas, rather than necessarily optimising code speed.

6.2.3 Repeatability

As observed in Section 5.2 the manual measurement method is not repeatable and reproducible. It is important to have a measuring system of high accuracy and high repeatability to ensure the measurement and analysis is achieved correctly and with confidence.

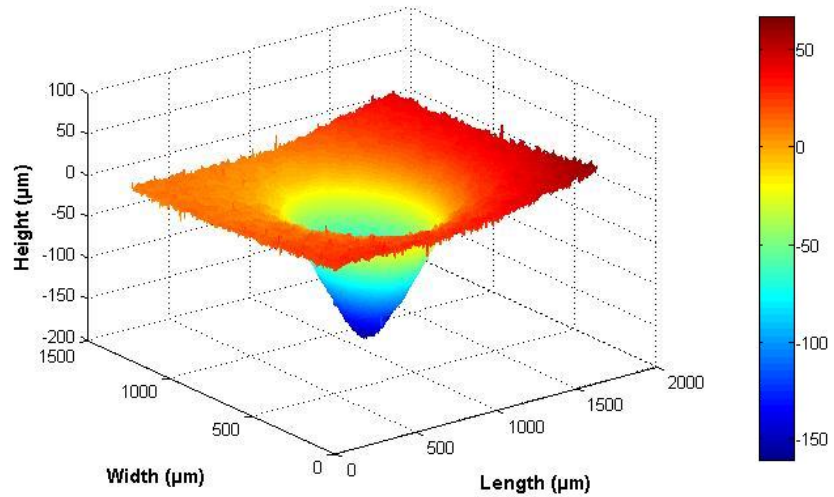
Using the novel algorithm, a defect softgauge of resolution of 1 unit was measured five times repetitively and the standard deviation was calculated in order to derive the repeatability of the novel algorithm. Table 6-4 illustrates the repetitive measurement of

the defect softgauge, showing no variation in any measurement and thus the standard deviation is zero.

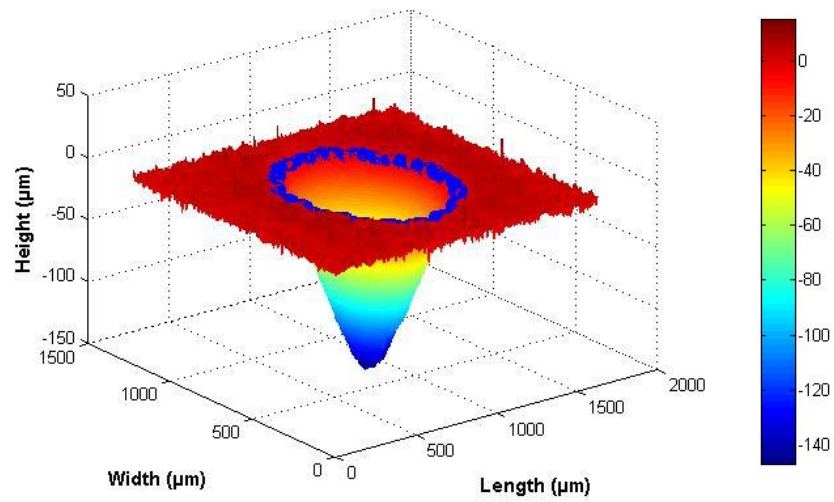
Table 6-4 Repeatability measurement

No of measurement	Depth	Area	Volume
1	48	9,409	147,410
2	48	9,409	147,410
3	48	9,409	147,410
4	48	9,409	147,410
5	48	9,409	147,410
Std Dev	0	0	0

In Section 5.2, it was demonstrated that the human driven manual measurement introduces variability. The single time measured conical defect was quantified five times repetitively using two different manual methods and the results showed (see Table 5-1, Table 5-2, Table 5-3 and Table 5-4) both of the manual measurement methods are less repeatable and less reproducible. The same conical defect Figure 6-11 (a) was quantified using the algorithm repetitively five times. The algorithm generated the residual surface and then isolated the defect from the residual surface as highlighted in Figure 6-11 (b).



(a)



(b)

Figure 6-11 A conical defect (a) Raw data (b) Isolated defect

Table 6-5 illustrates the repetitive quantification of the defect, showing no variation in any measurement and thus the standard deviation is zero. The results from the automatic quantification using the algorithm (Table 6-5) and the manual measurement methods (Table 5-1, Table 5-2, Table 5-3 and Table 5-4) are compared.

Table 6-5 Repeatable quantification of the conical defect

No. of measurement	Depth (μm)	Area (mm²)	Volume (μm³)
1	144.2	0.4	18,678,740
2	144.2	0.4	18,678,740
3	144.2	0.4	18,678,740
4	144.2	0.4	18,678,740
5	144.2	0.4	18,678,740
Mean	144.2	0.4	18,678,740
Std Dev	0	0	0
%RSD	0	0	0

Table 6-6 shows the comparison between the manual measurement methods and the automatic method using the algorithm in quantifying the depth of the defect. Both manual methods (Test method 1 and Test method 2) measure the depth of the defect of 185.2 μm with the standard deviation of 5.6 μm, and 155.4 μm with the standard deviation of 13.4 μm respectively. The automatic measurement method measures the depth of the defect as being 144.2 μm with no standard deviation.

It is noted that automatic process measures depth as being 144.2 μm which is significantly lower compared to both manual test methods. However, Test method 1 utilizes the user defined 2D profile to derive the depth of the defect. Moreover, this method does not have well defined surface reference points to measure depth and thus embedded roughness of the surface influences the estimation of the defect depth. Similarly, due to the lack of well-defined standards for defect isolation, it is very difficult to obtain the defect boundary in Test method 2. High ambiguity associated in defining the defect boundary in both test methods, leads to overestimates of the defect depth with high variation.

Table 6-6 Comparison of the manual and automatic depth measurement

No. of measurement	Depth Measurement (μm)		
	Manual		Automatic
	Method 1	Method 2	
1	186	166	144.2
2	178	159	144.2
3	190	162	144.2
4	181	158	144.2
5	191	132	144.2
Mean	185.2	155.4	144.2
Std Dev	5.6	13.4	0
%RSD	3	8.6	0

Table 6-7 shows the comparison between the manual method (Test method 2) and the automatic method for quantification of the defect (depth, area and volume). The automated process computes each measuring quantity with no variation whilst the manual measurement method (Test method 2) introduces variation with the relative standard deviation for the measurement of depth, area and volume being 8.6 %, 25 % and 19.8 % respectively.

Table 6-7 Comparison of the manual and automatic quantification of the defect

No. of measurement	Quantification of the Defect					
	Manual			Automatic		
	Depth (μm)	Area (mm^2)	Volume (μm^3)	Depth (μm)	Area (mm^2)	Volume (μm^3)
1	166	0.5	25,383,759	144.2	0.4	18,678,740
2	159	0.4	21,362,812	144.2	0.4	18,678,740
3	162	0.4	23,000,530	144.2	0.4	18,678,740
4	158	0.4	21,889,223	144.2	0.4	18,678,740
5	132	0.3	14,191,377	144.2	0.4	18,678,740
Mean	155.4	0.4	21165540.2	144.2	0.4	18678740
Std Dev	13.4	0.1	4194107.3	0	0	0
%RSD	8.6	25	19.8	0	0	0

Each manual measurement method consistently reports a larger value than the automated process. Furthermore, the variability of both of the manual measurement processes is also higher than the automated process using the algorithm. Both of these differences are a function of the subjectivity of the profile/region selection by the user when completing the manual measurements.

The algorithm is a completely quantity based mathematical solution that computes the input data every single time in a same manner and that is the primary reason for obtaining zero standard deviation. The raw data from the 3D measuring instrument is given as an input to the algorithm and the algorithm automatically determines the boundary of the defect followed with the quantification of the defect as an output. If the same defect is quantified by a different person using the algorithm, there will be no variation observed thus the algorithm is highly reproducible as well.

Hence, the algorithm to quantify surface defects is validated using a developed novel standard defect softgauge and it is observed that the novel algorithm is highly accurate, highly repeatable, highly reproducible and traceable to known mathematical geometry.

6.3 Artefact measurement

The novel algorithm was validated and evaluated using a standard known size geometry defect softgauge, however it was also important that the algorithm was established as being effective in measuring more standard real defect artefacts as well. In the following section, different types of defect artefact were measured using the Heliotis and the raw data was then processed using the algorithm in order to explore the functional capabilities of the algorithm.

In the context of this chapter, Relative Standard Deviation (RSD) is used for better representation of experimental data and for effective graphical representation of the data. Log scales are used due to the high magnitude of the quantities. Moreover, RSD is illustrated on a secondary vertical axis in each graph. It is noted that the value of RSD illustrates the repeatability of the measuring instrument not the repeatability of the algorithm. Each defect artefact was measured repetitively five times using the Heliotis H3 unit and each was analysed once using the algorithm, hence the RSD value represents the repeatability of the instrument. The repeatability of the algorithm has

been defined in previous Section with a zero value. It is also noted that the bar charts in this chapter represent the average of each measured quantity (such as depth, area and volume)

6.3.1 Artefacts in different Plate substrates

Conical defects (approximately 250 μm in depth) in four flat Plates A to D (R_q values in the range of 0.06 μm to 1.27 μm) were measured five times repetitively using the Heliotis H3 unit having the experimental setup as explained in Section 4.4.4. Each raw data set was processed using the novel algorithm and was observed that the algorithm isolated the defects embedded in each of the different substrates. Table 6-8 shows the depth, area and volume measurement of the four different defect artefacts and Figure 6-12 charts the measured quantities of all four defects on a logarithmic scale. The main purpose of this experimentation was to illustrate the functional behaviour of the algorithm on different scales of surface roughness.

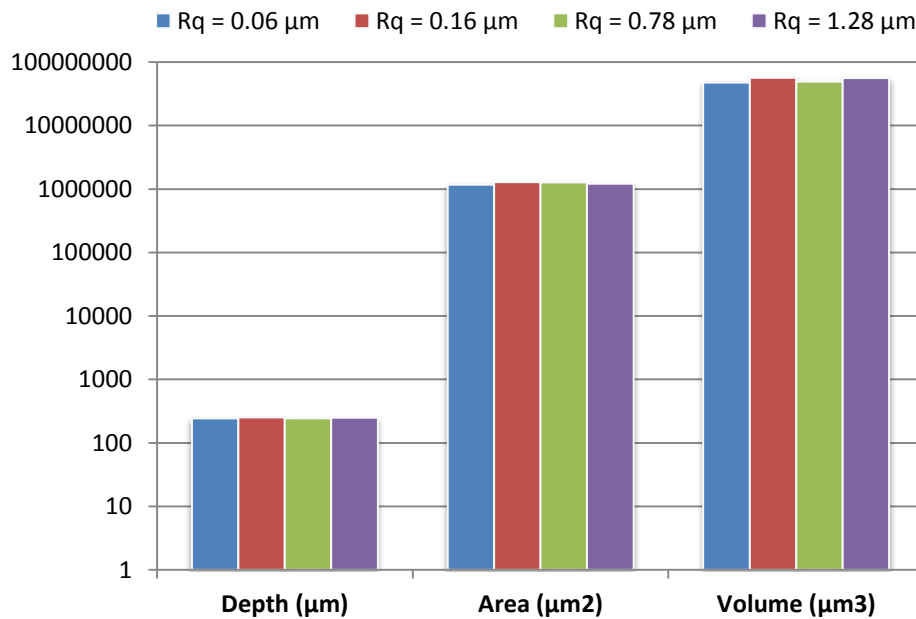


Figure 6-12 Comparison of measured quantities of artefacts in different roughness substrates

Table 6-8 Measurement of artefacts in different roughness substrates

No.of Exp	<i>Rq</i> = 0.06 μm (Plate D)			<i>Rq</i> = 0.16 μm (Plate A)			<i>Rq</i> = 0.78 μm (Plate C)			<i>Rq</i> = 1.28 μm (Plate B)		
	Depth (μm)	Area (μm^2)	Volume (μm^3)	Depth (μm)	Area (μm^2)	Volume (μm^3)	Depth (μm)	Area (μm^2)	Volume (μm^3)	Depth (μm)	Area (μm^2)	Volume (μm^3)
1	243.9	1164992	4.75E+07	252.6	1274880	5.69E+07	244.2	1283136	4.99E+07	248.3	1214272	5.61E+07
2	244.4	1167552	4.76E+07	252.4	1282944	5.72E+07	244.0	1260160	4.90E+07	248.1	1217152	5.64E+07
3	243.9	1184704	4.72E+07	252.9	1278720	5.71E+07	243.9	1265600	4.95E+07	248.3	1221056	5.62E+07
4	244.3	1174720	4.80E+07	251.9	1286208	5.70E+07	244.3	1276480	5.00E+07	247.9	1215936	5.61E+07
5	244.9	1177664	4.73E+07	252.5	1286528	5.69E+07	243.9	1265280	4.79E+07	247.9	1220352	5.60E+07
Avg	244.3	1173926	4.75E+07	252.5	1281856	5.70E+07	244.1	1270131	4.92E+07	248.1	1217754	5.61E+07
%RSD	0.2	0.7	0.6	0.1	0.4	0.2	0.1	0.7	1.7	0.1	0.2	0.2

Using the algorithm, the conical defect artefact's depth was measured as being 244.3 μm , 252.5 μm , 244.1 μm and 248.1 μm in substrates of increasing roughness with RSD values of less than 0.2 % as seen in Figure 6-13.

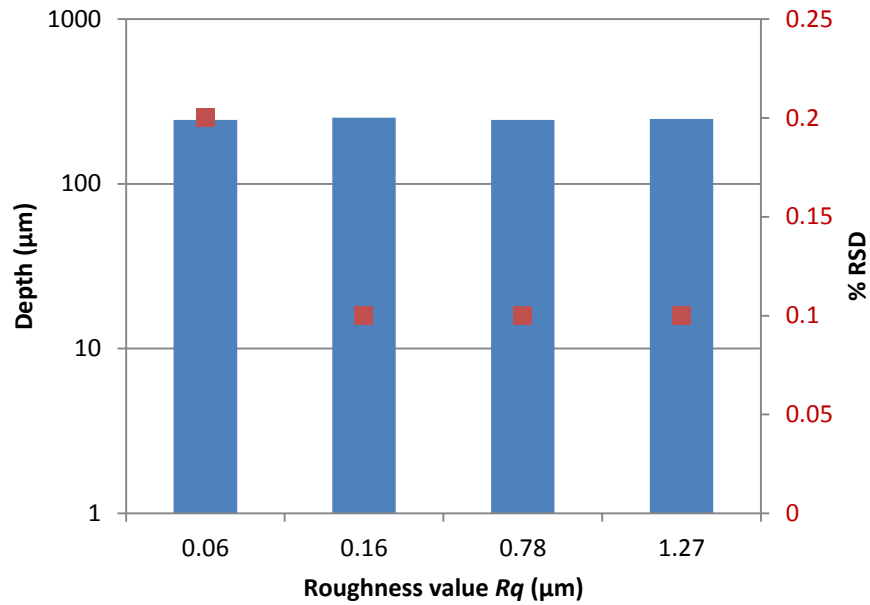


Figure 6-13 Depth measurement of artefacts in different roughness substrates

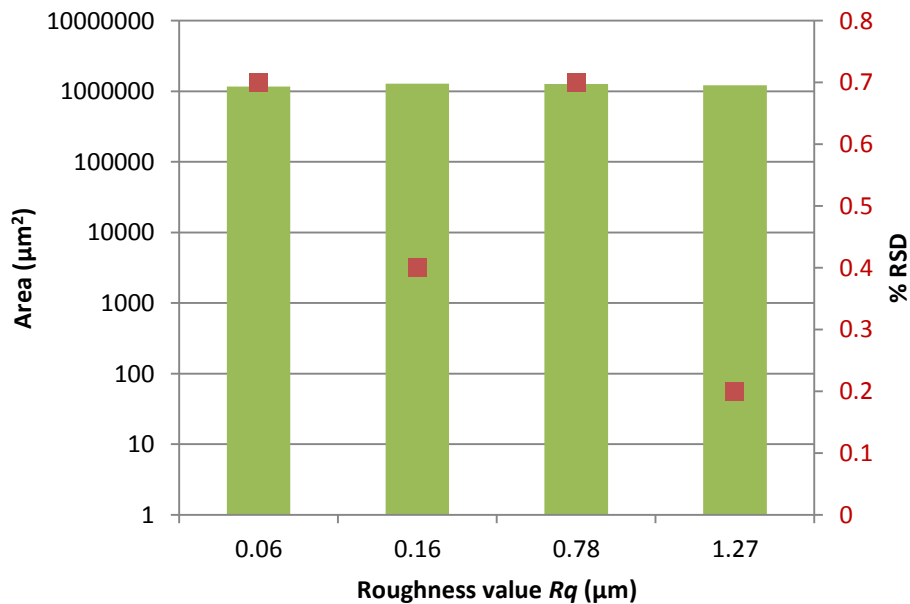


Figure 6-14 Area measurement of artefacts in different roughness substrates

The area of the defect artefacts was measured with a RSD value less than 0.7 % as seen in Figure 6-14, while the volume of the defect artefacts was measured with a RSD value of less than 1.7 % as illustrated in Figure 6-15, values which are higher than both the depth and area measurement.

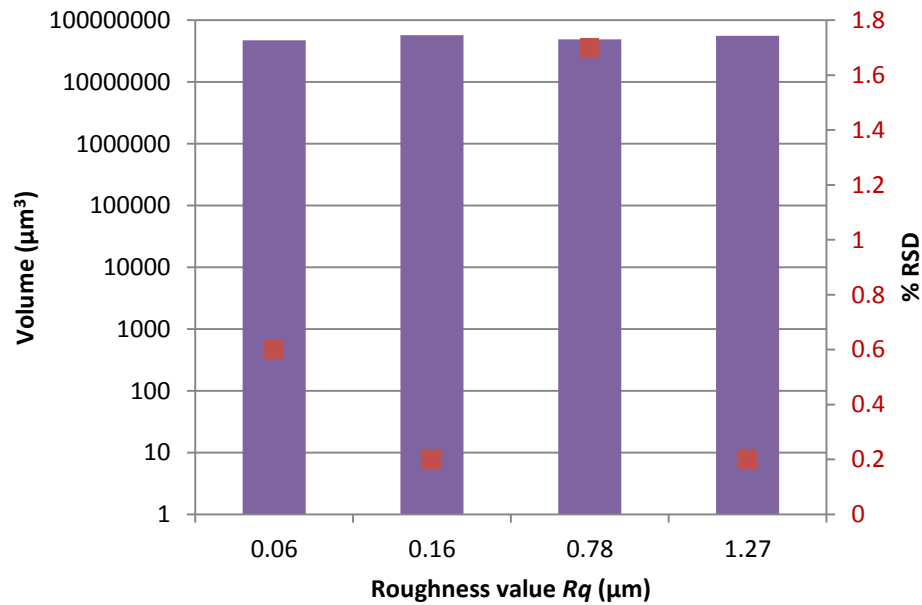


Figure 6-15 Volume measurement of artefacts in different roughness substrates

Despite having varying roughness, the Heliotis H3 unit in combination with the novel algorithm is able to measure the defect artefact with high repeatability with approximately 0.2 % of RSD in measuring depth, approximately 0.7 % of RSD in measurement of area and less than 1.7 % of RSD in calculating volume. It has been successfully demonstrated that the novel algorithm is able to detect and quantify defects automatically and successfully in a range of substrates exhibiting a varying roughness.

6.3.2 Artefacts of different size

Four conical defects of different size on the Plate A were repetitively measured five times using the Heliotis H3. The nominal depth of these defects was 300 μm , 250 μm , 180 μm and 40 μm . The acquired raw data was analysed using the algorithm and Table 6-9 shows the results of depth, area and volume measurement of the four different size defect artefacts and Figure 6-16 illustrates the measured quantities of all defects on a logarithmic scale.

Table 6-9 Measurement of different size artefact on Plate A ($R_q = 0.16 \mu\text{m}$)

No.of Exp	Defect 1			Defect 2			Defect 3			Defect 4		
	Depth (μm)	Area (μm^2)	Volume (μm^3)	Depth (μm)	Area (μm^2)	Volume (μm^3)	Depth (μm)	Area (μm^2)	Volume (μm^3)	Depth (μm)	Area (μm^2)	Volume (μm^3)
1	305.2	1424960	8.80E+07	252.6	1274880	5.69E+07	177.5	1137792	2.48E+07	38.2	28928	4.34E+05
2	304.9	1434240	8.78E+07	252.4	1282944	5.72E+07	177.5	1131712	2.48E+07	38.3	28160	4.32E+05
3	304.9	1422848	8.79E+07	252.9	1278720	5.71E+07	177.9	1136384	2.49E+07	39.3	29160	4.48E+05
4	304.5	1423744	8.79E+07	251.9	1286208	5.70E+07	177.3	1135040	2.48E+07	38.2	28352	4.18E+05
5	304.3	1424576	8.78E+07	252.5	1286528	5.69E+07	178.1	1134208	2.49E+07	38.8	28416	4.23E+05
Avg	304.8	1426074	878E+07	252.5	1281856	5.70E+07	177.7	1135027	2.48E+07	38.6	28603.2	4.31E+05
%RSD	0.1	0.3	0.1	0.1	0.4	0.2	0.2	0.2	0.3	1.2	1.5	2.7

The intention behind these experiments was to demonstrate the effectiveness of the novel algorithm on different sizes of defect. Using the novel algorithm, the different sizes of conical defect artefact's depth was measured as 304.8 μm , 252.5 μm , 177.7 μm and 38.6 μm . It is observed that as the size of the defect decreases, the RSD of the measured depth increases and the same phenomenon is observed for volume measurement.

The smallest defect (38.17 μm deep) is measured with 1.2 % of RSD in depth, 1.5 % of RSD in area and 2.7 % of RSD in volume measurement whilst for the bigger defects (above 180 μm in depth), less than 0.4 % RSD is observed in depth, area and volume measurement. This may be due to the repeatability of manufacturing of standard defect artefacts and the measurement uncertainty of the 3D measuring instruments. However, it is difficult to specifically identify the cause behind these phenomena.

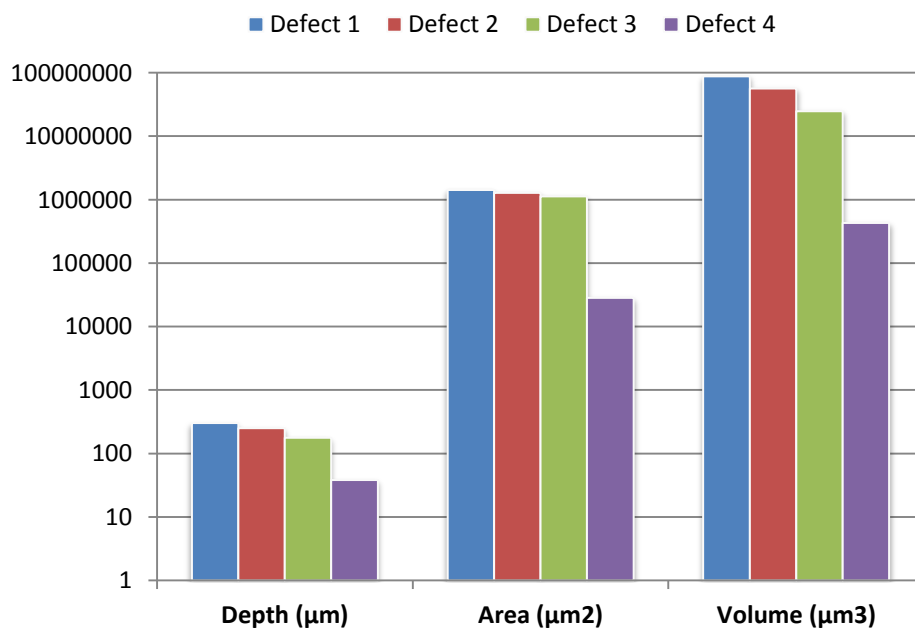


Figure 6-16 Comparison of measured quantities of artefact of different size

Figure 6-17 shows that the RSD in the depth measurement increases as the depth of the defect decreases. For the defect depth below 180 μm , the RSD is measured at less than 0.2 % while for the smallest defect the RSD has increased to 1.2 %

Figure 6-18 shows the bar chart illustrating the average area measurement of the different sized defects and the RSD associated with the measuring area. It is observed that for the smallest defect area (28,603.2 μm^2), the calculated RSD is 1.5 % which is

the highest among all the defects, while for rest of the defects values of less than 0.4% RSD are obtained.

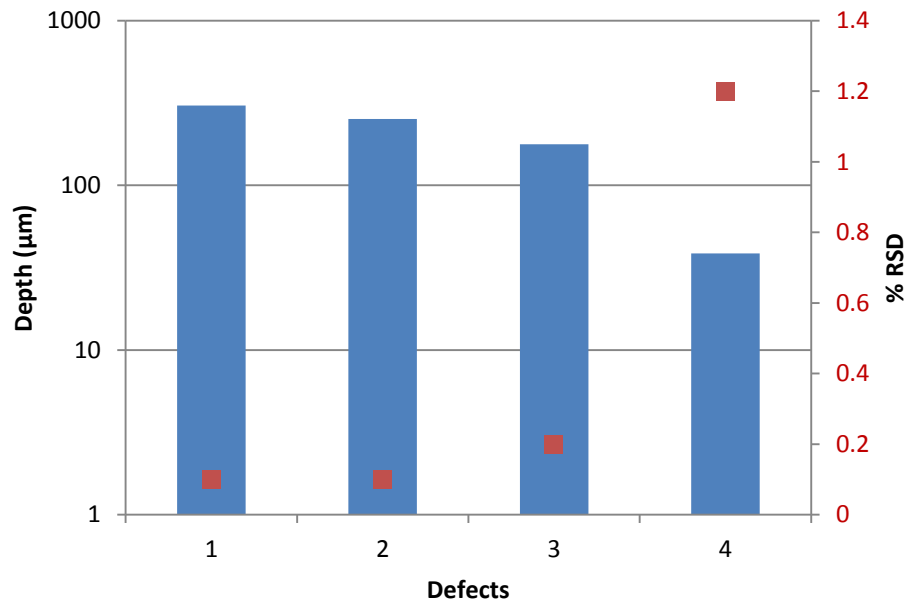


Figure 6-17 Depth measurement of artefacts of different sizes

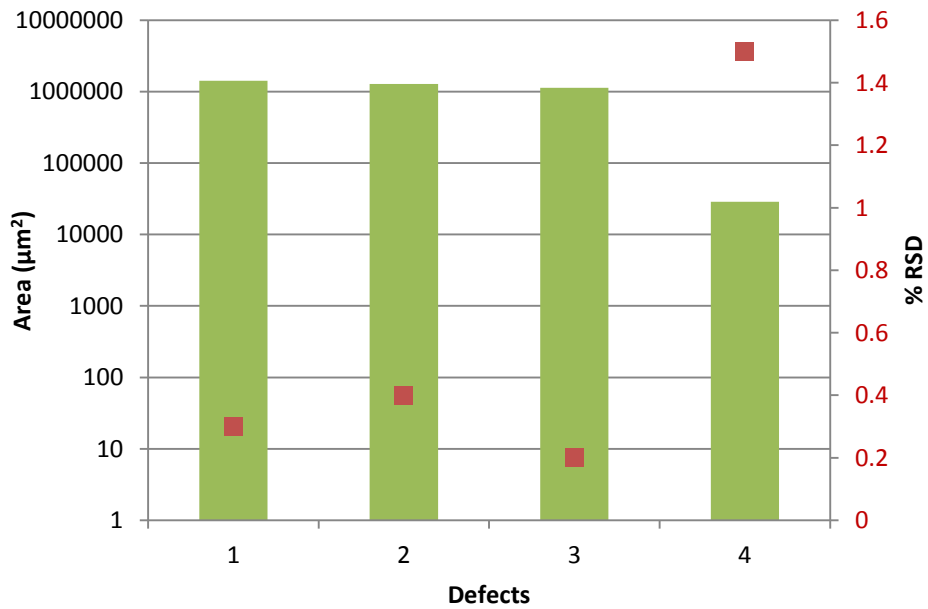


Figure 6-18 Area measurement of artefacts of different sizes

Figure 6-19 is a graphical representation of the average volume measurement of the different sized defects and the RSD associated with the measurement on the secondary vertical axis. For the smallest defect, measured RSD is 2.7 % for volume measurement and for the biggest defect, 0.1 % RSD is observed. Hence as the volume of the defect decreases, RSD for volume measurement increases.

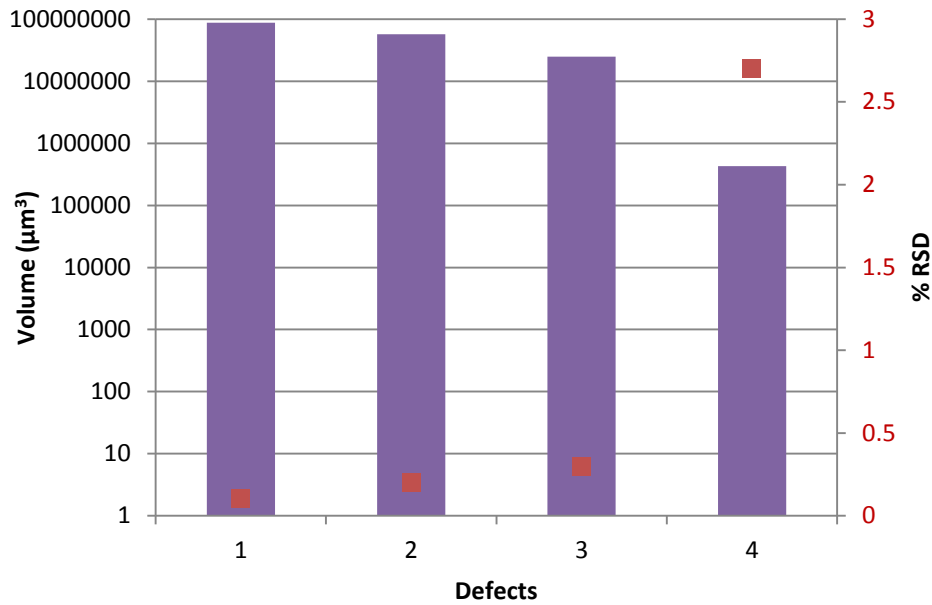


Figure 6-19 Volume measurement of artefacts of different sizes

There is a strong correlation observed between the size of the defect (especially depth and volume) and the relative standard deviation of the measurement. Again, this may be due to the uncertainties in the defect generation process and defect measurement process. If the size of the defect goes up, the relative standard deviation for depth and volume measurement goes down hence the RSD for measuring different sizes of defect is inversely proportional to the size of the defect. The algorithm is capable of quantifying defects of different sizes.

6.3.3 Artefacts in different shapes of substrate

Conical defects of similar size on a flat plate (Plate A), a single curvature plate and a double curvature plate were measured five times repetitively using the Heliotis H3 unit having the experimental setup as explained in Section 4.4.4. The nominal size of these defects was 250 μm in depth. The reasoning behind this experimentation was to learn the effectiveness and functional measuring capabilities of the algorithm to quantify defects that were embedded in different shapes of substrate.

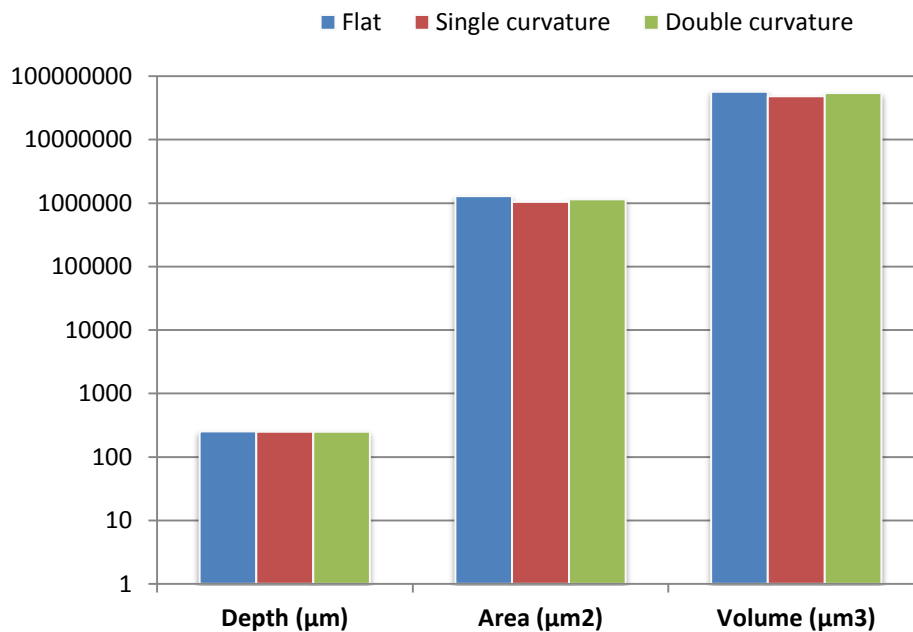


Figure 6-20 Comparison of measured quantities of artefact in different shapes of substrate

The 3D measured data of the defects was processed using the algorithm and Table 6-10 shows the results of depth, area and volume measurement of three similar size defect artefacts embedded in different shapes of substrate. Figure 6-20 illustrates the measured quantities of all three defects.

The algorithm computed the depth of the conical defects as 252.4 μm , 249.8 μm and 250.8 μm in the flat plate, single curvature plate and double curvature plate respectively. The depth of all three defect artefacts was measured with RSD values less than 0.3 % as illustrated in Figure 6-21.

Table 6-10 Measurement of artefacts in different shape of substrate

No.of Exp	Flat Plate (Plate A)			Single Curvature			Double Curvature		
	Depth (μm)	Area (μm^2)	Volume (μm^3)	Depth (μm)	Area (μm^2)	Volume (μm^3)	Depth (μm)	Area (μm^2)	Volume (μm^3)
1	252.6	1274880	5.69E+07	249.92	1053824	4.84E+07	250.98	1163968	5.39E+07
2	252.3	1282944	5.72E+07	249.68	1054080	4.84E+07	250.76	1161216	5.46E+07
3	252.9	1278720	5.71E+07	249.83	1062016	4.84E+07	249.94	1138752	5.36E+07
4	251.9	1286208	5.70E+07	249.64	1030272	4.82E+07	251.89	1164096	5.44E+07
5	252.5	1286528	5.69E+07	249.92	1026368	4.83E+07	250.55	1118016	5.35E+07
Avg	252.4	1281856	5.70E+07	249.8	1045312	4.83E+07	250.8	1149210	5.40E+07
%RSD	0.1	0.4	0.2	0.1	1.5	0.2	0.3	1.8	0.9

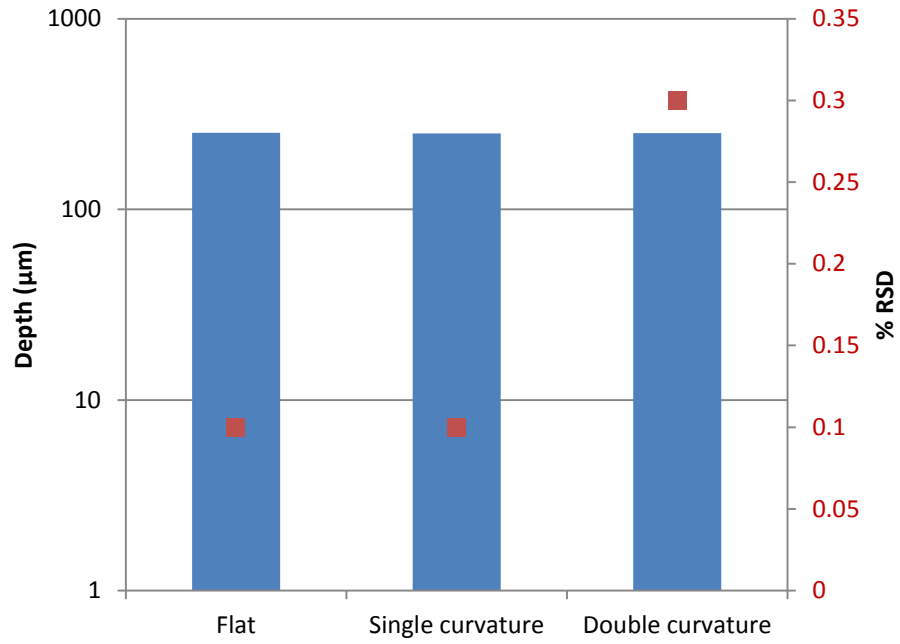


Figure 6-21 Depth measurement of artefacts in different shapes of substrate

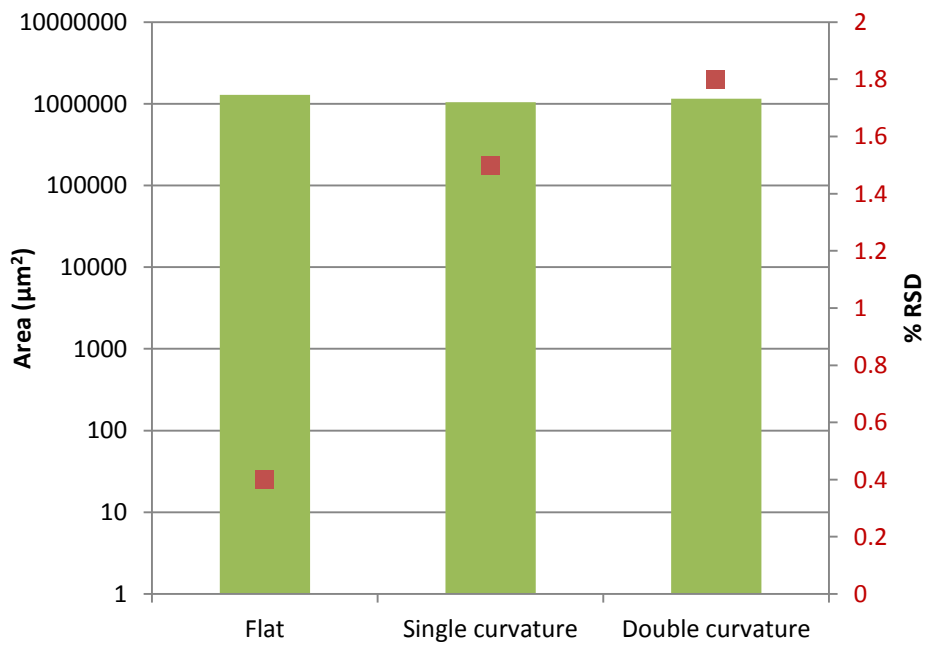


Figure 6-22 Area measurement of artefacts in different shapes of substrate

Figure 6-22 shows the bar chart illustrating the area measurement of the three conical defect artefacts embedded in the different shapes of substrate and the RSD associated with the measuring area. It is observed that for the defect embedded both in the single curvature plate and double curvature plate, the RSD for the area measurement is calculated as 1.5 % and 1.8 % respectively which is higher than for the defect embedded in the flat plate (0.4 %). Hence it is concluded that the complexity of the substrate causes the higher variation in area measurement of the surface defect.

Figure 6-23 describes the volume measurement of defects embedded in the different shapes of substrate. Volume measurement of all three defects were achieved with less than 1 % RSD but it is noted that the RSD in volume measurement of the defect embedded in the double curvature plate is 0.9 % which is higher compared to the flat plate (0.2 %) and the single curvature plate (0.1 %).

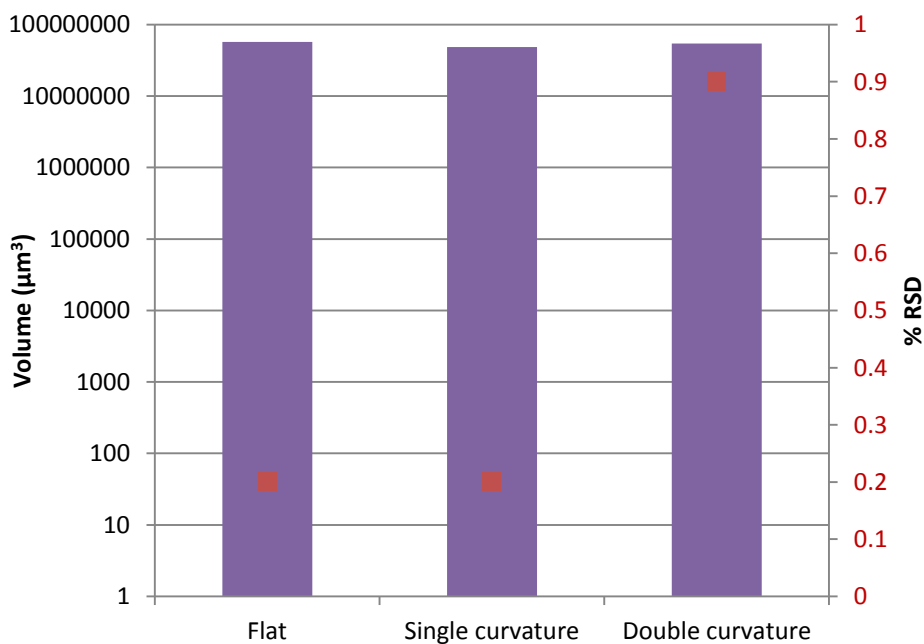


Figure 6-23 Volume measurement of artefacts in different shapes of substrate

It is observed that the shape of the substrate may affect the variation in measurement of the defect. This may be because of the optical limitation of the measuring instrument. The algorithm successfully demonstrated the functional ability of detecting the defects and quantifying them automatically even though they were embedded in complex shaped substrates.

6.3.4 Artefacts of different shape

The main reason for this experimentation was to demonstrate the ability of the novel algorithm to quantify defects that exhibited different shape. Spherical shaped and pyramidal shaped defects, embedded in Plate A ($Rq = 0.16 \mu\text{m}$), were measured five times repetitively using the Heliotis having the experimental setup as explained in Section 4.4.4. The nominal sizes of the spherical shaped and the pyramidal shaped defects were $12 \mu\text{m}$ and $36 \mu\text{m}$ in depth respectively.

The acquired 3D data of each defect artefact was processed using the algorithm. It can be seen that the algorithm isolates the defects of different shape. Table 6-11 and Table 6-12 show the results of depth, area and volume measurement of the spherical shaped defect and the pyramidal shaped defect respectively, embedded in the flat plate.

Table 6-11 Measurement of the spherical shaped artefact

No.of Exp	Spherical Defect		
	Depth (μm)	Area (μm^2)	Volume (μm^3)
1	12.3	46144	2.40E+05
2	12.5	44608	2.37E+05
3	12.3	45760	2.35E+05
4	12.3	44992	2.41E+05
5	12.2	47040	2.48E+05
Avg	12.3	45708.8	2.40E+05
%RSD	0.9	2.1	2.0

The algorithm calculates the depth of the spherical defect as $12.3 \mu\text{m}$ with a RSD value of 0.9 % as seen in Table 6-11 and Figure 6-24. The result also shows the area and volume measurement of the spherical shaped defect is achieved with a RSD value of approximately 2.0 % in both cases.

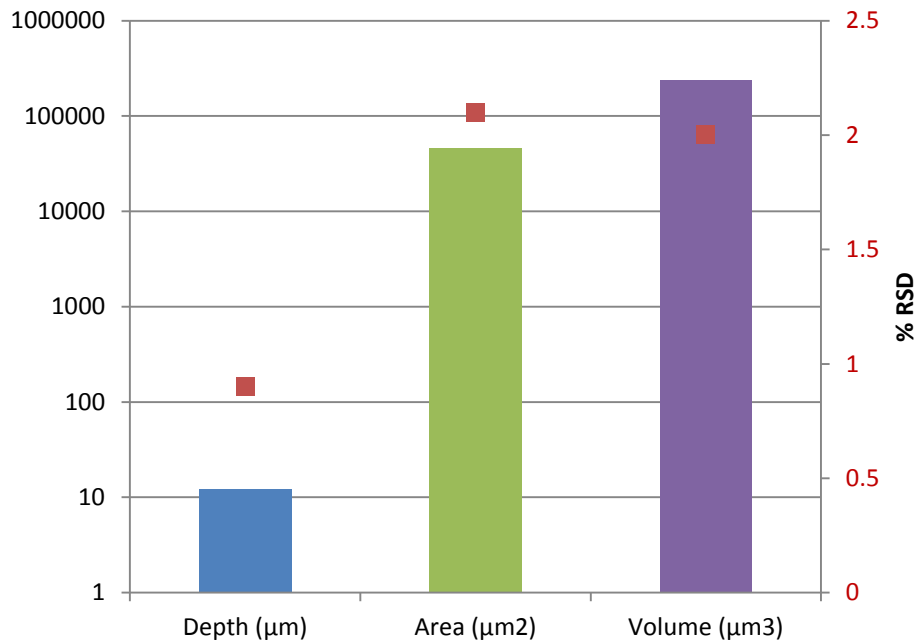


Figure 6-24 Measurement of the spherical shaped defect

The algorithm calculated the depth of the pyramidal defect as 36.8 µm with a RSD value of 0.8 % as seen in Table 6-12 and Figure 6-25. The result also shows the area measurement with a RSD value of 1.0 % and volume measurement with a RSD value of 2.3 %.

Table 6-12 Measurement of the pyramidal shaped defect

No.of Exp	Pyramidal Defect		
	Depth (µm)	Area (µm ²)	Volume (µm ³)
1	37.1	29440	3.63E+05
2	36.9	29376	3.52E+05
3	36.3	28992	3.43E+05
4	36.9	29696	3.48E+05
5	36.9	29696	3.46E+05
Avg	36.8	29440	350434
%RSD	0.8	1.0	2.3

For both defects, the size of each defect is small and hence the measured RSD value is high which was also observed in section 6.3.2. The algorithm successfully demonstrated

the functional capability of detecting the defects with different shapes (conical, spherical and pyramidal) and quantifying them automatically.

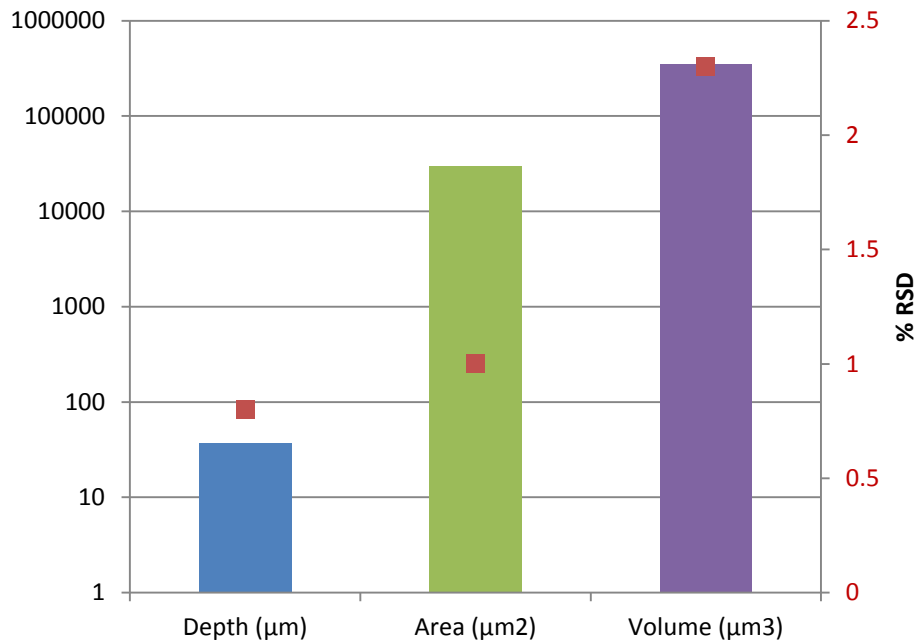


Figure 6-25 Measurement of the pyramidal shaped defect

6.4 Summary

In this chapter, a novel defect softgauge was designed to validate the developed novel algorithm in order to gain confidence in analysis of measured surface defects. A pyramidal shaped defect softgauge was developed with a known standard geometry (50 units in depth, 10,000 units in area and 166,666.67 units in volume) and then processed using the algorithm. The results were compared with theoretical values of the defect softgauges. Measurement error was observed in the depth measurement, area measurement and volume measurement as a function of resolution of the generated defect softgauge but measurement error was minimised by increasing the resolution. It is noted that by increasing the resolution, the computational time also increased as a function of the number of data points that generated the defect softgauge matrix. Moreover, the algorithm detected, isolated and quantified the surface defect with zero standard deviation leading to high repeatability and reproducibility.

The functional capabilities of the novel algorithm have been evaluated by conducting measurements of various real standard defect artefacts using the Heliotis H3 unit and then processing the data using the algorithm.

Observations made from the various experiments are identified below:

- The algorithm has successfully demonstrated its ability to detect and to quantify surface defects embedded in flat plates that have Rq values in the range of 0.06 μm to 1.27 μm . Less than 1 % of relative standard deviation is observed in measuring the geometrical quantities in the majority of defects.
- The algorithm is able to characterise surface defects with different sizes (300 μm , 250 μm , 180 μm and 40 μm in depth). It was also observed that the relative standard deviation in measuring geometrical quantities was 2.0 % to 3.0 % for the smallest defect which was higher compared to the bigger defect (typically more than 180 μm in depth) which is less than 1%. This may be due to uncertainties associated with the defect generation process, and measuring instrument. It is difficult to find particular reason behind this phenomena at this stage of this research and further work needs to be done in this aspect.
- The algorithm is capable of isolating and quantifying defects that are embedded in different shapes of substrate with relative standard deviation values of approximately 1.0 % to 2.0 % of measuring the geometrical quantities.
- The algorithm is effective in quantifying surface defects that have various shapes (for instance conical, pyramidal and spherical) automatically in 3D

The algorithm has been validated and it has been demonstrated that the novel algorithm is highly repeatable and traceable to the known size geometry (pyramidal shape). It is also capable of quantifying surface defects that have different shape, different size and embedded in different roughness and embedded in different shape of substrates, automatically in 3D. It is also noted that, ironically, a drawback with all of this research work was a that there was no way to achieve a better independent measurement of the defect size, area and volume.

7 MEASUREMENT OF INDUSTRIAL COMPONENTS

7.1 Introduction

The developed software has been validated through the simulated defect –“Softgauge” and standard defect artefacts have been measured using the algorithm as detailed in Chapter 6. However, it is important to know the capability of the implemented algorithm on defects embedded in the real industrial components. In this chapter, defects on automotive components, such as a piston crown and a plain bearing are measured and quantified automatically in 3D. The capability of the Heliotis H3 instrument and the algorithm is also evaluated as solder joints on a PCB are measured and quantified automatically in 3D. The work reported here focuses on measuring and quantifying the surface defects only. The cause of the defect and their functional analysis is out of the scope of this study. It should also be noted that the testing of the software algorithm was also completed using aerospace components. Due to issues of commercial confidentiality, the results from the aerospace components have not been reported in this thesis.

7.2 Automotive components

In the automotive industry, the engine can be called the heart of the car and the piston may be considered as one of the most important parts of an engine. In the engine, the purpose of the piston is to transfer the force from expanding gases in the cylinder to the crankshaft via connecting rods. The piston crown is crucial to the operation of the piston. The crown is the upper part of the piston structure, which forms the base of the engine combustion chamber within the cylinder. Surface defects on a piston crown is one of the reasons that may cause engine degradation and failure over the long term.

Plain bearings are placed on the inner side of the cap of the connecting rods. Plain bearing are also called shell bearings because each consists of a pair of semi-circular steel shells with the inner surface coated with a layer of special bearing material that provides the running surface for the crankshaft. Plain bearings operate by means of a thin lubricating oil film which is maintained between the crankshaft and bearing surface

when the engine is operating. Surface defects on the surface of the bearings can result in the breakdown of the oil film, resulting in metal to metal contact and excessive wear leading ultimately to bearing failure and crankshaft damage [160].

The automotive industry may reject defective components (piston crown and plain bearings, in this case) in the engine during the manufacturing process, because a minor defect may cause a functional failure at a later in-service stage. Thus it is very important to detect, and to quantify defects at an early stage, for example depth, area and volume of the defects are key parameters in quality assurance in order to determine pass/failure of the automotive components.

The work reports here an assessment of defects on a plain bearing and a piston of a car engine. By close manual visual inspection, the plain bearing is observed to have a surface defect on the concave side and two defects on the convex side. The piston crown is observed to have a typical surface defect.

7.2.1 Bearing shell

By manual human visual inspection, a very small and shallow surface defect was observed on the convex surface of the plain bearing. This defect is highlighted in Figure 7-1.

The defect was measured five times repetitively using the Heliotis H3 unit. For measuring the defect on the plain bearing, the defective region of the bearing was placed under the Heliotis H3 unit and manual focus on the defective region was obtained. The measuring parameter for Heliotis H3 unit was fixed and has been previously detailed in Chapter 4.

The defect on the convex side (Defect ID – 1) was measured and Figure 7-2 shows the raw data of the defect. It can be seen that the defect is masked by the large scale of geometric form, with the suspicious defect region highlighted. It thus follows that for precise detection of the defect, isolation from the surrounding substrate, and its quantification, is very important.

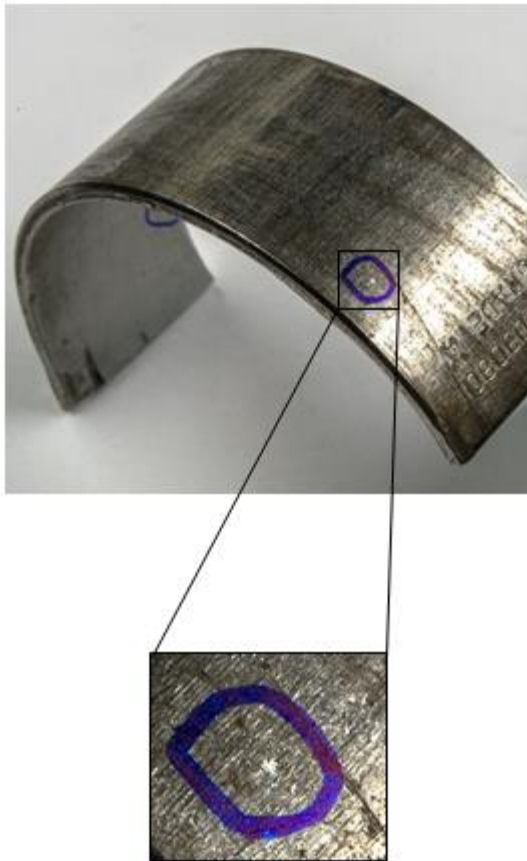


Figure 7-1 Defect on the convex side of the plain bearing (Defect ID – 1)

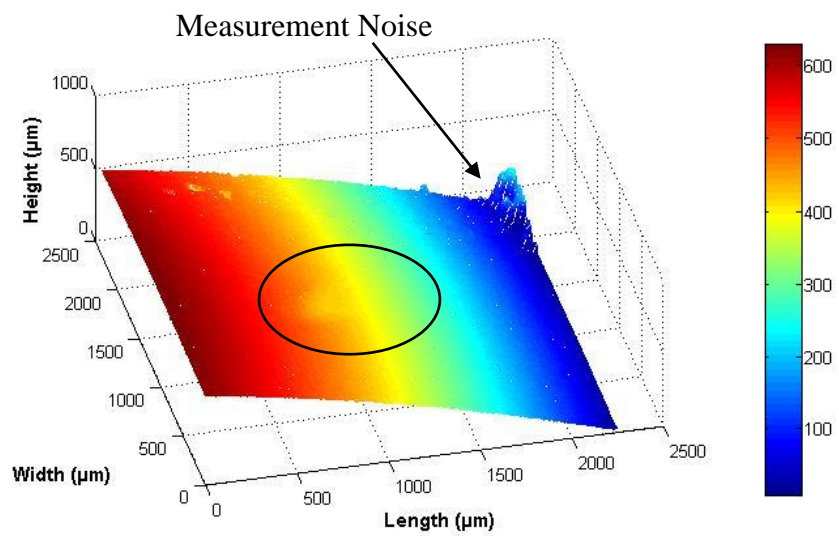
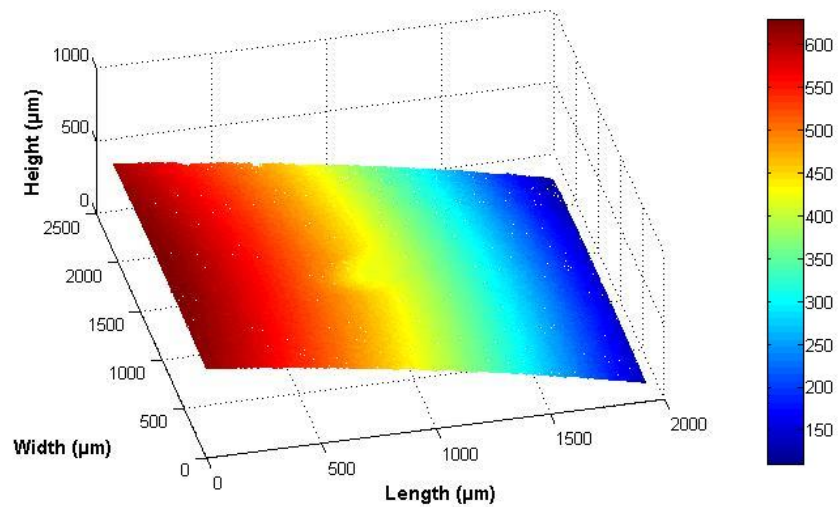
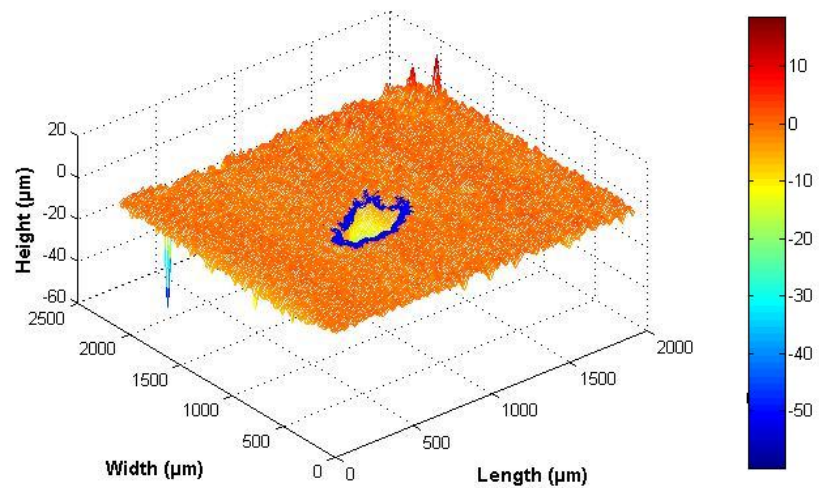


Figure 7-2 Raw data of the defect on the convex side (Defect ID -1)

It is also observed from Figure 7-2 that one of the edges contains a significant amount of measurement noise. Such measurement noise is observed because the depth of field of the measuring instrument is very small (1 mm) and the curvature of the surface is bigger than the depth of field and hence in the given the field of view the measuring surface is out of focus. Such out of focus surface elements are prone to measurement noise.



(a)



(b)

Figure 7-3 (a) Cropped raw data (b) Isolated defect in residual surface

It was important to remove such measurement noise before further analysis of the surface defect. The algorithm cannot cope with the data set of the surface defect that contains such measurement noise. This is due to a current limitation of the algorithm that it does not have a bespoke filter that removes such noise. In order to resolve this issue, only in-focus surface data points were considered in the calculation for the algorithm. At this point in time, this was achieved by cropping the noisy data points manually from the raw data.

Such noise was eliminated manually for efficient analysis and the cropped data (see Figure 7-3 (a)) was input into the algorithm for detecting the surface defect. The algorithm eliminated the large amount of form and thus obtained the residual surface and detected the boundary of the defect which is highlighted in Figure 7-3 (b).

Table 7-1 Quantification of Defect ID – 1

No. of Exp	Defect ID – 1		
	Depth (μm)	Area (μm^2)	Volume (μm^3)
1	25.9	196224	1.53E+06
2	25.3	189120	1.50E+06
3	25.7	193452	1.52E+06
4	26.4	197720	1.57E+06
5	25.7	187064	1.51E+06
Avg	25.8	192716	1.52E+06
%RSD	1.5	2.3	1.5

Table 7-1 shows the computed depth, area and volume of Defect ID – 1 using the algorithm. The average depth of the defect was 25.8 μm and the average volume was 1526780 μm^3 with a RSD value of 1.5 % in both measurements. The average area of the defect was 192716 μm^2 with a RSD value of 2.3 %.

A very shallow defect illustrated in Figure 7-4 on the concave side (Defect ID – 2) was observed on the plain bearing. It was found that the defect was very small and it was quite difficult to identify whether the defect was positive or negative (going into surface or coming out of the surface). The defect was measured using the Heliotis H3 unit and Figure 7-5 represents the raw data of the defect.

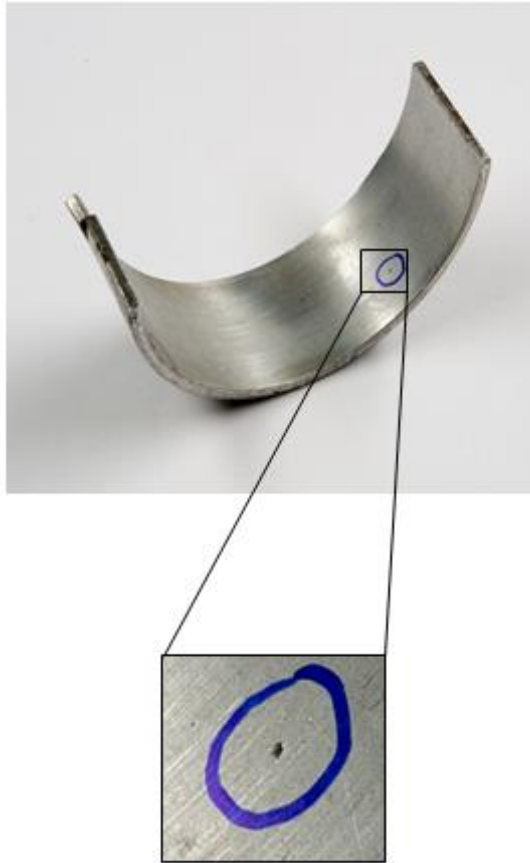


Figure 7-4 Defect on the concave side of the plain bearing (Defect ID – 2)

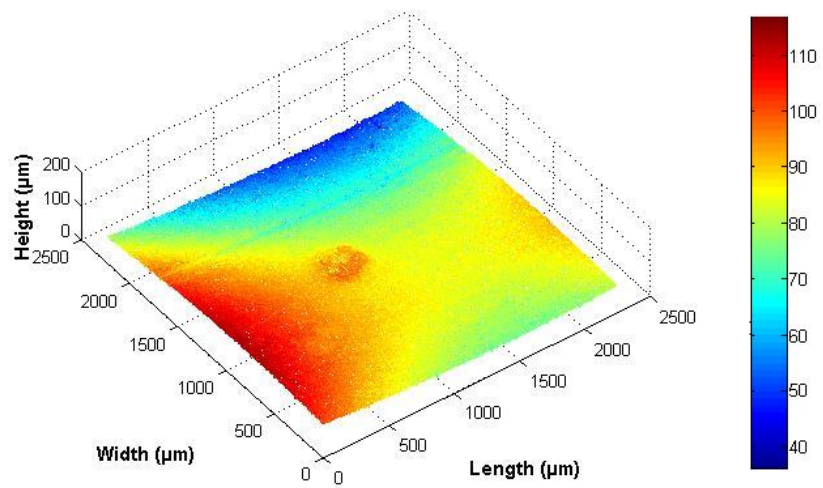


Figure 7-5 Raw data of Defect ID – 2

By completing close inspection, it was found that the surface defect was on the positive side of the surface instead of negative side (i.e. coming out of the surface). It appears to have some foreign material deposited on the inner surface of the plain bearing. Such a type of defect (combination of positive and negative aspects) was difficult to measure and to quantify using the algorithm. This is because the algorithm was only capable of detecting and quantifying negative defects that go below the surface of the substrate.

To resolve this issue for the efficient quantification of both the positive and negative defects, different methods were used. In this approach, the 3D data of the residual surface in a matrix form was inverted. By matrix inversion, the positive side of the defect turned into the negative side and such data was then given to the algorithm for further analysis. Inversion of the residual surface data was achieved by the scalar multiplication of the data matrix of the residual surface by minus one.

The inversion of the raw data can be seen in Figure 7-6

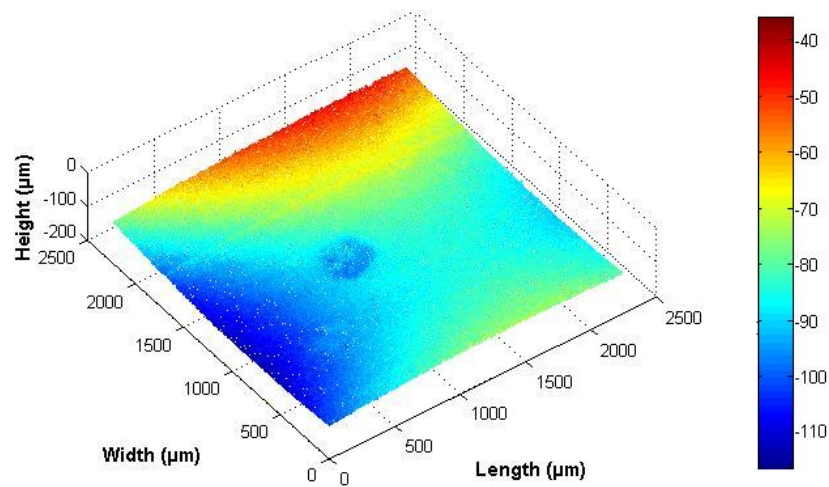


Figure 7-6 Inverted raw data

The inverted raw data was input into the algorithm and the algorithm computed the residual surface. Once the residual surface was obtained the boundary of the defect was derived and is illustrated in Figure 7-7. Once the boundary was obtained the algorithm quantified the defect.

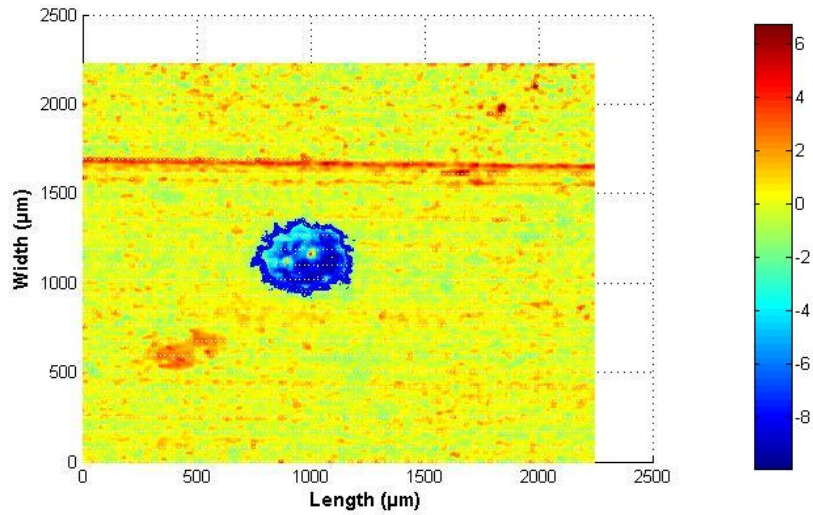


Figure 7-7 Isolated defect in the residual surface (Top view)

The residual surface with the positive defect can be seen in Figure 7-8 which was achieved by again inverting the previously inverted residual surface data.

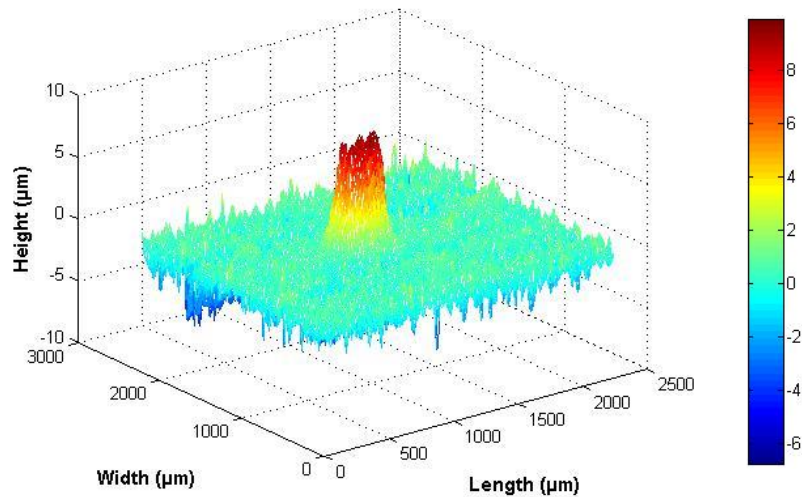


Figure 7-8 Positive Defect ID – 2

Table 7-2 shows the quantification of the positive defect (Defect ID – 2) which was obtained using the algorithm. The calculated average height of the positive defect was 9 μm with a RSD value of 2.2 %. The RSD values for depth and volume were higher than

the RSD value for the area of the defect. This is due to the measurement uncertainty of the measuring instrument.

Table 7-2 Quantification of Defect ID – 2

No.of Exp	Defect ID – 2		
	Height (μm)	Area (μm^2)	Volume (μm^3)
1	9.1	1.45E+05	6.16E+05
2	8.8	1.43E+05	5.67E+05
3	9.2	1.41E+05	5.93E+05
4	8.9	1.40E+05	5.65E+05
5	8.8	1.44E+05	6.05E+05
Avg	9.0	1.43E+05	5.89E+05
%RSD	2.2	1.4	3.9

A second surface defect was observed on the concave side of the plain bearing as highlighted in Figure 7-9, in a more challenging position.

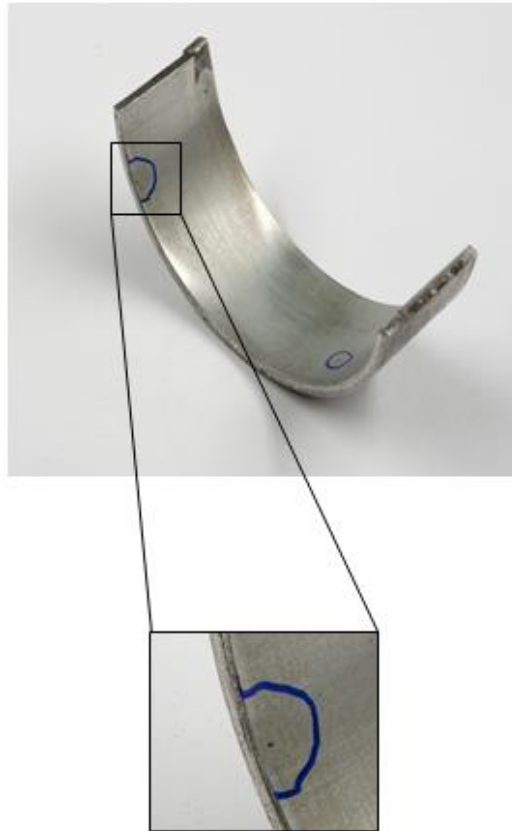


Figure 7-9 The defect on the concave side of the plain bearing (Defect ID – 3)

The second concave defect was quite similar to Defect ID – 2 in appearance. It was noted that the surface defect was located at the sharp edge of the plain bearing. Moreover, the defect was very small and it was really difficult to judge whether the defect was positive or negative. The defect was measured using the Heliotis H3 unit, although it was difficult to get the surface defect in-focus using Heliotis H3 because of the curvature of the surface and the location of the surface defect.

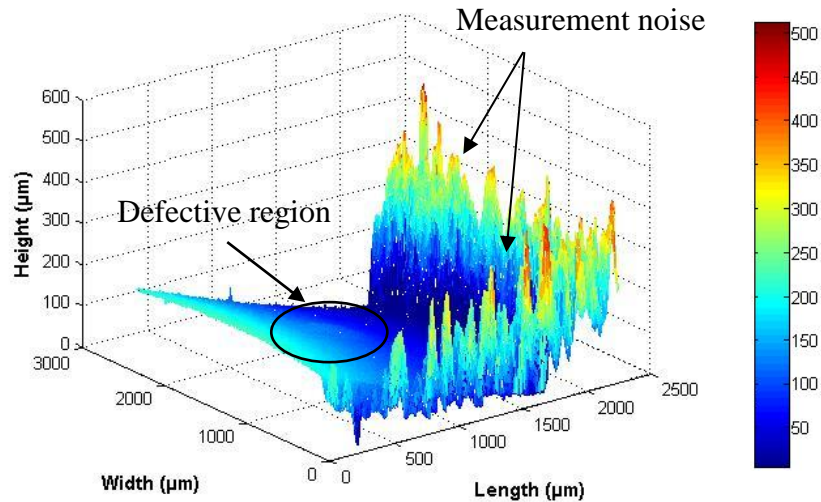


Figure 7-10 Raw data of Defect ID – 3

With significant difficulty, raw data containing the surface defect was obtained which is illustrated in Figure 7-10. However, a very significant amount of measurement noise was also obtained due to the curvature of the surface and the location of the defect. If the data was given to the algorithm in such a state, the algorithm would have been unable to detect the correct surface defect thus the noise removal was essential. Measurement noise was removed manually by cropping the noisy region and the remaining cropped data comprising the focused surface and defect can be seen in Figure 7-11.

By close inspection of the raw and the cropped 3D data in Figure 7-10 and Figure 7-11 respectively, a very small positive bump can be observed. Hence the inversion of the cropped data was essential to quantify the defect using the novel algorithm. The inverted cropped data can be seen in Figure 7-12.

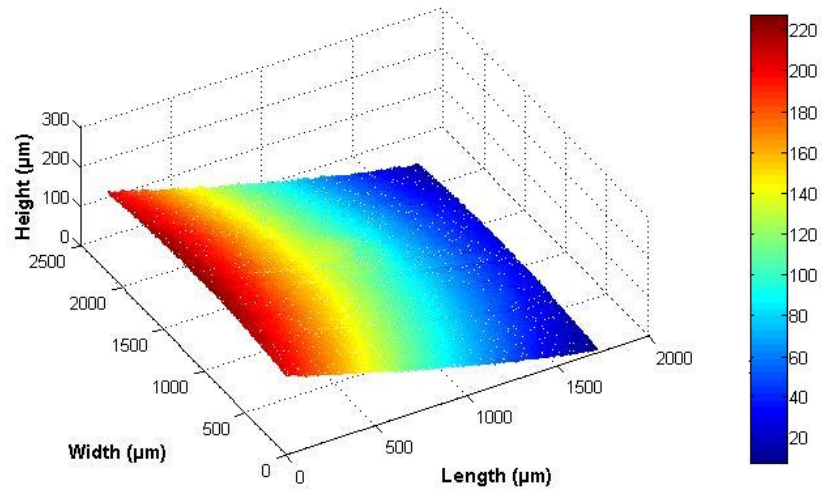


Figure 7-11 Cropped raw data of Defect ID – 3

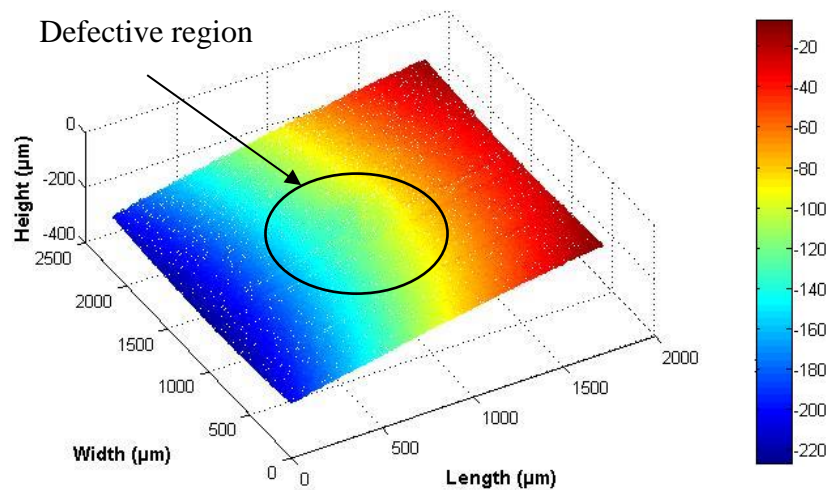


Figure 7-12 Inverted cropped data

The inverted 3D data was passed into the algorithm and the large form was removed for further detection of the defect followed by its quantification. Figure 7-13 demonstrates the isolated defect region obtained using the algorithm in the residual surface.

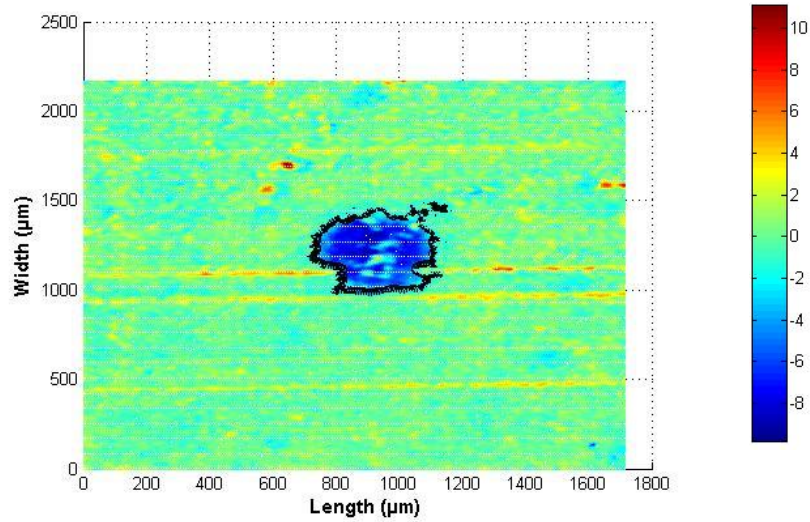


Figure 7-13 Isolated defect in the residual surface (Top view)

Table 7-3 Quantification of Defect ID – 3

No.of Exp	Defect ID – 3		
	Height (µm)	Area (µm ²)	Volume (µm ³)
1	8.5	1.59E+05	6.34E+05
2	8.3	1.59E+05	5.93E+05
3	8.6	1.64E+05	6.23E+05
4	8.1	1.66E+05	6.16E+05
5	8.1	1.63E+05	6.04E+05
Avg	8.3	1.62E+05	6.14E+05
%RSD	2.4	2.0	2.6

Table 7-3 illustrates the computed average depth, area and volume of the defect. The algorithm computed the average height of the positive defect as being 8.3 µm with 2.4 % of RSD. The average area and volume of the defect was 162708.8 µm² and 614010 µm³. Once the geometrical quantities of the defect were calculated, the 3D data was again converted back into its original format and the positive defect can be clearly seen in the residual surface. Figure 7-14 illustrates a very shallow positive defect embedded in the surface of the plain bearing.

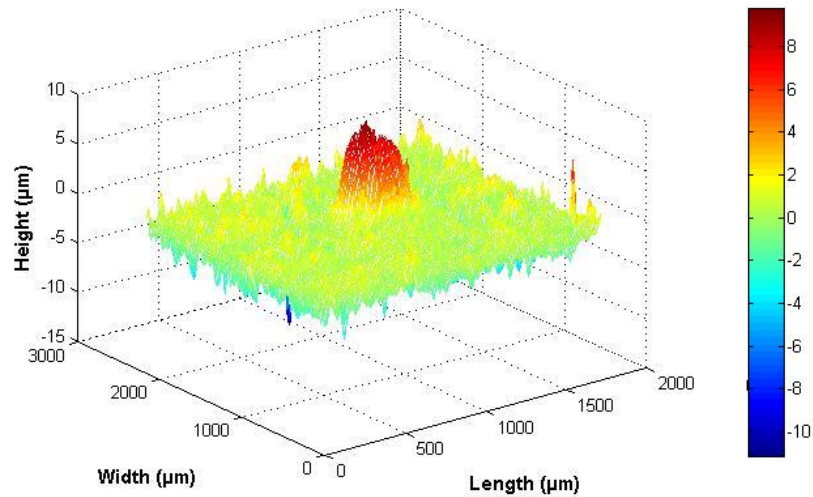


Figure 7-14 Positive Defect ID – 3

Automatic detection and 3D quantification of defects in the plain bearing was achieved uniquely using the combination of Heliotis H3 unit and the novel algorithm.

7.2.2 Piston

The piston crown was observed to have a surface defect (Defect ID – 4) with a lateral size of approximately 15 mm, highlighted in Figure 7-15. The Heliotis H3 unit was unable to measure such a large sized defect as the field of view for the system was 2.4 mm x 2.4 mm. Moreover, the Heliotis H3 did not have field or image stitching capabilities to cover larger field of view and depth of field.

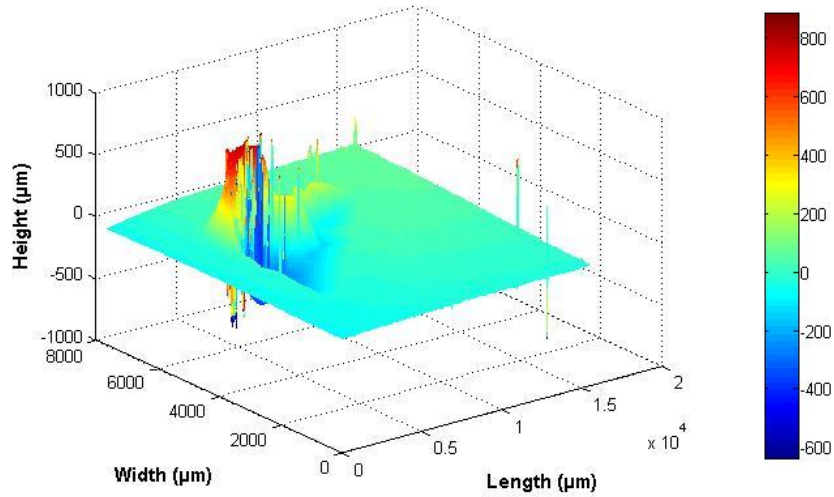
To measure this defect, the Alicona InfiniteFocus 3D measuring instrument, was used because it has lateral image stitching capabilities. Measuring parameters for Alicona InfiniteFocus used for this particular application are identified as follows:

- Field of view: 8 mm x 15 mm
- Depth of Field : 3 mm
- Number of Images : 5 rows x 7 columns (35 images)
- Lateral resolution: 8 μm
- Vertical resolution: 4 μm
- Stand-off distance: 17 mm
- Number of measuring points: 2161 x 4371

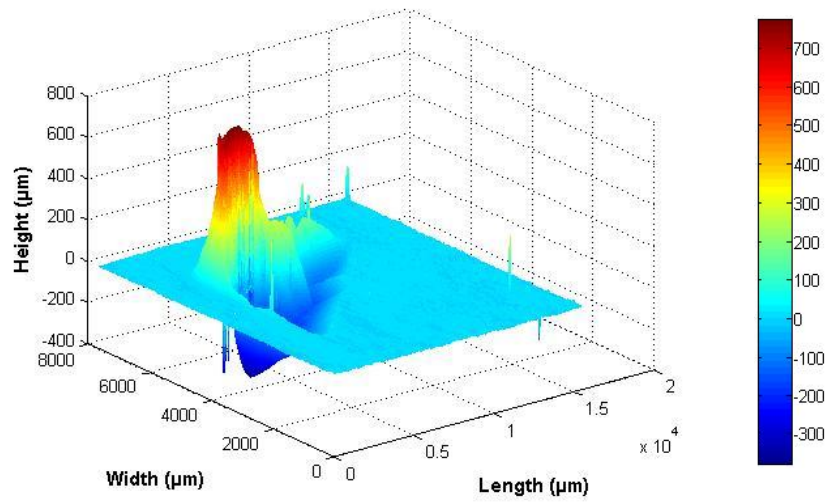


Figure 7-15 Surface defect (Defect ID – 4) embedded in the piston crown

The defect was measured five times repetitively, taking approximately 20 minutes to measure the defect each time. The raw data of the measured defect can be visualized in Figure 7-16 (a) which contains a large number of spurious spikes. The raw data was input into the novel algorithm for further analysis. In built filters in the algorithm remove the unwanted spikes from the data set and also removed the form of the surface resulting in the residual surface (see Figure 7-16 (b)).



(a)



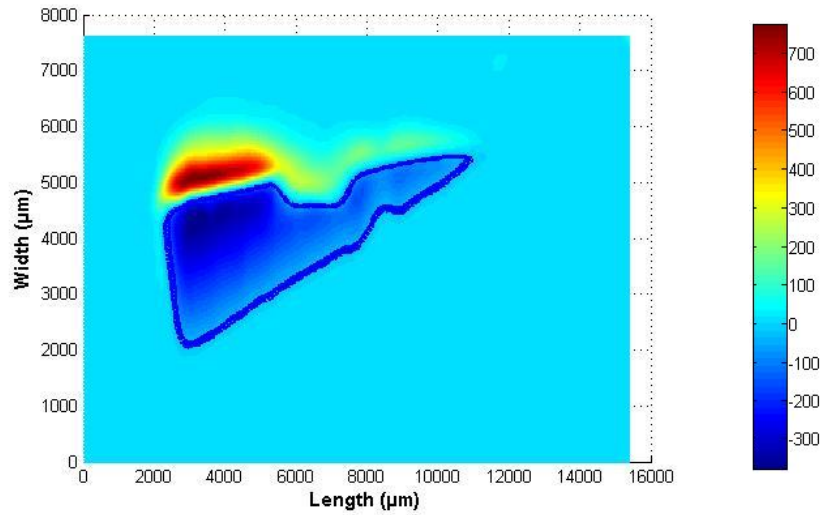
(b)

Figure 7-16 (a) Raw data (b) Residual surface

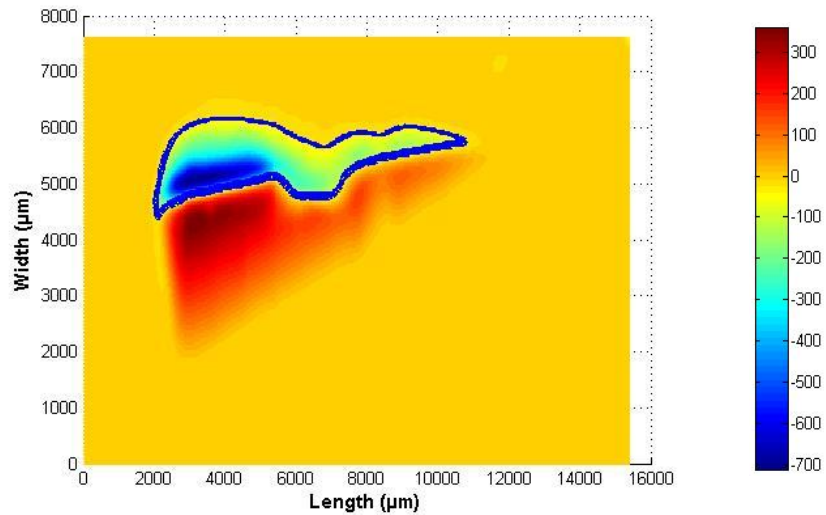
From the residual surface, a typical positive bump is observed on one of the edges of the surface defect. The defect was difficult to measure. Manual human driven measurement methods struggled to quantify this defect because there was high ambiguity in selecting the correct cross-section profile for measuring the depth/height of the defect and consequently reliable measurement of area and volume measurement was difficult. Again, the challenge for the application of the algorithm was to deal with the positive and negative aspects of the very large defect.

To resolve this issue for efficient quantification of both the positive and negative sides of the defect using the algorithm, a different method was developed and divided into two steps. In the first step, the boundary of the negative side was derived, using the normal operation of the algorithm, from the residual surface. Once the negative side of the defect was detected and quantified, in the second step, the residual surface data was inverted. Inversion of the residual surface data was again achieved by the scalar multiplication of the data matrix of the residual surface by minus one. By matrix inversion, the positive side of the defect became the negative side and negative side of the defect turned into the positive side. Inverse residual data was provided to the algorithm and the algorithm successfully detected the boundary of the defect.

Figure 7-17 (a) and Figure 7-17 (b) highlight the boundary of the negative side and the positive side of the defect respectively which were derived from the algorithm. It should be noted at this stage of the algorithm development that the catering for such a double sided defect requires an element of manual manipulation of the matrix (inversion operations). It is anticipated that further development of the software will include automated routines to cater for double sided defects with positive and negative attributes.



(a)



(b)

Figure 7-17 (a) Isolated negative part of the defect (b) Isolated positive part of the defect

Following the detection of the boundary, the algorithm computed the depth, area and volume individually for both sides of the defect as identified in Table 7-4. The average depth of the negative side of the defect was 421.4 μm and the maximum height of the defect was 722.2 μm . The computed average area and the average volume for the negative side were bigger than the positive side. The novel algorithm successfully computed all the quantities with a RSD value less than 2 %. Considering the large

number of data points in the measured surface, the algorithm took approximately one hour to quantify this defect. The computational time can be reduced by the implementing the algorithm; using parallel computing in a higher level language and/or in the form of executable code.

Table 7-4 Quantification of both positive and negative side of the Defect ID – 4

No. of Exp	Negative Defect			Positive Defect		
	Height (μm)	Area (μm^2)	Volume (μm^3)	Height (μm)	Area (μm^2)	Volume (μm^3)
1	420.5	1.24E+07	1.48E+09	734.9	7.36E+06	1.47E+09
2	418.6	1.25E+07	1.42E+09	705.7	7.15E+06	1.42E+09
3	415.7	1.25E+07	1.47E+09	720.2	7.35E+06	1.47E+09
4	423.2	1.27E+07	1.47E+09	719.4	7.35E+06	1.47E+09
5	428.8	1.28E+07	1.41E+09	730.9	7.14E+06	1.42E+09
Avg	421.4	1.26E+07	1.45E+09	722.2	7.27E+06	1.45E+09
%RSD	1.2	1.3	2.1	1.6	1.6	1.9

The piston crown example has demonstrated the capability of the algorithm to detect and quantify embedded critical surface defects. It has also demonstrated that the algorithm is capable of handling 3D data from both the Heliotis H3 and the Alicona InfiniteFocus instruments and datasets in the range from micrometres to tens of millimetres. The algorithm is capable of computing large 3D image stitched datasets, it can process large scale defects and provides a unique quantification solution.

7.3 Solder joints on a Printed Circuit Board (PCB)

The work reported here was the inspection of solder joints on a Printed Circuit Board (PCB). It should be noted that solder joints are not defects. The solder joints are formed using the deposition of molten Tin-led solder on the PCB track/pads. For the functional operation of the PCB it is important to know the height, area and volume of the solder joint in the process of quality assurance. As seen in previous sections, if the solder joints are measured using 3D instruments and the raw data is inverted then the novel algorithm can potentially be useful to quantify the solder joint.

In electronics manufacturing, inspection of the PCB is very important. As PCB assembly manufacturers aim for very high quality standard, it is important to detect poor quality solder joints because these will cause poor connection of the components with the PCB tracks. Hence it is very important to detect such defective solder joints in the early stages of the manufacturing process as the detection at later stages may be time consuming and costly to repair. Height, area and volume measurement of the solder joint is one of the key parameters to assess the quality of solder joints [161].

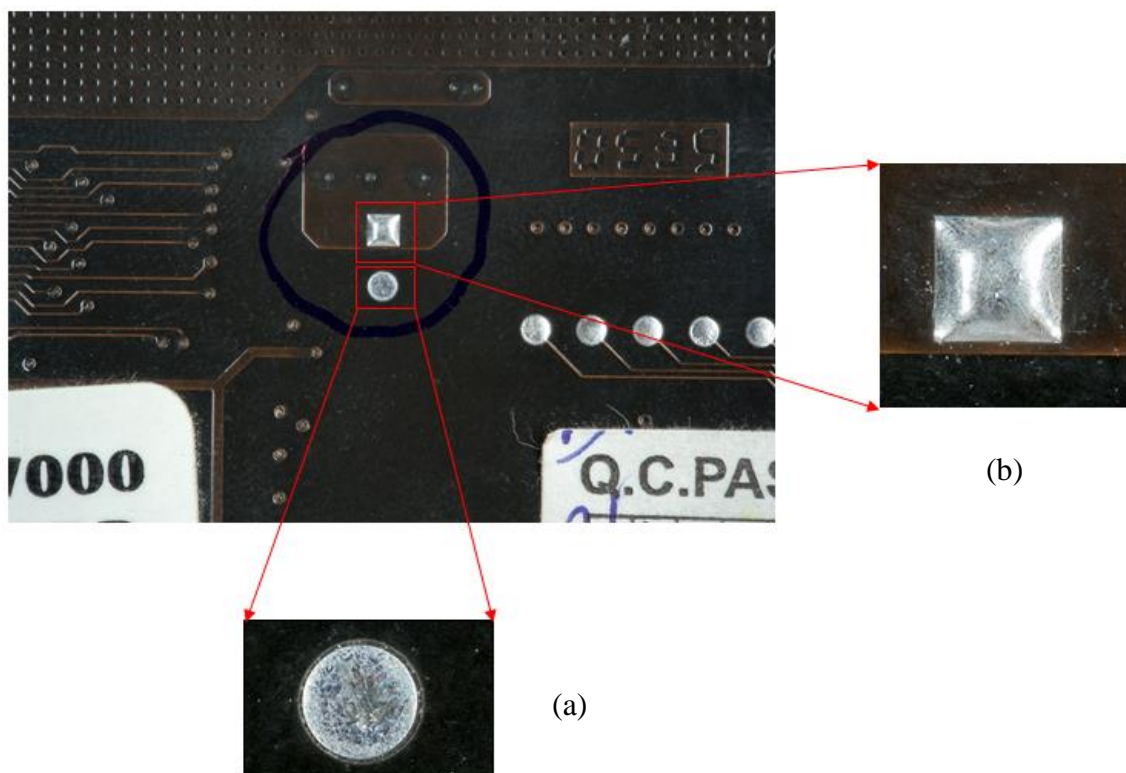


Figure 7-18 PCB (a) Circular solder joint (b) Square solder joint

To evaluate the capability of the Heliotis H3 unit and the algorithm, two different solder joints were assessed on a PCB (see Figure 7-18). A circular solder joint as shown in Figure 7-18 (a) was measured repetitively five times. The raw data of the circular solder joint can be seen in Figure 7-19 which was obtained from the Heliotis H3 unit. The raw data was inverted for further assessment using the algorithm.

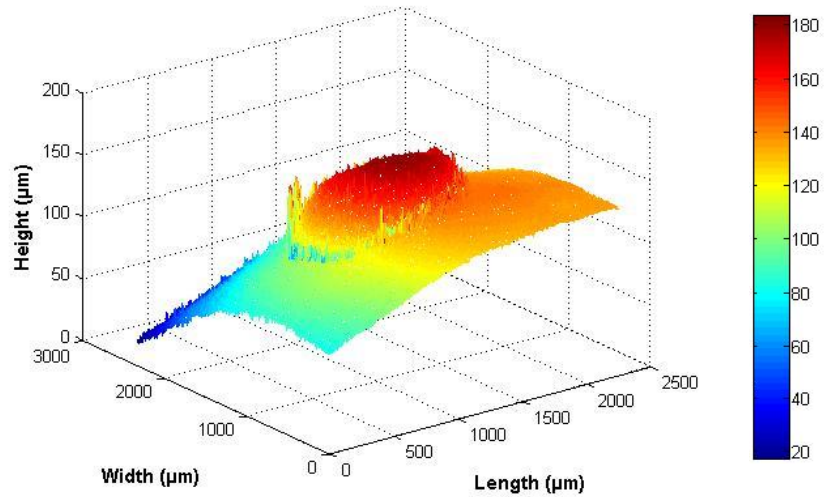
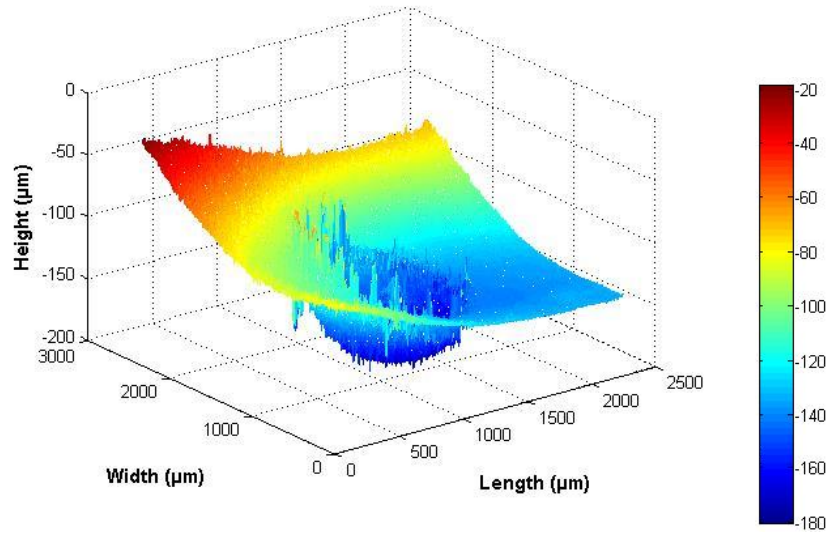
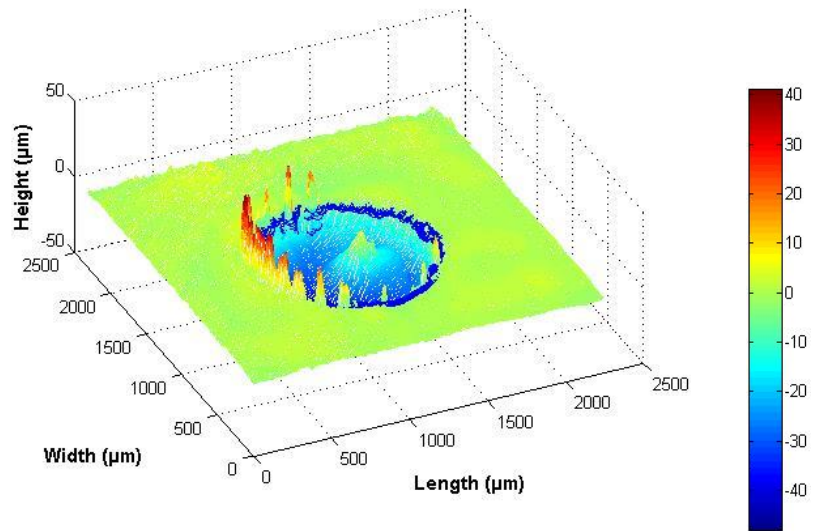


Figure 7-19 Raw data of circular solder joint

Figure 7-20 (a) highlights the inversion of the raw data which was achieved by scalar multiplication of minus one with the raw data. The algorithm generated the residual surface by removing the form of the surface. Once the residual surface was obtained the surface defect (on in this case surface feature) was derived as illustrated in the Figure 7-20 (b). The inverted data was reinverted back into its original format to visualise the solder joint in a form-free surface (see Figure 7-21). It can be clearly seen that the quality of the solder joint is not good as the solder paste is not distributed evenly in the solder joint. The solder bump should be a continuous rounded structure.



(a)



(b)

Figure 7-20 (a) Inverted raw data (b) Isolated circular solder joint

Table 7-5 Quantification of the circular solder joint

No.of Exp	Defect		
	Depth (μm)	Area (μm^2)	Volume (μm^3)
1	50.1	1123840	3.47E+07
2	49.6	1150304	3.32E+07
3	50.6	1123840	3.47E+07
4	49.7	1132864	3.42E+07
5	49.9	1131264	3.42E+07
Avg	50.0	1134422	3.42E+07
%RSD	0.8	1.0	1.8

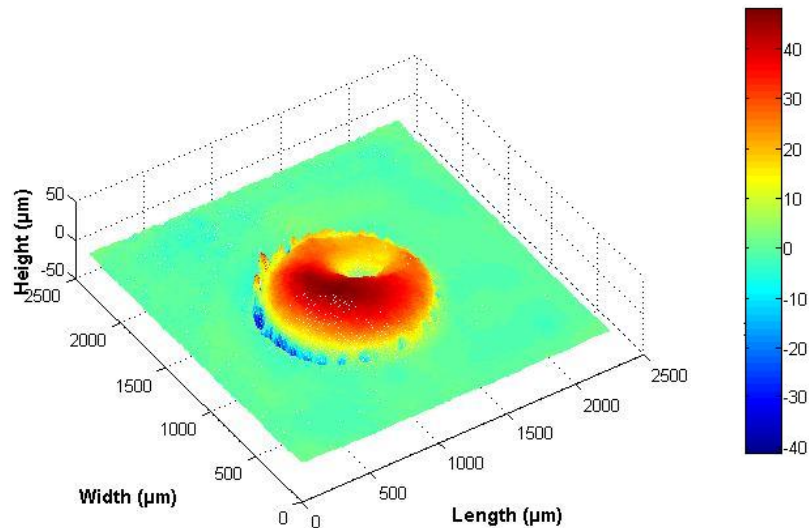


Figure 7-21 Isolated solder joint on the PCB surface

Table 7-5 highlights the geometric quantities of the solder joint computed using the algorithm, computing the average maximum height of the solder joint as being 50 μm with a RSD value of 0.8 %, the average area as being 1134422 μm^2 with 1 % of RSD and volume as being 34213400 μm^3 with a RSD value of 1.8 %

A square solder joint above the circular joint was measured repetitively five times. The raw data was obtained using the Heliotis H3 unit (see Figure 7-22) and it was again

inverted for further assessment using the algorithm. Figure 7-23 (a) highlights the inverted raw data of the square solder joint.

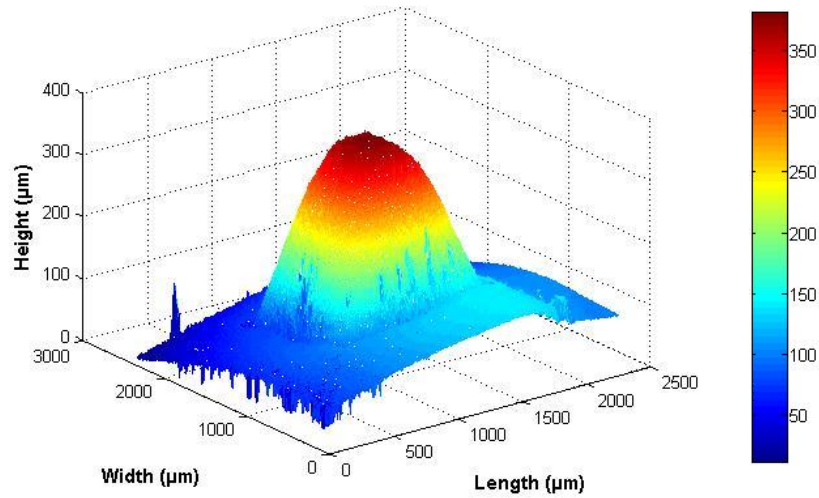
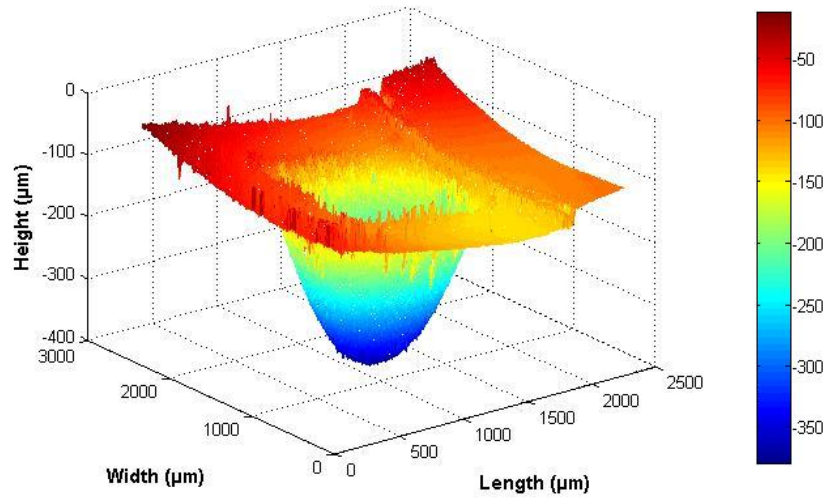


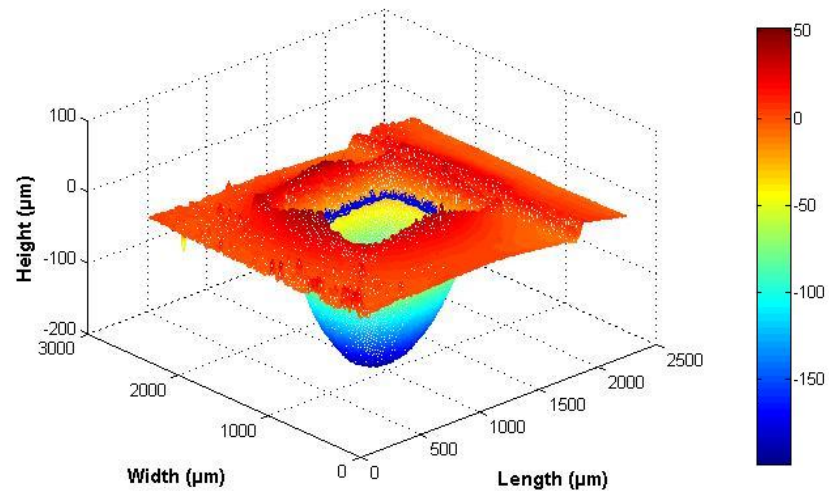
Figure 7-22 Square solder joint raw data

The algorithm computed the residual surface of the inverted measured data then it derived the boundary of the solder joint as identified in Figure 7-23 (b).

Once the detection and quantification was achieved, the inverted residual surface was again inverted into the original format for better visualization purposes (see Figure 7-24). Table 7-6 indicates the computed the height, area and volume of the solder joint using the algorithm. The average maximum height of the solder joint was 237.5 μm. The overall measurement RSD for all quantities was obtained at less than 1%.



(a)



(b)

Figure 7-23 (a) Inverted raw data (b) Isolated solder joint

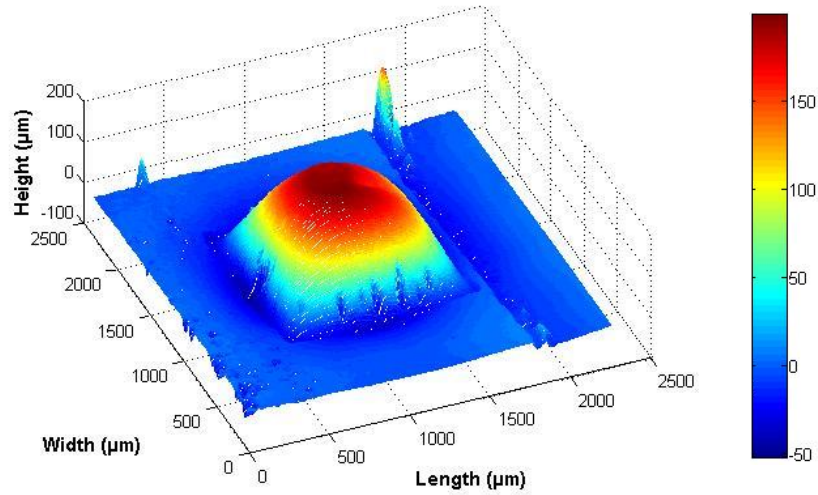


Figure 7-24 Isolated solder joint in the surface

Table 7-6 Quantification of the square solder joint

No.of Exp	Defect		
	Depth (μm)	Area (μm ²)	Volume (μm ³)
1	238.1	1214784	1.55E+08
2	237.1	1216256	1.54E+08
3	236.6	1213248	1.54E+08
4	237.8	1215936	1.55E+08
5	238.1	1214592	1.56E+08
Avg	237.5	1214963	1.55E+08
%RSD	0.3	0.1	0.5

This application demonstrated the successful automatic detection and quantification of PCB solder joints using the combination of the Heliotis H3 unit and the novel algorithm in 3D. It further reinforces the applicability of the software solution to a wide range of a surface defects and surface manufactured features.

7.4 Summary

In this chapter, automotive industrial components (bearing shell and piston crown) with embedded defects and solder joints on a PCB have been measured and quantified automatically in 3D.

Defects on the plain bearing were measured five times repetitively using the Heliotis H3 unit. Positive defects were observed on the concave side of the plain bearing and strategies were developed to quantify using the processing algorithm. The Heliotis H3 unit has demonstrated the successful measurement of the majority of the surface defects. However, defects embedded at critical locations such as on curved edges were measured with large amounts of measurement noise due to the small depth of field (1 mm) of the Heliotis H3 unit. It typically took 2 seconds to measure the surface defect. The algorithm successfully detected and extracted the defects from the free-form surfaces and quantified them automatically in 3D. However the algorithm currently cannot remove the measurement noise and to resolve this issue the measurement noise is eliminated manually.

The defect on the piston crown was measured using the Alicona InfiniteFocus. The Heliotis H3 unit did not have stitching capability in 3D to measure a large field of view and large depth of field. The surface defect on the piston crown was large (15 mm in length) compared to other defects (1 mm – 2 mm in length) hence the Heliotis H3 unit was unable to measure this defect. The Alicona InfiniteFocus took approximately 20 minutes to measure the defect. The defect on the piston crown was found to be distributed above and below the surface. The algorithm handled the positive defect successfully by inverting the raw data followed with detection and quantification of the defect. The algorithm took approximately one hour to detect and quantify both the positive and negative parts of the defect. The solder joints on the PCB were again measured using the Heliotis H3 unit. By inverting the raw data, the positive solder joints were quantified automatically in 3D.

The novel algorithm automatically detects and quantifies surface defects in 15 s to 20 s if measured using the Heliotis H3 unit. It has been demonstrated that the combination of the Heliotis H3 unit and the novel algorithm provides a high speed solution to measure and quantify surface defects on industrial components automatically in 3D

8 CONCLUSION & FUTURE WORK

8.1 Introduction

The research work presented in this thesis has been very challenging, because in order to achieve the objectives, expertise and motivation has had to be gained in two key underpinning disciplines:

- 3D measurement techniques
- 3D quantification techniques

Both of these disciplines could form research projects in their own right, and the Future Work identified in Section 8.3 offers further measurement and quantification issues that require more effort.

8.2 Conclusion

With reference to the aims and objectives identified in Chapter 1, key conclusions based on this research are presented as follows:

- This work has clearly demonstrated the feasibility of using the Rockwell and Vickers hardness test equipment to generate a variety of controlled and traceable standard defect artefacts on various substrates, both in terms of surface roughness and shape functions.
- Four non-contact metrology techniques were identified as being potential candidates for defect measurement. For the first time, these instruments have been evaluated in a comparative manner using standard calibrated slip-gauges to provide known step heights. From the step-height measurement, conclusions are made as follow; The Zygo NewView 5000 was the most repeatable but the least accurate instrument. The Alicona InfiniteFocus was the most accurate but less repeatable than the Zygo NewView 5000. The GFM MikroCAD Lite was the least repeatable and the least accurate instrument. The Heliotis H3 was slightly

less accurate than the Alicona InfiniteFocus and less repeatable than the Zygo NewView 5000.

- Standard defect artefacts have been used for the first time to complete a novel inter-comparison of the functional capabilities of the four selected instruments. From the standard defect artefact measurement, it was noted that the Alicona InfiniteFocus was a constantly repeatable instrument on the majority of the defects however the instrument struggled to measure surface defects on specularly reflective surfaces. The Alicona InfiniteFocus provided optics interchange ability and data stitching which was not the case in the Heliotis H3 unit.
- The measuring performance of the Zygo NewView 5000 was found to be inconsistent as the acquired data contained significant amounts of non-measuring data points due to nature of the defects. Moreover, the Zygo NewView 5000 was the slowest instrument thus this system was not deemed to be useful for the measurement of surface defects in production environments.
- The GFM MikroCAD Lite was identified as the least repeatable and least suitable instrument for measuring small defects and defects embedded on specularly reflective surfaces. However the GFM MikroCAD Lite system provided highest measuring volume with a high stand-off distance and high speed data acquisition.
- The Heliotis H3 unit was the most repeatable and fastest measuring instrument that measured defects on a range of rough substrates, hence the Heliotis was identified as the most suitable instrument for surface defect measurement in the context of this research. A total of 48 different standard defect artefacts have been measured repetitively five times on each instrument.
- An investigation of manual software methods using 3rd party packages for quantifying surface defects, suggests that such methods lead to significant issues of repeatability and reproducibility and rely heavily on operator subjectivity.

Hence a novel MATLAB based mathematical algorithm has been developed and implemented to quantify surface defects automatically in 3D.

- The implemented algorithm uses existing knowledge of filtration processes to separate topographical components of the surfaces. It has been identified that existing histogram based methods were not feasible for isolating surface defects in 3D thus a new method for considering the surface roughness component was implemented to isolate the surface defect. A unique mathematical approach has been adopted to measure depth, area and volume of the surface defect. This unique solution has been provided to detect a surface defect following with quantification of the defect automatically in 3D. The algorithm takes approximately 18 s to 20 s to compute the results.
- Currently the algorithm is capable of quantifying a single defect that has maximum area within the given field of view.
- Recognition has been given for the need to traceably test the algorithm using mathematically defined datasets. Profile and areal surface texture softgauges have just been developed by other researchers but defect softgauges do not exist. A mathematically data based defect has been developed which is dimensionless and multi-scalable. With known predefined mathematical geometry, the defect softgauge has been used to rigorously test the novel algorithm.
- Validation of the implemented algorithm has been demonstrated by developing a simulated known size geometrical shape defect. Issues of repeatability and reproducibility in the existing manual defect quantification methods are resolved in the implemented algorithm as the results shows no variations on quantifying a single defect multiple times, removing inspection subjectivity.
- Functional capabilities of the validated algorithm have been evaluated by quantifying a range of surface defects (different sizes and different shapes) embedded in substrates with different levels of surface roughness and different shape of substrates measured using the Heliotis H3 unit.

- Applicability of the software algorithm has been investigated. 3D measurement and quantification of defects on different industrial components have been demonstrated. Defects on a plain bearing and piston crown from the automotive industry have been measured and quantified. Solder joints on a PCB have been measured and uniquely quantified using the implemented algorithm.

Objectives and perceived novelty of this work were originally identified in Chapter 1 (Section 1.2) of this thesis. Table 8-1 identifies how well these objectives have been met and the resultant perceived novelty value of each element of the work.

Table 8-1 Objectives completion and resultant novelty

Objectives	Outcomes	Chapter	Novelty
1	A range of non-contact metrology instruments have been identified and evaluated. Focus Variation (FV), Coherence Scanning Interferometer (CSI), Digital Fringe Projection (DFP) and Parallel Optical Coherence Tomography (pOCT) techniques were selected for experiments to find the most suitable technique for defect measurement.	1	No novelty.
2	Different shapes of standard surface defect artefacts were generated using Rockwell and Vickers hardness test equipment on different substrates and different shapes of substrates. An Alicona InfiniteFocus instrument was used to measure the defects. A Talysurf Intra was used to measure surface roughness. DigitalSurf MountainMap was used to calculate roughness parameters and depth of the standard defect artefacts.	2	Low/Medium level of novelty in the context of the surface defect generation.
3	Accuracy and repeatability assessment of the Alicona InfiniteFocus , Zygo NewView 5000, GFM MikroCAD Lite and Heliotis H3 was achieved using 100 μm step height measurement. Different defect artefacts were measured using these instruments and results were compared.	3	Medium/High level of novelty with respect to surface defect measurement.

	The Heliotis H3 was chosen as the most appropriate tool for repeatable and accurate surface defect measurement in the context of this research work.		
4	Investigated methods to quantify the surface defect. Identified the need for an automatic defect quantification tool. MATLAB based mathematical algorithm has been designed developed and implemented to quantify surface defects automatically in 3D.	4	High level of novelty in terms of automatic defect quantification.
5	A standard mathematically defined scalable softgauge has been generated to validate the implemented mathematical algorithm. Evaluated the functional capabilities of the algorithm by quantifying a range of real standard defect artefacts measured using the Heliotis H3 automatically in 3D.	5	Very high level of novelty with respect to designing and implementing the defect softgauge, validating the novel algorithm and using standard defects artefacts.
6	Critical surface defects on industrial components were measured and quantified. Defects on automotive components (piston and plain bearing) and solder joints on a PCB were measured and quantified automatically in 3D.	6	Very high level of novelty in terms of quantifying surface defects and features automatically on a range of industrial components.

8.3 Future work

This research has already successfully demonstrated automatic quantification of the surface defect in 3D, however further time and effort still needs to be invested in various aspects of the work. The priority of the work has been to demonstrate novel working solutions, but code optimisation and execution speed are iterative in nature and should form part of further development.

The future priorities can be summarized as follows:

- To evaluate an uncertainty budget for the optical instruments to complete the traceability chain for developed standard defect artefacts. Noted that this is a global challenge being defined by NPL.
- Development and implementation of the algorithm to detect and quantify multiple defects in a given field of view. However, the threshold limit for defects needs to be identified before the implementation.
- Investigation of parallel computing methods that will help to quantify the surface defect faster than the current solution with the potential for on-line inspection.
- Investigate different classification techniques such as neural network, fuzzy logic and support vector machine techniques to classify surface suspicious features. Typical classification techniques are widely used in 2D for feature classification. Now that a robust, repeatable software solution has been developed extension to 3D is now possible.
- Investigate methods such as frequency analysis and wavelet analysis to develop bespoke filters that can detect typical measurement noise and remove it. Moreover, develop a filter that can precisely quantify the cut-off wavelength of the form of the surface to obtain the residual surface for more precise quantification of the defect in 3D.

- Extend the development of standard defects. Investigate different approaches to identify length, width, shape, radius (if any), and angle for further characterization of defects.
- Develop different shape and sized scratches or grooves as a standard artefact using laser machining techniques. This will allow the further evaluation of the functional behaviour of 3D instruments
- Develop new softgauges that simulate different types of defect; conical, hemisphere, scratch etc. to better define algorithm functionality.
- Further explore the use of the algorithm with other types of sensor system such as, confocal microscopy, atomic force microscopy, scanning laser triangulation, etc. It is anticipated that as long as a valid 3D dataset can be generated/supplied, the core algorithm should be able to cope.
- Develop a robust and user friendly graphical user interface for the algorithm, thus making the solution more available.
- Integrate the Heliotis H3 unit with linear motorized x-y-z stages to cover a larger field of view and a larger depth of field.
- Investigate different 3D data stitching techniques such as mechanical stitching and feature based technique. This will allow patching of 3D data obtained using the measuring instrument integrated with linear motorized stages.
- The ideas and concepts developed in this work need to be exploited for alternative industries such as agriculture, marine, medical etc.
- The majority of this work has considered negative defects, but opportunity for positive defects has been recognised. An additional action is to develop positive defect artefacts and investigate methodologies for better quantification.

REFERENCES

- [1] Jia H, Murphey Y, Shi J and Chang T. An intelligent real-time vision system for surface defect detection. ICPR 2004. Proceedings of the 17th International Conference on Pattern Recognition, UK, 239-242, 2004.
- [2] Chou P, Rao A, Sturzenbecker M, Wu F and Brecher V. Automatic defect classification for semiconductor manufacturing, *Machine Vision and Applications*, 9(4), 201-214, 1997.
- [3] Sidorov D, Wei W, Vasilyev L and Salerno S. Automatic defects classification with p-median clustering technique. 10th International Conference on Control, Automation, Robotics and Vision, ICARCV 2008, Vietnam, 775-780, 2008.
- [4] Satorres Martínez S, Gómez Ortega J, Gámez García J, Sánchez García A. A sensor planning system for automated headlamp lens inspection, *Expert Systems with Applications*, 36(5), 8768-8777, 2009.
- [5] Xue-wu Z, Yan-qiong D, Yan-yun L, Ai-ye S and Rui-yu L. A vision inspection system for the surface defects of strongly reflected metal based on multi-class SVM, *Expert Systems with Applications*, 38(5), 5930-5939, 2011.
- [6] Rosati G, Boschetti G, Biondi A and Rossi A. Real-time defect detection on highly reflective curved surfaces, *Optics and Lasers in Engineering*, 47(3-4), 379-384, 2009.
- [7] Sun Y, Bai P, Sun H and Zhou P. Real-time automatic detection of weld defects in steel pipe, *NDT & E International*, 38(7), 522-528, 2005.
- [8] Lin H. Computer-aided visual inspection of surface defects in ceramic capacitor chips, *Journal of Materials Processing Technology*, 189(1-3), 19-25, 2007.
- [9] Li W and Tsai D. Automatic saw-mark detection in multicrystalline solar wafer images, *Solar Energy Materials and Solar Cells*, 95(8), 2206-2220, 2011.

- [10] Wan G and Nosekabel E. Surface inspection on bodies in white in automotive industry. Proc SPIE 3824, Optical Measurement Systems for Industrial Inspection, Germany, 329-333, 1999.
- [11] Armesto L, Tornero J, Herraiez A and Asensio J. Inspection system based on artificial vision for paint defects detection on cars bodies. IEEE International Conference on Robotics and Automation (ICRA), 2011, USA, 1-4, 2011.
- [12] Prasad R and Ganesh N. Defect Analysis in Aerospace Systems Using Non-destructive Testing. National Seminar on Non-Destructive Evaluation, India, 2006.
- [13] Burchfield J. Lord Kelvin and the Age of the Earth. : Macmillan Publications; 1975.
- [14] Coleman D and Waters T. Fundamentals of touch trigger probing. : Touch Trigger Press; 1997.
- [15] BIPM I, IFCC I, IUPAC I and ISO OIML. International vocabulary of metrology—Basic and general concepts and associated terms (VIM), 3rd edn, JCGM 200, 2008.
- [16] Leach R. Optical Measurement of Surface Topography. : Springer Verlag; 2011.
- [17] Harvey G and Jones J. Small turbine blade inspection using laser strain techniques, Insight-Non-Destructive Testing and Condition Monitoring, 51(3), 137-139, 2009.
- [18] Ejaz N, Salam I and Tauqir A. An air crash due to failure of compressor rotor, Engineering Failure Analysis, 14(5), 831-840, 2007.
- [19] Xi N, Zhong P, Huang H, Yan H and Tao C. Failure investigation of blade and disk in first stage compressor, Engineering Failure Analysis, 7(6), 385-392, 2000.
- [20] Heredia-Ortiz M and Patterson E. On the industrial applications of Moiré and fringe projection techniques, Strain, 39(3), 95-100, 2003.
- [21] Andersson A. Evaluation and visualization of surface defects - a numerical and experimental study on sheet - metal parts. Proceedings of the 6th International Conference and Workshop on Numerical Simulation of 3D Sheet Metal Forming Process, USA, 113-118, 2005.

- [22] Sárosi Z, Knapp W, Kunz A and Wegener K. Detection of surface defects on sheet metal parts by using one-shot deflectometry in the infrared range. FLIR Technical Series - Application Note for Research & Science Zurich; 2010.
- [23] Beretta S, Blarasin A, Endo M, Giunti T and Murakami Y. Defect tolerant design of automotive components, *International Journal of Fatigue*, 19(4), 319-333, 1997.
- [24] Sikder A, Ramakrishnan V, Sinha M, Watkins V, Marks M and Shuler S. A methodology to quantify surface mar, *SAE International Journal of Materials & Manufacturing*, 5(1), 195-204, 2012.
- [25] Sharland S. A review of the theoretical modelling of crevice and pitting corrosion, *Corrosion Science*, 27(3), 289-323, 1987.
- [26] Wu W, Liu Z and Krysz D. Improving laser image resolution for pitting corrosion measurement using Markov random field method, *Automation in Construction*, 21, 172-183, 2012.
- [27] Fang H, Young D and Nesic S. Corrosion of mild steel in the presence of elemental sulfur, *Corrosion* 2008, 08637, 2008.
- [28] Fan K. A non-contact automatic measurement for free-form surface profiles, 10(4), 277-285, 1997.
- [29] Whitehouse D. *Surfaces and their measurement*. London: Hermes Penton Ltd; 2002.
- [30] Whitehouse DJ. Comparison between stylus and optical methods for measuring surfaces, *CIRP Annals - Manufacturing Technology*, 37(2), 649-653, 1988.
- [31] Li Y and Gu P. Free-form surface inspection techniques state of the art review, *Computer-Aided Design*, 36(13), 1395-1417, 2004.
- [32] Goldstein J, Newbury DE, Joy D, Lyman C, Echlin P and Lifshin E. *Scanning electron microscopy and X-ray microanalysis*. : Springer; 2003.
- [33] Eaton P and West P. *Atomic force microscopy*. : Oxford University Press, New York; 2010.

- [34] Moring I. Active 3-D vision system for automatic model-based shape inspection, *Optics and Lasers in Engineering*, 10, 149-160, 1989.
- [35] Blais F. Review of 20 years of range sensor development, *Journal of Electronic Imaging*, 13(1), 231-240, 2004.
- [36] Chen F, Brown G and Song M. Overview of three-dimensional shape measurement using optical methods, *Optical Engineering*, 39(1), 10-22, 2000.
- [37] Lee K and Park H. Automated inspection planning of free-form shape parts by laser scanning, *Robotics and Computer-Integrated Manufacturing*, 16(4), 201-210, 2000.
- [38] Huntley J. Automated analysis of speckle interferograms. In: Rastogi P, editor. *Digital speckle pattern interferometry and related techniques*: Wiley; 59-139, 2001.
- [39] Danielson B and Boisrobert C. Absolute optical ranging using low coherence interferometry, *Applied Optics*, 30(21), 2975-2979, 1991.
- [40] De Groot P and Deck L. Three-dimensional imaging by sub-Nyquist sampling of white-light interferograms, *Optics Letters*, 18(17), 1462-1464, 1993.
- [41] Windecker R and Tiziani H. Optical roughness measurements using extended white-light interferometry, *Optical Engineering*, 38(6), 1081-1087, 1999.
- [42] Petzing J, Coupland J and Leach R. Guide for the measurement of rough surface topography using coherence scanning interferometry, National Physics Laboratory, Measurement Good Practice Guide No. 116, 2010.
- [43] Hillmann W, Brand U and Krystek M. Capabilities and limitations of interference microscopy for two-and three-dimensional surface-measuring technology, *Measurement*, 19(2), 95-102, 1996.
- [44] Rhee H, Vorburger T, Lee J and Fu J. Discrepancies between roughness measurements obtained with phase-shifting and white-light interferometry, *Applied Optics*, 44(28), 5919-5927, 2005.

- [45] Leach R, Chetwynd D, Blunt L, Haycocks J, Harris P, Jackson K, Oldfield S and Reilly S. Recent advances in traceable nanoscale dimension and force metrology in the UK, *Measurement Science and Technology*, 17(3), 467, 2006.
- [46] Gao F, Leach R, Petzing J and Coupland J. Surface measurement errors using commercial scanning white light interferometers, *Measurement Science and Technology*, 19(1), 015303, 2008.
- [47] Windecker R, Franz S and Tiziani H. Optical roughness measurements with fringe projection, *Applied Optics*, 38(13), 2837-2842, 1999.
- [48] Ruiz P, Huntley J and Wildman R. Depth-resolved whole-field displacement measurement by wavelength-scanning electronic speckle pattern interferometry, *Applied Optics*, 44(19), 3945-3953, 2005.
- [49] Tomlins P and Wang R. Theory, developments and applications of optical coherence tomography, *Journal of Physics D: Applied Physics*, 38(15), 2519, 2005.
- [50] Beaufort E, Boccara A, Lebec M, Blanchot L and Saint-Jalmes H. Full-field optical coherence microscopy, *Optics Letters*, 23(4), 244-246, 1998.
- [51] Ducros M, Laubscher M, Karamata B, Bourquin S, Lasser T and Salathe R. Parallel optical coherence tomography in scattering samples using a two-dimensional smart-pixel detector array, *Optics Communications*, 202(1), 29-35, 2002.
- [52] Beer S, Zeller P, Blanc N, Lustenberger F and Seitz P. Smart pixels for real-time optical coherence tomography, *Electronic Imaging 2004*, 21-32, 2004.
- [53] Lambelet P. Parallel optical coherence tomography (pOCT) for industrial 3D inspection. *Proc SPIE 8082, Optical Measurement Systems for Industrial Inspection VII*, Germany, May, 80820X-80820X-12, 2011.
- [54] Reid G. Moiré fringes in metrology, *Optics and Lasers in Engineering*, 5(2), 63-93, 1984.
- [55] Asundi A. Computer aided Moiré methods, *Optics and Lasers in Engineering*, 18(3), 213-238, 1993.

- [56] D'Acquisto L, Fratini L and Siddiolo A. A modified Moiré technique for three-dimensional surface topography, *Measurement Science and Technology*, 13(4), 613, 2002.
- [57] Hocken R, Chakraborty N and Brown C. Optical metrology of surfaces, *CIRP Annals-Manufacturing Technology*, 54(2), 169-183, 2005.
- [58] Jones R and Wykes C. *Holographic and speckle interferometry.*: Cambridge University Press; 1989.
- [59] Lokberg O. Electronic speckle pattern interferometry. *Proc. SPIE 0673, Holography Applications, China*, 346-353, 1988.
- [60] Moore A and Tyrer J. Two-dimensional strain measurement with ESPI, *Optics and Lasers in Engineering*, 24(5), 381-402, 1996.
- [61] Shellabear M and Tyrer J. Application of ESPI to three-dimensional vibration measurements, *Optics and Lasers in Engineering*, 15(1), 43-56, 1991.
- [62] Srinivasan V, Liu H and Halioua M. Automated phase measuring profilometry of 3D diffuse objects, *Applied Optics*, 23, 3105-3108, 1984.
- [63] Jalkio J, Kim R and Case S. Three dimensional inspection using multistripe structured light, *Optical Engineering*, 24(6), 966-974, 1985.
- [64] Gorthi S and Rastogi P. Fringe projection techniques: whither we are? *Optics and Lasers in Engineering*, 48(2), 133-140, 2010.
- [65] Frankowski G and Hainich R. DLP-based 3D metrology by structured light or projected fringe technology for life sciences and industrial metrology. *Proc SPIE 7210 Emerging Digital Micromirror Device Based Systems and Applications, USA*, 72100C-72100C, 2009.
- [66] Huang P, Jin F and Chiang F. Quantitative evaluation of corrosion by a digital fringe projection technique, *Optics and Lasers in Engineering*, 31(5), 371-380, 1999.
- [67] Jang P, Arunkumar R, Long Z, Mott M, Okhuysen W, Su Y, Monts D, and Kirk P. Quantitative imaging evaluation of corrosion in Oak Ridge research reactor pool. *Proceedings of 32nd Annual Waste Management Symposium, USA*, 2006.

- [68] Spagnolo G and Ambrosini D. Diffractive optical element based sensor for roughness measurement, *Sensors and Actuators A: Physical*, 100(2), 180-186, 2002.
- [69] Lagarde J, Rouvrais C, Black D, Diridollou S and Gall Y. Skin topography measurement by interference fringe projection: a technical validation, *Skin Research and Technology*, 7(2), 112-121, 2001.
- [70] Jaspers S, Hopermann H, Sauermann G, Hoppe U, Lunderstädt R and Ennen J. Rapid in vivo measurement of the topography of human skin by active image triangulation using a digital micromirror device, *Skin Research and Technology*, 5(3), 195-207, 1999.
- [71] Nayar S and Nakagawa Y. Shape from focus: an effective approach for rough surfaces. *IEEE International Conference on Robotics and Automation, USA*, 218-225, 1990.
- [72] Noguchi M and Nayar S. Microscopic shape from focus using active illumination. *Proceedings of the 12th IAPR International Conference on Computer Vision & Image Processing, Israel*, 147-152, 1994.
- [73] Choi T and Yun J. Three-dimensional shape recovery from the focused-image surface, *Optical Engineering*, 39(5), 1321-1326, 2000.
- [74] Subbarao M and Choi T. Accurate recovery of three-dimensional shape from image focus, *IEEE Transactions on Pattern Analysis and Machine Intelligence*, 17(3), 266-274, 1995.
- [75] Danzl R, Helmlí F and Scherer S. Focus variation—a robust technology for high resolution optical 3D surface metrology, *Strojniški vestnik-Journal of Mechanical Engineering*, 57(3), 245-256, 2011.
- [76] Turnbull A, Mingard K, Lord J, Roebuck B, Tice D, Mottershead K, Fairweather N and Bradbury A. Sensitivity of stress corrosion cracking of stainless steel to surface machining and grinding procedure, *Corrosion Science*, 53(10), 3398-3415, 2011.
- [77] Mahat M, Aris A, Jais U, Yahya M, Ramli R, Bonnia N and Mamat M. A preliminary study on microbiologically influenced corrosion (MIC) of mild steel by

pseudomonas aeruginosa by using infinite focus microscope (IFM). AIP Conference Proceedings 1455, Malaysia , 117, 2010.

[78] Doyle P and Scala C. Crack depth measurement by ultrasonics: a review, Ultrasonics, 16(4), 164-170, 1978.

[79] Charlesworth J, Temple J and Andrew G. Engineering applications of ultrasonic time-of-flight diffraction. : Research Studies Press, UK, 1989.

[80] McKerrow P and Hallam J. An introduction to the physics of echolocation. Third National Conference on Robotics, Australia, 198-209, 1990.

[81] Jolic K, Nagarajah C and Thompson W. Non-contact, optically based measurement of surface roughness of ceramics, Measurement Science and Technology, 5(6), 671, 1994.

[82] Mondal S and Sattar T. An overview TOFD method and its mathematical model, NDT.net, 5(4), 2000.

[83] Raja J, Muralikrishnan B and Fu S. Recent advances in separation of roughness, waviness and form, Precision Engineering, 26(2), 222-235, 2002.

[84] Whitehouse D. Surfaces—a link between manufacture and function, Proceedings of the Institution of Mechanical Engineers, 192(1), 179-188, 1978.

[85] Whitehouse D. Handbook of surface metrology. : Taylor & Francis; 1994.

[86] Thomas T. Trends in surface roughness, International Journal of Machine Tools and Manufacture, 38(5), 405-411, 1998.

[87] Jiang X, Scott P, Whitehouse D and Blunt L. Paradigm shifts in surface metrology. Part I. Historical philosophy, Proceedings of the Royal Society A: Mathematical, Physical and Engineering Science, 463(2085), 2049-2070, 2007.

[88] Jiang X, Scott P, Whitehouse D and Blunt L. Paradigm shifts in surface metrology. Part II. The current shift, Proceedings of the Royal Society A: Mathematical, Physical and Engineering Science, 463(2085), 2071-2099, 2007.

- [89] Lou S, Zeng W, Jiang X and Scott P. Robust filtration techniques in geometrical metrology and their comparison, *International Journal of Automation and Computing*, 10(1), 1-8, 2013.
- [90] ISO 4287. Geometrical product specification (GPS). Surface texture: Profile method. Terms, definition and surface texture parameters, 1997.
- [91] Liu J and MacGregor J. Estimation and monitoring of product aesthetics: application to manufacturing of “engineered stone” countertops, *Machine Vision and Applications*, 16(6), 374-383, 2006.
- [92] ISO 11562. Geometrical product specifications (GPS)—surface texture: profile method—metrological characteristics of phase correct filters, 1996.
- [93] Zeng W, Jiang X and Scott P. Fast algorithm of the robust Gaussian regression filter for areal surface analysis, *Measurement Science and Technology*, 21(5), 055108, 2010.
- [94] Bodschwinn H and Brinkmann L. Chapter 4 : Advanced Gaussian Filter. In: L Blunt X Jiang, editor. *Advanced Techniques for Assessment Surface Topography*: London: Kogan Page Science; 2003.
- [95] Seewig J. Linear and robust Gaussian regression filters, *Journal of Physics: Conference Series* 13, UK, 254-257, 2005.
- [96] ISO 16610-31. Geometrical product specification (GPS) - Filtration. Part 31. Robust profile filters: Gaussian regression filters, 2010.
- [97] ISO 16610-71. Geometrical product specifications (GPS). Filtration. Part 71. Robust areal filters: Gaussian regression filters, 2012.
- [98] Krystek M. Form filtering by splines, *Measurement*, 18(1), 9-15, 1996.
- [99] Lou S, Jiang X and Scott P. Algorithms for morphological profile filters and their comparison, *Precision Engineering*, 36(3), 414-423, 2012.
- [100] Whitehouse D. *Handbook of surface and nanometrology*. : CRC press; 2011.
- [101] Newman T and Jain A. A survey of automated visual inspection, *Computer Vision and Image Understanding*, 61(2), 231-262, 1995.

- [102] Sahoo P, Soltani S and Wong A. A survey of thresholding techniques, *Computer Vision, Graphics, and Image Processing*, 41(2), 233-260, 1988.
- [103] Lee S, Chung S and Park R. A comparative performance study of several global thresholding techniques for segmentation, *Computer Vision, Graphics, and Image Processing*, 52(2), 171-190, 1990.
- [104] Glasbey C. An analysis of histogram-based thresholding algorithms, *Computer Vision, Graphics and Image Processing*, 55(6), 532-537, 1993.
- [105] Sezgin M and Sankur B. Survey over image thresholding techniques and quantitative performance evaluation, *Journal of Electronic Imaging*, 13(1), 146-168, 2004.
- [106] Liu S and Jernigan M. Texture analysis and discrimination in additive noise, *Computer Vision, Graphics, and Image Processing*, 49(1), 52-67, 1990.
- [107] Tsai D and Huang T. Automated surface inspection for statistical textures, *Image and Vision Computing*, 21(4), 307-323, 2003.
- [108] Chan C. Fabric defect detection by Fourier analysis, *IEEE Transactions on Industry Applications*, 36(5), 1267-1276, 2000.
- [109] Polzleitner W and Schwingskakl G. Quality classification of wooden surfaces using Gabor filters and genetic feature optimization. *Proc SPIE 3837, Intelligent Robots and Computer Vision XVIII, USA*, 220-231, 1999.
- [110] Lee C, Choi S. Surface defect inspection of cold rolled strips with features based on adaptive wavelet packets, *Institute of Electronics, Information and Communication Engineer Transactions on Information and Systems*, 80(5), 594-604, 1997.
- [111] Sari-Sarraf H and Goddard J. Robust defect segmentation in woven fabrics. *Proceedings of IEEE Computer Society Conference on Computer Vision and Pattern Recognition, USA*, 938-944, 1998.
- [112] Xie X. A review of recent advances in surface defect detection using texture analysis techniques, *Electronic Letters on Computer Vision and Image Analysis*, 7(3), 1-22, 2008.

- [113] Kong L, Cheung C, Jiang X, Lee W, To S, Blunt L and Scott P. Characterization of surface generation of optical microstructures using a pattern and feature parametric analysis method, *Precision Engineering*, 34(4), 755-766, 2010.
- [114] Otsu N. A threshold selection method from gray-level histograms, *Automatica*, 11, 285-296, 1975.
- [115] ISO 25178-2. Geometrical product specification (GPS)—surface texture: areal. Part 2. Terms, definitions and surface texture parameters, 2010.
- [116] Recknagel R, Kowarschik R and Notni G. High-resolution defect detection and noise reduction using wavelet methods for surface measurement, *Journal of Optics A: Pure and Applied Optics*, 2(6), 538, 2000.
- [117] Blunt L, Jiang X, Leach R, Harris P and Scott P. The development of user-friendly software measurement standards for surface topography software assessment, *Wear*, 264(5), 389-393, 2008.
- [118] ISO 5436-2. Geometrical product specifications (GPS) Surface texture: Profile method, *Measurement standards, Software measurement standards*, 2012.
- [119] Harris P, Smith I, Leach R, Giusca C, Jiang X and Scott P. Software measurement standards for areal surface texture parameters: Part 1—algorithms, *Measurement Science and Technology*, 23(10), 105008, 2012.
- [120] Harris P, Smith I, Wang C, Giusca C and Leach R. Software measurement standards for areal surface texture parameters: Part 2—comparison of software, *Measurement Science and Technology*, 23(10), 105009, 2012.
- [121] Leach R. Some issues of traceability in the field of surface topography measurement, *Wear*, 257(12), 1246-1249, 2004.
- [122] Leach R, Giusca C and Coupland J. Advances in calibration methods for micro- and nanoscale surfaces. *Proc. SPIE 8430, Optical Mirco and Nanometrology IV*, 84300H, 2012.
- [123] www.rubert.co.uk, Assessed: September, 2012.
- [124] www.vlsistandards.com, Assessed: September, 2012.

- [125] Chandler H. Hardness testing. : ASM International; 1999.
- [126] BS EN ISO 6508-1. Metallic materials - Rockwell hardness test - Test method, , 2005.
- [127] BS EN ISO 6507-1. Metallic materials - Vickers hardness test - Test method, , 2005.
- [128] www.digitalsurf.fr/en/index.html, Assessed: March, 2012.
- [129] <http://www.aliconaco.uk>, Assessed: March, 2012.
- [130] <http://www.zygo.com>, Assessed: March, 2012.
- [131] <http://www.gfm3d.com>, Assessed: June, 2012.
- [132] <http://www.heliotis.ch>, Assessed: June, 2012.
- [133] Danzl R, Helml F and Scherer S. Focus variation - a new technology for high resolution optical 3D surface metrology. Proceedings of the 10th International Conference of the Slovenian Society for Non-Destructive Testing, Slovenia, 2009.
- [134] Danzl R, Helml F, Rubert P and Prantl M. Optical roughness measurements on specially designed roughness standards. Proc SPIE 7102, Optical Fabrication, Testing and Metrology III, UK, 71020M, 2008.
- [135] Leach R, Brown L, Jiang X and Blunt R. Guide to the Measurement of Smooth Surface Topography using Coherence Scanning Interferometry, Measurement Good Practice Guide No. 108. 2008.
- [136] NewView 5000 Operating Manual OMP-0423H, Zygo Corporation.
- [137] Salvi J, Pages J and Batlle J. Pattern codification strategies in structured light systems, Pattern Recognition, 37(4), 827-849, 2004.
- [138] Wang B, Lohry W, Zhang S and Hu H. Development of a digital fringe projection technique to characterize the transient behaviour of wind-driven droplet/rivulet flows, American Institute of Aeronautics and Astronautics(AIAA) Aerospace Science Meeting, USA, January 2012.

- [139] Zhang S. Recent progresses on real-time 3D shape measurement using digital fringe projection techniques, *Optics and Lasers in Engineering*, 48(2), 149-158, 2010.
- [140] <http://www.gfm3d.com>, Assessed: August, 2012.
- [141] Beer S and Seitz P. Real-time tomographic imaging without x-rays: a smart pixel array with massively parallel signal processing for real-time optical coherence tomography performing close to the physical limits, *Research in Microelectronics and Electronics*, 135-138, 2005.
- [142] Beer S, Zeller P, Blanc N, Lustenberger F and Seitz P. Smart pixels for real-time optical coherence tomography. *Proc. SPIE 5302, Three-Dimensional Image Capture and Applications VI, USA*, 21-32, 2004.
- [143] Gilgen HH, Novak RP, Salathe RP, Hodel W and Beaud P. Submillimeter optical reflectometry, *Journal of Lightwave Technology*, 7(8), 1225-1233, 1989.
- [144] Huang D, Swanson E, Lin C, Schuman J, Stinson W, Chang W, Hee M and Flotte T. Optical coherence tomography, *Science*, 254(5035), 1178-1181, 1991.
- [145] Schmitt JM. Optical coherence tomography (OCT): a review, *IEEE Journal of Selected Topics in Quantum Electronics*, 5(4), 1205-1215, 1999.
- [146] Bourquin S, Monterosso V, Seitz P and Salathé R. Video-rate optical low-coherence reflectometry based on a linear smart detector array, *Optics Letters*, 25(2), 102-104, 2000.
- [147] Beer S and Seitz P. Real-time tomographic imaging without x-rays: a smart pixel array with massively parallel signal processing for real-time optical coherence tomography performing close to the physical limits, *Research in Microelectronics and Electronics*, 135-138, 2005.
- [148] ISO 10360-2. Geometrical product specifications (GPS) Acceptance and reverification tests for coordinate measuring machines (CMM). CMMs used for measuring linear dimensions, 2010.
- [149] <http://www.digitalsurf.fr/en/index.html>, Assessed: February, 2012.

- [150] BIPM I, IFCC I and ISO I. Evaluation of measurement data-Guide to the expression of uncertainty in measurement, 2008.
- [151] MATLAB R. The MathWorks, Inc., Natick, MA, 2012.
- [152] ISO 16610 series. Geometrical product specifications (GPS) - Filtration, 2010.
- [153] ISO 25178-3. Geometrical product specification (GPS)—surface texture: areal. Part 3. Specification operators, 2008.
- [154] Zeng W, Jiang X, Scott PJ and Xiao S. A fast algorithm for the high order linear and nonlinear Gaussian regression filter. 9th International Conference of the European Society for Precision Engineering and Nanotechnology, Spain, 2009.
- [155] Sezgin M. Survey over image thresholding techniques and quantitative performance evaluation, *Journal of Electronic Imaging*, 13(1), 146-168, 2004.
- [156] Senthilkumaran N and Rajesh R. Edge detection techniques for image segmentation—a survey of soft computing approaches, *International Journal of Recent Trends in Engineering*, 1(2), 250-254, 2009.
- [157] <http://www.mathworks.co.uk/help/images/ref/regionprops.html>, Accessed: April 2012.
- [158] <http://www.mathworks.co.uk/help/images/ref/bwboundaries.html>, Assessed: April 2012.
- [159] Nie M, Liu X and Jiang X. Design of softgauge for surface profile evaluation. *Journal of Physics: Conference Series* 48, China, 138, 2006.
- [160] Manning J. Internal combustion engine design. UK: Ricardo UK Limited; 2012.
- [161] Guerra E and Villalobos J. A three-dimensional automated visual inspection system for SMT assembly, *Computers & Industrial Engineering*, 40(1–2), 175-190, 2001.